Jaeger, J.M., Gulick, S.P.S., LeVay, L.J., and the Expedition 341 Scientists
Proceedings of the Integrated Ocean Drilling Program, Volume 341

Expedition 341 summary[1]

J.M. Jaeger, S.P.S. Gulick, L.J. LeVay, H. Asahi, H. Bahlburg, C.L. Belanger, G.B.B. Berbel, L.B. Childress, E.A. Cowan, L. Drab, M. Forwick, A. Fukumura, S. Ge, S.M. Gupta, A. Kioka, S. Konno, C.E. März, K.M. Matsuzaki, E.L. McClymont, A.C. Mix, C.M. Moy, J. Müller, A. Nakamura, T. Ojima, K.D. Ridgway, F. Rodrigues Ribeiro, O.E. Romero, A.L. Slagle, J.S. Stoner, G. St-Onge, I. Suto, M.H. Walczak, and L.L. Worthington[2]

Chapter contents

Abstract

Global climate during the Neogene is distinguished by the transition into a colder, more variable world dominated by the onset and intensification of major Northern Hemisphere glaciations. This transition into the icehouse world corresponds to a global increase in erosion rates and sediment delivery to ocean basins. The effects of this increased erosion may be profound, as analyses of orogenic belts worldwide have shown that Earth systems cannot be considered to be the product of a series of distinct, decoupled tectonic and climatic processes. Rather, there is complex interplay between crustal deformation, exhumation, and climate systems. Exhumation plays a key role in controlling the regional distribution of metamorphic rocks, local climate change, and the development of structures throughout an orogen. Tectonic processes influence regional climate conditions by raising mountains that alter orographic precipitation patterns. The Neogene climate changes, in turn, likely affected tectonic processes through changes in erosion rates, which redistributed mass and subsequently altered stress regimes in orogenic wedges. Analytical models examining the coupling between glacial erosion and orogenic processes reveal that glacial erosion can significantly modify the patterns and rates of deformation in an orogenic wedge. A critical question is: At which stage of the deteriorating Neogene climate is an orogen ultimately driven into a subcritical state? And does this state lead to increased exhumation in the glaciated core of a mountain belt, enhanced topographic relief, and migration of the locus of sediment accumulation to the toe of an orogen thus impacting deformation patterns?

Addressing the linkages between global climate change, modification of surficial process dynamics, and subsequent tectonic responses requires integrated studies of orogenic and sedimentary systems in areas where specific end-members of the problem are encountered. The Gulf of Alaska borders the St. Elias orogen of Alaska and Canada, the highest coastal mountain range on Earth and the highest range in North America. This orogen is <30 m.y. in age, and mountain building occurred throughout a period of significant global climate change. This situation allowed Integrated Ocean Drilling Program Expedition 341 to examine the response of an orogenic system to the climatically driven establishment of a highly erosive glacial system. Additionally, the implications of Neogene glacial growth in the circum-North Pa-

---

[1] Jaeger, J.M., Gulick, S.P.S., LeVay, L.J., Asahi, H., Bahlburg, H., Belanger, C.L., Berbel, G.B.B., Childress, L.B., Cowan, E.A., Drab, L., Forwick, M., Fukumura, A., Ge, S., Gupta, S.M., Kioka, A., Konno, S., März, C.E., Matsuzaki, K.M., McClymont, E.L., Mix, A.C., Moy, C.M., Müller, J., Nakamura, A., Ojima, T., Ridgway, K.D., Rodrigues Ribeiro, F., Romero, O.E., Slagle, A.L.,Stoner, J.S., St-Onge, G., Suto, I., Walczak, M.H., and Worthington, L.L., 2014. Methods. *In* Jaeger, J.M., Gulick, S.P.S., LeVay, L.J., and the Expedition 341 Scientists, *Proc. IODP,* 341: College Station, TX (Integrated Ocean Drilling Program). doi:10.2204/iodp.proc.341.101.2014

[2] **Expedition 341 Scientists' addresses.**

cific reach beyond the issue of tectonic response to increased glacial erosion and exhumation. As climate conditions determine the timing and patterns of precipitation, they control glacial dynamics, erosion, and sediment/meltwater and chemical fluxes to the ocean. Establishing the timing of northwestern Cordilleran ice sheet advance–retreat cycles in southern Alaska will address a major challenge in Neogene paleoclimatology: to determine whether glacial advances occurred synchronously around the world and what the driving mechanisms were for global millennial-scale warming–cooling cycles. Evidence for substantial changes in surface productivity in the Gulf of Alaska since the Last Glacial Maximum indicates that millennial-scale climate changes and eustasy in the northeast Pacific Ocean have a first-order effect on primary productivity and marine ecosystems. Thick Pleistocene glacimarine deposits of the Gulf of Alaska continental margin contain a rich history of climate change recorded in both proxy climate data and sediment accumulation rates that can help decipher the architecture of massive Neogene high-latitude Northern Hemisphere continental margin sedimentary sequences. Exceptionally high rates of glacigenic sediment accumulation in this region also allow for the development of a paleomagnetic record of geomagnetic field variability on submillennial scales to assess geomagnetic persistence, a signature of the mantle's influence on the geodynamo and the paleomagnetic record.

A cross-margin transect was drilled during Expedition 341 to investigate the northeast Pacific continental margin sedimentary record formed during orogenesis within a time of significant global climatic deterioration in the Pliocene–Pleistocene that led to the development of the most aggressive erosion agent on the planet, a temperate glacial system.

Major objectives for drilling in the Gulf of Alaska were as follows:

- Document the tectonic response of an active orogenic system to late Miocene to recent climate change;
- Establish the timing of advance and retreat phases of the northwestern Cordilleran ice sheet to test its relation to dynamics of other global ice sheets;
- Implement an expanded source-to-sink study of the complex interactions between glacial, tectonic, and oceanographic processes responsible for creation of one of the thickest Neogene high-latitude continental margin sequences;
- Understand the dynamics of productivity, nutrients, freshwater input to the ocean, and surface and subsurface circulation in the northeast Pacific and their role in the global carbon cycle; and
- Document the spatial and temporal behavior during the Neogene of the geomagnetic field at extremely high temporal resolution in an undersampled region of the globe.

Drilling during Expedition 341 recovered a 3240 m sedimentary record that extends from the Late Pleistocene/Holocene through the middle Miocene. Drilling at Sites U1417 and U1418 recovered distal and proximal deepwater sedimentary records, respectively. Site U1417 contains a complete and continuous interval from the mudline to 220.4 m core composite depth below seafloor (CCSF-D), the base of which was dated shipboard to 1.7–1.8 Ma, and additional material was recovered to 709 m core depth below seafloor (CSF-A). Site U1417 contains no apparent hiatuses through the late Miocene based on initial shipboard biostratigraphy and magnetostratigraphy. Site U1418 contains a complete and continuous interval from the mudline to 271 m CCSF-D, which was dated shipboard to 0.2–0.3 Ma, and additional material was recovered to 941 m CSF-A. Site U1418 contains no apparent hiatuses through 1.2 Ma based on initial shipboard chronostratigraphy. Drilling at Sites U1419 and U1421 sampled the transitional environment along the continental slope. Site U1419 is located on a small ridge at 780 m water depth between two large shelf-crossing glacial troughs, whereas Site U1421 is located downslope of the Bering Trough. Site U1419 contains a complete and continuous interval from the mudline to 100 m CCSF-D and recovered core to ~177 m CCSF-B. Shipboard chronostratigraphy indicates the cored interval is younger than 0.3 Ma, and oxygen isotopes of foraminifers analyzed immediately postcruise further constrain the recovered interval to span <0.06 m.y. Site U1421 contains a continuous interval to ~30 m CCSF-D, and an interval to 694 m CSF-A was recovered that accumulated in <0.3 m.y. based on shipboard chronostratigraphy. Lastly, Site U1420 is located most proximal to the orogen on the continental shelf within, but near the flank of, the shelf-crossing Bering Trough. Site U1420 cores consist of drilled clasts, lonestones, diamict, and mud that were deposited <0.78 m.y. ago based on shipboard biostratigraphy and magnetostratigraphy. All Expedition 341 sites reveal notable changes in seismic reflection facies and stratigraphy that can be integrated at the nested core–downhole log–seismic reflection profile scales.

A remarkable expedition discovery is the substantial sediment volume accumulating on the shelf, slope, and deep sea fan since the early Pleistocene intensification of Northern Hemisphere glaciation and more significantly since the mid-Pleistocene transition. The Expedition 341 cross-margin transect discovered

transitions in sediment accumulation rates from >100 m/m.y. in the distal fan to >800 m/m.y. in the proximal fan to >1000 m/m.y. on the slope and continental shelf that provide a telescoping view of strata formation from the Miocene to the Holocene. All five sites sampled Middle Pleistocene to recent sediment and demonstrate exceptional accumulation rates. The 709 m of sediment recovered at Site U1417 records Miocene to recent deposition in the distal Surveyor Fan, including the onset of glaciation at the Pliocene/Pleistocene boundary when sedimentation rates doubled to ~100 m/m.y. Site U1418 contains an expanded Middle to Late Pleistocene sedimentary record that also includes significant increases in sedimentation from ~400 m/m.y. in the Middle Pleistocene to >1200 m/m.y. in the Late Pleistocene. Slope Site U1421 and shelf Site U1420, both proximal to the Bering Glacier during glaciations, provide cores penetrating thick sequences of poorly sorted glacigenic sediments ranging from mud to boulders, accumulating at a rate of at least 1 km/m.y. Slope Site U1419 is slightly west of the Bering Trough mouth and also has exceptional Late Pleistocene sedimentation rates (~3 km/m.y.).

Stratal lithofacies span from biogenic ooze to clast-rich diamict, both punctuated with ash, indicating a dynamic Neogene depositional environment. Lithofacies were interpreted shipboard as reflecting deposition from suspension fallout, sediment gravity flows, large-scale mass wasting, ice rafting, variation in organic productivity/preservation, and subaerial volcanic eruptions. Pleistocene strata are dominated by glacigenic sediments at all sites. The retrieval of Holocene interglacial sediments and microfossils at slope and fan sites provides a means to identify comparable interstadial periods in the deeper sedimentary record. An exceptional shipboard paleomagnetic chronology and a biosiliceous and calcareous biostratigraphy provide a temporal framework to guide future analyses of particular glacial–interglacial periods. Shipboard analyses indicate that sedimentation at slope and fan sites corresponds to major global Pleistocene climate patterns. A notable discovery at Site U1418 is that proximal deepwater sediment depocenters can contain an expanded record of fjord-like glacimarine facies during periods of maximum glacigenic sediment accumulation. Site U1420 demonstrates the potential for extremely thick Pleistocene depocenters in shelf settings where accommodation space can be maintained; consequently, individual glacial advance–retreat facies cycles can be seismically mapped. Postcruise analyses of sediment provenance will constrain this locus of erosion, linking it to onshore patterns of exhumation to ultimately test whether rapid erosion has the potential to lead to positive feedback in exhumation in an active orogen.

Introduction

Global climate during the Neogene to Quaternary is distinguished by the transition into a colder, more variable world dominated by the onset and intensification of major Northern Hemisphere glaciations (Zachos et al., 2001; Lisecki and Raymo, 2005). Corresponding to this alteration is a generally acknowledged global increase in sediment accumulation in both continental and marine sedimentary basins (Donnelly, 1982; Molnar and England, 1990; Zhang et al., 2001; Hay et al., 2002; Molnar, 2004; Willett, 2010), which is attributed to increased erosion in orogenic belts related to larger amplitude climate fluctuations (Zhang et al., 2001; Willett, 2010). For many orogenic settings, this increased erosion may be driven by the expansion of alpine ice, but the direct correlation between increased erosion and specific climate drivers is lacking. However, the consequences of increased erosion are potentially far reaching. Worldwide analyses of orogenic belts (Koons, 1995; Pinter and Brandon, 1997; Pavlis et al., 1997; Zeitler et al., 2001; Hoth et al., 2006; Roe et al., 2006; Stolar et al., 2006; Whipple, 2009; Koons et al., 2013) have shown that Earth systems cannot be considered to be the product of a series of distinct, decoupled tectonic and climatic processes. Rather, there is complex interplay between crustal deformation, exhumation, and climate systems.

Exhumation plays a key role in controlling the regional distribution of metamorphic rocks, local climate change, and development of structures throughout an orogen. As tectonic processes influence regional climate by raising mountains that enhance orographic precipitation intensity, the Neogene–Quaternary climate transition likely affected tectonic processes through changes in erosion rates that redistributed mass and subsequently altered stresses in orogenic wedges (Willet, 1999; Roe et al., 2006; Whipple, 2009). Analytical models examining the coupling between glacial erosion and orogenic processes reveal that glacial erosion can significantly modify the patterns and rates of deformation in an orogenic wedge (Roe et al., 2006; Tomkin, 2007; Tomkin and Roe, 2007). Glacial climate interacts with mountain building through erosion and sediment transport, dispersal, and accumulation. Within a critically tapered wedge, erosion in the inner part of an orogen results in increased thrusting in an attempt to maintain critical taper (e.g., Berger et al., 2008a; Whipple, 2009). Deposition of the eroded sediments in the outer part of an orogen can, in turn, suppress deformation due to loading (e.g., Simpson, 2010; Worthington et al., 2010). A critical question: At what stage of the deteriorating Neogene climate is an orogen ultimately driven into subcriticality? And does this lead to increased exhumation in the glaciated core of a mountain belt, enhanced topographic relief, and migration of the locus of sediment accumulation to the toes of an orogen, which impacts deformation patterns?

Addressing the linkages between global climate change, modification of surficial process dynamics, and subsequent tectonic responses requires integrated studies of orogenic systems in areas that exemplify specific end-members of the problem. The Gulf of Alaska borders the St. Elias orogen of Alaska and Canada, the highest coastal mountain range on Earth and the highest range in North America (Fig. F1). This orogen is younger than 30 Ma, and mountain building occurred during a period of significant global climate change (Fig. F2), allowing this expedition to examine the response of an orogenic system to the establishment of a highly erosive glacial system (Hallet et al., 1996; Jaeger et al., 1998; Sheaf et al., 2003; Berger et al., 2008b; Enkelmann et al., 2010; Spotila and Berger, 2010; Finzel et al., 2011; Headley et al., 2013). The sediments emanating from the orogen are deposited in a geographically relatively confined area offshore, providing a rare opportunity to use the stratigraphic record to quantify spatial and temporal variations in the erosional flux from land to sea. Geological processes in southern Alaska are comparable to those observed in the Himalayan orogeny and include extremely high erosion rates, active faulting beneath mountains and alpine glaciers, and orogenesis coincident with extensive glacial cover. Important advantages of Alaska over the Himalayas include the proximity of a high coastal mountain range next to an energetic ocean with essentially no intervening basins to trap sediment. Therefore, tectonic and climatic signals have the potential to be quickly recorded in offshore areas with little modification resulting from long transport in rivers or temporary storage in intervening sedimentary basins.

Additionally, the implications of Neogene glacial growth in the circum-North Pacific reach beyond a tectonic response to increased glacial erosion and exhumation. As climate determines the timing and patterns of precipitation, it controls glacial dynamics, erosion, and sediment/meltwater fluxes to the ocean. Establishing the timing of northwestern Cordilleran ice sheet (NCIS) advance–retreat cycles will address a major challenge in Quaternary paleoclimatology, which is to know whether glacial advances occurred globally synchronously, and what the driving mechanisms were for potentially propagating millennial-scale warming–cooling cycles around the world (oceanic, atmospheric, or both) (Clapperton, 2000; Mix et al., 2001; Hill et al., 2006). Many paleoclimate and glaciologic records provide strong evidence for millennial-scale climate change along the Gulf of Alaska margin (i.e., Last Glacial Maximum [LGM], Younger Dryas, early Holocene Hypsithermal, and late Holocene Neoglacial) (Peteet and Mann, 1994; Mann et al., 1998; Calkin et al., 2001; Davies et al., 2011). However, the timing and character of these variations in relation to North Atlantic or Southern Ocean records over the Pliocene–Pleistocene are largely still unknown. NCIS glaciation is fueled by low rates of evapotranspiration, extensive North Pacific moisture delivery, and extreme rates of precipitation due to the predominant storm track coupled with orographic lift along the high coastal mountain range (Royer, 1982; Emile-Geay et al., 2003; Neal et al., 2010). Melting of this ice and return of the freshwater to the modern coastal ocean results in high specific discharge, presently two- to sixfold higher than the Amazon and Congo (Neal et al., 2010). This discharge creates nearly estuarine-like salinity conditions in the coastal ocean and is a substantial contributor to the freshwater budget of the Bering Sea and the Arctic Ocean (Weingartner et al., 2005), which in turn may impact the thermohaline stability of the North Atlantic during interglacials (Keigwin and Cook, 2007). North Pacific Intermediate Water episodically forms in the Gulf of Alaska (You et al., 2000) but may have been much more significant during the last deglacial (Heinrich Event 1), potentially linked to global adjustment of thermohaline circulation and teleconnections that impact atmospheric moisture delivery to the North Pacific (Okazaki et al., 2010; Menviel et al., 2012). Besides its oceanographic significance, the Gulf of Alaska/North Pacific Ocean is the largest high-nutrient–low-chlorophyll (HNLC) area in the Northern Hemisphere, and productivity in this area is largely iron limited (Harrison et al., 1999). Shelf oceanographic processes and surface water discharge appear to play a role in regulating surface-ocean iron concentrations in this region (Stabeno et al., 2004; Schroth et al., 2009; Wu et al., 2009). Evidence of substantial changes in surface productivity in the Gulf of Alaska since the LGM (Davies et al., 2011; Addison et al., 2012) indicates that millennial-scale climate change and eustasy in the northeast Pacific Ocean has a first-order effect on primary productivity. Furthermore, the modes of transfer of glacigenic sediments and the spatio-temporal variation in transfer rates are critical to deciphering the architecture of the massive (as thick as 5 km), high-latitude Neogene and Quaternary Northern Hemisphere continental margin sedimentary sequences (Riis, 1992; Vagnes et al., 1992; Eidvin et al., 1993; Lagoe et al., 1993; Elverhøi et al., 1995; Powell and Cooper, 2002; Dahlgren et al., 2005). These thick deposits contain a rich history of climate change recorded in both proxy climate data (e.g., iceberg-rafted debris and microfossils) and sediment accumulation rates that, in part, reflect climate-driven glacial sediment yields. Exceptionally high rates of glacigenic sediment accumulation in the northeast Pacific also allow development of a paleomagnetic record of geomagnetic field variability on submillennial scales to assess geomagnetic persistence, a signature of the mantle's influence on the geodynamo and the paleomagnetic record (Gubbins et al., 2007; Stoner, 2009; Amit et al., 2010).

Integrated Ocean Drilling Program (IODP) Expedition 341 investigated the northeast Pacific continental margin sedimentary record formed during orogenesis within a time of significant global climatic deterioration in the late Miocene to recent, which led to the development of the most aggressive erosion agent on the planet, a temperate glacial system. Sediment provenance and paleoclimatic, glacimarine, and structural/sedimentary indicators tied to a multicomponent chronology will be used to generate detailed records of changes in the locus and magnitude of glacial erosion, sediment and freshwater delivery to the coastal ocean, their impact on oceanographic conditions in the Gulf of Alaska, and the resulting continental margin sedimentary record on the interaction of these processes. Additionally, drilling on the Surveyor Fan, which is both subducted and accreted at the Aleutian Trench (Fig. F3), may recover a detailed Pleistocene tephra record of regional volcanism that will aid in understanding how sediment inputs influence subduction zone processes. Because the oceanographic processes in the Gulf of Alaska directly impact the Bering Sea, Expedition 341 strongly complements IODP Expedition 323 by addressing the late Neogene evolution of continental glaciation, freshwater, and nutrient inputs in a more proximal location to the glacial drivers of many of these processes.

Background

Geological setting

Continental margin strata in southern Alaska are the product of sediment derived from the Yakutat Terrane and several antecedent Mesozoic–modern accreted terranes that compose much of the northern North American Cordillera (Fig. F4) (Plafker, 1987; Plafker et al., 1994). The Yakutat Terrane was likely excised from western Canada and translated to the northwest along the dextral Queen Charlotte-Fairweather Fault system (Plafker, 1987; Plafker et al., 1994; Landis, 2007; Perry et al., 2009). The age of initial Yakutat-North America subduction, when the leading edge of the microplate encountered the Aleutian Trench and initiated flat-slab subduction, is poorly constrained but may have occurred as early as ~25 Ma (Benowitz et al., 2011; Finzel et al., 2011). Increased uplift has occurred in the past 10 m.y. associated with the convergence of increasingly thick crust and the formation of a syntaxial bend in the Pacific/North American plate boundary (Plafker et al., 1994; Rea and Snoeckx, 1995; White et al., 1997; Enkelmann et al., 2010). Ongoing collision and flat-slab subduction of thick (up to 35 km) oceanic plateau crust and cover strata (Christeson et al., 2010; Worthington et al., 2012) is constructing the present high topography of the Chugach and St. Elias Ranges (Pavlis et al., 2004; Eberhart-Phillips et al., 2006; Gulick et al., 2007). It also causes active tectonic deformation spread throughout southern Alaska and northwestern Canada (Fig. F3) (Plafker et al., 1994; Mazzotti and Hyndman, 2002; Pavlis et al., 2004; Spotila et al., 2004; Eberhart-Phillips et al., 2006; Meigs et al., 2008; Spotila and Berger, 2010; Enkelmenn et al., 2010; Worthington et al., 2010; Finzel et al., 2011). Focused deformation occurs in two indentor corners (Fig. F3), one in the west that is experiencing thin-skinned young deformation (Bruhn et al., 2004) and the other in the east (Seward corner) (Spotilla and Berger, 2010; Enkelmann et al., 2010) where intense strain and high exhumation rates ("tectonic aneurysm") are associated with the change from strike-slip to collision (Enkelmann et al., 2008, 2010; Elliot et al., 2010; Koons et al., 2010, 2013). The active deformation front for this convergence cuts diagonally from the eastern syntaxis near Mt. St. Elias along the Malaspina Fault, reaching Icy Bay, and then across the shelf at the Pamplona Zone and down the slope to the Aleutian Trench (Fig. F3), thereby linking Yakutat-North America deformation structures with the Pacific-North America faults (Bruns, 1983; Worthington et al., 2010; Gulick et al., 2013). The northward boundary, or backstop, of deformation within the St. Elias orogen is debatable because of extensive ice cover and may include the Chugach-St. Elias Fault or the Contact Fault (Fig. F5) (Spotila and Berger, 2010; Enkelmann et al., 2010; Bruhn et al., 2012). However, there are suggested far-field effects >1000 km away (Mazzotti and Hyndman, 2002; Redfield et al., 2007).

The Yakutat Terrane consists of Eocene to modern sedimentary rocks of the Kulthieth, Poul Creek, and Yakataga Formations, which are primarily siliciclastic marine and glacimarine strata interbedded with volcanics and coal beds (Plafker et al., 1994). The Kulthieth Formation sediments are the oldest, deposited at

~60–35 Ma, and are composed of nonmarine to shallow-marine deltaic feldspathic and micaceous sandstone and siltstone formed during a relative sea level regression (Risley et al., 1992; Plafker et al., 1994; Perry et al., 2009). The Poul Creek Formation conformably overlies the Kulthieth, ranging in age from Oligocene to Miocene (Risley et al., 1992; Plafker et al., 1994). The Poul Creek Formation is characterized by a high abundance of argillaceous sediment that is in part glauconitic and organic rich, representing deposition during a general marine transgression in outer shelf/slope environments. It also contains waterlain basaltic tuff, andesitic breccia, pillow lava, and related deposits of the intertonguing Cenotaph volcanics (Plafker, 1987; Risley et al., 1992; Plafker et al., 1994). The Yakataga Formation represents glacimarine siliciclastic shelf/slope deposits dating from the onset of St. Elias glaciation in the late Miocene (~5.5 Ma) to the present (Plafker et al., 1994; Lagoe et al., 1993; Risley et al., 1992; Plafker, 1987; Eyles et al., 1991). It consists of a lower diamict interval, possibly deposited by debris flows, which transitions upward into sandstone, diamict, and mudstone with occasional coquinas and boulder pavements. The uppermost Yakataga Formation mostly comprises facies that indicate significant development of the shelf ice margin (paraglacial mudstones to boulder pavements).

Volumetrically, the major potential contributors of sediment deposited on the Yakutat Terrane during the Cenozoic are the Wrangellia, Alexander, Chugach, and Yukon-Tanana Terranes (Fig. F4). The Kulthieth and Poul Creek Formations are likely derived from a parent source in British Columbia (Cowan, 1982; Plafker, 1987; Plafker et al., 1994; Landis, 2007; Perry et al., 2009). At the time of deposition of the Kulthieth and Poul Creek Formations, sediment transport pathways likely originated from the east, deriving material from the Intermontaine Belt (Cache Creek, Nisling, and the Stikine Terranes), Coast Belt (Coast Plutonic Complex and Central Gneiss Complex), and Insular Belt (Wrangellia, Alexander, Chugach, and Yakutat Terranes) in British Columbia (Gehrels and Berg, 1994; Plafker et al., 1994). The Wrangellia Terrane consists of a lower section of Permian to Middle Triassic limestone, chert, and pelitic strata. These units are overlain by 4–5 km of Middle Triassic mafic lava flows and associated mafic and ultramafic rocks, providing a diagnostic isotopic and compositional marker of sediment derived from the Wrangellia Terrane (Jones et al., 1977; Nokleberg et al., 2000; Trop et al., 2002). The Alexander Terrane consists of Precambrian(?) through Middle(?) Jurassic sedimentary, metamorphic, and plutonic rocks (Gehrels and Berg, 1994) with distinctive magnetic mineralogies (Cowan et al., 2006). The Chugach Terrane consists mainly of highly deformed, weakly metamorphic Upper Cretaceous graywacke and slate. These accretionary prism strata are interpreted to have been mainly derived from plutonic and volcanic rocks of the Coast Plutonic Complex in British Columbia (Dumoulin, 1987). The final major terrane that may have contributed sediment to the Yakutat Terrane is the Yukon-Tanana Terrane. Polydeformed metamorphic rocks of this terrane consist mainly of quartz-mica schist, quartzite, metarhyolite, and gneissic plutonic rocks (Foster et al., 1994). Protolith ages are only partly known but include middle Paleozoic radiometric dates for some of the igneous rocks and Devonian paleontologic ages for some of the carbonate strata (Gehrels and Saleeby, 1987; Plafker, 1987; Haeussler et al., 2006).

The provenance of the Yakataga Formation is likely a combination of detritus supplied mostly from the onshore Neogene thrust belt (Fig. F5). The Yakutat Group, Kulthieth, Poul Creek, and Yakataga Formations are exposed in the thrust belt. Potential sources of sediment in the "backstop region" include of the Chugach and Prince William Terranes, with possible minor contributions from more inboard terranes (Fig. F5). The Chugach and Prince William Terranes are a subduction complex welded onto the continent when the Kula-Farallon Ridge subducted beneath the margin, resulting in high-temperature, low-pressure metamorphism (Plafker et al., 1994; Pavlis et al., 2004). The Chugach and Prince William Terranes are lithologically similar and have been considered one composite terrane (Kusky et al., 1997). Age distributions of detrital zircons suggest metasedimentary flyschoidal rocks of the Chugach Terrane are derived from inboard accreted terranes of British Columbia (Haeussler et al., 2006; Perry et al., 2009). The lithologies of the Chugach Terrane are dominated by graywacke flysch and mélange units with substantial basaltic constituents. These mafic units have undergone very low grade metamorphism in the westernmost terrane, increasing in metamorphic grade to amphibolite-facies and phyllitic units of the Orca and Valdez Groups in the Prince William Terrane in the St. Elias region (Fig. F5) (Plafker et al., 1994; Haeussler et al., 2006). The Valdez Group of the Prince William Terrane north of the St. Elias Mountains is characterized by volcaniclastic graywacke and argillite with subordinate metavolcanic strata and weakly foliated green glassy tuff (Plafker et al., 1994). Volcanic rocks of the southern margin of the Valdez Group also include tholeiitic pillow basalts with island-arc to mid-ocean-ridge basalt (MORB) compositions (Plafker et al., 1994). The Orca Group dominates the Prince William Terrane within the St. Elias Range. As with the Valdez Group, this group is a deep-sea flysch complex with abundant oceanic basaltic rocks, sheeted dikes, and gabbroic intrusions of an ophiolite complex and underlies the Bagley Icefield along the Contact Fault system, from which the Bering Glacier sources (Plafker et al., 1994; Richter et al., 2006). Yakataga Formation strata accumulated in the later stages of the accretionary history of the Yakutat Terrane. Sedimentary petrography of Yakataga lithic fragments reveals sedimentary, metasedimentary, and volcanic rock fragments. Zircon fission track, U-Th/He, and U/Pb analyses of the Yakataga Formation indicate intermixing of sediment derived from two or more sources, likely the Chugach-Prince William composite terrane and recycling of Poul Creek and Kulthieth rocks (Plafker et al., 1994; Enkelmann et al., 2008; Perry et al., 2009; Witmer et al., 2009).

Physical and oceanographic setting

The morphology of the Gulf of Alaska shelf has been strongly influenced by active tectonics and glacial deposition overprinted by glacial erosion (Carlson et al., 1982; Elmore et al., 2013). Locally, the shelf bathymetry has been shaped by glacial and tectonic forces that produced five distinct shelf-crossing troughs and valleys in the study area: the Alsek Sea Valley, the Yakutat Sea Valley, the Bering Trough, the Kayak Trough, and the Hinchinbrook Sea Valley (Figs. F1, F6). These have U-shaped profiles, contain poorly sorted, glacially derived diamict along their flanks, and presumably formed during the advance of major ice streams and glaciers (Carlson et al., 1982). The extent of grounded ice covering the shelf during the last sea level lowstand is poorly constrained, but it may have ranged from only the across-shelf valleys to the entire shelf (Fig. F7) (Molnia, 1986; Manley and Kaufmann, 2002). There is evidence of grounded ice to the shelf edge within the shelf-crossing troughs based on erosional surfaces mapped in the Bering Trough (Berger et al., 2008a) and Yakutat and Alsek Sea Valleys (Elmore et al., 2013). Little sampling has occurred on the continental slope or on Surveyor Fan. Grab samples recovered diamict from the continental slope, which likely dates to the LGM (Molnia and Sangery, 1979). The jumbo piston Core EW0408-85JC on the continental slope at Site U1419 reveals slow sedimentation (<1 mm/y) of Holocene-age silty clay in the vicinity of the Alaska Coastal Current (Davies et al., 2011). Jumbo piston Core EW0408-87JC on the proximal Surveyor Fan (Site U1418) also records slow sedimentation (<1 mm/y) of likely Holocene-age silty clay that may be derived from intermediate nepheloid layers supplied with sediment from the Alaska Coastal Current (Jaeger et al., 2008).

The modern oceanographic environment in the Gulf of Alaska is characterized by high wintertime wave and wind energy, pronounced coastal currents, and deepwater gyres (Stabeno et al., 2004). The regional meteorology of the Gulf of Alaska is chiefly affected by energetic storms associated with the Aleutian Low Pressure System (ALPS). The Gulf of Alaska experiences mean wind speeds and frequency of gale-force winds similar to those of the western and central North Pacific (Stabeno et al., 2004). Cyclonic motion of the subarctic gyre drives circulation in the outer Gulf of Alaska, with the inner Gulf being dominated by the Alaska Coastal Current, a wind- and buoyancy-forced coastal jet (Fig. F6) (Stabeno et al., 2004). The southern boundary of the subarctic gyre, the North Pacific drift, diverges as it impinges on the North American continental margin, with the northward branch becoming the Alaska Current (Fig. F6). The Alaska Current dominates flow along the southwestern and southern Alaska continental slope, eventually transitioning into the Alaskan Stream farther to the west. Several large, semipermanent to seasonal eddies form within the Alaska Current, leading to mixing of water masses across the continental margin (Stabeno et al., 2004).

Water and sediment are dispersed on the continental shelf by the Alaska Coastal Current (Feely et al., 1979; Stabeno et al., 2004; Weingartner et al., 2005). The current is generally confined to within 40 km of the coast and has flow velocities occasionally exceeding 50 cm/s and mean annual transport of ~106 m^3/s (Royer, 1982; Stabeno et al., 1995). Although primarily wind driven, the Alaska Coastal Current is enhanced by a baroclinic response to coastal freshwater discharge to the Gulf of Alaska (Royer, 1981, 1982). This freshwater flux is delivered via a series of small mountainous drainages that experience high precipitation rates (2–6 m/y) due to adiabatic cooling of warm, moist air associated with the cyclonic storm systems of the ALPS (Weingartner et al., 2005). Freshwater and sediment discharge are lowest in winter, when much of the precipitation is stored as snow, and peak in late summer/fall, when meltwater and precipitation fluxes are greatest (Stabeno et al., 2004; Neal et al., 2010). Runoff creates a sharp shallow (<50 m) halocline of salinity contrast >3 psu over the shelf in the fall, but during the winter it is mixed (>100 m) and much more subdued (contrast of ~1 psu) as a result of strong storms (Stabeno et al., 2004). Strong cyclonic winds dominate from fall through spring, peaking in December and January at 9 m/s, and fast (>14 m/s) easterly coastal jets forced by mountain topography can occur (Stabeno et al., 2004). These winds lead to downwelling conditions and near-bed (3 m above bed) nontidal maximum currents of 0.15 m/s in the summer and >0.3 m/s in the winter (Hayes and Schumacher, 1976; Hayes, 1979). Wave energy is highest in the winter months, decreasing in the summer. Monthly mean significant wave heights at National Oceanic and Atmospheric Administration (NOAA) Buoy 46001 (Fig. F6, inset) averaged over 25 y are 3.5 ± 2 m (1σ), and maximum significant wave heights are 14 m in November and December (Gilhousen et al., 1983). Summer significant wave heights average 1.5 m at Buoy 46001, but maxima of 6–10 m can occur.

Regional productivity in the Gulf of Alaska is strongly influenced by the interaction of high freshwater runoff and regional meteorology dictated by the ALPS. During fall through spring, strong cyclonic winds associated with the ALPS support onshore surface Ekman transport and downwelling on the shelf, along with storm-induced vertical mixing (Stabeno et al., 2004; Childers et al., 2005). During summer, the onshore winds and subsequent downwelling conditions relax, allowing occasional brief periods of coastal upwelling in this dominantly downwelling system (Stabeno et al., 2004). Primary productivity in the Gulf of Alaska in the winter is inhibited by low insolation and enhanced vertical mixing that limits the near-surface residence time of algae. Algal blooms on the shelf are related to early spring increased solar irradiance, wintertime replenished nutrient supply, and the onset of water column stratification leading to enhanced algal residence time in surface waters. Productivity near the coast remains relatively high through early summer but is followed by a reduction in summer because of nutrient limitation created by the strong halocline (Childers et al., 2005; Stabeno et al., 2004). Key nutrients (nitrate, silicic acid, and phosphate) are derived mostly from the subsurface ocean via open-ocean upwelling, onshore Ekman transport, tidal pumping, and storm or eddy mixing (Childers et al., 2005). Nutrients delivered by the fluvial system include iron and silicic acid (Stabeno et al., 2004). Relatively few data are available on the cycling of iron in this system, although shelf processes and surface water discharge may play a role in regulating surface-ocean iron concentrations (Stabeno et al., 2004; Schroth et al., 2009; Wu et al., 2009; Davies et al., 2011; Addison et al., 2012). The central Gulf of Alaska is a HNLC region (Stabeno et al., 2004); here primary productivity is likely limited by micronutrients such as iron (Boyd et al., 2004; Tsuda et al., 2005). Sources of iron to the central basin include curl-driven upwelling, eolian dust (Mahowald et al., 2005), advection of dissolved iron from the continental shelf and slope (Chase et al., 2007; Lam and Bishop, 2008), and terrestrial runoff (Stabeno et al., 2004; Royer, 2005). Expedition 341 drill sites span from the productive nitrate-limited shelf system to the iron-limited open-ocean system.

Northwestern Cordilleran ice sheet dynamics

The glacial history of the Gulf of Alaska margin has been constructed through a combination of surface outcrop sampling (e.g., Lagoe et al., 1993; Lagoe and Zellers, 1996; White et al., 1997), scientific drilling (Rea, Basov, Janecek, Palmer-Julson, et al., 1993; Rea and Snoeckx, 1995; Prueher and Rea, 1998), and industry well cuttings (Lagoe et al., 1993; Zellers, 1995; Lagoe and Zellers, 1996). The chronology of glaciation of the Alaskan margin has been mostly established through paleomagnetic and diatom/radiolarian biostratigraphic control at Ocean Drilling Program (ODP) Site 887 (Barron et al., 1995). Supporting information comes from tephrochronology, paleomagnetic, and biostratigraphic control at Deep Sea Drilling Project (DSDP) Site 178 (von Huene et al., 1973; Lagoe et al., 1993), and foraminiferal biostratigraphy in industry wells on the shelf (Zellers, 1995) and in the onshore exposures of the Yakataga Formation (Lagoe et al., 1993). A summary of glacial history and the associated sediment record is shown in Figure F2. Alpine glaciation along the margin is speculated to have initiated as early as ~7 Ma (Lagoe et al., 1993) and increased in coverage by 5.5 Ma (Lagoe et al., 1993; Rea and Snoeckx, 1995; White et al., 1997), when elevation of the Chugach-St. Elias mountain belt was sufficient to trap precipitation from storms generated in the Gulf of Alaska. Initial onset of tidewater glaciation, Lagoe et al.'s (1993) "Glacial Interval A," is linked to the appearance of diamict in the Yakataga Formation exposed at Yakataga Reef, dated to ~5.5 Ma from a K-Ar glauconite age and at Site 887 from ~5 Ma (Krissek, 1995) to 4.3 Ma (Rea and Snoeckx, 1995) (Fig. F2). A reduction in glacimarine sedimentation correlating with the ~4.5–2.8 Ma mid-Pliocene warm period (MPW; Shackleton et al., 1995) is observed in marine and nonmarine records, though timing varies between different locales in the Gulf of Alaska region. In outcrop and continental shelf samples, the MPW lasts from 4.2 Ma to 3.5–3.0 Ma (Lagoe and Zellers, 1996). At Site 887, the MPW lasts from 3.6 to 2.8 Ma (Rea et al., 1993; Rea and Snoeckx, 1995). Renewed onset of intense glaciation after ~3 Ma, "Glacial Interval B" (Lagoe et al., 1993), is characterized by an increase in ice-rafted debris (IRD) accumulation at 2.6 Ma within deep-sea records (Lagoe et al., 1993; Krissek, 1995; Prueher and Rea, 1998) and by thick successions of diamict in onshore exposures (Lagoe et al., 1993).

At ~1 Ma, the rate of terrigenous sedimentation at Site 887 doubled, likely caused by widespread glacial advance associated with the mid-Pleistocene transition (MPT) that may be responsible for erosion of a series of U-shaped shelf-crossing troughs (Carlson, 1989; Lagoe et al., 1993; Rea and Snoeckx, 1995; Elmore et al., 2013). This glacial intensification is referred to as "Glacial Interval C" (Berger et al., 2008a). Since the onset of the MPT a series of 100 k.y. glacial–interglacial cycles characterize the Late Pleistocene climate record (Clark et al., 2006; McClymont et al., 2013). Recent high-resolution seismic reflection profiles in the Bering Trough image glacial erosion surfaces that extend to the shelf edge, likely correlating with widespread Pleistocene glacial advances potentially associated with Glacial Interval C (Berger et al., 2008a). The northwestern lobe of the Cordilleran ice sheet was present on the shelf during the LGM (Fig. F7) (Davies et al., 2011), although the full extent of ice cover is poorly known (Molnia, 1986; Manley and Kaufman, 2002). Terrestrial records suggest that the regional LGM expression lasted from 23,000 to 14,700 calendar years before present (cal y BP), with evidence for millennial-scale cooling and transient glacial readvances during deglaciation (Engstrom et al., 1990; Mann and Peteet, 1994; Briner et al., 2002; Hu et al., 2006; Davies et al., 2011). Retreat of the Bering Glacier off the continental shelf following the LGM likely occurred after 16,000 cal y BP, as indicated by peat accumulation in parts of the Bering foreland, and had apparently retreated well onshore by 14,700 cal y BP (Peteet, 2007; Davies et al., 2011).

Continental margin and Surveyor Fan stratigraphy

Varying degrees of glacial erosion, tectonic deformation, and rock exhumation in southern Alaska and northwestern British Columbia since the Miocene (Lagoe et al., 1993; Rea and Snoeckx, 1995; Enkelmann et al., 2010; Spotila and Berger, 2010) supplied sediment into the Gulf of Alaska, leading to periodic depositional pulses on the continental margin and Surveyor Fan (Stevenson and Embley, 1987; Lagoe et al., 1993; Rea and Snoeckx, 1995; Zellers, 1995; Worthington et al., 2010; Reece et al., 2011).

The seismic stratigraphy of the Bering Trough between the Kayak Island Zone and Pamplona Zone (Fig. F3) has been imaged at several scales (Fig. F8). Regional seismic surfaces, deformation structures, and seismic sequences are observed (Table T1; Figs. F9, F10), but age control based on cuttings from industry wells is limited (Zellers, 1995). Taken together, the geometries of the upper and lower sedimentary packages within the Bering Trough record glacial dynamics of the shelf-crossing Bering Glacier (Fig. F11, F12).

Depositional basins inboard of the Khitrov Ridge along the continental slope west of the Bering Trough contain a sedimentary record of glacial–interglacial sedimentation overprinted by active tectonic deformation (Fig. F13). The seismic facies at this site are interpreted to represent contrasting hemipelagic (interglacial) and glacimarine (glacial maxima) cyclicity in sediment lithofacies.

The Neogene record of sedimentation on the Surveyor Fan, a terrigenous depocenter that comprises the majority of the Alaskan Abyssal Plain (Fig. F6), comes from DSDP Leg 18 and ODP Leg 145 drilling. Leg 18 drilled and cored five sites across the southwestern corner of the Surveyor Fan, across the Aleutian Trench, and up the slope of the accretionary prism (Fig. F1) (Kulm, von Huene, et al., 1973). In 1992, Leg 145 occupied an additional site (887) in the far southwestern Gulf of Alaska on the Patton-Murray Seamounts (Figs. F1, F6) (Rea, Basov, Janecek, Palmer-Julson, et al., 1993). At DSDP Site 178, terrigenous turbidites, gravelly to diatomaceous mud, and claystone of the Surveyor Fan overlie marine chalk, barren clay, and basaltic basement of Pacific plate crust (Fig. F14) (Kulm, von Huene, et al., 1973). The Chirikof and Surveyor Channel systems control present-day Surveyor Fan morphology and sediment distribution, but unlike other large deep-sea channels they are not associated with major fluvial systems or submarine canyons (Fig. F6) (Ness and Kulm, 1973; Stevenson and Embley, 1987; Carlson et al., 1996; Reece et al., 2011). The Surveyor Channel is >700 km long with three major tributaries (Ness and Kulm, 1973; Stevenson and Embley, 1987; Carlson et al., 1996; Reece et al., 2011). Early studies divided the Surveyor Fan into two major sequences (Ness and Kulm, 1973; von Huene and Kulm, 1973; Stevenson and Embley, 1987), termed "upper" and "lower," that were based on sedimentation rates and differences in acoustic facies imaged in 2-D seismic reflection profiles. The boundary between the two sequences hypothetically represented a shift from a lower, coarser grained facies to an upper, finer grained facies possibly associated with Surveyor Channel inception and its influence on fan sediment distribution during deposition of the upper sequence (Ness and Kulm, 1973; Stevenson and Embley, 1987). Reece et al. (2011) used reprocessed U.S. Geological Survey (USGS) and 2004 high-resolution and 2008 crustal-scale seismic reflection data to correlate stratigraphic changes and fan morphology through time. In contrast to the previous interpretation of two seismic sequences within the fan, they recognized three sequences (I to III) that are regionally extensive deposits likely related to increases in exhumation on land and regional response to global changes in climate (Figs. F14, F15). Two-way traveltime (TWT) thickness (isopach maps) for the three sequences shows a changing depositional history on the Surveyor Fan (Reece et al., 2011). Sequence I depocenters are prevalent in topographic lows between basement highs, showing no significant spatial variation, which reflects infilling of preexisting Pacific plate topography. Deposits of Sequences II and III exhibit a distinct change in the locus of accumulation to shelf proximal depocenters that thicken into the Yakutat slope, with Sequence III being thicker and covering a much larger area (Fig. **F16**).

The correlation between seismic reflection profiles projected into the stratigraphy at Site 178 places tentative ages on sequence boundaries (Fig. **F14**). The Sequence I/II boundary occurs ~330 m within the drilled interval at Site 178 and is placed at ~5 Ma, near the beginning of Glacial Interval A, based on ^{40}Ar/^{39}Ar dating of ash layers (Hogan et al., 1978). At 130 mbsf, the Sequence II/III boundary is tentatively dated ~1 Ma based on correlation with a magnetic polarity reversal identified at Site 178 (von Huene et al., 1973), making it coincident with the onset of Glacial Interval C. Both sequence boundaries are synchronous with doubling of terrigenous sediment fluxes observed at Site 887 at ~5 and ~1 Ma, but based on this chronology no regional sequence boundary projected into Site 178 correlates with the onset of Glacial Interval B (Reece et al., 2011).

Spatial variability in seismic facies and stratigraphy reveals the temporal evolution of fan stratigraphy. The thickening of Sequences II and III into the Yakutat Terrane continental slope is evidence of the long-term connection of the Surveyor Fan to the Yakutat shelf (Stevenson and Embley, 1987; Reece et al., 2011). Because of the dextral transform motion of the Pacific plate and Yakutat Terrane along the Queen Charlotte-Fairweather Fault, Surveyor Fan provenance likely varied from southern Coast Mountains sources in older fan sediment to St. Elias Range sources in younger fan sediment, similar to the sedimentary strata on the Yakutat microplate (Fig. **F17**) (Perry et al., 2009). The onset of Glacial Interval A may have led to reorganization of fan sedimentation by spurring Surveyor Channel genesis (Reece et al., 2011). The youngest phases of the Surveyor Channel created shelf-proximal depocenters at the base of the Yakutat Terrane slope. Glacial Interval C, with its corresponding ice advances to the shelf edge, markedly increased sediment flux to the Surveyor Fan via an extended Surveyor Channel. The Surveyor Channel system is a unique deepwater sediment delivery pathway because of its glacial source and its trench terminus, both of which may contribute to the Surveyor's ability to maintain a major channel and evade avulsion over long periods of time (Stevenson and Embley, 1987; Reece et al., 2011).

Tectonic-climate interactions

Climatic influence on the width, structural style, and distribution of deformation in mountain belts is well established through analog, numerical, and analytical modeling studies based on critical wedge theory (Willett, 1999; Roe et al., 2006; Stolar et al., 2006; Whipple, 2009). Generally, an increase in erosional intensity through glacial or fluvial processes is predicted to accelerate rock exhumation and decrease orogen width and relief (Whipple and Meade, 2004; Roe et al., 2006). In the Chugach-St. Elias Mountains, spatial patterns along the windward side of the orogen including increased exhumation rates and exhumation of rocks from greater depth, a relative deficiency of activity along the leeward side, and relatively shallow particle exhumation pathways are all indicative of a coupled tectonic-climate "wet prowedge" system (Fig. **F5**) (Berger et al., 2008a, 2008b; Meigs et al., 2008). Based on apatite (U-Th)/He thermochronometry, in conjunction with offshore seismic data and modeling results, Berger et al. (2008a) proposed that a structural reorganization of the St. Elias orogen occurred in association with the onset of Glacial Interval C and the MPT. The proposed structural reorganization includes initiation of a large-scale backthrust onshore and deactivation of faults in the offshore frontal portion of the wedge (Fig. **F5**). However, faulting has remained active in the St. Elias Range, primarily associated with the Pamplona Zone deformation front (Bruns and Schwab, 1983; Chapman et al., 2008; Plafker et al., 1994; Meigs et al., 2008). Recent modeling (Malavieille, 2010; Simpson, 2010) suggests that the extent of active faulting and folding in a frontal wedge is highly dependent on the details of mass redistribution by climate drivers and the magnitude of incoming sediment load.

However, the localization of exhumation solely along the windward equilibrium line altitude, as indicated by apatite (U-Th)/He thermochronometry (Berger et al. 2008b), has been questioned based on reinterpretation of bedrock samples and observations of detrital thermochronometry from glaciers draining from the St. Elias Range (Enkelmann et al., 2008, 2010). A purely tectonic explanation has been proposed for the observed patterns of exhumation. These patterns are interpreted not as reflecting a temporal increase in exhumation rates over the Pleistocene, but rather as being simply driven by a southward progression of the Yakutat fold-and-thrust belt, perhaps influenced by the westward arrival of the leading edge of the thicker sedimentary cover and crust of the Yakutat Terrane (Meigs et al., 2008; Enklemann et al., 2009, 2010; Christenson et al., 2010;

Worthington et al., 2012). However, onshore thermochronometry data alone cannot uniquely distinguish between orographically versus tectonically controlled temporal changes in erosion (Meigs et al., 2008).

Gulf of Alaska paleoceanography

The Gulf of Alaska, located in the subarctic northeast Pacific Ocean, is an important component of the Northern Hemisphere climate system. Modern observations indicate linkages between the ALPS atmospheric conditions, North Pacific circulation, and marine ecosystem productivity, yet paleoceanographic data describing past changes in this system are sparse. Previous paleoceanographic studies of the Gulf of Alaska have been limited to lower temporal resolution records retrieved from lower sediment accumulation rate locales that were chosen to avoid dilution by turbidites and to remain above the carbonate compensation depth (Zahn et al., 1991; McDonald et al., 1999; Galbraith et al., 2007; Gebhardt et al., 2008). The Late Pleistocene millennial-scale climate variability typical of the North Atlantic has been inferred from earlier work in the Gulf of Alaska but has only recently been confirmed for the Expedition 341 region (Barron et al., 2009; Davies et al., 2011; Addison et al., 2012).

Core EW0408-85JC, collected on Khitrov Ridge at Site U1419, provides a detailed record of the last deglacial period to the present based on lithofacies analyses, siliceous microfossils, organic matter composition and biogenic silica concentrations, redox-sensitive metals, and oxygen isotope data from planktonic and benthic foraminifers, all tied to a high-resolution age model (44 ^{14}C dates spanning 17,400 y) (Fig. **F18**). Surface water freshening likely due to glacial meltwater input began at 16,650 ± 170 cal y BP during an interval of relatively ice proximal sedimentation probably sourced from the Bering Glacier (Davies et al., 2011). A sharp lithofacies transition from diamict to laminated hemipelagic sediments indicates retreat of regional outlet glaciers onto land or into fjords at 14,790 ± 380 cal y BP. A sudden warming and/or freshening of the Gulf of Alaska surface waters corresponds to this lithofacies transition and coincides with the Bølling interstadial of Northern Europe and Greenland. Cooling and/or higher surface water salinities returned during the Allerød interval, coincident with the Antarctic Cold Reversal, and continued until 11,740 ± 200 cal y BP, when onset of warming coincided with the end of the Younger Dryas (Davies et al., 2011). Two laminated opal-rich intervals (deglacial Bølling-Allerød and early Holocene) reveal discrete periods of enhanced water column productivity that likely correlate to similar features observed elsewhere on the margins of the North Pacific and are coeval with episodes of rapid sea level rise (Barron et al., 2009; Davies et al., 2011; Addison et al., 2012).

Proxy-based Holocene productivity was consistently higher than during the colder periods of expanded regional glacial activity. The finding of low productivity during the glacial and stadial intervals is consistent with previous findings from the open Gulf of Alaska but is inconsistent with the hypothesis that such changes are the result of higher upper-ocean stratification during cold intervals (Sigman et al., 2004; Jaccard et al., 2005). The Bølling-Allerød interval is laminated and enriched in redox-sensitive metals. Sedimentary δ^{15}N is higher than normal seawater values in these laminated intervals. Based on these observations, enhanced nitrate utilization and/or relatively weak denitrification may have occurred in the North Pacific at these times (Addison et al., 2012). Remobilization of iron from continental shelves may have helped to fuel elevated primary productivity and hypoxia during these episodes (Davies et al., 2011; Addison et al., 2012).

A temporal correspondence exists between water column and sedimentation events observed in Core EW0408-85JC and last deglacial–early Holocene climate. In addition to the Bølling interstadial diamict–laminated facies transition, an early termination of the Bølling-Allerød warm interval observed in Core EW0408-85JC relative to the North Atlantic appears in a number of high-latitude North Pacific records (Davies et al., 2011). When compared to the δ^{18}O ice core records from Antarctica (Ruth et al., 2007) and Greenland (Andersen et al., 2006; Rasmussen et al., 2006; Svensson et al., 2006), the planktonic oxygen isotope pattern of Core EW0408-85JC bears some similarity to both of these records, lending support to the idea that North Pacific climate records reflect both North Atlantic and Southern Ocean forcing (Mix et al., 1999; Davies et al., 2011).

Site survey data acquisition

In 2004, 1800 km of high-resolution multichannel seismic (MCS) reflection profiles were collected in the Gulf of Alaska aboard the R/V *Maurice Ewing* (Fig. **F8**). For the shelf and fjord profiles, the source was a dual 45/45 inch^3 generator-injector (GI) air gun array producing frequencies that provide 3–5 m vertical resolution. For the deeper water lines over the Surveyor Fan, dual 105/105 inch^3 GI guns were used. Processing included trace regularization, normal move-out correction, bandpass filtering, muting, frequency-wave number (f-k) filtering, stacking, water-bottom muting, and finite-difference migration (Gulick et al., 2007; Berger et al., 2008a).

In 2008, ~1250 km of MCS reflection data and ~500 km of wide-angle seismic refraction data were acquired in the Gulf of Alaska as part of the St. Elias Erosion and Tectonics Project (STEEP; Fig. F8). The primary tectonic survey targets included the offshore Yakutat-North America deformation front, the offshore St. Elias orogenic wedge, known as the Pamplona Zone fold-and-thrust belt, and the Yakutat Terrane crustal structure. The survey also targeted the Transition Fault (results presented in Christeson et al., 2010; Gulick et al., 2013) and the offshore zone of seismicity in the Pacific plate known as the Gulf of Alaska Shear Zone (Gulick et al., 2007; Reece et al., 2013). Primary stratigraphic targets included mapping the shelf and Surveyor Fan sediments to basement.

In 2011, ~3022 km of MCS reflection and ~600 km of wide-angle seismic refraction data were acquired with supporting sonobuoy refraction data (Fig. F8). The purpose of the Gulf of Alaska seismic mapping program was to image the distal parts of the Surveyor and Baranof Fans and the northern Pacific plate crustal structure that these sediment bodies interact with. The program was funded through the USGS as part of the United States assessment of Article 76 of the Law of the Sea Convention. The survey design targeted two areas for assessment and a series of science targets to better understand the tectonic-sedimentary system within the Gulf of Alaska. The two regions where the Alaskan deep-sea fans cross the U.S. Exclusive Economic Zone are where the Surveyor Fan system interacts with Aja Fracture Zone, potentially forming a thickened deposit, and with the Baranof Fan (Walton et al., in press). Science targets included the Surveyor Channel and its interaction with the Aleutian subduction zone, the Aja Fracture Zone, the Chirikof Channel, and the channels of the Baranof Fan. Site U1417 is in the imaged distal part of the Surveyor Fan to the north and west of Surveyor Channel.

Acquisition parameters for both the 2008 and 2011 seismic reflection data included a seismic source of 36 Bolt air guns with a total volume of 6600 inch^3 fired every 50 m. Receivers were hydrophones in an 8 km long solid streamer with a 12.5 m channel spacing. Common midpoint spacing was 6.25 m. Seismic data processing included trace regularization, normal move-out correction, bandpass filtering, muting, stacking, and f-k migration using Paradigm Geophysical FOCUS software (detailed seismic processing work flow in Worthington, 2010). Vertical resolution at the seafloor for this data set is 20–30 m.

Locations of a 1975 USGS survey and a 1979 survey by Western Geophysical are shown in Figure F8 (black lines crossing shelf and slope). These seismic profiles provide ~30 m vertical resolution and reliably image up to 4 s TWT of the subsurface, ~3.5 km at 1750 m/s seismic velocity. These profiles image major faults, fault-related folds, and unconformities, roughly illustrating stratigraphic and structural relationships along the margin (Bruns, 1983, 1985; Bruns and Schwab, 1983; Lagoe et al., 1993; Zellers, 1995). Also shown in Figure F8 (thin black lines crossing slope and fan) are single-channel seismic profiles acquired as part of the 1980s USGS GLORIA program. Within the Surveyor Fan, these lines generally penetrated to basement (ocean crust) and provided a ~30 m vertical resolution at the seafloor. Processing of the 1970s USGS data used in Reece et al. (2011) and Worthington et al. (2010) included bandpass filtering, muting, normal move-out correction, and stacking. The 1980s USGS data processing included trace editing and balancing, muting, and bandpass filtering.

In addition to MCS data, high-resolution subbottom profiles and multibeam bathymetry exist for the Expedition 341 region. High-resolution subbottom profiles were collected during the 2004 *Maurice Ewing* cruise using a Bathy 2000-P compressed high-intensity radar pulse (CHIRP) subbottom profiler. High-resolution (5–20 m^2) multibeam sonar data were collected at the proposed drill sites. At water depths <800 m, a SIMRAD EM1002 midwater high-resolution multibeam sonar was used, and in deeper water (i.e., Site U1418), a STN ATLAS Hydrosweep DS-2 multibeam sonar was used. Additionally, in 2005, >162,000 km^2 of high-resolution (~100 m^2) multibeam sonar data were collected along the base of the Yakutat slope in the Gulf of Alaska in support of the United Nations Law of the Sea extended continental shelf investigation (Fig. F1). Data were collected aboard the R/V *Kilo Moana* and postprocessed at the University of New Hampshire Center for Coastal Studies (USA; Mayer et al., 2005; Gardner et al., 2006). Vertical accuracy is ~0.3%–0.5% of the water depth. Additional high-resolution SeaBeam multibeam data were collected in 1988 by NOAA on the continental slope and proximal Surveyor Fan southwest of Kayak Island.

The supporting site survey data for Expedition 341 are archived at the **IODP Site Survey Data Bank** and available at the Academic Seismic Portal hosted by the University of Texas Institute for Geophysics (**www.ig.utexas.edu/sdc/**).

Scientific objectives

The aim of drilling the southern Alaska margin is to obtain a Neogene–recent sedimentary record of NCIS glaciation and its influence on tectonic processes and relationship with regional and global paleoclimatic changes. Focus is placed on establishing the timing and locus of NCIS expansion during the Pliocene and Pleistocene and its impact on surface processes and freshwater and sediment fluxes to the subarctic Pacific Ocean. Erosion and sediment redistribution during glacial–interglacial cycles may have had a direct effect on mountain building and deformation; thus, one goal is to determine the timing of changes in deformation patterns and sedimentary fluxes to the continental shelf and the adjacent deep-sea sediment fan. Priority is placed on documenting the NCIS response to global climate forcing. A unique component of Expedition 341 is the availability of extensive adjacent onland studies of glacial and tectonic processes and existing seismic coverage on the margin, which, when coupled with the age and stratigraphic controls provided by ocean drilling, will allow for a more complete source-to-sink study of the depositional history, glacial record, and sequence stratigraphic significance of these strata. Sampling the rapidly accumulating Neogene glacimarine sediments will document the spatial and temporal behavior of the geomagnetic field at extremely high temporal resolution. Such data are missing from this part of the planet and are required to assess the geodynamo processes that control secular variation and geomagnetic polarity reversals.

To address these objectives, we cored, logged, and analyzed sedimentary records from a five-site depth transect from the distal Surveyor Fan to the zone of active deformation on the outer shelf to recover strata that contain a record of the most significant climate and tectonic events of the southern Alaska continental margin with varying temporal resolution and stratigraphic completeness (Table T2). Of particular note are stratigraphic intervals that have the potential to preserve records of key phases of NCIS evolution, such as the late Miocene onset of glaciation, warm early Pliocene events, large-scale early Pleistocene expansion of glacial coverage, and the Middle Pleistocene glacial intensification leading to the development of highly erosive ice streams (Fig. F2). The expected chronostratigraphy and integrated multidisciplinary sediment provenance and climatic proxy record–based reconstructions of glacial dynamics are fundamental to understanding tectonic-climate interplay and the processes responsible for developing high-latitude continental margin stratigraphy.

The specific scientific objectives for Expedition 341 are as follows.

1. Document the tectonic response of an active orogenic system to Pliocene and Middle Pleistocene climate change.

Our fundamental hypothesis is that the St. Elias orogen has undergone perturbation that has markedly changed the patterns and rates of deformation and exhumation in the orogenic wedge (Figs. F2, F5). Enhanced glacial erosion associated with the MPT and the establishment of highly erosive ice streams led to substantial mass redistribution in the wedge, shutting down existing regions of active deformation and refocusing the deformation and exhumation patterns of the orogen (Berger et al., 2008a; Worthington et al., 2008, 2010; Chapman et al., 2008). Testing the hypothesis that the MPT led to rapid intensification of erosion along the windward side of the mountain range first requires that we establish the baseline erosion conditions in the orogen prior to this climate perturbation, which involves integration of results of the Surveyor Fan seismic reflection data sets (Fig. F16) and sediment mass fluxes and provenance records from the most distal Site U1417. Documenting climatic influence on enhanced exhumation requires a connection between a change in sediment provenance to more windward source rocks (e.g., Yakutat Terrane) and establishing glacial conditions. This connection will be based on sediment accumulation rates and provenance records from Sites U1417 and U1418, as they likely contain distal (and complete) and proximal records of the Surveyor Fan sequences, respectively, but are still within a reasonable drilling depth. Lastly, addressing the hypothesis that the onset of ice streams completely altered the deformation and exhumation patterns in the orogenic wedge (Berger et al., 2008a) will require age control, sediment accumulation rates, and provenance records from the more proximal Sites U1419–U1421 near the Bering Glacier, where tectonic deformation patterns have been shown to evolve synchronous with sedimentation (Worthington et al., 2010). Drilling will also allow testing the alternative hypothesis that rates of exhumation and erosion have not changed in the past 5 m.y. and that the locus of exhumation has steadily progressed southeastward with the encroachment of thicker crust (Enkelmann et al., 2008, 2009, 2010).

2. Establish the timing of Neogene advance and retreat phases of the northwestern Cordilleran ice sheet to test its relation to global ice sheet dynamics.

Previous scientific drilling on glaciated margins similar to southern Alaska has provided rich and detailed records of global Neogene ice dynamics including DSDP Legs 18 (Kulm, von Huene, et al., 1973) and 28 (Hayes, Frakes, et al., 1975); ODP Legs 105 (Srivastava, Aurthur, Clement, et al., 1987), 113 (Barker, Kennett, et al., 1990), 119 (Barron, Larsen, et al., 1989), 145 (Rea, Basov, Janecek, Palmer-Julson, et al., 1993), 152 (Larsen, Saunders, Clift, et al., 1994), 178 (Barker, Camerlenghi, Acton, et al., 1999), and 188 (O'Brien, Cooper, Richter, et al., 2001); and IODP Expedition 318 (Escutia, Brinkhuis, Klaus, and the Expedition 318 Scientists, 2011). We expect that drilling on this glaciated margin will complement earlier expeditions by filling a substantial gap in knowledge of North American ice dynamics via establishing the timing of advance and retreat phases of the NCIS throughout the Quaternary. Establishing the timing of NCIS advance–retreat cycles will address a major challenge in Quaternary paleoclimatology regarding the extent to which Pleistocene climate changes occurred synchronously across the globe, and what the driving mechanisms were for potentially propagating millennial-scale warming–cooling cycles (oceanic, atmospheric, or both) (Clapperton, 2000; Mix et al., 2001; Hill et al., 2006). Many records provide strong evidence for millennial-scale climate change in the northeast Pacific in the Quaternary (Clark and Bartlein, 1995; Behl and Kennett, 1996; Hendy and Kennett, 1999; Grigg et al., 2001; Hendy and Cosma, 2008; Davies et al., 2011). However, the timing and character of these variations in relation to North Atlantic or Southern Ocean records are still unknown, largely because of uncertainties resulting from the scarcity of high-resolution records from the North Pacific. The Expedition 341 drilling transect addresses these issues because the regional climate and oceanography are highly sensitive to atmospheric-oceanic dynamics in the North Pacific (Bartlein et al., 1998). The Expedition 341 drilling provides a higher resolution chronology and a more complete record of glacial activity in the St. Elias orogen, which will allow us to assess the timing of the changes relative to the established records of global forcing (i.e., global $\delta^{18}O$ stack).

3. Conduct an expanded source-to-sink study of the complex interactions between glacial, tectonic, and oceanographic processes responsible for formation of Neogene high-latitude continental margin sequences.

The Gulf of Alaska margin offers the opportunity for an expanded study of the complex interactions between glacial, tectonic, and oceanographic processes responsible for forming one of the thickest, most complete Neogene high-latitude continental margin sequences (Stevenson and Embley, 1987; Lagoe et al., 1993; Worthington et al., 2010; Reece et al., 2011). In southern Alaska, high sediment accumulation rates driven by the interaction of glacial processes with a dynamic tectonic setting have resulted in the substantial growth of this continental margin (Figs. **F11, F12, F16**) (Lagoe et al., 1993; Plafker et al., 1994; Willems, 2009; Worthington et al., 2010). The Expedition 341 drilling transect, coupled with the onshore work accomplished as part of STEEP to examine sediment production and transfer, will allow us to document the depositional history, glaciological record, and sequence stratigraphic significance of these strata in a source-to-sink context. To test hypothetical models of glacial-sequence formation for temperate glacimarine settings (Dunbar et al., 2008) and those specific to Alaska (Fig. **F11**) (Powell and Cooper, 2002; Willems, 2009), we make use of the extensive seismic coverage on the shelf and the age and stratigraphic controls provided by our drilling program. Emphasis will be placed on documenting how the sedimentary "signals" of tectonic- and climate-induced changes in sediment production vary through the morphodynamic elements of glacimarine sediment dispersal systems.

4. Understand the dynamics of productivity, nutrients, freshwater input to the ocean, and surface and subsurface circulation in the northeast Pacific and their role in the global carbon cycle.

Drilling on the Gulf of Alaska continental margin will create a high-resolution (millennial) view of variability in productivity and water column circulation under a range of different forcings, including global-scale factors such as insolation and CO_2 and regional factors such as sea ice and freshwater runoff. The North Pacific is currently a low-salinity region, which inhibits large-scale intermediate and deepwater formation (Emile-Geay et al., 2003). However, evidence exists for enhanced Pacific meridional overturning circulation in the past that had antiphase activity with Atlantic meridional overturning circulation (Okazaki et al., 2010; Menviel et al., 2012). The dynamics of Northern Hemisphere freshwater and precipitation fluxes to the respective Atlantic and Pacific Oceans may be the primary control on large-scale intermediate and deep water circulation in the Pacific. Drilling also will allow us to compare and contrast the magnitude and scales of variability in water-column productivity between glacial, interstadial, and interglacial conditions, which differ in their insolation forcing, sea level, and so on. Productivity maxima events are widespread around the rim of the North Pacific (e.g., Mix et al., 1999). At Site U1419, a high-resolution chronology based on nearby shallow piston coring links these events locally to episodes of global sea level rise, leading Davies et al. (2011) to conclude that remobilization of iron and other limiting nutrients from continental shelves and inundated estuaries during sea level rise (e.g., Lam and Bishop, 2008; Severmann et al., 2010) contributes to events of productivity and hypoxia around the margins of the North Pacific. Assessing this hypothesis will require finding similar events associated with earlier sea level rises in the region.

A consequence of this episodic enhancement of productivity coupled with glacial-induced changes in terrigenous carbon supply is variability on a range of timescales and forcing conditions in the fluxes and burial of C, N, and Si and plankton assemblages on the Gulf of Alaska margin (Davies et al., 2011; Addison et al., 2012). In general, the paleoproductivity questions addressed by this expedition are fairly unique and significant because this understudied region is very productive and hosts important fisheries and ecosystems (Stabeno et al., 2004). Drilling offers a unique opportunity to study how the past Gulf of Alaska marine ecosystem behaved during earlier periods of warmth, several of which are likely models for future warming trends.

5. Document the spatial and temporal behavior during the Neogene of the geomagnetic field at extremely high temporal resolution in an undersampled region of the globe.

Over the last decade, our understanding of the paleomagnetic record during the Pliocene–Pleistocene has improved substantially, providing new techniques and significantly improving stratigraphic resolution and reliability. Resulting largely from ODP/IODP drilling of ocean sediments, we now know that the strength of Earth's magnetic field (paleointensity) has varied globally on suborbital timescales for at least the last 1.5 m.y. (e.g., Channell et al., 2009) and that short-duration (millennial or less) geomagnetic polarity events (magnetic excursions) are not only real but also common components of field behavior (e.g., Lund et al., 2001, 2005; Channell et al., 2002). Ocean drilling has shown that polarity transitions display complex but reproducible behavior (e.g., Channell et al., 1998; Clement, 2004; Mazaud et al., 2009). These results hint at the dynamics that drive geomagnetic change. New records have also resulted in improved chronologies (Channell et al., 2008), allowing increasingly reliable temporal calibrations and improved resolution of magnetic stratigraphic techniques. Global relative paleointensity (RPI) stacks providing orbital resolution tuning targets extend back over 2 m.y. (Valet et al., 2005), suborbital resolution stacks extend back over 1.5 m.y. (Channell et al., 2009), and multimillennial records are available for the last 75 k.y. (Laj et al., 2004). Though constrained by fewer records, a western Pacific regional stack since 3 Ma (Yamazaki and Oda, 2005) provides additional tuning targets that may prove to be globally applicable. The RPI record is being refined through ongoing IODP research, and its integration with other stratigraphic and absolute dating techniques was a primary objective of North Atlantic IODP Expeditions 303 and 306 (e.g., Channell, Kanamatsu, Sato, Stein, Alvarez Zarikian, Malone, and the Expedition 303/306 Scientists, 2006). RPI, together with the recognition of short-duration polarity events (e.g., Keigwin, Rio, Acton, et al., 1998; Keigwin, Rio, Acton, and Arnold (Eds.), 2001; Guyodo and Valet, 1999; Channell et al., 2002; Singer et al., 2002), provides additional stratigraphic opportunities through what has been termed the geomagnetic instability timescale (Singer et al., 2002).

However, much of this understanding is derived from data obtained from a limited part of the world. Historical data, dynamo models, and some paleomagnetic records attest to the importance of regions of concentrated flux that result in longitudinal asymmetry of the geomagnetic field. These asymmetries include subdued secular variation in the Pacific relative to the Atlantic hemisphere and regions of concentrated geomagnetic flux (flux lobes or bundles) over Canada and Siberia at ~60°N latitude (Fig. F19). If truly long-lived, these asymmetries imply that the structure of the geodynamo reflects lower mantle control, possibly through regulation of the long-term heat flux from the core (Bloxham and Gubbins, 1987; Bloxham, 2000). As such, these mantle-controlled nonaxisymmetric flux concentrations could provide organizing structures that may control much of the dynamics of the geomagnetic field.

The ability to develop magnetic stratigraphies that allow regional to global correlation over a range of timescales will be important to the success of IODP drilling in southern Alaska. Preliminary paleomagnetic results from the Gulf of Alaska (Davies et al., unpubl. data) suggest that the proposed sites record geomagnetic field variability consistent on submillennial scales with independently dated Holocene paleosecular variation records from Alaskan lakes (Geiss and Banerjee, 2003) and across North America (Lund, 1996). Long paleomagnetic time series constrained by independent chronologies from radiocarbon dating, tephrochronology, and stable isotope stratigraphies would allow Pacific paleomagnetic secular variation and relative paleointensity to be compared with the many records from the Atlantic (e.g., Channell, 1999, 2006; Stoner et al., 2000; Lund et al., 2005). Outside of reversals and excursions, few of these studies focused on the directional record, concentrating instead on relative paleointensity. By linking paleomagnetic directions and intensity between these regions, we will be able to assess geomagnetic persistence, a signature of the mantle's influence on the geodynamo and the paleomagnetic record (Gubbins et al., 2007; Stoner, 2009; Amit et al., 2010), and to facilitate a test of the hypothesis that heterogeneities of the lowermost mantle influence the structure of the geodynamo and, therefore, the behavior of the geomagnetic field (Cox and Doell, 1964).

Principal results

Continental margin sedimentation in the subarctic northeast Pacific Ocean

Expedition 341 drill sites were arranged in a cross-margin transect to recover sediment supplied from the exhuming mountains formed by the Yakutat Terrane convergence with North America during a period of abrupt Neogene climate change (Fig. **F6**). The recovered sedimentary record extends from the late Miocene through the Pleistocene/Holocene (Figs. **F20, F21**). Sites U1417 and U1418 recovered distal and proximal deepwater sedimentary records from the Surveyor Fan, respectively. Site U1417 contains a complete and continuous interval from the mudline to 220.4 m core composite depth below seafloor (CCSF-D; splice method), the base of which was dated shipboard to 1.7–1.8 Ma, and additional material was recovered to 709 m core depth below seafloor (CSF-A). Site U1417 contains no apparent hiatuses through the late Miocene based on initial shipboard biostratigraphy and magnetostratigraphy. Site U1418 contains a complete and continuous interval from the mudline to 271 m CCSF-D, which was dated shipboard to 0.2–0.3 Ma, and additional material was recovered to 941 m CSF-A. Site U1418 contains no apparent hiatuses through 1.2 Ma based on initial shipboard chronostratigraphy. Sites U1419 and U1421 sampled the transitional environment along the continental slope. Site U1419 is located on a small ridge at ~780 m water depth in between two large shelf-crossing glacial troughs, whereas Site U1421 is located in a trough-mouth fan downslope of the Bering Trough, in the direct sediment transport pathway associated with the seaward extent of the Bering Glacier. Site U1419 contains a complete and continuous interval from the mudline to 100 m CCSF-D and recovered core to ~177 m CCSF-B. Shipboard chronostratigraphy indicates the cored interval is younger than 0.3 Ma, and oxygen isotopes of foraminifers analyzed immediately postcruise further constrain the recovered interval to span <0.06 m.y. At Site U1421, 694 m of sediment was recovered that accumulated in <0.3 m.y. based on shipboard chronostratigraphy. Site U1420 is located proximal to the orogen on the continental shelf, within the Bering Trough. Recovered material consists of drilled clasts, lonestones, diamict, and mud that were deposited within <0.78 m.y. based on shipboard biostratigraphy and magnetostratigraphy. The high sediment accumulation rates and preservation of calcareous foraminifers at Sites U1419 and U1421 imply the potential for additional matching of recovered sediments to the global $\delta^{18}O$ stratigraphy. Despite incomplete recovery at Site U1421, very high accumulation rates may allow use of $\delta^{18}O$ and radiocarbon techniques to establish a chronology and refine the sediment accumulation rates at this site. All sites are associated with notable changes in seismic reflection facies and stratigraphy, some of which correlate to changes in sediment properties according to preliminary integration of core descriptions, physical properties, and downhole logging data with available seismic profiles. Because of high sediment accumulation rates at shelf, slope, and deepwater sites, Expedition 341 cores have the strong potential to provide a high–temporal resolution record of climate-tectonic interactions.

Shipboard results from Expedition 341 indicate an approximate doubling (>10 cm/k.y.) in sedimentation rates at ~2.6 Ma at Site U1417, which we interpret to result from the onset of significant glacial coverage in the St. Elias Range after the Pliocene–Pleistocene transition (PPT) (Fig. **F21**). This interpretation agrees with results from Site 887 in the more distal southwestern Gulf of Alaska. However, the correlation of the PPT with a prominent regional seismic reflector (seismic Unit I/II boundary; Reece et al., 2011) indicates that sediment fluxes to the Surveyor Fan were higher than previous estimates by a factor of 2 after 2.56 Ma. Also, the recovery and discovery of a temporally expanded Middle–Late Pleistocene section at Sites U1418–U1421 (Fig. **F20, F21**) is a significant achievement that confirms one of the Expedition 341 hypotheses that the onset of temperate glaciers in the Pleistocene led to increased mass flux from the orogen. The observation that the key angular unconformity penetrated on the shelf at Site U1420 is significantly younger than the MPT was a surprising finding of Expedition 341. According to this observation, rates of sediment flux from onshore to offshore are even higher than expected and potential tectonic responses to climatic forcing through glacial redistribution of sediments occur on unexpectedly short timescales ($<10^6$ y).

Lithostratigraphic summary

A major result of Expedition 341 is documentation of a dynamic sedimentary environment in the Neogene as represented by the presence of 21 distinctive lithofacies and subfacies (Table T1). The dominant recovered facies is mud, but the remaining minor facies, although volumetrically much less significant, are distinctive and allow us to organize the cores at each site into lithostratigraphic units (Fig. F20). Common lithofacies include massive mud with and without lonestones; laminated mud; silt; interbedded silt and mud; sand; interbedded sand and mud; diamict; interbedded mud and diamict; diatom ooze; biosiliceous ooze; calcareous/carbonate-bearing mud; volcanic ash; volcaniclastic mud, sand, and diamict; and intrastratal contorted mud and diamict. These facies reflect deposition from suspension fallout, sediment gravity flows, large-scale mass wasting, ice rafting, variable biogenic productivity, and subaerial volcanic eruptions.

At all sites, mud with lonestones and/or diamict are prevalent in the Pleistocene (Fig. F20), indicating the persistent transport of glacigenic sediment by icebergs or sea ice rafting. The composition of ice-rafted clasts is different between Site U1417, located in the subarctic gyre, and the more proximal slope/inner fan/shelf Sites U1418–U1421, which currently are influenced by the Alaska Current and/or the Alaska Coastal Current. An unanticipated observation is the often sharp transitions between these ice-dominated facies and more biogenic rich, often bioturbated muddy lithologies that might be related to increased biological productivity, enhanced nutrient supply, and/or decreased input of terrigenous sediments. Laminated mud and interbedded silt with mud and/or diamict are common lithofacies during what are interpreted to be glacial intervals. At Site U1418, thin-bedded diamict layers bounded by laminated mud are similar to gravelly mud beds and laminated mud described from southeast Alaskan glacial fjords that were deposited by sea ice rafting and turbid meltwater plumes (Cowan et al., 1997, 1999; Jaeger and Nittrouer, 1999). The alternation of massive mud with lonestones and laminated mud may point to time intervals characterized by a weaker glacimarine signal that alternate with intervals of more intense ice rafting. Interbedded silt and mud, and interbedded sand and mud facies indicative of deposition from sediment gravity flows are potential indicators of maximum glacial extent to the shelf edge when sediment-rich, subglacial discharge was deposited on the upper slope, feeding into the Surveyor Channel and Aleutian Trench. Postcruise analyses, including the development of higher resolution chronologies, will allow assessment of orbital to millennial controls on variations between glacigenic and biogenic-influenced sedimentation.

A secondary but notable set of lithofacies is interpreted as large-scale, highly episodic sediment gravity-flow deposits derived from the continental shelf and/or slope. These lithofacies include (1) muddy and sandy diamict characterized by mud rip-up clasts, coal clasts, and woody plant detritus at Site U1417; (2) soft-sediment deformation at Sites U1418 and U1421; and (3) intrastratal contortions at Site U1418. At Site U1418, interpretation of seismic reflection profiles suggests that a seismic unit (II*), which appears chaotic, is a mass transport deposit (MTD) (Reece et al., submitted). The coring results confirm this interpretation, with the MTD likely occurring at ~1.0–1.2 Ma based on a tentative interpretation of the Cobb Mountain Subchronozone (C1r.2n) at the top of this unit. The second type of gravity-flow deposit found in the late Miocene to Pliocene at Site U1417 indicates direct input from terrestrial sources, as noted by the freshwater diatoms, coal, and plant detritus, which are tentatively interpreted to have been derived from the coal-bearing Eocene Kulthieth Formation, which has been exhumed and is exposed in the Chugach-St. Elias Mountains onshore (e.g., Plafker, 1987).

The presence of chlorite, mica, and ferromagnesian minerals in bulk and sand samples from all units indicates the potential contribution from the Yakutat Terrane and/or a metamorphic/mafic source, perhaps the Chugach Metamorphic Complex. A more diverse range in lithologies of lonestone clasts was found at the more proximal sites (U1418–U1421) relative to Site U1417, along with some suggestion of greater numbers of sedimentary clasts at Sites U1420 and U1421 (Fig. F22). The main clast lithologies integrated over all drill sites are, in order of decreasing abundance, sedimentary, igneous, and metamorphic. Clasts may be derived from the St. Elias Mountains, the Chugach Mountains, and/or coastal ranges located along the southern coast of Alaska and northwestern British Columbia. Volcanic ash and volcaniclastic-bearing sand at all sites indicates that the locations were proximal enough to either the Aleutian or Wrangell volcanic belts to have received periodic influxes of pyroclastic detritus.

Paleoproductivity and paleoclimate indicators

One of the primary objectives of Expedition 341 was to understand the dynamics of productivity and the circulation of surface and intermediate water masses in the northeast Pacific and their roles in the global carbon cycle. Addressing this objective requires retrieval of well-preserved microfossils suitable for isotope geochemistry and faunal and floral studies. All Expedition 341 sites contained biosiliceous and calcareous microfossils of variable preservation states that indicate dynamic water column productivity and/or variable bottom water oxygenation. Previous work in the southern Gulf of Alaska at Site 887 (Barron et al., 1995; Rea and Snoeckx, 1995) showed that a robust Neogene biosiliceous biostratigraphy was achievable and that opal and calcareous accumulation rates varied at submillion-year timescales. At Expedition 341 sites, higher sediment accumulation rates of silt- and clay-rich terrigenous sediment preserved both calcareous and siliceous microfossils, allowing us to examine this Neogene variability at higher biostratigraphic resolution.

At deeper water Sites U1417 and U1418, both calcareous and siliceous microfossil groups were observed and vary from poor to good in preservation. In the middle to Late Pleistocene, both microfossil groups are present in the upper 200 m CCSF-B at Sites U1417 and U1418. Calcareous microfossils were present in variable abundance and degree of preservation through the Pleistocene at Site U1417, but older sediments became too indurated for separation. Biosiliceous microfossil abundance and preservation at Site U1417 varied in time, with abundance being high in the Middle to Late Pleistocene, Pliocene, and late Miocene but low in the early Pleistocene. At the more proximal Site U1418, calcareous microfossils are consistently preserved between 200 and 600 m CCSF-B. Deeper than 600 m CCSF-B, sediments are mostly barren of siliceous microfossils, whereas the more consistent occurrence of planktonic and benthic foraminifers suggests that accumulation of calcareous taxa persisted. At shelf and slope sites, microfossil abundance and preservation varies depending on skeletal composition. Calcareous microfossils (planktonic and benthic foraminifers and calcareous nannofossils) are well preserved and nearly continuously abundant at all sites, with only a few barren samples. Siliceous microfossil preservation and abundance is less consistent, but it tends to be highest in distinct intervals of generally clast free mud.

At deepwater Sites U1417 and U1418, strong variations in environmentally sensitive planktonic foraminifers, radiolarians, and diatoms record the alternation of warming and cooling intervals. In addition, variations of bottom water oxygenation are suggested by species changes in the benthic foraminiferal fauna. At Site U1417, planktonic foraminifer and radiolarian species abundances indicate cooler conditions from 0 to 250 m CCSF-B (within the Pleistocene) than found in the older sediments (pre-Pleistocene). Temperate radiolarian taxa are present throughout the record but have higher relative abundance in the Pliocene and Miocene. Rare occurrences of coastal diatoms, diatom resting spores, and shallow-water benthic foraminifers indicate at least some input from shelf and neritic settings. At Site U1418, variations in diatom abundance and changes in species composition likely reflect changes in paleoproductivity, transport from shallow coastal waters, and intermittent sea ice influence.

At shelf and slope Sites U1419–U1421, cold-water diatom and radiolarian species dominate the assemblage when present. Specific radiolarian taxa were also encountered at shelf/slope sites that previously have been observed occurring in association with high terrigenous sediment supply. In spite of low total abundances, sea ice–related species and warm- and temperate-water diatom species are intermittently present downhole. The planktonic foraminiferal assemblages are also dominated by species associated with cold-water conditions. Changes in the composition of the benthic foraminiferal fauna at Site U1420 suggest changes in water depth ranging from inner neritic to upper bathyal, and the observation of inner neritic benthic species at the bottom of Sites U1419 and U1420 and throughout Site U1421 probably reflects downslope sediment reworking. Variations of bottom water oxygenation are suggested by species changes in benthic foraminiferal fauna.

Given the high accumulation rates, these sediments will allow for high-resolution studies of paleoproductivity proxies that are dependent upon siliceous microfossils (diatoms and radiolarians), foraminiferal assemblages, and biomarkers. Especially high sedimentation rates during the Late Pleistocene hold promise for future studies related to suborbital-scale variability in paleoproductivity. Another valuable aspect of the recovered Expedition 341 sediment is the possibility to study changes in bottom water oxygenation and paleoproductivity across the drilled depth transect that spans from the more productive shelf-slope break to the less productive HNLC subarctic gyre.

Paleomagnetism and magnetic stratigraphy

Expedition 341 recovered an exceptional paleomagnetic record at five sites that spans a range of depositional environments with varying biogenic and terrigenous input. At all sites, the natural remanent magnetization (NRM) intensities of recovered materials were generally strong before (>10^{-1} A/m) and after (10^{-2} to 10^{-3} A/m) alternating field (AF) demagnetization, with only some intervals at Site U1419 having significantly weaker intensities (10^{-4} A/m) after demagnetization. In general, well-resolved paleomagnetic records could be extracted from the recovered material at each site, adding a key chronostratigraphic tool to interpret the sedimentary record.

At Site U1417, we recovered a long, continuous record with outstanding magnetic properties. The interval from 0 to 150 m CCSF-B contains a continuous record of interpretable polarity with well-defined magnetic transitions. Initial results suggest that normalized remanence should primarily reflect the strength of the geomagnetic field and therefore is applicable for paleointensity studies and paleointensity-assisted chronological development for at least the last 1.2 m.y. Polarity transitions (Matuyama/Brunhes and upper and lower Jaramillo) show substantial structure with a temporal resolution comparable to the best records from the North Atlantic. Several Matuyama polarity excursions are well preserved, particularly an event tentatively interpreted as the Punaruu polarity excursion (~1092 ka; e.g., Channell et al., 2008) where two complete and two partial copies are preserved. The extended core barrel (XCB)/rotary core barrel (RCB) part of the Site U1417 record also obtained well-resolved polarity transitions, including what appears to be the Gauss/Matuyama polarity transition (recovered in Holes U1417B, U1417D, and U1417E). Older polarity transitions are also well resolved, though further postcruise analyses are required for unambiguous interpretation.

At Site U1418, well-resolved Matuyama/Brunhes and upper and lower Jaramillo polarity transitions are observed at exceptional depths below seafloor (>600 m CCSF-B), attesting to the rapid Middle to Late Pleistocene sedimentation rates (~80 cm/k.y.) at this location. The RCB-recovered material appears to preserve a high-fidelity paleomagnetic record that is likely to provide long records of paleosecular variation and potentially RPI time series. The upper and lower Jaramillo polarity transitions were recovered in extended records at exceptionally high temporal resolution and will build upon the records of these same transitions from multiple holes at Site U1417 that are preserved at lower but still considered high resolution.

The slope and shelf Sites U1419–U1421 contain strata with normal polarity interpreted as being entirely within the Brunhes Chron extending in some cases to deeper than 1000 m CCSF-B, indicating exceptionally high sedimentation rates (90–300 cm/k.y.). At all sites, variations in magnetic properties are likely to prove valuable for ascertaining sediment source changes.

A high-latitude continental margin geochemical depth-time transect

The completion of a high-latitude continental margin depth transect provides a unique opportunity to examine a time-varying Neogene sedimentary geochemical record that spans from an open ocean gyre to a continental shelf. This includes examining the relative role of glacial dynamics, surface productivity, and volcanigenic input on the geochemical flux to the seafloor and diagenetic processes within the sediments. A major result of Expedition 341 is the documentation of substantially different geochemical environments from the deeper water submarine fan sites to the more proximal slope and shelf sites. In general, all sites have low organic carbon (<1 wt%) and carbonate (<5 wt%) contents, typical of a high-latitude oligotrophic marine setting with periods of intermittent productivity and/or terrigenous sedimentation. However, organic matter burial rates at proximal sites are much higher because of higher bulk sediment accumulation rates. In terms of organic matter preservation and degradation, organic matter remineralization increases significantly from distal to proximal drill sites, as reflected in increasing ammonium, alkalinity, and methane concentrations but decreasing sulfate penetration depths. There is evidence for authigenic carbonate formation at all sites, mostly in relation to sulfate–methane transition zones and sometimes resulting in carbonate-cemented sand or silt layers, especially at the deepwater sites. In addition, at the deepwater sites, dissolution of volcanic ash and/or biogenic opal likely leads to the liberation of dissolved calcium and silica, whereas the possible formation of authigenic clay minerals results in the removal of magnesium and potassium from the pore waters. Although pore water profiles shallower than the sulfate/methane interface are generally associated with different organic matter degradation pathways, the pore water composition in the methanogenic zone is mostly controlled by desorption from, and adsorption to, clay minerals. Chlorinity and salinity at the distal sites decrease with burial depth in the sediments, most likely due to clay mineral dehydration. The slope and shelf sediments have greatly reduced pore water chlorinity and salinity values relative to seawater at a few tens of meters below the seafloor and subsurface minima at several hundred meters depth. The source of the less saline pore water component is unknown, but it likely related to freshwater infiltration to coastal sediments from glacial sources and its storage within the shelf and slope deposits.

Physical properties

Collection of Whole Round Multisensor Logger (WRMSL) physical properties data allows us to correlate lithologic variability between holes, aiding in the generation of complete stratigraphic splices at Sites U1417–U1419. The whole-round and discrete physical properties data also allow us to tentatively correlate intervals between downhole log data and recovered cores at Sites U1417, U1418, and U1421. Changes in magnetic susceptibility (MS) and bulk density follow large-scale lithologic variability; intervals in which those parameters are high generally reflect coarse-grained facies, whereas low MS and density indicate a shift to more biogenic lithofacies. Changes in porosity and shear strength within and between sites indicate that the lithostratigraphic units recovered on the shelf and slope are largely underconsolidated and that sediment accumulation rates are high. Additionally, consolidation curves (porosity vs. depth) show that distal Sites U1417 and U1418 exhibit a well-constrained exponential relationship, but there is increased variance in the shallow-water sites with no apparent overall trend (Fig. F23).

Physical properties data were also used to integrate lithostratigraphic interpretation with seismic profiles at each site. For Sites U1417, U1418, U1420, and U1421, both core and logging data were available for integration. Spectral and total gamma ray and MS data from logging have been correlated to lithostratigraphic units, in particular to distinguish diamict from biosiliceous intervals. Where velocities are well constrained, lithostratigraphic features often correlate with major seismic units defined by changes in acoustic facies or a truncation surface as seen in seismic reflection profiles. Changes in physical properties at these sites seem to be related to lithologic indicators of proximity to glacial sediment sources.

Stratigraphy and seismic facies

Expedition 341 provided new constraints on the ages of the major seismic units on the Surveyor Fan (Reece et al., 2011), which in turn significantly alter our interpretation of the geologic evolution of the St. Elias orogen and continental margin. Sequence III is characterized by smooth, continuous reflectors and limited seismic transparency and is mappable throughout the Surveyor Fan. At Site U1417, the Sequence II/III boundary (~5.8 ms TWT) is defined by high-amplitude variation (Fig. F24). Based on a preliminary shipboard traveltime-depth relationship, Sequence III corresponds to dark gray mud with thin beds of volcanic ash (lithostratigraphic Subunit IA) and gray mud with thin beds of volcanic ash and diatom ooze (Subunit IB) (Fig. F20). Magnetostratigraphy places this sequence boundary near the top of the Jaramillo Subchronozone (C1r.1n ~0.988 Ma). At Site U1418, Sequence III includes three subunits underlain by the Surveyor MTD (seismic Unit II*) (Reece et al., submitted) (Fig. F25), and a transition was observed in the cores from laminated mud, diamict, and lonestones (lithostratigraphic Unit II) to laminated and bioturbated mud, normal faulting, and beds of clast-rich muddy diamict containing rip-up clasts (Unit III) to intrastratal contorted sediments (Unit IV). Within Sequence III at Site U1418, the top of the youngest aggradational seismic package that comprises the northwest flank of the Bering Channel (seismic Unit IIIB) corresponds both to a change in seismic amplitude and to the boundary between lithostratigraphic Unit I (mud with silt and sand beds and lonestones) and Unit II.

Smooth, continuous reflectors that are semitransparent in seismic data characterize Sequence II throughout the Surveyor Fan. Based on our shipboard correlations at Site U1417, this sequence corresponds to several lithostratigraphic units. These include gray mud with few centimeter-thick interbeds of fine sand and coarse silt (lithostratigraphic Unit II); thick beds of clast-poor and clast-rich diamict, both indicative of IRD, interbedded with gray mud (Unit III); and highly bioturbated gray mud with diatom-bearing intervals (Unit IV) (Fig. F20). The lithostratigraphic Unit III/IV boundary, which marks the first arrival of IRD material to Site U1417, tentatively correlates to the lower part of Sequence II and to the Gauss/Matuyama boundary at 2.581 Ma (Fig. F21).

Sequence I, which lies beneath the regionally mappable Sequence I/II boundary (Figs. F15, F24), includes the Pliocene and Miocene sections recovered during Expedition 341. These intervals contain a series of lithologic changes within lithostratigraphic Unit V, including mud with sandy diamict, interbedded silt and sand, and diatom ooze. Some diamicts display evidence of terrigenous input, including wood fragments and coal, indicative of Miocene–Pliocene tectonic exhumation and subsequent transport to the deep basin.

Sites U1420 and U1421 are linked by mappable seismic sequences and unconformities associated with the Bering Trough (Fig. F9). Seismic sequences stratigraphically above angular unconformity Horizon H1 are acoustically semitransparent and semichaotic packages that, where recovered (lithostratigraphic Unit I at Site U1420), correspond to massive clast-rich diamict. Lithostratigraphic Unit II at Site U1420 consists primarily of washed pebbles and drilled clasts of varying lithologies. Using velocities from the sonic log recorded in Hole U1420A for preliminary shipboard TWT-depth conversions, we appear to have logged across the Horizon H1 unconformity and into the uppermost aggradational seismic packages that are truncated by Horizon H1. Core recovery increased at the top of lithostratigraphic Unit III at Site U1420, and the sediments within this unit consist primarily of clast-poor and clast-rich diamict with occasional intervals of mud and bioturbation (Fig. F20), demonstrating the dominance of glacially related seismic and sedimentary facies. Growth strata marking the cessation of local thrusting at Site U1420 were likely not penetrated by drilling. Based on the sediment interval recovered at Site U1420, it appears that these growth strata are significantly younger than originally proposed (Worthington et al., 2010). At slope Site U1421, ~700 m of diamict, mud, laminated diatom ooze, and interbedded sand and mud were drilled and interpreted shipboard to represent slope and potential trough-mouth fan deposits recording mass wasting, deposition from surface plumes, and ice-rafted sediment transport. Given their location directly downslope of the Bering Trough mouth, the interpreted seismic sequences may distinguish individual thick glacial packages and thinner interstadial or interglacial periods (Fig. F9).

In summary, sediments recovered during Expedition 341 mark key transitions that can be mapped regionally using seismic reflection profiles. These transitions include the intensification of Northern Hemisphere glaciation (INHG) at 2.56 Ma at Site U1417, the MPT at Sites U1417 and U1418, and transitions in sedimentary and seismic facies within the Middle Pleistocene at Sites U1418, U1420, and U1421 that need further study into their exact timing.

Expedition 341 preliminary scientific assessment

Expedition 341 was an outstanding success in terms of sediment recovered and objectives addressed across the Gulf of Alaska margin. Regional seismic data indicate transitions in seismic facies and sequences within the Surveyor Fan and continental margin that lead to interpretations of climate-driven increases in sediment transport and deposition with potential feedback on the orogenic belt. Testing these interpretations required recovery of sediment across this glaciated margin. Meeting the scientific objectives by drilling a high–depositional rate continental margin transect demanded essentially complete recovery of important climate transitions recorded in the uppermost strata and adequate recovery of challenging deep-penetration targets exceeding 700 m CSF-A in both deep (>4000 m) and shallow (<300 m) waters. In both aspects, the resultant drilling was a notable success. Material was recovered along a cross-margin transect from the deepwater Surveyor Fan at both distal (Site U1417) and proximal (Site U1418) locations, the mid-slope region (Sites U1419 and U1421), and the continental shelf (Site U1420). Recovery was very good (70% at Site U1417) to excellent (86% at Site U1418) on the Surveyor Fan sites and very good on the upper slope Site U1419 (77%). At these three sites, real-time correlation among holes developed long intervals of verified 100% recovery that provide the opportunity for ultrahigh-resolution studies. Recovery was limited both at shelf Site U1420 (14%) and slope Site U1421 (23%) because of the expected challenges of deep subseafloor drilling on a glaciated margin setting. Nevertheless, recovered intervals proved critical to the overall expedition objectives. At Sites U1417–U1419, a complete stratigraphic splice was developed to depths exceeding 100 m CCSF-B, spanning a telescoping temporal record with increasing resolution from ~1.8 Ma at Site U1417 to ~0.2 Ma at Site U1418 and ~0.04 Ma at Site U1419. The corresponding sedimentation rates (8–13 cm/k.y. at Site U1417 and 100–150 cm/k.y.) within the spliced intervals at the two fan sites provide the potential to resolve Middle–Late Pleistocene changes in sedimentation and climate on glacial–interglacial and higher resolution timescales. On the shelf and slope, Sites U1420 and U1421 recovered sediments that are all <0.781 Ma based on magnetostratigraphy, with the slope site biostratigraphically constrained to be <0.3 Ma; these ages correspond to sedimentation rates of >100 cm/k.y. The sedimentary record from Site U1417 allows us to examine the paleoceanography, regional tectonics, and deep-sea sedimentary environment from the late Miocene to the present through key Neogene climatic transitional intervals, including the MPW, the early Pleistocene INHG, and the MPT. We observed 24 tephra layers at Site U1417 that record Neogene and Quaternary volcanic activity in the Gulf of Alaska, and we expect that these tephra will provide important independent chronological constraints for the Pleistocene. The Site U1418 record provides the opportunity to resolve how paleoceanography and sedimentation varied within and following the MPT at exceptionally high (submillennial) temporal resolution. Sites U1419–U1421 contain glacially influenced strata that have accumulated since the MPT on the shelf and slope and provide a chronostratigraphy and sedimentary record to test Expedition 341's fundamental climate-tectonic hypotheses. The continuous spliced record at Site U1419 provides a key proximal record of contrasting intervals of glacial and biogenic sedimentation in the Late Pleistocene at intermediate water depths.

The overarching goal of Expedition 341 was to document continental margin sedimentation during a period of strong tectonic and climatic forcing. In this respect, Expedition 341 has given us a unique opportunity to understand the interaction of tectonics, climate, and sedimentation on a high-latitude continental margin. Our success demonstrates that scientific ocean drilling has the potential to recover similar records from other optimally located high-latitude settings. All primary science objectives were addressed. Below we explore these objectives and highlight major results within each.

Documenting the tectonic response of an active orogenic system to late Miocene to recent climate change

A fundamental hypothesis tested by Expedition 341 is that the onset of an erosive temperate glacial environment can radically alter mass fluxes within an orogenic wedge, which in turn leads to a tectonic setting that is out of equilibrium, causing a positive feedback response of exhumation, erosion, and sedimentation. The sedimentary record collected during Expedition 341 spans several important climate transitions (MPW, INHG, and MPT) and contains a high-quality biostratigraphic and paleomagnetic record, leading toward a refined chronostratigraphy that allows us to test this hypothesis. A remarkable discovery from the expedition is the apparently very young depositional age and extraordinarily high Pleistocene sediment accumulation rates of the shelf and slope strata recovered at Sites U1420 and U1421. A significant mass flux from the orogen since the MPT is demonstrated by (1) the existence of >1 km of Middle to Late Pleistocene poorly sorted (from mud to boulders) glacigenic sediment on the shelf and (2) ~700 m on the upper slope that is partly coeval with accumulation of >1 km thick finer grained glacimarine and hemipelagic strata in the proximal fan at Site U1418. Burial of an outer shelf thrust fault by >130 cm/k.y. glacial sedimentation likely resulted in cessation of thrusting on this structure while shortening continued both onshore and seaward from the locus of accumulation within the Bering Trough (Pavlis et al., 2012; Worthington et al., 2010). These exceptionally high Pleistocene near-shore fluxes are supported by the notable discovery from the Surveyor Fan at Site U1417 that the boundary between the lowermost seismic unit and the overlying strata (Sequence I/II) dates to only the INHG (~2.56 Ma; Glacial Unit B of Lagoe et al., 1993), rather than the older ~5–6 Ma onset of Glacial Unit A of Lagoe et al. (1993). This finding implies much greater sediment delivery from onshore sources in the Pleistocene than previously calculated. Additionally, sediment accumulation rates apparently increased in both the distal and proximal Surveyor Fan across the MPT and further increased into the Late Pleistocene, when extremely high sedimentation rates (100–300 cm/k.y.) are also observed on the shelf and slope. Another finding is that some key stratigraphic changes are observed within the Middle Pleistocene, including the first advance of the Bering Glacier to the shelf edge, the associated change to a possible trough-mouth fan depositional system on the slope, and a transition in facies and accumulation rate within the proximal fan, which may or may not be coeval. These increases in sediment accumulation rates possibly reflect enhanced exhumation due to positive feedback between glacial erosion and tectonic shortening within the St. Elias orogen. Pleistocene sediment on the margin and fan is potentially derived from both the Bering Glacier (Sites U1418–U1421) and the Malaspina/Seward/Hubbard Glaciers (Site U1417) based on seismic reflection mapping (Reece et al., 2011; Worthington et al., 2010); the recovered sediments reflect bedrock sources that both glacial systems are currently eroding. The recovery of a long and relatively continuous sequence of sediment that spans from the Miocene to Holocene allows us to evaluate the relative influence of climate change on exhumation throughout the St. Elias orogen. Postcruise analysis of sediment provenance will constrain this locus of erosion, linking it to onshore patterns of exhumation to ultimately test whether rapid erosion has the potential to lead to a positive feedback in exhumation in an active orogen.

Establishing the timing of advance and retreat phases of the NCIS to test its relation to dynamics of other global ice sheets

Expedition 341 drilling recovered an unprecedented North Pacific Pleistocene sedimentary record of glacigenic sediments, accumulating at rates that likely resolve orbital- and suborbital-scale influences. An important first-order observation of the expedition is that glacial conditions dominated the region during the Pleistocene. Interglacial events were brief and extreme. Within the glacial intervals, variations in lithofacies indicate dynamic advances and retreats of regional outlet glaciers and likely also the northern Cordilleran ice sheet feeding into them. The glacial signal in the deep sea is recorded as thin beds of diamict and laminated mud, whereas on the shelf and slope it is dominated by clast-bearing to laminated mud and diamict. The retrieval at Sites U1417–

U1419 and U1421 of Holocene interglacial sediments and microfossils provides a means to identify comparable interstadial intervals in the deeper sedimentary record. The shipboard chronology allows us to place the stratigraphy and proxies of glacial–interglacial intervals into an initial temporal context. The good preservation of calcareous microfossils at all sites is potentially sufficient to provide radiocarbon and oxygen isotope chronostratigraphic control. An exceptional shipboard paleomagnetic reversal chronology provides a temporal framework to guide future analyses of particular glacial–interglacial intervals. In particular, the influx of fine-grained glacial material combined with high accumulation rates leads to exceptional paleomagnetic records that are likely to result in highly resolved RPI chronologies.

The depth-transect drilling approach allowed us to address this particular objective at four scales. First, at Site U1417 the Gauss/Matuyama paleomagnetic polarity transition (2.581 Ma) occurred slightly deeper than the first evidence of ice-rafted sediment deposition at the site, providing a key chronostratigraphic marker that will allow Alaskan tidewater glaciation to be put into a global context. This increase of glacial sediment input in the northeast Pacific first occurred near the Pliocene/Pleistocene boundary and accelerated in the Middle Pleistocene. These results demonstrate long-term synchronicity of local impacts with global climate and demand a global cause. Second, Site U1418 provides an ultrahigh-resolution (potentially millennial-scale) record of climate and glacial erosion over the past ~1 m.y. With high-resolution chronologies being developed post-cruise, this site will demonstrate possible relationships between Cordilleran and global glaciation in response to orbital and greenhouse gas forcing. Site U1419 provides an ice-proximal view of glacier advances, with potentially century-scale resolution over the past ~60 k.y. This site provides key material for detailed study of glacier dynamics over the past glacial cycle, with the potential for a highly resolved chronology. Finally, Sites U1420 and U1421 demonstrate the existence of extremely thick Pleistocene depocenters of glacigenic sediment in shelf/slope settings where tectonic forcing drives accommodation. Seismic images linking these sites show a stratigraphic transition from an interval of a glaciated inner shelf, aggradational outer shelf, and associated slope sequences to a time of glacial advances to the shelf edge and prograding grounding line wedges that transition into a possible trough-mouth fan on the slope. Examination of these sequences and correlation to $\delta^{18}O$ chronostratigraphy may allow the determination of the timing of glacial advances to the outer shelf edge that coincided with the angular unconformity and the transition in sequences on the slope that reflects shelf-edge progradation (Fig. F9). This unconformity and associated change in slope sequences, which is clearly younger than the MPT and not associated directly with it, may or may not tie with the changes in sedimentation and sediment routing on the Surveyor Fan, which are observed at Site U1418 within the Middle Pleistocene section.

Consequently, the sedimentary record has the temporal fidelity to regionally map individual advance–retreat cycles of grounded ice and the ice-proximal and ice-distal facies. These drilled sequences may provide global analogs for shelf/slope records of glacial cycles.

Implementing an expanded source-to-sink study of the complex interactions between glacial, tectonic, and oceanographic processes responsible for creation of one of the thickest Neogene high-latitude continental margin sequences

The integration of existing high-quality seismic reflection data with the sedimentary and downhole record collected during Expedition 341 allows for post-cruise interpretation of seismic facies based on the ability to correlate with lithostratigraphic units and downhole logs. By assigning lithologic facies, representing various sedimentary processes, to seismic facies mappable throughout the Surveyor Fan and by tying these facies relationships into high-resolution chronology and proxy records of paleoenvironment and sediment provenance, we have a truly unique opportunity to constrain the timing and mechanisms of sediment transfer and accumulation from a high-latitude continental shelf to the deep sea. The establishment of an independent chronology from the MPT to the present along a depth transect of sites allows for unprecedented ability to link the transfer from shelf-to-slope/inner fan to distal fan throughout the Late Pleistocene. By mapping Expedition 341 age-calibrated seismic reflectors between Sites U1417 and U1418 and throughout the Surveyor Fan, insight into how sediment is routed from shelf sources to deep-sea sinks is possible. Notable examples of how this objective was addressed include the following:

- We have established the relative timing of a transition from a distributed, likely nonglacial Miocene–Pliocene deep-sea fan depocenter to the glacial Pleistocene Surveyor Channel, creating a channel-lobe system with the lobe extending into, and being truncated and subducted along, the Aleutian Trench.
- Results from Site U1418 provide evidence for the potential relationship between the Surveyor Fan

MTD within the proximal fan, dated at ~1.0–1.2 Ma, and the subsequent formation of wide-channel systems that may be conduits of glacigenic sediment into the Aleutian Trench.

- We have documented the rapid formation of a middle to Late Pleistocene glacially dominated shelf depocenter beneath the modern Bering Trough.
- The combined results from Sites U1418, U1420, and U1421 indicate that there was a Middle–Late Pleistocene continental margin stratigraphic transition, possibly driven by the glacigenic filling of tectonically created accommodation space, that ultimately led to the development of shelf-crossing troughs and the direct delivery of sediments to the Surveyor Fan.
- Lastly, we note that the variable contribution from, and likely composition of, organic matter found from proximal to distal sites indicates evolving source regions of sediment supplied to the Gulf of Alaska and/or evolving transport pathways for such sediment (e.g., ice rafting, mass transport, or marine primary productivity).

Understanding the dynamics of productivity, nutrients, and freshwater input to the ocean and surface and subsurface circulation in the northeast Pacific and their role in the global carbon cycle

The sedimentary, micropaleontological, and geochemical observations made during Expedition 341 indicate a dynamic Neogene setting spanning from the late Miocene to the present. Variable accumulation of biosiliceous and calcareous material in both space and time attests to a surface ocean that is sensitive to forcing by regional controls on productivity. Preliminary pore water, headspace gas, and sediment geochemistry data reveal that the accumulation rates of organic matter and the intensity of its remineralization within the sediments have changed with time. Although total carbon (organic and carbonate) contents are similar between sites, higher sediment accumulation rates at proximal sites indicate greater burial of biogenic matter at these locations. There is downcore evidence at all sites for fluctuating concentrations of marine and terrestrial organic matter, confirming that productivity and carbon cycling have changed over a range of timescales. The diverse micro- and sometimes macrofossil content at most sites records a biogenic transect from the deep sea to the shelf from the modern oligotrophic (iron-limited and nitrate-replete) central gyre to the eutrophic (iron-replete and nitrate-limited) shelf. This transect opens opportunities for postcruise study of biogenic sedimentation related to overlying production. Site U1419 on the continental slope offers an excellent opportunity to constrain the history of intermediate water ventilation over the past 60 k.y. Regarding freshwater input to the northeast Pacific, pore waters at ice-proximal Sites U1419–U1421 show significantly reduced salinity and chlorinity values from a few tens of meters subseafloor to several hundred meters depth. This finding indicates that glacial meltwater was stored, or is actively flowing, through these deposits and thus documents a yet-unstudied component to glacial meltwater dynamics in glacially influenced continental shelf/slope deposits beyond ocean-surface meltwater plumes.

Documenting spatial and temporal behavior during the Neogene of the geomagnetic field at extremely high temporal resolution in an undersampled region of the globe

The Gulf of Alaska is a location where paleomagnetic records are likely to be sensitive to important geomagnetic features such as high-latitude flux lobes and the Pacific dipole window. With a glaciated, tectonically active margin that ensures an almost continuous supply of fine-grained lithogenic material accumulating at exceptionally high rates, quality paleomagnetic records that can provide much-needed stratigraphic information are likely to exist. The sites drilled during Expedition 341 provide, for the first time, the quality of material required to explore such geomagnetic concepts. Shipboard measurements of NRM from half-core sections constrained by, and enriched from, the determination of physical, chemical, biological, and lithostratigraphic properties highlight the paleomagnetic potential of this expedition. At each site, we recovered paleomagnetic records of normalized remanence and paleomagnetic secular variation, and at Sites U1417 and U1418, we recovered several polarity transitions, some in exceptional temporal detail and in replicate core sections. There is high-fidelity magnetic material to the recovered material, with relatively little diagenetic overprint and little magnetic dissolution. Sites U1417 and U1418 within the Surveyor Fan represent the highest resolution deep-sea paleomagnetic record yet recovered from the North Pacific Ocean. Site U1417 recorded an expanded record across the Matuyama/Brunhes boundary, the upper and lower Jaramillo Subchron, and several reversals within the Gauss Chron. Site U1418 sediments include an extremely high resolution record of paleointensity variations within the Brunhes Chron. Site U1418 also includes one of the highest-resolution upper and lower Jaramillo events globally. Site U1419 largely contains a well-resolved Late Pleistocene paleomagnetic record that can potentially be tied to radiocarbon and oxygen isotope chronologies to examine paleomagnetic secular variation and paleointensity during this time interval. At Sites U1420 and U1421, NRM indicating normal polarity of the Brunhes Chron is a key temporal component of our age model for these critical sites in terms of testing climate-tectonic interactions. The potential for radiometric and $\delta^{18}O$ age control likely suggests that we will tie these new high-resolution views of magnetic field variability to independent chronologies, providing additional constraints on the process of magnetic reversals and secular variations, practical chronostratigraphic constraints based on relative paleointensity, and opportunities for environmental reconstruction.

Site summaries

Site U1417

Setting and objectives

Site U1417 is located in the distal Surveyor Fan in the Gulf of Alaska in 4200 m water depth (Fig. **F6**). DSDP Site 178 was drilled ~2 km from Site U1417 with ~40% recovery, most of which was Late Pleistocene in age (Fig. **F14**). Site U1417 is ~60 km from the Surveyor Channel, which delivers sediment to this site via overbank processes.

Site U1417 drilling targets were three major regional seismic boundaries and associated seismic sequences mapped by Reece et al. (2011) using reprocessed USGS, 2004 high-resolution, and 2008 crustal-scale seismic reflection data to correlate stratigraphic changes and fan morphology through time. Sequences I and II exhibit layered, laterally semicontinuous reflectors consistent with turbiditic deposition (Reece et al., 2011) (Fig. **F15**). Sequence III is thinly layered and contains reflectors that are laterally continuous, flatter, and smoother than those in the other sequences (Fig. **F15**). Stratal relationships at sequence boundaries are highly variable and greatly influenced by basement topography. Sequence II onlaps Sequence I in areas where Sequence I exhibits topography but is conformable in other locations. Sequence III downlaps Sequence II in parts of the distal fan where both sequences pinch out farther from the Surveyor Channel sediment source (Reece et al., 2011). At Site U1417, Sequences I–III appear to be conformable (Fig. **F26**).

Site U1417 lies at the intersection of two crustal-scale seismic profiles acquired during the 2011 R/V *Langseth* U.S. Extended Continental Shelf project for the U.N. Law of the Sea. The shallow primary target for the site is the Sequence III/II boundary from Reece et al. (2011), which has been mapped onto the 2011 profiles. This sequence boundary, which is mappable throughout the Surveyor Fan (Fig. **F16**), is proposed to represent an increase in sediment supply to the site as a result of an intensification of glaciation at the MPT. The deeper primary target is the Sequence II/I boundary (Reece et al., 2011), which was also mapped onto the 2011 data, and which is proposed to correspond to the onset of tidewater glaciation and the start of Surveyor Fan deposition in the late Miocene. Additional divisions of these sequences for the purpose of core-log-seismic integration are displayed in Figure **F24.**

Site U1417 was chosen to provide a sedimentary record of Neogene glacial and tectonic processes occurring in the adjacent orogen (Fig. **F2**). All of Sequences II and III are estimated to correspond to this time period, which would include early tectonic uplift of the St. Elias orogen within the Miocene; preglacial to glacial conditions from the late Miocene to Pleistocene, including the initiation of the NCIS and the INHG; and the potential intensification of glacial extent following the MPT. These sequences may also contain a provenance record reflecting the locus of sediment created during the exhumation and uplift of the St. Elias Mountains.

By drilling into Sequence I, Site U1417 allows us to examine deposition prior to the onset of the sedimentation associated with establishment of the Surveyor Channel. The channel is proposed to have formed in response to increased sediment supply from the adjacent coastal mountains, the timing of which may correspond to the initiation of the NCIS (Reece et al., 2011). Sequence I includes several seismic facies (Fig. **F24**) that may yield clues to the changes in depositional setting from the late Oligocene (approximate age of basement) through the Miocene, as this site tectonically migrated northwestward from near modern-day British Columbia toward southern Alaska. These sediments may give insight into the initial uplift of the St. Elias orogen, which provided the enhanced elevation needed for later glaciation.

Results

At Site U1417, Holes U1417A, U1417B, U1417C, U1417D, and U1417E were drilled to total depths of 168.0, 358.8, 225.0, 470, and 709.5 m CSF-A, respectively (Fig. **F27**). In Hole U1417A, only the 9.5 m long (full) advanced piston corer (APC) system was used. In Holes U1417B–U1417D, both the full and the half-length (4.7 m long) APC coring systems were used to refusal. Following refusal of the half-length APC system, the XCB system was used in Hole U1417B to 358.8 m CSF-A and in Hole U1417D to 470.3 m CSF-A. In Hole U1417E, the RCB system was used to interval core from 264 to 302.2 m CSF-A and continuously core from 399.0 to 709.5 m CSF-A. A total of 198 cores were recovered for the site. A total of 811.18 m of core over an 836.5 m interval were recovered using the APC system (97% recovery). The cored interval with the XCB system was 381.8 m with a recovery of 140.77 m (36.9%). The cored interval with the RCB system was 348.7 m with a recovery of 146.92 m (42.1%). The overall recovery percentage for Site U1417 was 70.1% (Fig. F27). Drilling and XCB coring to basement in Hole U1417D was not possible because of repeated mechanical cutting shoe failure during XCB operations, necessitating a separate RCB hole. As a result of time lost during XCB coring in Hole U1417D, the decision was made to limit RCB coring to the upper portion of the deepest seismic unit only and not core all the way to basement.

Real-time stratigraphic correlation at Site U1417 was achievable because of the presence of high-amplitude signals in the physical properties data. The depths of the cores acquired from each hole (in meters CSF-A) cannot be directly correlated without the direct comparison of physical properties data. Thus, a composite depth scale was constructed for Site U1417 from 0.0 to 750.82 m core composite depth below seafloor (CCSF-A) with data from all holes and including core expansion. A splice was chosen of one complete and continuous interval from the mudline to 220.4 m CCSF-D. Deeper than 220.4 m CCSF-D, intervals of correlation were found between holes but were not considered sufficiently continuous to warrant development of a deeper “floating” shipboard splice. To the extent possible, the splice was constructed from Holes U1417C and U1417D because Hole U1417A was sampled at sea and the shallowest 10 cores from Hole U1417B were recovered during heavy weather, when ship heave compromised the quality of many of the cores. The composite depth scale (CCSF-A) and the splice scale (CCSF-D) are based primarily on the stratigraphic correlation of the WRMSL MS and gamma ray attenuation (GRA) density, natural gamma radiation (NGR), split-core color reflectance data, and digital line-scan images. Of these variables, MS and GRA density offered the most reliable tools for correlation at Site U1417; the other variables served primarily as verification data. An additional depth scale (CCSF-B; method: scaled by factor) was created to compress and shift the correlated cores into the correct total drilled interval. This correction was done by applying the relationship between correlated depth and drilled depth using the affine table. Where appropriate, results are reported in this depth-corrected composite depth scale CCSF-B).

The sediment recovered at Site U1417 contains 17 lithofacies that are identified based on variations in the amount of mud, silt, and sand; the style of interbedding of lithologies; and abundances of ash, lonestones, diamict, and biosiliceous material. Based on characteristic facies associations, five major lithostratigraphic units and 12 subunits are defined (Fig. F28). The sedimentary succession cored at Site U1417 extends from the Miocene to Holocene. Mud with varying amounts of biogenic and coarser facies is the dominant lithology observed throughout all Site U1417 holes. There are noticeable variations in the amount of biogenic components, ash, lonestones, diamict, and interbedded mud/sand and mud/silt lithologies. Contacts between lithostratigraphic units at Site U1417 are usually gradational.

Lithostratigraphic Unit I (Fig. F28) is denoted by dark gray mud with subordinate thin interbeds of volcanic ash, primarily of vitric (glass) framework grains and varying amounts of biosiliceous material. Dispersed granule- to pebble-size lonestones (outsized clasts) commonly occur through the unit. Subunit IA contains greenish gray intervals of diatom-bearing mud with a few local intervals of diatom ooze alternating with barren gray mud, whereas Subunit IB includes recurring intervals of diatom ooze ranging in thickness up to 10 cm and rare thin silt and sand beds. Lithostratigraphic Unit II contains gray to greenish gray mud with distinct thin interbeds of fine sand and coarse silt beds that commonly have sharp lower contacts and are massive to normally graded. Relative to Unit I, this unit has fewer lonestones and less frequent occurrences of volcanic ash and diatom-rich intervals. Lithostratigraphic Unit III contains muddy diamict interbedded with bioturbated gray mud. The diamict contains gravel-size subangular to subrounded clasts in a muddy matrix. Diamict intervals have gradational lower and sharp upper contacts. Clast abundance increases uphole in individual diamict beds. Lithostratigraphic Unit IV consists of dark gray to greenish gray well-indurated mud lacking lonestones that is commonly highly bioturbated with common *Zoophycos* trace fossils. Diatom-bearing intervals are common in the mud, and fine sand beds are rare. Lithostratigraphic Unit V, divided into 10 subunits, is composed of dark gray moderately bioturbated diatom-rich mud, often color-banded, with interbeds of diamict and sand and thick intervals of diatom ooze. Subunits are identified based on the relative abundance of diamict versus diatom ooze intervals. Poorly sorted diamict beds with abundant clasts have sharp lower contacts and gradational upper contacts. Diamict beds contain subrounded to rounded mud clasts, and some beds contain plant debris. Diamict beds have sharp contacts and are dominated by angular black granules of shale and possibly coal (~60% total organic carbon [TOC]). Carbonate-cemented siltstone and sandstone beds are occasionally recovered. Bioturbation in the subunits of diatom ooze is absent to heavy and includes *Zoophycos* trace fossils.

Overall at Site U1417, there is a strong link between lithofacies types and physical properties, especially MS (Fig. **F29**). This relationship allows us to use physical properties as a predicative tool for lithofacies identification. Mineralogical characterization from X-ray diffraction (XRD) analysis indicates an overall similar bulk composition for the entire stratigraphic section. Composition from smear slides supports the XRD analyses but is more variable on the bed-level scale.

The sedimentology of lithostratigraphic Units I–V is consistent with mud deposition from hemipelagic/pelagic fallout and overbank levee deposition by turbidity currents. Sediment reworking and redeposition could also be related to temporal variations in bottom current strength and direction. Lonestones are interpreted to be IRD. Thin interbeds of fine sand and coarse silt suggest deposition from sediment gravity flows. Biosiliceous-rich mud and diatom oozes may reflect enhanced primary productivity and/or low terrigenous sedimentation and/or improved biosilica preservation. Lithostratigraphic Unit V is divided into subunits to distinguish periods of higher biological productivity, better preservation, and/or reduced terrigenous supply (diatom ooze) from periods of higher flux of terrigenous sediment (mud) (Fig. **F28**). Interspersed through both types of lithofacies associations are sandy diamict and breccia deposits. The transport of clasts of coal and wood in intervals of coarse detritus to the distal fan are interpreted as an indication of increasing orogenesis along the southern margin of Alaska, implying a connection between onshore tectonics and the introduction of coarse siliciclastic detritus to the offshore deepwater depocenter. Lonestone composition indicates that the sources for most of the ice-rafted sediment accumulating at Site U1417 are the St. Elias Mountains and Chugach Mountains located along the southern coast of Alaska. There is an extensive record of volcanism in the upper 200 m of the core in the form of ash. The fairly even distribution of volcanic ash throughout the record suggests that the location was proximal enough to the Aleutian and Wrangell volcanic belts to have periodic influxes of pyroclastic detritus.

The biostratigraphy of radiolarians, diatoms, and planktonic and benthic foraminifers indicates that the sediment intervals recovered at Site U1417 are Late Pleistocene to Miocene in age (Fig. **F30**). The preservation and abundance of all fossil groups vary downhole. For the upper 200 m CCSF-B, both calcareous and siliceous microfossil groups are preserved and vary from poor to good in preservation. From 200 to 280 m CCSF-B, calcareous microfossils are more consistently observed and siliceous microfossils are nearly absent. Calcareous microfossils are rarely observed from 300 to 450 m CCSF-B because of problems with sediment disaggregation, and no samples were analyzed in Hole U1417E because of sediment induration. From 300 to 450 m CCSF-B and from 600 to 708 m CCSF-B, some siliceous microfossils are observed, and between 450 and 600 m CCSF-B, siliceous microfossils are largely absent. Diatom biozones are constrained from 0 to 200 m CCSF-B and indicate a Pleistocene age. Radiolarian datums are constrained from 0 to 250 m CCSF-B and include Pleistocene to late Pliocene fauna. A second zone of well-constrained ages based on diatoms and radiolarians occurs from 325 to 425 m CCSF-B and includes microfossils that are Pliocene in age. Deeper than 600 m CCSF-B, rare occurrences of datum species indicate a Miocene age. Planktonic foraminiferal coiling directions and subarctic radiolarian taxa abundances shallower than 250 m CCSF-B indicate cooler conditions within the Pleistocene than those found deeper in the site. Cool, temperate radiolarian taxa are present throughout the record but have higher relative abundance in the Pliocene and Miocene. Rare occurrences of coastal diatoms, diatom-resting spores, and shallow-water benthic foraminifers indicate at least some component of the sediments are derived from shelf to coastal environments.

Paleomagnetic investigations at Site U1417 involved analysis of archive halves from all five holes. NRM intensities at Site U1417 in APC-cored intervals are strong before and after AF demagnetization, and intensities show variability at both the meter scale and tens of meters scale, reflecting lithology and geomagnetic variability for the demagnetized intensity. A clear record of polarity is preserved, including apparently expanded polarity transitions. Deeper than the APC-recovered sequence, magnetic intensities have greater variability, reflecting lithologic changes and variable core quality and recovery of the XCB- and RCB-cored materials. A composite polarity log was correlated to the geomagnetic polarity timescale of Hilgen et al. (2012). Interpretation of polarity chrons and subchrons, based on inclination, can be made.

The Matuyama/Brunhes boundary and the upper Matuyama Chronozone containing the Jaramillo (1r.1n) Subchronozone are clearly identified. Two short intervals of normal polarity are observed underlying the Jaramillo Subchronozone, with the older of the two tentatively interpreted as the Cobb Mountain Subchronozone (Fig. **F31**). The Gauss (2An) to Matuyama (2r) polarity transition is clearly and reproducibly observed, and much of the Gauss is reproduced across holes. Deeper than this transition, however, variable polarity interpretations can be made for the base of the Gauss (2An) and the normal polarity subchrons of the Gilbert (2Ar). A tentative correlation to the oldest of these subchrons (Thvera; 3n.4n) is made. This interval is underlain by extended recovery of material with reversed polarity, consistent with the lower part of the Gilbert Chronozone. Deeper than 500 m CCSF-B, inclination data are derived from a single Hole (U1417E), and therefore caution must be employed with any polarity interpretation made. Using the smoothed and expanded inclination record, an interpretation is made that is generally consistent with the biostratigraphic datums to ~600 m CCSF-B (Fig. **F32**). Deeper than 600 m CCSF-B, the placement of polarity boundaries is equivocal. Postcruise analysis with discrete measurements may both improve upon and resolve these correlations.

All the available paleomagnetic and biostratigraphic age datums are integrated to construct minimum and maximum preliminary shipboard age models, which together span most of the uncertainty in the datums based on shipboard work (Fig. **F32**). Based on these initial age models, sedimentation rates increase through time, peaking at values of 112 ± 4 m/m.y. in the interval 0–2.5 Ma. Such a rise in sedimentation rates is consistent with the gradual northward tectonic drift of the site, as well as acceleration of sediment inputs from tectonic and glacial forcing.

The physical properties program for Site U1417 included routine runs on multisensor core loggers and discrete sampling. Whole-round cores were analyzed for GRA bulk density, MS, *P*-wave velocity, and NGR. Split cores were imaged, and color spectrometry, color reflectance, and MS data were collected. Discrete *P*-wave velocity and vane shear strength were analyzed, and discrete samples were taken for moisture, density, and porosity measurements from Holes U1417A, U1417D, and U1417E. The NGR data together with the MS and GRA density data were used to correlate the five holes drilled at Site U1417 and to define a composite record. Core logger–based bulk density and *P*-wave velocity recorded to ~220 m CCSF-B on average with depth from 1.5 to 2.0 g/cm^3 and from ~1500 to 1600 m/s, respectively (Figs. **F33, F34**). Discrete values are similar for the overlapping depths and then show ranges from 2.0 to 2.1 g/cm^3 and from ~1600 to >1800 m/s, respectively. Deeper than ~420 m CCSF-B, isolated elevated velocities (~2420–5700 m/s) are correlated to cemented intervals, whereas lower values (<1650 m/s) are associated with diatom oozes. NGR values gradually increase downhole between 0 and 220 m CCSF-B in Holes U1417A–U1417D, interrupted by a short-term decrease in counts between 220 and 360 m CCSF-B and partially returning to higher values deeper than 360 m CCSF-B. Low NGR counts deeper than 220 m CCSF-B may partly be attributed to the smaller diameter of recovered core and/or section voids during XCB coring. Core logger NGR and MS measurements are normalized using the GRA density measurement (Fig. **F33**). These normalizations reduce ~50% of the variance in the XCB/RCB sections, showing that core logger NGR and MS measurements are affected by core section recovery volume. However, the decrease in NGR observed between 225 and 360 m CCSF-B persists (less pronounced) deeper than 300 m CCSF-B, and we propose that the lower volume-normalized NGR values between 300 and 360 m CCSF-B correspond to a lithology change in the late Pliocene. Discrete moisture and density (MAD) samples indicate that this interval is a zone of low density/high porosity values. There is close agreement between bulk density derived from GRA and MAD. Shear strength increases with depth with a change in slope at ~40 m CCSF-B, with greater scatter in the data deeper than 100 m CCSF-B.

Routine headspace gas analyses were carried out on samples from Holes U1417A, U1417B, U1417D, and U1417E, and 196 samples were taken for analyses of carbonate, carbon, and nitrogen content. Furthermore, 78 interstitial water (IW) samples and 12 rhizon samples were taken for pore water characterization, and splits from the IW samples were analyzed onboard. Solid-phase geochemical results indicate that Site U1417 is a typical oligotrophic, deepwater, subarctic setting with low TOC (generally 0.1–0.6 wt%), total nitrogen (TN) (0–0.3 wt%), and carbonate (0–1.5 wt%) content. Deviations of these values occur in specific lithologies (e.g., diatom oozes, diamict, and cemented siltstones of lithostratigraphic Unit V). The strongest organic matter remineralization occurs in the upper ~40 m CCSF-B and at ~375 m CCSF-B (Fig. **F35**). Total sulfate depletion is reached around 200 m CCSF-B, possibly linked to authigenic carbonate formation consuming dissolved magnesium and alkalinity. Methane is by far the dominant hydrocarbon gas detected, and concentrations are generally very low. However, they vary by several orders of magnitude (maximum concentration = 5117 ppmv at ~500 m CCSF-B), and methane production is restricted to an interval between 420 and 650 m CCSF-B. An upcore decrease in methane concentration is not related to anaerobic methane oxidation at a sulfate–methane transition. However, a deep sulfate–methane transition exists at the bottom of the methanogenic zone around 650 m CCSF-B, with sulfate likely provided from a deep source of seawater at the basement/sediment contact. Chloride and sodium concentrations are elevated from 10 to 60 m CCSF-B, documenting relict glacial seawater. Barite is dissolved in the sulfate-depleted zone deeper than 200 m CCSF-B and possibly reprecipitates as authigenic barite upon contact with sulfate-containing pore water. Downcore calcium and lithium increases may indicate significant leaching of underlying oceanic basalt by seawater.

Downhole logging measurements in Hole U1417E were made to a total depth of 624 m wireline depth below seafloor (WSF) after completion of RCB coring in the hole. Four tool strings were deployed in the following order: the triple combo, the Formation MicroScanner (FMS)-sonic, the magnetic susceptibility sonde (MSS), and the Versatile Seismic Imager (VSI). The borehole is variable in diameter, ranging from the maximum extent of the logging tool calipers (18 inches) to as small as <5 inches (Fig. **F36**). Logging data were affected by the rugosity of the borehole wall, particularly in the interval between 87 and 305 m WSF. Despite the rugose borehole, adequate traveltimes were recorded at one depth station during the vertical seismic profile (VSP). Based on hole conditions and characteristic trends and features in the data, two distinct logging units are identified for Hole U1417E. Logging Unit 1 (from the base of the drill pipe to 305 m wireline matched depth below seafloor [WMSF], where the matching is a correlation between logging runs based on the gamma ray measurement on each tool string) is defined primarily by highly variable borehole diameter. Within this unit, gamma ray, MS, and compressional wave velocity (V_P) logs are the most robust to borehole conditions. Logging Unit 2 (305–624 m WMSF) is characterized by improved borehole conditions, and the quality of the logging data is higher throughout this unit. Subunit 2A (305–476 m WMSF) shows elevated gamma ray, density, and velocity values relative to the overlying unit. The MS log is more emergent and generally matches features observed in the gamma ray log. Subunit 2B (476–624 m WMSF) is distinguished by an initial rapid decrease in density, resistivity, and velocity with depth, followed by general increases. The MS log displays a lower signal in this subunit. Together, these data indicate that downhole logs are likely responding to variations in lithology.

Initial core-log-seismic integration was attempted following collection of downhole logging data. Sediment core observations, physical properties data, and downhole logging data were used to (1) evaluate how representative the recovered cores are relative to the portion of the sedimentary sequence that was logged, (2) evaluate the nature and extent of sediment not recovered in the XCB/RCB drilling process, and (3) examine whether observed sedimentary facies can be related to borehole and seismic reflection data. In general, downhole and whole-core MS data exhibit similar trends and scatter when compared over the same measured interval. Transitions between intervals of high and low MS in the downhole log data correspond to lithostratigraphic boundaries in the core (Fig. **F37**). We also observe an association between described occurrences of sand with relatively high downhole log MS values. Another primary observation is that the highest MS measured in the downhole logs between 350 and 440 m CCSF-B corresponds to the occurrence of muddy diamict in lithostratigraphic Subunit VA and at the Subunit VB–VC transition. In general, we observe multiple examples where volcaniclastic sands/silts correspond to increases in standardized downhole profiles of total gamma ray and K. Sand layers generally have high MS and low gamma ray counts. Overall, the logging data provide additional evidence for widespread distribution of muddy diamict in Unit V that are likely underestimated in the cored intervals.

Shipboard correlations of downhole logging data with core-based physical properties measurements focused on the depth interval from ~305 to 615 m CCSF-B/WMSF. This interval is where the borehole condition is best, and thus the logging data are of higher quality (Fig. **F36**). The gamma ray log shows good agreement with the core NGR to within a few meters; the latter of these measurements has been corrected for volume using GRA density. Bulk density data also show variable agreement between downhole logging, core logging, and discrete core samples. There is more scatter in the GRA from the core logger; however, the downhole density log values generally correspond to the higher end in the range of GRA values. Discrete MAD measurements overlap with the downhole density log, showing a similar range in values. Discrete *P*-wave velocity measurements on cores show good correspondence to the *P*-wave velocity log down to ~430 m CCSF-B/WMSF. At greater depth, the *P*-wave velocity log shows generally higher velocities than the discrete core data. MS data show reasonable agreement between the log and core measurements.

Seismic Lines MGL1109MSC01 (Fig. **F34**) and MGL1109MSC14 (Fig. **F24**), acquired in 2011 aboard the R/V *Marcus Langseth*, cross at Site U1417 (Fig. **F26**). The primary seismic sequences on each profile, Sequences I–III, are interpreted after Reece et al. (2011). In preparation for core-log-seismic integration, Sequence I was divided into three subsections: IA, IB, and IC. Subsection IC was further divided into intervals: IC1 and IC2. Two check shots at ~211 m WMSF correlate to the seismic data at 5.87 s TWT within Sequence II, allowing some confidence for integration shallower than this depth (Fig. **F34**). Sequence III is characterized by smooth, continuous reflectors and limited seismic transparency. At Site U1417, the Sequence II/III boundary (~5.8 ms TWT) is defined by high amplitude variation. Based on a preliminary traveltime-depth relationship, Sequence III corresponds with dark gray mud with thin beds of volcanic ash (lithostratigraphic Subunit IA) and gray mud with thin beds of volcanic ash and diatom ooze (Subunit IB). Smooth, continuous reflectors that are semitransparent in the seismic profile characterize Sequence II. Based on our correlations, this sequence corresponds to gray mud with 1–5 cm thick interbeds of fine sand and coarse silt (Unit II), thick beds of muddy diamict interbedded with gray mud (Unit III), and highly bioturbated gray mud with diatom-bearing intervals (Unit IV). The Unit III/IV boundary correlates generally to the lower part of Sequence II, where a pair of medium-amplitude reflectors lies stratigraphically above the high-amplitude package that defines the Sequence II/I boundary.

The Sequence II/I boundary is located at the top of a prominent grouping of high-amplitude reflectors that are slightly more chaotic and discontinuous than those observed in Sequence II. The lithostratigraphic Unit IV/V boundary at ~350 m CCSF-B may correlate to ~6 s TWT, which is near the top of Sequence I (Fig. **F34**). This boundary is defined as the top of a series of thick, high-amplitude reflectors that comprise this boundary and may be related to the presence of cemented intervals that inhibited core recovery at this depth. Lithologically, the boundary between Units IV and V represents a change from to highly bioturbated gray mud with diatom-bearing intervals (Unit IV) to gray mud with sandy diamict, interbedded silt and sand, and diatom ooze (Unit V). Because of the lack of check shots deeper than ~211 m WMSF, precise correlation between Sequence I, Units IV and V, and logging Unit 2 will need to be undertaken postcruise; however, some comparisons between lithofacies, seismic facies, and log character can be discussed. In general, the increased velocity and density contrasts within logging Subunit 2A and the upper part of Subunit 2B likely correspond to the series of brighter reflectors that define Sequence IC and in turn may correlate with the various lithofacies of Unit IV to Subunit VC or VD. The boundary between logging Subunits 2A and 2B may be associated with a large negative amplitude reflector that separates seismic Subunits 1B and 1C at ~6.2 s TWT (Fig. **F34**). A way to check on correlations deeper in the borehole will be to use the basement depth of 780 m from Site 178, located ~2 km away, and create a pinned traveltime/depth boundary at the top of the basement during the creation of a synthetic seismogram.

Site U1418

Setting and objectives

Site U1418 is located at 3667 m water depth on a slightly elevated region of the proximal Surveyor Fan. It is located between a modern channel that feeds into the Aleutian Trench and a wide channel-like feature, termed the Bering Channel, that also likely terminated into the trench when active. These two channels appear to originate at the base of the slope seaward of the continental shelf break between Bering Trough and the Pamplona Zone (Fig. **F38**). This site also lies below the westward-flowing Alaska Current, a boundary current within the Alaska Gyre that commonly contains eddies and meanders (Stabeno et al., 2004). Seasonal high productivity is often associated with these eddies (Ladd et al., 2007). The site likely has been supplied with sediment from hemipelagic settling and sediment gravity flows through these adjacent channels, creating a thick (~1 km) seismically stratified deposit (Fig. **F25**). A large deposit of chaotic seismic facies interpreted as a MTD is found at ~5.8 s TWT (Fig. **F25;** Reece et al., submitted). The top of the MTD lies beneath a seismic reflector (Surveyor Fan Sequence II/III boundary; Fig. **F15**) that can be mapped to Site U1418 (Fig. **F16**) and is ~1.0–1.2 Ma in age based on magnetostratigraphy, suggesting that this depocenter may contain an expanded Middle–Late Pleistocene sedimentary sequence.

Drilling objectives at Site U1418 are to develop a high temporal resolution, proximal sedimentary record of Late Pleistocene glacial–interglacial dynamics, fan sedimentation and development, and paleoceanography. A primary objective of drilling at Site U1418 is to constrain the timing of glacial events on the Pacific side of the NCIS, testing its relation to dynamics of Northern and Southern Hemisphere ice sheets. Doing so would allow for the examination of the timing of ice rafting, sediment gravity flow processes, and proximal fan strata formation relative to glacial advance–retreat cycles, including the age of the seismically imaged MTD. The observation of an abandoned and buried Bering Channel shallower than the MTD (Fig. **F25**) suggests that it formed subsequent to the MTD, perhaps as a consequence of Middle–Late Pleistocene changes in glacigenic sediment delivery. An expanded Pleistocene record of glacigenic sediment deposition also allows for the documentation of the spatial and temporal behavior of the geomagnetic field (paleointensity and paleosecular variation) during this time period in an undersampled region of the globe.

Site U1418 lies at the crossing of seismic reflection Profiles GOA3202 and STEEP07, which reveal a seismically stratified depocenter overlying a unit with high-amplitude chaotic reflectors (Figs. **F25, F39**). Near-horizontal reflectors of varying intensity are mappable over tens of kilometers, implying deposition from suspension and/or overbank flow from turbidity currents. Higher amplitude reflectors may indicate periods of enhanced deposition of ice-rafted sediment and/or coarser sediment gravity flows that originated from melting of the Bering and other tidewater glaciers. Seismic units at this site were identified for Expedition 341 to guide core-log-seismic integration (Fig. **F25**). The uppermost, stratified seismic units are identified as subunits that are expected to be time-correlative with Sequence III at Site U1417, with the lowermost chaotic unit (seismic Unit II*) interpreted as a MTD (Reece et al., submitted). The lowermost seismic Subunit IIIA at Site U1418 is reflective in the higher resolution GI gun data on Line GOA3201. Based on interpretation of Line F-6-89-GA-26 (a 1989 seismic reflection line with a vertical resolution in between STEEP07 and GOA3201 collected by the USGS ~10 km northeast of Site U1418), these reflective facies may be correlative with deposition associated with the relict Bering Channel (Fig. **F25;** see Fig. **F3** in the "Site U1418" chapter [Jaeger et al., 2014]). The Subunit IIIA/IIIB boundary is at a reflector (5.25 s TWT) interpreted to represent the cessation of sediment transport through the Bering Channel, possibly corresponding with the formation of the eastward extension of the Aleutian Trench (Fig. **F38**). The higher amplitude reflectors of Subunit IIIC correspond with erosion of the unit at its northern extent, likely by gravity flows moving downslope into the Aleutian Trench. Subunit IIIC consequently is expected to contain evidence of gravity flow deposition. These seismic unit boundaries are therefore primary targets while drilling to the base of Sequence III and the top of Sequence II*.

Results

At Site U1418, Holes U1418A, U1418B, U1418C, U1418D, U1418E, and U1418F were drilled to total depths of 209.9, 17.0, 230.7, 305.8, 181.6, and 948.7 m CSF-A, respectively (Fig. **F40**). In Holes U1418A–U1418D, both the full- (9.5 m long) and the half-length (4.7 m long) APC coring system were used to refusal. Only the full APC system was used in Hole U1418E, and the RCB system was used in Hole U1418F. Cores from Hole U1418B were collected to cover the sediment section that was disturbed in the first two cores from Hole U1418A. Following a drilled interval to 78 m CSF-A, full-length APC cores were collected from Hole U1418E to fill in gaps identified by the stratigraphic correlators.

Following refusal of the half-length APC system, the XCB system was used in Hole U1418D to 305.8 m CSF-A, after which the hole was terminated because of mechanical cutting shoe failure during XCB operations. In Hole U1418F, the RCB system was used to drill to 260.0 m CSF-A and to continuously core to 948.7 m CSF-A. A total of 185 cores were recovered for the site. A total of 819.08 m of core over an 810.0 m interval were recovered using the APC systems (101% recovery). The cored interval with the XCB system was 48.5 m with a recovery of 22.8 m of core (47%). The cored interval with the RCB system was 688.7 m with a recovery of 498.2 m of core (72%). Overall recovery for Site U1418 was 86% (Fig. **F40**).

Real-time stratigraphic correlation at Site U1418 was achievable because of the presence of strong signals in the physical properties data. A composite depth scale at Site U1418 was constructed from 0.0 to 948.7 m CCSF-A with data from all holes, and it includes core expansion. A splice was chosen that results in one complete and continuous interval from the mudline to 271.4 m CCSF-D. Deeper than 271.4 m CCSF-D, intervals of correlation were found between holes but were not considered sufficiently continuous to warrant development of a deeper "floating" shipboard splice. To the extent possible, the splice was constructed from Holes U1418C–U1418E because Hole U1418A was sampled at sea and Hole U1418B consisted of only two special-purpose cores for pore water sampling. The composite depth scale (CCSF-A) and the splice (CCSF-D) are based primarily on the stratigraphic correlation of WRMSL MS and GRA density, NGR, and color reflectance data from the Section Half Multisensor Logger. Of these variables, MS and GRA density offered the most reliable tools for correlation at Site U1418; the other variables served primarily as verification data. As with Site U1417, an additional depth scale (CCSF-B) was created to compress and shift the correlated cores to produce the correct total drilled interval. Where appropriate, results are reported in this depth-corrected composite depth scale.

The sediment recovered at Site U1418 contains 15 facies. The dominant facies are gray to dark greenish gray mud and interbedded mud and silt and account for >90% of the core recovered. The remaining minor facies, although volumetrically much less significant, are distinctive and allow us to organize the cores into lithostratigraphic units. Lithofacies include massive mud with lonestones, massive mud without lonestones, laminated mud, silt, interbedded silt and mud, very fine to coarse sand, muddy diamict, interbedded mud and diamict, diatom ooze, biosiliceous ooze, calcareous/carbonate bearing mud, volcanic ash, volcaniclastic mud and sand, rock, and intrastratal contorted mud and diamict. These facies reflect deposition from suspension fallout, sediment gravity flows/large-scale mass wasting, ice rafting, variation in organic productivity/preservation, and subaerial volcanic eruptions. Based on facies associations, four major lithostratigraphic units were defined (Units I–IV; Fig. **F41**). Unit II is further divided into Subunits IIA–IID based on the characteristics of diamict intervals. The contacts between lithostratigraphic units at Site U1418 are usually gradational.

Lithostratigraphic Unit I is dark gray to dark greenish gray mud with interbedded silt that alternates with intervals of up to 15.5 m thick color-banded dark gray mud. Bioturbation is mostly absent or slight, and diatom ooze and diatom-bearing to diatom-rich mud occurs within numerous cores. Each interval with diatoms has gradational contacts and greater bioturbation intensity, and black mottling is often present. Graded sand beds with sharp lower contacts occur infrequently. Ash beds and volcaniclastic-bearing to volcaniclastic-rich mud occur irregularly. Lonestones appear deeper than ~3 m CSF-A and are present throughout. Unit II is dominated by mud interbedded with intervals of clast-poor diamict that range in thickness from a few centimeters to >1 m. Mud with clast concentrations ranging from dispersed to abundant is also present. Unit II extends over 546 m CCSF-B at Site U1418 and is divided into four subunits based on the relative thickness and occurrence of the diamict facies within the mud facies. Subunits IIA and IIC are dark gray to dark greenish gray muddy clast-poor diamict interbedded with dark gray mud and/or mud with dispersed clasts. The mud is weakly laminated, and coarse sand, granules, and lonestones of variable composition occur within both the diamict and mud. Subunits IIB and IID are dark gray to dark greenish gray laminated mud that is interbedded with mud with dispersed clasts and clast-poor diamict. Some intervals are calcareous bearing, and volcanic ash occurs as burrow fills and in dispersed intervals of moderate to heavy bioturbation. Lonestones occur throughout. Unit III is composed of laminated and bioturbated dark gray mud with thinly bedded, very dark carbonate-cemented gray sandstone and siltstone that are minor but distinctive components. Clast-rich muddy diamict containing rip-up clasts occurs near the base of the unit. A small number of lonestones occurs throughout this unit. Microfossils and ash are also rare. Unit IV is a very dark greenish gray mud mixed with a very dark gray clast-rich muddy diamict. Both facies are characterized by soft-sediment deformation and intrastratal contortions. There is a range of soft-sediment deformation fabrics, and normal faults are common in this unit. Rare lonestones were identified.

Figure **F41** shows the lithostratigraphic unit boundaries and core recovery at Site U1418. Unit I consists mainly of dark gray mud with thin silt and sand beds that is interpreted as originating from suspension settling through the water column and mud-rich sediment gravity flows originating at the shelf/slope. The lonestones in Unit I are interpreted to be IRD mostly deposited by icebergs calved from tidewater glaciers and/or from sea ice. The diatom intervals in Unit I might be related to increased biological productivity in the water column, and/or decreased input of terrigenous sediments. The strong influence of icebergs and/or sea ice on the deposition of facies within Unit II is indicated by the presence of IRD in the form of lonestones deposited in massive or laminated mud, as well as the accumulation of diamict. Rare intervals of moderate to heavy bioturbation may suggest a slower sediment accumulation rate than that of the laminated mud intervals. Thin-bedded diamict intervals bounded by thinly laminated packages of mud are similar to gravelly mud beds and laminated mud described from southeast Alaskan glacial fjords deposited by sea ice rafting and turbid meltwater plumes. The thin diamict beds may record the presence of sea ice during glacial periods. Unit III is similar to Unit II with interbedded laminated mud and massive/bioturbated mud being the two dominant facies. This unit additionally contains silt/sand beds and diamict that show evidence of sediment gravity flows. Despite the decrease in the number of lonestones and diamict beds relative to Unit II, their presence in this unit indicates that glacially derived and transported sediment was an important contributor during deposition. The cycles of interbedded massive and bioturbated mud (with dispersed clasts and few diamict beds) and laminated mud may point to periods characterized by a weaker glacimarine signal that alternate with periods of more intense ice rafting. The mixture of gray to dark gray mud and clast-rich muddy diamict characterized by soft-sediment deformation and intrastratal contortions of Unit IV is interpreted as the product of one or more mass transport events, which were interpreted from seismic reflection data (see **"Setting and objectives"**) (Reece, 2012). The presence of chlorite, mica, and ferromagnesian minerals in the bulk and sand samples in all units indicates the potential contribution from the Yakutat Terrane and/or a metamorphic/mafic source, perhaps the Chugach Metamorphic Complex. Site U1418 contains a more diverse range in lithologies of lonestones than Site U1417. The main lonestone lithologies are, in order of decreasing abundance, argillite, siltstone, basalt, sandstone, granitoid, and limestone. Metasedimentary lonestones may be derived from the St. Elias Mountains, Chugach Mountains, and/or ranges located along the southern coast of Alaska and northwestern British Columbia, but the combination of metagabbro, quartzite, rhyolite, and limestone suggests that the rocks of the Alexander Terrane may be considered as a possible source for some of the IRD. Rare volcanic ash and volcaniclastic-bearing sand at Site U1418 indicate that the location was proximal enough to either the Aleutian or Wrangell volcanic belts to have periodic influxes of pyroclastic detritus.

Based on the downcore occurrence of microfossils at Site U1418, two distinct intervals were identified. A rich siliceous and calcareous community was observed in the upper 200 m CCSF-B. Deeper than 200 m CCSF-B, calcareous microfossils are consistently preserved; however, the presence of siliceous microfossils is sporadic (Fig. **F42**). The rare occurrence of diatoms and radiolarians deeper than 200 m CCSF-B impeded identification of reliable biostratigraphic datums. The oldest datum encountered is the last occurrence of the planktonic foraminifer *Neogloboquadrina inglei*, which suggests that sediments around 600 m CCSF-B are older than 0.7 Ma (Fig. **F43**). This age is close to the Matuyama/Brunhes reversal found at ~660 m CCSF-B (Fig. **F44**).

Strong variations in environmentally sensitive planktonic foraminifers and radiolarians record the alternation of warming and cooling intervals during the last 1.2 m.y. (Fig. **F42**). In addition, variations of bottom water oxygenation are suggested by species changes in benthic foraminiferal fauna. Variations in diatom abundance and changes in species composition indicate changes in paleoproductivity, transport from shallow coastal waters, and a period of sea ice influence over Site U1418.

The NRM intensities of the APC-recovered (Holes U1418A–U1418C, Cores 341-U1418D-1H through 32H, and Hole U1418E), XCB-recovered (Cores 341-U1418D-33X through 37X), and RCB-recovered (Hole U1418F) materials were strong before (10^{-1} A/m) and after (10^{-2} to 10^{-3}A/m) demagnetization. Intensities show variability at both the meter and tens of meters scale. Inclinations of the RCB sections reveal an almost continuous sequence allowing correlation to the GPTS (Cande and Kent 1995; Hilgen et al., 2012) (Fig. **F44**). Even though the Matuyama/Brunhes polarity transition was not completely recovered, the transition from reversed polarity in Core 341-U1418F-43R to normal polarity in Core 41R is clear. Polarity transitions into and out of the Jaramillo (1r.1n) Subchronozone are clearly observed. Two short intervals of normal polarity are observed stratigraphically below the Jaramillo Subchronozone, with the older possibly indicating the Cobb Mountain Subchronozone (C1r.2n); this interpretation is consistent with the biostratigraphic datums. Shore-based analyses will allow significant refinement of these interpretations, especially within the APC-recovered sections. Focusing on the splice that contains the best recovered intervals and sampling within the most pristine central part of the core should result in a noticeably improved record. Additionally, discrete sampling through polarity transitions observed within the RCB-recovered interval would likely improve understanding of these features.

All available paleomagnetic and biostratigraphic age datums were integrated to construct minimum and maximum preliminary shipboard age models (Figs. **F43, F45**), which together span most of the uncertainty in the shipboard datums. All identified paleomagnetic datums (Matuyama/Brunhes boundary, top and base of the Jaramillo Subchron) observed in Hole U1418F are included in the shipboard minimum and maximum age models. Of the biostratigraphic constraints, the depth to the youngest observed datum (last occurrence of the radiolarian *Lychnocanoma nipponica sakaii*; 0.03 ± 0.03 Ma) is found in Hole U1418D. The shipboard minimum and maximum age models are calculated in increments of 0.2 m.y. between 0 and 1.2 Ma. Within these intervals, inferred sedimentation rates in the past 0.2 m.y. are 128 ± 23 cm/k.y. Over the interval 0.2–1.0 Ma, sedimentation rates are on average a bit lower, ~70 cm/k.y., but uncertainty ranges between 8 and 35 cm/k.y. when the calculation is made at 0.2 m.y. intervals. At ages ~1.0–1.2 Ma (all sediments shallower than the MTD), paleomagnetic constraints suggest even lower sedimentation rates of 45 ± 11 cm/k.y.

The physical properties program for Site U1418 included the same strategy for runs on the multisensor core loggers and sampling for discrete measurements as for Site U1417. Discrete *P*-wave velocity and vane shear strength were analyzed, and samples were taken for moisture, density, and porosity measurements from Holes U1418A, U1418B, U1418D, and U1418F. NGR data together with MS and GRA density data were used to correlate the six holes drilled at Site U1418 and to define a composite record.

Whole-round GRA density averages ~1.96 g/cm^3 in the APC cores and displays downhole cyclic variability on the order of ~0.4 g/cm^3, abruptly decreasing at ~220 m CCSF-B, corresponding to the transition to XCB coring (Fig. **F46**). Whole-round GRA density from XCB/RCB cores averages ~1.9 g/cm^3 but fluctuates with depth. After Gaussian smoothing of whole-round MS to accommodate for the differing response function of the instruments, we used this relationship to calculate the volume-corrected mass MS (χ). As at Site U1417, >50% of the variance in the uncorrected MS record can be attributed to reduced sediment volume. Mass MS averages ~50 cm^3/g downhole (Fig. **F47**). High-amplitude cyclic variations between 60 and 120 cm^3/g are present in the core shallower than ~220 m CCSF-B, transitioning to reduced scatter centered at ~40 cm^3/g in the deeper sections. This corresponds with the approximate depth of APC refusal and may reflect a concurrent change in lithology and/or incomplete volumetric correction of the WRMSL volume MS data. A return to a higher MS >60 cm^3/g deeper than 810 m CCSF-B may reflect the transition between lithostratigraphic Units III and IV. Compressional wave velocity was measured on the WRMSL *P*-wave logger (PWL) in Holes U1418A–U1418C at depths to ~200 m CSF-A at a resolution of 2.5 cm. Reasonable measurements could only be obtained for core depths shallower than ~200 m CSF-A because of the development of void spaces within the core liners after switching to XCB coring in Hole U1418D. Between ~110 and 180 m CSF-A, gas expansion prevented *P*-wave measurement using the PWL, as this sediment interval has high methane contents. PWL velocity values gradually increase downhole, closely following GRA densities, ranging from ~1450 m/s at the seafloor to ~1650 m/s at ~200 m CSF-A. PWL and discrete *P*-wave measurements using the *P*-wave caliper (PWC) were taken in Holes U1418A, U1418C, U1418D, and U1418F. Discrete measurements from Holes U1418A and U1418C overlapped PWL measurements deeper than ~200 m CCSF-B. PWC values appear systematically slower than the PWL measurements, but both follow similar downhole trends. PWC values show significant scatter from ~100 to 200 m CCSF-B, likely due to the presence of methane within the cores. Deeper than ~200 m CCSF-B, the range of values narrows and shows a slight increase with depth until ~560 m CCSF-B, where there is an ~20 m/s shift in the value range to ~1700 m/s. There are inflection points at ~700 m CCSF-B (~1750 m/s) and ~800 m CCSF-B (>1800 m/s), where velocities begin to increase at a faster rate, reaching ~2100 m/s at the bottom of the site at ~908 m CCSF-B. NGR values show downcore rhythmic fluctuations between 16 and 45 cps with mean and standard deviations of 33 and 3, respectively. High-frequency variations in NGR values are likely coupled with changes in clay contents and consequently parallel trends in GRA bulk density and *P*-wave velocity from the core logger measurements, particularly from 0 to 230 m CCSF-B in Holes U1418A and U1418C. A transition to lower volume-normalized NGR values stratigraphically below 810 m CCSF-B corresponds to lithostratigraphic Units III and IV. Shear strength indicates that sediments range from very soft (0–20 kPa) to very stiff (120–180 kPa). Generally, the rate of change of shear strength with depth is constant downhole. Values drop slightly off the trend between ~100 and ~130 m CCSF-B in the interval with high methane concentrations.

Routine headspace gas analyses were carried out on samples from Holes U1418A, U1418C, U1418D, and U1418F, and 117 samples were analyzed for carbonate, carbon, and nitrogen. A total of 105 interstitial water samples were taken for pore water characterization. Solid-phase geochemical results characterize Site U1418 as an oligotrophic, deepwater, subarctic setting. Although both TOC (0.2–1.0 wt%) and TN (0–0.1 wt%) contents are low, their respective accumulation rates are substantially higher than at Site U1417 because of much higher sedimentation rates at Site U1418. The carbonate contents are also low (0–5 wt%) but slightly higher than Site U1417. Chloride, sodium, bromide, and salinity are elevated in the uppermost 30 m CCSF-B, documenting relict glacial seawater (Fig. **F48**). Higher organic matter accumulation rates at Site U1418 are reflected in the more pronounced diagenetic processes. Strong organic matter remineralization occurs at ~30, ~70, and ~150 m CCSF-B, as indicated by the ammonium, alkalinity, and methane profiles (Fig. **F48**). Based on the composition of interstitial waters, Site U1418 can be broadly divided into two biogeochemical zones, one reaching from the core top to ~70 m CCSF-B (suboxic-anoxic diagenesis) and the other reaching from ~70 m CCSF-B to the bottom of the record (methanogenesis). Thus, Site U1418 documents a classic catabolic reaction sequence, including the reduction of manganese, iron, sulfate, and methanogenesis. Sulfate depletion is reached at ~76 m CCSF-B, and methane increases deeper than ~80 m CCSF-B (ranging from 5,000 to 63,000 ppmv), marking a distinct sulfate–methane transition zone. Geochemical variability within the expanded methanogenic zone is mostly driven by variable organic matter degradation intensities and by clay mineral adsorption-desorption processes. Elevated ammonium and alkalinity around 500–600 m CCSF-B indicate organic matter degradation by methanogenesis (Fig. **F48**), probably related to labile marine organic matter availability. Here, preferential adsorption of ammonium to clay mineral surfaces releases barium, lithium, and boron from the adsorption sites. Shallower and deeper than the high-ammonium zone, these cations readsorb to (partly authigenic) clay minerals.

Logging at Site U1418 was done in Hole U1418F and consisted of successful triple combo logs, without the porosity sonde, from 0 to 600 m WSF and FMS-sonic logs from 0 to 582 m WSF. The downhole logged interval in Hole U1418F is assigned to one logging unit (Fig. **F46**) because the character of the logs changes gradually downhole without major shifts. At the scale of this unit, the NGR signal ranges on average from 35 to 55 gAPI units, with the exception of anomalously low values corresponding to washed-out intervals. The natural radiation signal is generally dominated by potassium and thorium content, with minor uranium contribution. For the most part, the three radioactive elements trend similarly, suggesting that they are mainly responding to clay mineralogy or content. Density measurements do not show specific characteristics in the logged interval. Resistivity data show a slight decrease with depth over the logged interval, which is counter to the expected increasing trend with depth due to compaction; however, lower mean values deeper than 462 m WMSF may simply be a response to the wider borehole diameter in this interval. MS data do not trend noticably downhole, and velocity measurements show a generally increasing trend with depth.

Sediment core descriptions, core physical properties measurements, and downhole logging data obtained from Site U1418 were combined to examine the coherence between the different data sets and evaluate the completeness of the recovered sediment record. High and low MS measurements derived from the sediment core correlate with intervals of high and low MS values in the logging data (Fig. **F47**). At a finer scale (<10 m), we observe high MS in the logging data associated with diamict and sand layers, whereas low values occur in intervals with diatom ooze, mud with laminations, and bioturbated mud. With the exception of washed-out sections of the borehole, the natural gamma ray log shows reasonable agreement with the volume-corrected core NGR, with a similar range in values and similar features occurring within a few meters offset in depth (Fig. **F46**). The washouts shown in the caliper log generally correspond to lower gamma ray values in core logger NGR data, which cannot be affected by borehole size, whereas the downhole logging data are. Thus, these washouts appear partly controlled by lithology within the upper part of the borehole, where the dominant lithology is interbedded silt and mud (lithostratigraphic Unit I). Silt or sand beds are more likely to wash out during drilling, leading to thin intervals of enlarged borehole diameter. This interpretation is supported by the lower gamma ray values measured on cores from some of the washed-out intervals (Fig. **F46**), as would be expected for a transition from muddy to more silty/sandy lithologies. Correspondence was also noted between the lithostratigraphic units, the distribution of diatom ooze and mud with clasts, and downhole changes in spectral gamma ray and total gamma ray. The bulk density log (Fig. **F46**) is strongly affected by the irregular borehole diameter, giving density values close to water in washed-out intervals. The highest downhole density values, however, show reasonable correspondence with maximum density values in the range of the GRA density data and show good agreement with the trends in discrete MAD measurements. The *P*-wave velocity log indicates higher formation velocities than discrete *P*-wave measurements on core over the logged interval (Fig. **F46**). The separation in velocity estimations increases with depth downhole. The discrete measurements may be biased toward lower velocity matrix material, whereas the downhole log is integrating lower velocity sediment matrix and higher velocity clasts, which were found to be a notable component in all lithostratigraphic units described at this site. Alternatively, the presence of gas in the formation may also play a critical role. Even though gas would affect both core and downhole log measurements of velocity, gas expansion in cores may have caused cracking and the development of void spaces, leading to poor contact with the instrument transducers and resulting in anomalously low velocities.

For preliminary correlation between lithostratigraphic units, logging units, and seismic features, lithostratigraphic and logging unit boundaries were converted from the CCSF-B (for core data) or WMSF (for logging data) scales to TWT using the average velocities of each unit. Average *P*-wave velocity was derived from physical properties measurements, using data from the PWC shallower than ~257 m (CCSF-B) and the downhole sonic logs at depths less than ~548 m (WMSF/CCSF-B). Deeper than ~548 m WMSF/CCSF-B, we used values calculated from the linear trendline of the downhole sonic log, though detailed correlations will require postcruise research. Seismic Subunit IIIC features a prominent reflection at ~5.04 s TWT (Fig. **F25**), separating the seismically more transparent facies at the top of the unit from the continuous horizons underlying the reflector. Line GOA3202 resolves an additional high-amplitude package of approximately four reflectors at ~5.1

s TWT (Fig. **F39**). Lithologically, these high-amplitude features could be associated with thick beds of mud separated by silt-rich intervals observed within lithostratigraphic Unit I. The boundary between seismic Subunits IIIB and IIIC at ~5.26 s TWT is located at the top of the youngest aggradational package that comprises the northwest flank of the Bering Channel (Fig. **F25**). At Site U1418, this boundary marks a subtle downsection change from higher to lower amplitude horizons, which is clearly resolved on the high-resolution Profile GOA-3202 (Fig. **F39**). Based on our traveltime-depth conversions, this boundary coincides with the boundary between lithostratigraphic Units I and II at ~257 m CCSF-B. Within seismic Subunit IIIB, two high-amplitude packages are resolved on the GOA3202 profile at ~5.31 and ~5.41 s TWT (Fig. **F39**). Each of these packages corresponds to a subtle change in brightness within the unit on the regional seismic Profile STEEP07 (Fig. **F25**). The boundary between lithostratigraphic Subunits IIA and IIB (~335 m CCSF-B) correlates to a reflector that lies between these two high-amplitude packages. The seismic Subunit IIIB/IIIA boundary correlates with the boundary between logging Subunits 1D and 1E at ~500–510 m WMSF. Both the density and velocity log values decrease at this boundary (Fig. **F39**). At the top of seismic Subunit IIIA, starting at ~5.54 s TWT, we observe both an increase in amplitude and a shift into slightly more chaotic facies. Deeper than ~5.75 s TWT, the seismic reflections are less stratified and more heterogeneous. The strata here are no longer parallel, and internal truncations and lobate geometry indicate either a more energetic depositional environment or deformation. Lithologic boundaries separating lithostratigraphic Subunits IIB–IID and Unit III are all located within seismic Subunit IIIA. Seismic Unit II* is defined by chaotic seismic facies starting at ~5.88 s TWT (Fig. **F39**). Some internal structure can be observed within the upper ~100 ms of Unit II*. The transition out of this 100 ms interval into the underlying noncoherent facies may be equivalent to the lithostratigraphic Unit III/IV boundary and the transition into an MTD.

Site U1419

Setting and objectives

Site U1419 is located at 687 m water depth on a relatively flat bank on the continental slope above Khitrov Basin and Ridge (Fig. **F38**). We informally refer to the feature as Khitrov bank (KB). The site is within the influence of the near-surface Alaska Coastal Current (Stabeno et al., 2004; Weingartner et al., 2005) and at a water depth possibly influenced by deeply rooted surface eddies and North Pacific Intermediate Water.

The drilling objectives at the site sought to capitalize on good preservation of carbonate microfossils and associated geochronologic methods that can be used to develop a high temporal resolution, proximal sedimentary record of Late Pleistocene glacial dynamics and paleoceanography (Davies et al., 2011; Addison et al., 2012). A primary objective was to constrain the timing of glacial events of the Pacific side of the NCIS to test its relation to changes of the larger ice sheets of the Northern and Southern Hemispheres and other global-scale climate effects. An allied goal is to understand the role of North Pacific sea-surface temperatures as a possible control on the glacial system over Late Pleistocene time, with the potential for decadal-to-centennial resolution in the glaciated and laminated intervals. The proximity of Site U1419 to regions of seasonally high surface productivity (Ladd et al., 2007) offers an opportunity to assess the relative roles of productivity and intermediate water circulation on hypoxia in the northeast Pacific and their importance in the global carbon cycle. The potential for a highly resolved radiocarbon and oxygen isotopic chronology (Davies et al., 2011) permits documentation of the interrelationship between paleomagnetic intensity and secular variation in the Pacific sector in comparison with records from the Atlantic sector.

Coring results and high-resolution CHIRP and MCS data reveal a complex depositional setting. The drill site is ~30 km west of the of Bering Trough mouth that may have been the terminus of the Bering Glacier at the LGM (Carlson and Bruns, 1997; Berger et al., 2008a) (Fig. **F38**). The site was surveyed during Cruise EW0408, resulting in a jumbo piston core (~11.5 m long) that contains a record of late glacial (~17.5 k.y.) to Holocene hemipelagic and glacimarine sedimentation (Barron et al., 2009; Davies et al., 2011; Addison et al., 2012). Seismic reflection data reveal variations in seismic facies that likely reflect the time-varying input of glacigenic sediment interspersed with biogenic-rich, potentially laminated hemipelagic facies (Fig. **F13A**). Processed CHIRP images (Fig. **F13B**), coincident with MCS profiles, reveal that an upper acoustic transparent layer on the profile corresponds to the upper ~8 m of postglacial sediment in Core EW0408-85JC, which dates to younger than 14.7 ka (Davies et al., 2011). The strong reflections in the CHIRP line and near the sediment/water interface to ~0.03 s (~8–25 m) in MCS Line GOA3201 likely represent the glacimarine sediments associated with the local LGM deposited at ~15–30 ka, at an average sedimentation rate of ~120 cm/k.y. (although with extremely high rates for brief intervals; Davies et al., 2011) (Fig. **F13**). It is hypothesized that the underlying, less reflective layered sediments in the MCS profile represent finer grained interglacial or interstadial events when the Bering Glacier terminus retreated relative to the shelf break and ice rafting of coarse sediment was reduced or absent. In contrast, the highly reflective intervals likely indicate times when ice rafting was active and there were higher accumulation rates of coarser glacigenic sediment.

Seismic Units A–K (Fig. **F49**) were selected at Site U1419 based on seismic facies possibly reflecting changes in glacial proximity. Active faulting is imaged in high-resolution seismic Profile GOA3101, showing surface deformation indicative of significant amounts of extension or transtension (Fig. **F13A**) (Worthington et al., 2008).

Results

At Site U1419, Holes U1419A, U1419B, U1419C, U1419D, and U1419E were drilled to total depths of 193, 113, 107.1, 103.7, and 75.5 m CSF-A, respectively (Fig. **F50**). Core recovery and refusal depths were significantly affected by frequent lonestones and diamict. For Holes U1419A, U1419B, U1419C, U1419D, and U1419E, full-length (9.7 m) APC refusals were encountered at 98.4, 81.8, 78.7, 80.16, and 69.0 m drilling depth below seafloor (DSF), respectively; half-length (4.7 m) APC refusals were encountered at 118.5, 114.03, 108.6, 114.15, and 98.76 m DSF, respectively. XCB coring using the soft-formation cutting shoe was used only in Hole U1419A from 118.5 to 189.68 m DSF. A total of 101 cores were recovered at the site. A total of 473 m of core over a 517.9 m interval was recovered using the APC systems (91% recovery). The cored interval with the XCB system was 74.4 m with a recovery of 14.86 m of core (20%). APC shot depths in Holes U1419B–U1419E were carefully planned with the aid of the stratigraphic correlators, but poor recovery required five holes to attain essentially complete recovery to ~100 m CCSF-B.

The composite depth scale at Site U1419 was constructed from 0.0–205.79 m CCSF-A. The shipboard splice extends from the mudline to 112.10 m CCSF-D. Weather was calm and ship heave was negligible while coring Site U1419, but the relatively lonestone rich ice-proximal environment proved challenging for core recovery and for interhole correlation. Intervals of core disturbance, incomplete recovery, and use of the half-length APC coring system presented complications in the development of composite depths and a spliced record. In particular, we observed many instances of flow-in, generally (but not always) near the base of cores, and some fall-in of rocky debris in core tops. Some parts of the splice are unique in an individual hole and are not well verified. We urge caution in using the splice from Site U1419 until it can be verified with postcruise data. An additional depth scale (CCSF-B) was created to compress and shift the correlated cores to produce the correct total drilled interval. Where appropriate, results are reported in this depth-corrected composite depth scale.

The sediment recovered at Site U1419 contains 14 facies. The dominant facies are dark gray to dark greenish gray mud and diamict. They account for >95% of the core recovered. Specific lithofacies include massive mud with and without lonestones, silt, interbedded silt and mud, very fine to coarse sand, interbedded sand and mud, interbedded mud and diamict, clast-poor diamict, clast-rich diamict, diatom ooze, biosiliceous ooze and biosiliceous rich/bearing mud, calcareous/carbonate-bearing mud, volcanic ash, and volcaniclastic mud and sand. These facies are inferred to reflect deposition from suspension fallout, sediment gravity flows, ice rafting, variations in productivity/preservation of biogenic material, and subaerial volcanic eruptions.

The main lithologies of the diamict clasts and lonestones recovered at Site U1419 are, in order of decreasing abundance, siltstone, argillite, sandstone, basalt, granitoid, and chert. The petrology of lonestones is similar to that found in the St. Elias and Chugach Mountains located along the southern coast of Alaska. The rare volcanic ash and volcaniclastic-bearing sand at Site U1419 indicate that the location was proximal enough to either the Aleutian or Wrangell volcanic belts to have some influxes of pyroclastic detritus. Smear slides and XRD analysis indicate similar bulk mineralogies downhole, although there are some variations in relative XRD diffraction peak intensities that may indicate slight variations in mineral content.

Based on facies associations, two lithostratigraphic units were defined at Site U1419 (Fig. **F51**). The contact between these units is gradational. Unit I lithologies largely consist of olive-gray to dark greenish gray diatom ooze to diatom-rich mud, dark gray to dark greenish gray mud with lonestones, and clast-rich diamict. The clast content increases deeper than ~90 m CCSF-B, forming intervals of mud with abundant clasts. Subordinate lithologies in Unit I include dark gray interbedded sand and mud, thin sand beds with sharp lower contacts, interbedded silt and mud, and volcanic ash. Unit II is dark gray muddy clast-poor diamict interbedded with dark gray laminated mud and thin coarse sand beds. A few meter-thick intervals of diatom and bisosiliceous ooze also are observed. Detailed description of Unit II is limited by incomplete recovery deeper than 114 m CCSF-B.

Both lithostratigraphic units are interpreted as reflecting sedimentation in a dynamic setting primarily influenced by glacimarine processes with secondary intervals of biogenic accumulation. The difference between the units may reflect the relative weighting of these different styles of sedimentation. The lonestones in Unit I are interpreted to have been rafted by icebergs calved from tidewater glaciers. The presence of diamict suggests that icebergs contributed large quantities of debris, larger than sand size, to this site. Some sediment gravity flows are inferred from the presence of sand beds and intervals with interbedded sand and mud. These sand beds typically have sharp lower contacts and are normally graded. Other thin sand beds have less definite contacts and may be deposited from turbid meltwater plumes and/or sea ice. The biosiliceous-rich intervals more prevalent in Unit I might reflect either increased biological productivity and/or decreased dilution with terrigenous sediment. The frequent alternation of diatom ooze and diatom-rich sediments with intervals dominated by mud with lonestones and diamict suggests a system influenced by changes in climate and glacier dynamics.

The diamict facies most prominent in Unit II likely has a glacigenic origin. Gradational contacts between facies and the observation of clast-rich diamict interstratified with mud (including mud with diatoms) indicate fluctuating sediment supply typical of a glacimarine environment. Massive diamict beds may indicate periods of more intense iceberg rafting with a high flux of sand and coarser sediment. Intervals of interbedded mud and thin diamict beds suggest the possibility of sea ice rafting in addition to iceberg rafting. Sediment gravity flows are indicated by interbedded sand and mud and thicker sand beds. Three prominent intervals of diatom/biosiliceous ooze, interbedded with diamict in Unit II, roughly similar to modern sedimentation at the site, imply some intervals of reduced glacial sediment supply. The exact timing of the observed lithologic and compositional transitions requires the development of a detailed chronology at Site U1419.

Microfossil abundance and preservation at Site U1419 varies depending on skeletal composition. Calcareous microfossils (planktonic and benthic foraminifers) and nannofossils are well preserved and continuously abundant in Site U1419 cores (Fig. F52). Fourteen planktonic foraminifer species were encountered at Site U1419, with faunal assemblages dominated by polar to subpolar species. Within the interval from ~80 to 90 m CCSF-B, diatom resting spores and planktonic and benthic foraminifers have an abundance peak and the benthic foraminifer *Eubuliminella exilis* dominates the assemblage, suggesting a strong environmental change in the water column and at the seafloor during the time represented by that interval.

Siliceous microfossil preservation and abundance is less consistent. Radiolarian fauna are moderately preserved in the upper 115 m CCSF-B, and their abundances fluctuate from rare to abundant (Fig. F52). Generally cold-water radiolarian taxa dominate the assemblages. Deeper than 115 m CCSF-B, most samples examined were barren of radiolarians. The diatom preservation and abundance trends are similar, but their preservation and abundance are lower than the radiolarians in the upper 115 m CCSF-B. Cold-water diatom species dominate the assemblage at Site U1419 and are most abundant in the uppermost 10 m CCSF-B and in the interval from 75 to 90 m CCSF-B (Fig. F53).

Sea ice–related warm and temperate diatom species are often noted when diatoms are observed, but these species are a relatively minor component of the assemblage and range between present and rare. The only diatom biozone recognized at Site U1419 is NPD 12 (present–[0.3 ± 0.1] Ma). The last occurrence of *Proboscia curvirostris* (Jousé) Jordan et Priddle (D120; 0.3 ± 0.1 Ma) is not observed. The last occurrence datum of radiolarian *Stylocontharium acquilonium* Hays (0.4 Ma) is also not encountered.

NRM intensities of the APC (Holes U1419A–U1419E) and XCB (Cores 341-U1419A-21X through 29X) cores were strong before AF demagnetization (10^{-1} A/m) but were significantly weaker after demagnetization (10^{-2} to 10^{-4} A/m). Intensities vary at both the meter and decameter scales, with discrete intervals of very low intensities (Fig. F54) corresponding to intervals of biosiliceous ooze and diatom-rich mud. Because inclinations indicate generally normal polarity, it is thought that the recovered sediment is exclusively within the Brunhes Chronozone and younger than 0.781 Ma (Cande and Kent, 1995; Hilgen et al., 2012).

Normal geomagnetic polarity in all cores implies that all sediments recovered are younger than 781 ka. The uppermost part of the sequence can be correlated with site survey Core EW0408-85JC, a radiocarbon-dated piston core from the same site (Davies et al., 2011), based on MS. The interval of relatively low MS from 0 to 6.4 m CCSF-A (0 to 5.5 m CCSF-B) at Site U1419 is assigned to Holocene and Late Pleistocene ages (0–15 ka), implying an average interglacial sedimentation rate of 40 cm/k.y. Oxygen isotopes of foraminifers picked at sea from the core catcher sample and analyzed immediately postcruise at Oregon State University, indicate that the maximum age of at the base of the site (205.79 m CCSF-A) is <60,000 years, implying an average glacial sedimentation rate of 380 cm/k.y.

Physical properties analyses included measurements on the multisensor core loggers and sampling for discrete measurements. Whole-round GRA density averages ~1.93 g/cm^3 in the APC cores and displays downhole recurring variability on the order of ~0.2 g/cm^3 (Fig. F55). Two intervals of relatively low GRA density (<1.8 g/cm^3) occur between ~0 and 6 and between ~80 and 87 m CCSF-B. After corrections for variable sediment volume within the core liner, mass MS averages around ~68 cm^3/g downhole (Fig. F55). An interval of high-amplitude variability between 55 and 90 cm^3/g is found shallower than 80 m CCSF-B. Whole-round loop MS trends largely parallel GRA bulk density trends from ~0 to 6 and ~80 to 90 m CCSF-B, but a shift to the opposite trends at finer scales is observed from 6 to 80 and 90 to 120 m CCSF-B, suggesting fundamental changes in lithofacies between these intervals. Compressional wave velocity was measured on the WRMSL. A near-continuous record of velocities was captured in Holes U1419C–U1419E between ~5 and 25 m CCSF-B and showed velocities <1600 m/s. At depths greater than ~25 m CCSF-B, WRMSL PWL velocity measurements were compromised because of the high gas content of the recovered sediment.

Discrete *P*-wave velocity and vane shear strength were analyzed, and samples were taken for moisture, density, and porosity measurements from Hole U1419A. Void spaces within the unconsolidated sections, gas expansion, and gaps in core recovery result in only a limited characterization of *P*-wave velocity, although all discrete measurements at this site were taken within the dominant lithology of the recovered interval. Velocity values show no significant overall trend with depth, though a region of higher velocity is observed at ~120 m CCSF-B where values increase to ~1800–2100 m/s (Fig. F51).

NGR measurements show recurring downhole variations between 14 and 43 cps with mean and standard deviations of 32 and 4, respectively. Downcore variability in raw NGR values closely parallels changes in GRA bulk density. Two notable intervals of reduced raw NGR (<30 cps) occur between ~0 and 6 and between ~80 and 87 m CCSF-B, corresponding to the uppermost and lowermost parts of lithostratigraphic Unit I, respectively (Fig. F56). MAD discrete values correspond well to GRA bulk densities measured on the WRMSL for Hole U1419A. MAD densities increase downhole from ~1.5–1.6 g/cm^3 at the seafloor to ~2.2–2.4 g/cm^3 at ~120 m CCSF-B. The interval between ~120 and ~140 m CCSF-B was not recovered. Deeper than ~140 CSF-A, density increases from ~2.0–2.1 to 2.2 g/cm^3 by ~180 m CCSF-B (Fig. F51). Porosity (percent pore space of wet sediment volume) measured on discrete samples generally decreases with depth. Between ~55 and 100 m CCSF-B, the values show more scatter than seen in grain density values in comparable depth intervals. Shear strength indicates that sediments range from very soft (0–20 kPa) to stiff (up to 79 kPa). Generally, shear strength increases with depth at a constant rate. An anomalous interval of elevated shear strength (~60–79 kPa) is present at ~115 m CCSF-B. This interval coincides with an increase in both *P*-wave velocity and density and a decrease in porosity (Fig. F51).

Routine headspace gas analyses were carried out on samples from Hole U1419A, and 20 samples were analyzed for carbonate, carbon, and nitrogen. A total of 22 interstitial water samples were taken for pore water characterization. TOC (0.4–1.0 wt%), TN (0–0.1 wt%), and carbonate (1.5–4.0 wt%) contents are within the range exhibited by Holocene to late glacial sediments at this location (Addison et al., 2012) (Fig. F57). Organic carbon/TN (C/N) ratios range between 10 and 22 (Fig. F57), consistent with a contribution from both marine and terrigenous organic matter and within the range exhibited by recent sediments in the area (Walinsky et al., 2009). Chloride, salinity, and sodium profiles document a significant freshening of pore waters with depth, related to gas hydrate dissociation or buried glacial meltwater. Biogeochemical processes at Site U1419 follow the catabolic sequence, with the exception of manganese reduction, which is apparently completed shallower than the depth of the uppermost pore water sample. Total sulfate depletion is reached at ~20 m CCSF-B, and methane production occurs deeper than 20 m (mostly 10,000–40,000 ppmv), indicating a sulfate–methane transition zone at ~20 m CCSF-B. Ammonium and alkalinity both exhibit broad maxima between ~20 and 90 m CCSF-B, suggesting that most organic matter degradation is occurring within the methanogenic zone. This process also seems to release organic matter–derived bromide, boron, and phosphate to the pore waters. At Site U1419, both ammonium and alkalinity show relatively high concentrations, indicating intense diagenesis likely driven by the input of more reactive organic matter, possibly reflecting the location of Site U1419 adjacent to the coastal Alaskan high-productivity zone.

Seismic Lines GOA3101 and GOA3102 cross Site U1419 (Fig. F13). At a gross scale, seismic character across both profiles changes from laterally continuous subhorizontal reflectors (seismic Units A–B) to generally more chaotic facies with intermittent semicontinuous units (seismic Units C–F) (Fig. **F51**). Unit A is defined by two high-amplitude, continuous reflectors between the seafloor and ~0.937 s TWT. This seismic unit correlates with a gray diatom ooze interval that comprises the top ~6 m CCSF-B of the core. This interval also displays relatively low MS, *P*-wave velocity, and density. Unit B (~0.937 to ~.0.997 s TWT) features conformable, subhorizontal, continuous reflectors. The corresponding interval of the cores (~5–55 m CCSF-B) consists of gray mud with lonestones. Some of the peaks in MS within this interval may be associated with occasional sand layers, whereas other peaks may be associated with individual clasts. The presence of diatomaceous material within this interval correlates with lows in MS at ~16 and ~60 m CCSF-B. Unit C (~0.997–1.045 s TWT) is defined by high-amplitude, semichaotic reflectors with some truncations. According to our depth conversion, the lower portion of Unit C correlates to an interval of low MS and density from ~80 to 90 m CCSF-B composed of diatom ooze and mud with lonestones. The boundary between seismic Units C and D correlates to the boundary between lithostratigraphic Units I and II, which is defined by a change from mud with lonestones (Unit I) to muddy clast-poor diamict interbedded with laminated mud and thin coarse sand beds (Unit II). Seismic Unit D (~1.045–1.095 s TWT) is composed of two packages of high-amplitude, semicontinuous reflectors. The lower portion of Unit D correlates with an interval of high density and velocity between ~113 and ~120 m CCSF-B, which consists of muddy clast-poor diamict that is interbedded with laminated mud and thin coarse sand beds (part of lithostratigraphic Unit II).

Site U1420

Setting and objectives

A fundamental hypothesis to be tested with results from Expedition 341 is that the St. Elias orogen has undergone perturbation that has markedly changed the patterns and rates of deformation and exhumation in the orogenic wedge. It is proposed that enhanced glacial erosion associated with the MPT and the establishment of highly erosive ice streams lead to substantial mass redistribution in the wedge, shutting down regions of active deformation and refocusing the deformation and exhumation patterns of the orogen (Berger et al., 2008a; Worthington et al., 2008, 2010; Chapman et al., 2008).

Site U1420 lies within the Bering Trough (Fig. **F10B**), a shelf-crossing trough likely formed by the Bering Glacier advancing across the shelf during glacial maxima (Carlson, 1989) at ~250 m current water depth. The site penetrates through an angular unconformity (Horizon H1; Fig. **F9**) at shallow subseafloor depths (180–200 mbsf expected) that has been suggested to be the first occurrence of grounded glaciers reaching as far as the modern shelf edge (Berger et al., 2008a). Underlying this angular unconformity are the waning folds of a portion of the Pamplona Zone, which is a fold-and-thrust belt that has accommodated some of the tectonic shortening caused by the underthrusting of the Yakutat Terrane beneath North America to form the St. Elias orogen (Worthington et al., 2010). Previous mapping suggests that the folding within the Pamplona Zone beneath the Bering Trough waned by the time of seismic Horizon H2 (Fig. **F9**) (Berger et al., 2008a; Worthington et al., 2010). Lack of significant deformation in the sequences stratigraphically above Horizon H2 indicates that the underlying faults were abandoned before the angular unconformity of Horizon H1 formed, possibly due to loading by sediments (Berger et al., 2008a; Worthington et al., 2010). The overall architecture of the continental margin is thus the product of coupled depositional and tectonic processes.

The drilling objective at the site was to address the hypothesis that the onset of ice streams has resulted in correspondingly high erosion rates that could markedly alter orogenesis (Berger et al., 2008a). Drilling targets are Horizons H1 and H2. Retrieval of sediments from the seafloor to Horizon H2 will provide age control, which is lacking for this location, thereby establishing sediment accumulation rates that can be used to test the hypothesis. Cored sediments can also provide provenance records that can be used to test the hypothesis that the locus of erosion is within the windward side of the orogen (Berger et al., 2008a).

Results

Cores 341-U1420A-1R through 106R (1020.8 m DSF) were drilled with the RCB. Recovery over the entire hole was problematic because of the presence of numerous rock clasts that continually jammed the core catchers and prevented core recovery. A total of 106 rotary cores were taken over a 1020.8 m interval with a total recovery of 139.91 m of core (14%) (Fig. **F58**). Because only a single hole was drilled/cored at Site U1420, no stratigraphic correlation was performed at this site. All results are presented on the CSF-A scale.

The limited sediment recovered at Site U1420 contains seven facies. Recovery from 58.2 to 448.5 m CSF-A was <10% but improved deeper than 448.5 m CSF-A, where several cores were collected with recoveries between 30% and 94%. Numerous drilled rocks and washed clasts were recovered in the hole without a supporting sediment matrix. The dominant facies are very dark gray to dark gray clast-rich and clast-poor diamict (Fig. **F59**). Additional facies include massive mud with and without lonestones, mud with diatoms/biosilica, calcareous/carbonate-bearing mud, and volcaniclastic mud and diamict. These facies are inferred to reflect deposition from suspension fallout, sediment gravity flows, ice rafting, and variable productivity/preservation of biogenic material.

The main lithologies of the drilled rocks, washed pebbles, clasts within the diamict, and rare lonestones contained in the sediment are, in order of decreasing abundance, sandstone, siltstone, basalt, and granitoids. The granitoid group includes intermediate and felsic intrusive rocks. Argillite, rhyolite, and metasandstone represent minor lithologies. The petrology of lonestones is similar to that found in the St. Elias and Chugach Mountains located along the southern coast of Alaska. The rare volcaniclastic-bearing mud at Site U1420 indicates that the location was proximal enough to either the Aleutian or Wrangell volcanic belts to have influxes of pyroclastic detritus. Smear slides and XRD indicate similar bulk mineralogies downhole, though there are some variations in relative XRD diffraction peak intensities, which may indicate slight variations in mineral content.

Based on characteristic facies associations, three lithostratigraphic units were defined, the contacts between which are not observed because of poor core recovery. Lithostratigraphic Unit I consists of very dark gray, muddy, clast-rich diamict interbedded with clast-poor diamict with angular to rounded clasts ranging in size from granule to pebble. The diamict beds are massive and have mainly silt and clay matrixes with some outsized sand grains. Recovery in Unit II ranged from 0% to 8%. The major lithology was not recovered, and cores mostly contain washed pebbles and cylindrical-shaped drilled rocks with abraded surfaces. Small amounts (<10 cm) of usually heavily disturbed sediment were occasionally recovered. Unit III consists of very dark gray clast-rich, muddy diamict and very dark gray to dark gray clast-poor, muddy diamict interbedded with very dark gray to dark greenish gray mud with or without clasts. Drilled rocks occasionally occur coincident with low core recovery.

These lithostratigraphic units are interpreted as reflecting sedimentation in a dynamic setting primarily influenced by glacimarine processes with intervals of biogenic deposition. Unit I diamict is interpreted as either deposited subglacially or by deposition from intense iceberg rafting along with mud from meltwater plumes. Both tentative interpretations for Unit I require additional sediment fabric analyses for verification. In Unit II, it is impossible to interpret the depositional environment of these isolated clasts without the context provided by the matrix and other "missing" finer grained lithologies. The cylindrical drilled rocks within Unit II are interpreted as being recovered from boulders within the formation; such boulders are observed in outcrops of the glacimarine Yakataga Formation.

The interbedded diamict and mud in Unit III is interpreted to represent fluctuations in the glacial grounding-line position relative to Site U1420, as well as variations in the supply of IRD and meltwater in a proglacial setting. The sources for clasts at Site U1420 are interpreted to be the St. Elias and Chugach Mountains located along the southern coast of Alaska.

Microfossil abundances are generally low at Site U1420 (Fig. **F60**). Diatoms and radiolarians are only observed in three intervals. Thus, age constraints are few, but they suggest an age younger than 0.7 Ma. Benthic and planktonic foraminifers are better preserved and occur throughout the record. Diatom occurrence is mostly low, and preservation is mostly poor. The diversity of the diatom community at Site U1420 is low and mainly consists of Pleistocene to Holocene species. Cold-water species are the most abundant, and coastal and benthic diatoms are observed. Radiolarians are mostly barren except for two intervals, and the fauna is mostly marked by the presence of cold shallow-water radiolarians, but deeper than ~750 m CSF-A, the assemblage is marked by relatively high abundances of deepwater species. Planktonic foraminifers are present, sometimes in high abundance, and the preservation is generally good. Planktonic foraminifers are mostly associated with cold-water conditions. Benthic foraminifers are present to abundant, and preservation varies between good and poor. Changes in the composition of the benthic foraminiferal fauna suggest changes in water depth ranging from inner neritic to upper bathyal.

The NRM intensities of the cores were strong before AF demagnetization (10^{-2} ~ 10^{-1} A/m), but were weaker after demagnetization (10^{-2} to 10^{-3} A/m). Because inclinations indicate generally normal polarity, it is thought that the recovered sediment is exclusively within the Brunhes Chronozone and younger than 0.781 Ma.

The biostratigraphy indicates that the cored sediments are in modern biozones. The recovered cores are all normal magnetic polarity. Because the Matuyama/Brunhes geomagnetic polarity boundary was not observed, we can conclude that the entire sedimentary sequence recovered at Site U1420 is younger than 0.781 Ma.

Physical properties analyses included measurements on the multisensor core loggers and sampling for discrete measurements. Whole-round GRA density averages ~1.8 g/cm^3 in the RCB cores and displays downhole variability on the order of ~0.3 g/cm^3 (Fig. **F59**). Densities measured with the WRMSL should be regarded as minimum estimates, as observed densities are likely influenced by the highly variable diameter of the recovered sediment in the cores. Mass MS averages ~54.3 cm^3/g downhole, with several successions of variability between 25 and 70 cm^3/g deeper than 550 m CSF-A that appear to increase deeper than ~940 m CSF-A, although limited core recovery hinders interpretation. Because of poor core recovery, only *P*-wave measurements using the PWC were taken from 0 to 449 m CSF-A. Deeper than ~449 m CSF-A, PWC values show no significant overall trend with depth and vary widely, sometimes within the same core section, likely because of the varying amounts and lithology of clasts in the diamict. Though values generally range from ~1500 to ~2000 m/s, occasional high values with velocities >2200 m/s are also observed (Fig. **F61**). Low-frequency variability in mass-normalized NGR activity is limited in the recovered cores, although an increase in activity deeper than 940 m CSF-A parallels changes in normalized MS (χ) and may reflect a change in lithology.

MAD bulk density values range from 2.0 to 2.4 g/cm^3 between ~40 and 440 m CSF-A in recovered intervals (Fig. **F62**). Deeper than ~450 m, MAD values vary from ~2.0–2.4 to ~2.1 g/cm^3 with no obvious overall trend with depth. Grain density values consistently display wide scatter from ~2.7 to 3.0 g/cm^3 and do not appear to correspond with lithology. Porosity measured on discrete samples generally decreases with depth, with some ~10–20 m thick intervals of wide scatter (~22–45 vol%) with higher values corresponding with muddy lithologies. Porosity is ~25–30 vol% in clast-rich diamict facies. Void ratio values mimic porosity with depth with typical values around 0.4. Figure **F62** shows these density, porosity, and void ratio values in relation to lithologic facies. Only four shear strength measurements were obtained, all shallower than 40 m CSF-A. All measurements were taken in the dominant lithology of the recovered sediment, which were soft (~20 kPa).

Routine headspace gas analyses were carried out on 34 samples, 41 samples were analyzed for carbonate, carbon, and nitrogen, and 20 interstitial water samples were taken for pore water characterization. Because of the highly variable core recovery and the sandy to gravelly composition of the sediment, the sampling resolution was overall low and irregular (Fig. **F63**), resulting in discontinuous profiles of chemical parameters that should be interpreted with caution.

TOC content at Site U1420 ranges between 0.4 and 0.9 wt% with no overall downcore trend, with the highest contents in the shallowest 40 m and between ~600 to 800 m CSF-A. TN content at Site U1420 ranges between 0 and 0.1 wt%, with highest values observed at ~790 m CSF-A. C/N ratios range between 11 and 77, consistent with dominantly terrigenous organic matter input. $CaCO_3$ values range between 1.4 and 4.2 wt%, with slightly elevated (4.2 and 3.8 wt%) values in two biosiliceous mud-rich samples. At Site U1420, low alkalinity (<2.5 mM) and phosphate (<4 µM) concentrations contrast with relatively high ammonium concentrations (up to 2.5 mM) because of the precipitation of authigenic carbonates and phosphate but limited adsorption of ammonium to clay minerals (Fig. **F63**). Sulfate at Site U1420 ranges from 2.2 to 7.6 mM, with the highest concentration in the shallowest sample (10.7 m CSF-A). Total sulfate depletion is not observed, although sulfate reduction likely occurs within the uppermost 40 m of the sediment, and methane production occurs mostly deeper than 410 m CSF-A (1,700–33,000 ppmv). At Site U1420, chloride, salinity, bromide, and sodium profiles document a significant freshening of pore waters in all recovered samples with respect to the overlying seawater. The freshening is particularly extreme in the shallowest 40 m and between ~760 and 900 m CSF-A (Fig. **F63**) and may be related to gas hydrate dissociation or burial of glacial meltwater.

Because of concerns about borehole stability based on poor core recovery and challenging coring conditions, only one logging tool string was deployed in Hole U1420A. This sonic-induction tool string was designed to provide the highest priority measurements to meet science objectives with the lowest risk to logging tools. The string comprised the Enhanced Digital Telemetry Cartridge (EDTC), Hostile Environment Litho-Density Sonde (HLDS) without neutron source, Dipole Shear Sonic Imager (DSI), and phasor dual induction–spherically focused resistivity tool (DIT) and measured total gamma radiation, borehole diameter, sonic velocity, and resistivity. Because of a bridge or collapsed borehole, the tool string was only able to record data from ~90 to 290 m WSF. Figure **F64** shows a summary of the main logging data recorded in Hole U1420A. The caliper measurement indicates that the borehole diameter exceeded 18 inches, the limit of the HLDS caliper arm, in the upper and lower sections of the logged interval. Borehole size was smaller (~15 inches) between ~140 and

200 m WMSF. Even with this large aperture, the data seem to be of good quality, as the measurements show relatively consistent variability throughout the logged interval.

The logged interval in Hole U1420A is assigned to a single logging unit, based on the minimal measurements recorded and the limited depth interval of the logging data in the context of the entire drilled depth. However, on the basis of distinctive changes in resistivity and velocity measurements, logging Unit 1 is divided into five subunits (Fig. **F64**). Logging Subunit 1A is characterized by a relatively constant mean trend in all data types, with little net downhole variation. Subunit 1B is distinguished by abrupt decreases in gamma ray and resistivity measurements. The deep resistivity curve likely measured formation, whereas the shallow and medium curves most likely reflect the resistivity of the borehole fluid, given the large borehole diameter. Gamma radiation, resistivity, and V_P all increase at the Subunit 1B/1C boundary, whereas gamma radiation decreases and resistivity and V_P increase across the Subunit 1C/1D boundary. All three of these logs then decrease and the caliper increases in Subunit 1E. Overall, resistivities in Hole U1420A are generally >3.0 Ωm, with the deepest resistivity curve showing values >8 Ωm in Subunit 1D. The relatively high sonic velocity values (~1700 to >2500 m/s) measured within this shallow logged interval from ~92 to 282 m WMSF support the notion that high resistivities are not simply because of reduced pore water salinity.

Each of the seismic profiles that cross Site U1420 exhibits a distinct change in stratal architecture across the regional unconformity marked by Horizon H1 (Fig. **F9**). At Site U1420, the seismic packages overlying Horizon H1 are acoustically semitransparent and semichaotic. Three subpackages are present, bounded by Subhorizons H1A and H1B (Fig. **F61**). Truncations shallower and deeper than each of these subhorizons indicate that these are erosional surfaces likely related to glacial advance–retreat cycles. According to the TWT-depth conversion using both the PWC and extrapolated sonic log values, Subhorizon H1A likely corresponds with the boundary between lithostratigraphic Units I and II. Lithologically, Unit I is characterized by a massive clast-rich diamict, whereas Unit II consists primarily of washed pebbles and drilled clasts of varying lithologies. Using velocities from the sonic log for preliminary shipboard TWT-depth conversions, we appear to have logged a portion of Unit II that starts between Subhorizons H1A and H1B and continues across the Horizon H1 unconformity that underlies H2A. Logging Subunits 1A–1D show changing velocity, natural gamma radiation, and resistivity that appear to correlate with changes in seismic facies. Subunit 1E coincides with the uppermost aggradational packages that are truncated by Horizon H1.

Deeper than logging Subunit 1E (~282 m WMSF), we observe increasing disparity between *P*-wave velocities measured by the PWC and those extrapolated from the sonic log. This velocity discrepancy creates potential errors in TWT calculation as large as ~0.2 s. Figure **F61** includes both sets of correlations, but postcruise analysis will be essential for further interpretations. Current results indicate that the boundary between lithostratigraphic Units II and III lies somewhere within the package of bright, continuous reflectors deeper than Subhorizon H2B. Core recovery increased at the top of Unit III, and the sediments within this unit consist primarily of clast-poor and clast-rich diamict with occasional intervals of mud and bioturbation.

Site U1421

Setting and objectives

Site U1421 is located at 721 m water depth on the continental slope seaward of the Bering Trough mouth (Figs. **F9**, **F10**). Whereas Site U1420 targeted strata overlying an inactive thrust fault, Site U1421 was positioned to sample correlative strata on the limb of an actively deforming structure, where more deeply buried seismic sequences on the shelf are observed slightly closer to the seafloor. The site is located downslope of the Bering Trough stratigraphically above the youngest two thrusts of the Pamplona Zone where they cut obliquely across the slope. The slope sediments trapped behind these folds are seismically reflective, and sequences within them are mappable onto the shelf. These sequences appear to aggrade up through seismic Horizon H1, roughly parallel with the modern slope surface. They include thinned distal extents of shelf sedimentary sequences as well as slope sequences that are correlative with upslope/shelf sequences truncated by the Horizon H1 unconformity (Fig. **F9**). Overlying Horizon H1, the slope sequence at Site U1421 is more uniform in thickness and includes higher amplitude reflections that may represent the formation of a glacial trough-mouth fan associated with glacier termini at the shelf edge during glacial maxima, which is first suggested to have initiated during the MPT (Fig. **F9**) (Berger et al., 2008a). Also, as with Site U1419, this site is within the influence of the near-surface Alaska Coastal Current (Stabeno et al., 2004; Weingartner et al., 2005).

Similar to Site U1420, sedimentation at this site is affected by the combination of antecedent topography created by active faulting and the progressive input of glacigenic sediments. At the southeastern end of the STEEP09 seismic profile (Fig. F10A), two currently active faults (BT1 and BT2) are present at the continental slope, exhibiting less burial than the structures on the shelf. Scarps ~750 and ~300 m high associated with the active slope structures are visible on high-resolution bathymetry of the continental slope (Worthington et al., 2008). Site U1421 is located just landward of Fault BT2, which may have initiated after the PPT (Worthington et al., 2010), given the lack of growth strata observed deeper than Horizon H3 (Fig. F10). Between Horizons H1 and H2, the angle of the observed growth strata becomes less pronounced, indicating either a gradual decrease in fault growth rate during the early to Middle Pleistocene (Worthington et al., 2010) or an increase in accumulation rate. Overlying Horizon H1, sediments are truncated by the anticline and are very slightly tilted toward the shelf, indicating either minimal deformation on Fault BT2 since Horizon H1 or high accumulation rates.

The drilling objectives at Site U1421 seek to capitalize on good preservation of carbonate microfossils and associated geochronologic methods that can be used to develop a chronostratigraphy of a proximal sedimentary record of Late Pleistocene glacial dynamics. A secondary objective is to recover material for provenance studies. The key objective is to establish depositional ages of seismic sequences correlative with shelf units drilled at Site U1420. The target depth at this site is designed to penetrate seismic reflector Horizon H2 (expected to lie at ~1 km depth), which is mapped from the shelf where it marks the latest growth strata associated with a now-inactive thrust fault (Figs. F9, F10A). Determining the age of this horizon (hypothesized to be younger than the Pliocene/Pleistocene boundary) can allow us to infer the timing of when loading by increasing sediment accumulation forced accommodation of collisional stresses to be shifted elsewhere in the orogen (Worthington et al., 2010). Crossing the slope equivalent of the angular unconformity Horizon H1 will occur while drilling to the depth of Horizon H2, allowing for a second opportunity beyond Site U1420 to constrain the timing of Horizon H1 formation. The expected lithofacies are alternating diamict (IRD and debris flow deposits), turbidites, and hemipelagic mud (Fig. F65). This site is expected to provide a proximal provenance record of sediment supply from the Bering Glacier that can be used to locate the temporal and spatial loci of glacial erosion in the St. Elias orogen.

Results

At Site U1421, Holes U1421A, U1421B, and U1421C were drilled to total depths of 702.7, 6.2, and 38.2 m CSF-A, respectively (Fig. F66). Core recovery and refusal depths were significantly affected by frequent lonestones and diamict. For Hole U1421A, full-length (9.7 m) APC refusal was encountered at 65.5 m DSF; half-length (4.7 m) APC refusal was encountered at 96.4 m DSF. XCB coring using the soft-formation and hard-formation cutting shoes was used in only Hole U1421A from 96.4 to 702.7 m DSF. In Holes U1421B and U1421C, full-length APC cores were collected. A total of 92 cores were recovered at the site. A total of 114.47 m of core over a 140.8 m interval was recovered using the APC systems (81% recovery). A total of 66 XCB cores were drilled over 606.3 m with a recovery of 61.54 m (10%). The overall recovery for Site U1421 was 23.6%. APC shot depths in Holes U1421B and U1421C were carefully planned with the aid of the stratigraphic correlators.

The composite depth scale at Site U1421 is constructed from 0.0 to 695.72 m CCSF-A (the base of Core 341-U1421A-85X). The splice consists of one complete and continuous interval from the mudline to 33.21 m CCSF-D (the base of Core 341-U1421C-5H). Weather was calm and ship heave was negligible while coring Site U1421, but the relatively lonestone and gravel rich ice-proximal environment proved challenging for core recovery and for interhole correlation. Intervals of core disturbance, incomplete recovery, and use of the half-length APC coring system all presented complications in the development of composite depths and a spliced record. In particular, we observed many instances of flow-in. We urge caution in using the splice from Site U1421 until it can be verified with postcruise data.

The sediment recovered at Site U1421 contains nine facies. The dominant facies are dark gray to dark greenish gray mud and diamict. They account for >95% of the core recovered. Specific lithofacies include massive mud with and without lonestones, interbedded mud and diamict, clast-poor diamict, clast-rich diamict, diatom ooze, mud with diatoms/biosilica, calcareous/carbonate-bearing mud, and mud and diamict with volcanic ash. These facies are inferred to reflect deposition from suspension fallout, sediment gravity flows, ice rafting, and variations in productivity/preservation of biogenic material.

The main lithologies of the diamict clasts and lonestones recovered at Site U1421 are, in order of decreasing abundance, siltstone, sandstone, basalt, and argillite. The petrology of clasts is similar to that found in the St. Elias and Chugach Mountains located along the southern coast of Alaska. Smear slides indicate similar bulk mineralogies downhole.

Based on facies associations, two lithostratigraphic units were defined. Unit I from 0 to 57 m CSF-A is very dark gray (N 3) to dark greenish gray (10Y 4/1) mud interbedded with diatom-bearing mud and diatom-rich mud. The number of lonestones varies from dispersed to abundant deeper than 6.4 m CSF-A. One interval of olive-colored thin laminae was deposited stratigraphically above the uppermost lonestones. Unit II from 57 to 702.7 m CSF-A is very dark gray (N 3) clast-rich diamict interbedded with clast-poor diamict and mud with abundant clasts. Most common clast lithologies are siltstone, sandstone, basalt, and argillite.

The Unit I/II boundary is marked by an increase in GRA bulk density from 1.9 to 2.2 g/cm^3, and it remains high throughout the clast-rich intervals within Unit II. Vane shear strength of 78.8–69.9 kPa was measured from interval 341-U1421A-8H-2, 26 cm, to 8H-4, 42 cm, which is more than twice as high as the measurements in Unit I. This increased shear strength possibly represents overconsolidated sediment and suggests that either a coherent block of subglacial sediment was transported downslope from the Bering Trough or deposition occurred by glacigenic debris flows. Other evidence of downslope transport within Unit II includes erosive lower boundaries of diamict and soft-sediment deformation in intervals of laminated diatom ooze. Muddy intervals with biogenic silica and low clast abundance indicate reduced ice rafting and/or increased productivity. Biosilica-rich or diatom-rich mud occurs in Cores 341-U1421A-22X, 41X, and 55X through 57X. Diatom ooze occurs in Cores 61X through 63X and 75X. Dark greenish gray (10Y 4/1) finely laminated diatom ooze occurs in Section 63X-1.

Siliceous microfossils occur infrequently at Site U1421, whereas calcareous microfossils are continuously present (Fig. **F67**). Based on microfossil biostratigraphic data, the oldest collected sediments are between 0.03 and 0.3 Ma. Benthic foraminifers appear to be a mixture of transported specimens, largely shallow-water (neritic; <100 m) *Elphidium* spp., and in situ specimens comprised primarily of *Epistominella pacifica*, *Eubuliminella exilis*, and *Islandiella norcrossi*, which are expected to be abundant at middle neritic to upper bathyal water depths (~100–1000 m) in the Gulf of Alaska. *Elphidium* spp. specimens are often fragmented, further suggesting that they have a transport history. When the siliciclastic sand fraction is low and foraminiferal group abundances increase, the deeper water fauna dominates and *Elphidium* spp. are rare to absent, suggesting periods of lower downslope transport. However, sandy samples with *Elphidium* spp. dominate in the core catchers. Relatively more radiolarian and diatom taxa typically found in shallow water (neritic) are observed at the lower part of the section. Neritic radiolarian and planktonic foraminiferal species are typical for subarctic faunas. The ratio of cold-water to temperate-water planktonic foraminiferal species fluctuates, suggesting some changes in temperature in this record.

The NRM intensities of the APC (Holes U1421A–U1421C) and XCB (Cores 341-U1421A-20X through 85X) cores were relatively strong before AF demagnetization (10^{-2} ~ 10^{-1} A/m) but were weaker after demagnetization (10^{-2} to 10^{-3} A/m). Intensities were higher in the APC- than in the XCB-recovered intervals (Fig. **F68**). Development of a splice and placement of all holes on a CCSF-A depth scale allows comparisons to be made of the APC-recovered intervals, and intensities are consistent between holes and vary at both the meter and decimeter scale. Because inclinations indicate generally normal polarity, it is thought that the recovered sediment is exclusively within the Brunhes Chronozone and younger than 0.781 Ma (Cande and Kent, 1995, Hilgen et al., 2012).

Physical properties were measured on all cores from Holes U1421A–U1421C. All routine core logger measurements, including MS, GRA bulk density, *P*-wave velocity, and NGR, were collected. GRA bulk density increases downcore within the depths of APC coring, with slight drops at ~20 and ~50 m CSF-A. NGR measurements varied between 14 and 41 cps, illustrating downhole increases from 0 to 96 m CSF-A. *P*-wave velocity values from the track delineated between ~1500 and 2200 m/s. We could not measure *P*-wave velocity of the core sections on the core logger deeper than ~96 m CSF-A in Hole U1921A after switching from APC to XCB coring. Discrete *P*-wave measurements measured on the working-half sections ranged from ~1450 to 1975 m/s. *P*-wave values show significant scatter, with a slight increasing downhole trend. Shear strength measurements ranged from ~5 to 80 kPa and generally increase downhole, with increasing scatter observed starting at Core 341-U1421A-6H. We measured multiple instances of elevated (~50–80 kPa) shear strength at ~50, ~60, ~80 and ~110 m CSF-A in Hole U1421A. MAD measurements show generally increasing bulk density and decreasing porosity from ~0 to 50 m CSF-A in Hole U1421A. Deeper than ~50 m CSF-A in

Hole U1421A, bulk density values range from 1.9 to 2.4 g/cm^3 and porosities range from 28% to 45% with no significant trend.

At Site U1421, 64 headspace samples were analyzed for hydrocarbon gases; 44 discrete sediment samples were analyzed for carbon, nitrogen, and carbonate; and 26 interstitial water samples were taken, with sampling resolution in the deeper part of the hole becoming irregular because of spotty core recovery (Fig. F69). TOC contents are low overall, but accumulation rates are high, and C/N ratios indicate variable contributions from terrigenous organic matter. Carbonate contents are <2 wt% in most samples, but there are a few isolated peaks (3–13 wt%) that appear to be related to mud-rich lithologies. Downcore profiles of ammonium, alkalinity, and methane reflect moderate organic matter remineralization overall, with zones of higher alkalinity and ammonium (~30 and ~450 m CSF-A) likely related to the increased presence of more labile marine organic matter. Methane concentrations are highly variable, ranging between quantification limit and 34,000 ppmv, whereas in large parts of the record concentrations are <5,000 ppmv. Both chloride and salinity are low (340–530 mM and 20–25, respectively) throughout the record, with minima recorded at ~40–70 and ~485 m CSF-A, likely related to gas hydrate dissociation or burial of glacial meltwater.

Two tool strings (sonic-induction tool string and VSI tool string) were deployed in Hole U1421A on the basis of potentially unstable borehole conditions and limited time at the end of the expedition. The sonic-induction tool string, initially deployed in the previous hole (U1420A), was composed of the EDTC, HLDS without neutron source, DSI, and DIT, respectively measuring total gamma ray, borehole diameter, sonic velocity, and resistivity. The second tool string was the VSI tool string, run without the Hostile Environment Natural Gamma Ray Sonde because of concerns about borehole instability. With the exception of some thin washouts, borehole diameter varied smoothly and rarely exceeded 18 inches, the limit of the HLDS caliper arm (Fig. F70). The character of the borehole wall in Hole U1421A on the slope is a distinct change from the rugose character observed at the deeper water sites (U1417 and U1418). Shallower than 500 m WMSF, borehole diameter ranges from 10 to 17 inches, with an average diameter of ~15 inches. There is a distinct separation between the shallow resistivity curve and the medium and deep resistivity curves through much of the logged interval. Given that the borehole diameter is within the depth of investigation of all three curves, this could indicate that the shallow borehole wall was invaded by logging mud, which has relatively low resistivity. The only exception is one narrow spot indicated by the caliper log at ~300 m WMSF. The hole was nearly in-gauge deeper than ~500 m WMSF, with the exception of a washed-out zone between 583 and 591 m WMSF. High coherence in sonic waveforms was observed in the compressional velocity (V_P) and flexural velocity (V_S) logs throughout the entire borehole (Fig. F70). Gamma ray was measured through the entire hole, through the drill pipe from the seawater/seafloor boundary to the base of the pipe, and in the open hole to total depth. The gamma ray measurement is highly attenuated when the tool was inside the bottom-hole assembly (0–96 m WMSF). However, although the log signal is attenuated and there is a slight vertical offset, there is still a reasonable agreement between gamma ray from downhole logs and core logs, and similar trends are shown in both data sets. The VSP in Hole U1421A provides data for establishing a link between core and log data (recorded in depth) and seismic surveys (recorded in TWT) at the location of the borehole. Six out of nine stations yielded TWTs ranging from 1.278 s TWT below sea level at 284.7 m WMSF to 1.641 s TWT at 687 m WMSF.

References

Addison, J.A., Finney, B.P., Dean, W.E., Davies, M.H., Mix, A.C., Stoner, J.S., and Jaeger, J.M., 2012. Productivity and sedimentary δ^{15}N variability for the last 17,000 years along the northern Gulf of Alaska continental slope. *Paleoceanography,* 27(1):PA1206. doi:10.1029/2011PA002161

Amit, H., Aubert, J., and Hulot, G., 2010. Stationary, oscillating or drifting mantle-driven geomagnetic flux patches? *J. Geophys. Res.: Solid Earth,* 115(B7):B07108. doi:10.1029/2009JB006542

Andersen, K.K., Svensson, A., Johnsen, S.J., Rasmussen, S.O., Bigler, M., Röthlisberger, R., Ruth, U., Siggaard-Andersen, M.-L., and Steffensen, J.P., 2006. The Greenland ice core chronology 2005, 15–42 ka, Part 1: Constructing the timescale. *Quat. Sci. Rev.,* 25(23–24):3246–3257. doi:10.1016/j.quascirev.2006.08.002

Barker, P.F., Camerlenghi, A., Acton, G.D., et al., 1999. *Proc. ODP, Init. Repts.,* 178: College Station, TX (Ocean Drilling Program). doi:10.2973/odp.proc.ir.178.1999

Barker, P.F., Kennett, J.P., et al., 1990. *Proc. ODP, Sci. Results,* 113: College Station, TX (Ocean Drilling Program). doi:10.2973/odp.proc.sr.113.1990

Barron, J., Larsen, B., et al., 1989. *Proc. ODP, Init. Repts.,* 119: College Station, TX (Ocean Drilling Program). doi:10.2973/odp.proc.ir.119.1989

Barron, J.A., Basov, I.A., Beaufort, L., Dubuisson, G., Gladenkov, A.Y., Morley, J.J., Okada, M., Ólafsson, D.K., Pak, D.K., Roberts, A.P., Shilov, V.V., and Weeks, R.J., 1995. Biostratigraphic and magnetostratigraphic summary. *In* Rea, D.K., Basov, I.A., Scholl, D.W., and Allan, J.F. (Eds.), *Proc. ODP, Sci. Results,* 145: College Station, TX (Ocean Drilling Program), 559–575. **doi:10.2973/odp.proc.sr.145.145.1995**

Barron, J.A., Bukry, D., Dean, W.E., Addison, J.A., and Finney, B., 2009. Paleoceanography of the Gulf of Alaska during the past 15,000 years: results from diatoms, silicoflagellates, and geochemistry. *Mar. Micropaleontol.,* 72(3–4):176–195. **doi:10.1016/j.marmicro.2009.04.006**

Bartlein, P.J., Anderson, K.H., Anderson, P.M., Edwards, M.E., Mock, C.J., Thompson, R.S., Webb, R.S., Webb, T., III, and Whitlock, C., 1998. Paleoclimate simulations for North America over the past 21,000 years: features of the simulated climate and comparisons with paleoenvironmental data. *Quat. Sci. Rev.,* 17(6–7):549–585. **doi:10.1016/S0277-3791(98)00012-2**

Behl, R.J., and Kennett, J.P., 1996. Brief interstadial events in the Santa Barbara Basin, NE Pacific, during the last 60 kyr. *Nature (London, U. K.),* 379(6562):243–246. **doi:10.1038/379243a0**

Benowitz, J.A., Layer, P.W., Armstrong, P., Perry, S.E., Haeussler, P.J., Fitzgerald, P.G., and VanLaningham, S., 2011. Spatial variations in focused exhumation along a continental-scale strike-slip fault: the Denali fault of the eastern Alaska Range. *Geosphere,* 7(2):455–467. **doi:10.1130/GES00589.1**

Berger, A.L., Gulick, S.P.S., Spotila, J.A., Upton, P., Jaeger, J.M., Chapman, J.B., Worthington, L.A., Pavlis, T.L., Ridgway, K.D., Willems, B.A., and McAleer, R.J., 2008a. Quaternary tectonic response to intensified glacial erosion in an orogenic wedge. *Nat. Geosci.,* 1:793–799. **doi:10.1038/ngeo334**

Berger, A.L., Spotila, J.A., Chapman, J.B., Pavlis, T.L., Enkelmann, E., Ruppert, N.A., and Buscher, J.T., 2008b. Architecture, kinematics, and exhumation of a convergent orogenic wedge: a thermochronoligical investigation of tectonic–climatic interactions within the central St. Elias orogen, Alaska. *Earth Planet. Sci. Lett.,* 270(1–2):13–24. **doi:10.1016/j.epsl.2008.02.034**

Bloxham, J., 2000. The effect of thermal core–mantle interactions on the palaeomagnetic secular variation. *Philos. Trans. R. Soc., A,* 358(1768):1171–1179. **doi:10.1098/rsta.2000.0579**

Bloxham, J., and Gubbins, D., 1987. Thermal core–mantle interactions. *Nature (London, U. K.),* 325(6104):511–513. **doi:10.1038/325511a0**

Boyd, P.W., Law, C.S., Wong, C.S., Nojiri, Y., Tsuda, A., Levasseur, M., Takeda, S., Rivkin, R., Harrison, P.J., Strzepek, R., Gower, J., McKay, R.M., Abraham, E., Arychuk, M., Barwell-Clarke, J., Crawford, W., Crawford, D., Hale, M., Harada, K., Johnson, K., Kiyosawa, H., Kudo, I., Marchetti, A., Miller, W., Needoba, J., Nishioka, J., Ogawa, H., Page, J., Robert, M., Saito, H., Sastri, A., Sherry, N., Soutar, T., Sutherland, N., Taira, Y., Whitney, F., Wong, S.-K.E., and Yoshimura, T., 2004. The decline and fate of an iron-induced subarctic phytoplankton bloom. *Nature (London U. K.),* 428(6982):549–553. **doi:10.1038/nature02437**

Briner, J.P., Kaufman, D.S., Werner, A., Caffee, M., Levy, L., Manley, W.F., Kaplan, M.R., and Finkel, R.C., 2002. Glacier readvance during the late glacial (Younger Dryas?) in the Ahklun Mountains, southwestern Alaska. *Geology,* 30(8):679–682. **doi:10.1130/0091-7613(2002)030<0679:GRDTLG>2.0.CO;2**

Brocher, T.M., Fuis, G.S., Fisher, M.A., Plafker, G., Moses, M.J., Taber, J.J., and Christensen, N.I., 1994. Mapping the megathrust beneath the northern Gulf of Alaska using wide-angle seismic data. *J. Geophys. Res.: Solid Earth,* 99(B6):11663–11685. **doi:10.1029/94JB00111**

Bruhn, R.L., Pavlis, T.L., Plafker, G., and Serpa, L., 2004. Deformation during terrane accretion in the Saint Elias orogen, Alaska. *Geol. Soc. Am. Bull.,* 116(7–8):771–787. **doi:10.1130/B25182.1**

Bruhn, R.L., Sauber, J., Cotton, M.M., Pavlis, T.L., Burgess, E., Ruppert, N., and Forster, R.R., 2012. Plate margin deformation and active tectonics along the northern edge of the Yakutat terrane in the Saint Elias orogen, Alaska, and Yukon, Canada. *Geosphere,* 8(6):1384–1407. **doi:10.1130/GES00807.1**

Bruns, T.R., 1983. Model for the origin of the Yakutat block, an accreting terrane in the northern Gulf of Alaska. *Geology,* 11(12):718–721. **doi:10.1130/0091-7613(1983)11<718:MFTOOT>2.0.CO;2**

Bruns, T.R., 1985. Tectonics of the Yakutat block, an allochthonous terrane in the northern Gulf of Alaska. *Open-File Rep.–U.S. Geol. Surv.,* 85-13. **http://www.dggs.alaska.gov/webpubs/usgs/of/text/of85-0013.PDF**

Bruns, T.R., and Schwab, W.C., 1983. Structure maps and seismic stratigraphy of the Yakataga segment of the continental margin, northern Gulf of Alaska. *U.S. Geol. Surv.,* MF-1424.

Calkin, P.E., Wiles, G.C., and Barclay, D.J., 2001. Holocene coastal glaciation of Alaska. *Quat. Sci. Rev.,* 20(1–3):449–461. **doi:10.1016/S0277-3791(00)00105-0**

Cande, S.C., and Kent, D.V., 1995. Revised calibration of the geomagnetic polarity timescale for the Late Cretaceous and Cenozoic. *J. Geophys. Res.: Solid Earth,* 100(B4):6093–6095. **doi:10.1029/94JB03098**

Carlson, P.R., 1989. Seismic reflection characteristics of glacial and glacimarine sediment in the Gulf of Alaska and adjacent fjords. *Mar. Geol.,* 85(2–4):391–416. **doi:10.1016/0025-3227(89)90161-8**

Carlson, P.R., and Bruns, T.R., 1997. Bering Trough: a product of the Bering Glacier, Gulf of Alaska. *In* Davies, T.A., Bell, T., Cooper, A.K., Josenhans, H., Polyak, L., Solheim, A., Stoker, M.S., and Stravers, J.A. (Eds.), *Glaciated Continental Margins: An Atlas of Acoustic Images:* London (Chapman and Hall), 244–247. **doi:10.1007/978-94-011-5820-6_85**

Carlson, P.R., Bruns, T.R., Molnia, B.F., and Schwab, W.C., 1982. Submarine valleys in the northeastern Gulf of Alaska: characteristics and probable origin. *Mar. Geol.,* 47(3–4):217–242. **doi:10.1016/0025-3227(82)90070-6**

Carlson, P.R., Stevenson, A.J., Bruns, T.R., Mann, D.M., and Huggett, Q., 1996. Sediment pathways in the Gulf of Alaska from beach to abyssal plain. *In* Gardner, J.V., Field, M.E., and Twichell, D.C. (Eds.), *Geology of the United States' Seafloor: The View from GLORIA:* Cambridge, (Cambridge Univ.), 255–278. doi:10.1017/CBO9780511529481.021

Channell, J.E.T., 1999. Geomagnetic paleointensity and directional secular variation at Ocean Drilling Program (ODP) Site 984 (Bjorn Drift) since 500 ka: comparisons with ODP Site 983 (Gardar Drift). *J. Geophys. Res.: Solid Earth,* 104(B10):22937–22951. doi:10.1029/1999JB900223

Channell, J.E.T., 2006. Late Brunhes polarity excursions (Mono Lake, Laschamp, Iceland Basin and Pringle Falls) recorded at ODP Site 919 (Irminger Basin). *Earth Planet. Sci. Lett.,* 244(1–2):378–393. doi:10.1016/j.epsl.2006.01.021

Channell, J.E.T., Hodell, D.A., McManus, J., and Lehman, B., 1998. Orbital modulation of the Earth's magnetic field intensity. *Nature (London, U. K.),* 394(6692):464–468. doi:10.1038/28833

Channell, J.E.T., Hodell, D.A., Xuan, C., Mazaud, A., and Stoner, J.S., 2008. Age calibrated relative paleointensity for the last 1.5 Myr at IODP Site U1308 (North Atlantic). *Earth Planet Sci. Lett.,* 274(1–2):59–71. doi:10.1016/j.epsl.2008.07.005

Channell, J.E.T., Kanamatsu, T., Sato, T., Stein, R., Alvarez Zarikian, C.A., Malone, M.J., and the Expedition 303/306 Scientists, 2006. *Proc. IODP,* 303/306: College Station, TX (Integrated Ocean Drilling Program Management International, Inc.). doi:10.2204/iodp.proc.303306.2006

Channell, J.E.T., Mazaud, A., Sullivan, P., Turner, S., and Raymo, M.E., 2002. Geomagnetic excursions and paleointensities in the Matuyama Chron at Ocean Drilling Program Sites 983 and 984 (Iceland Basin). *J. Geophys. Res.: Solid Earth,* 107(B6):2114–2127. doi:10.1029/2001JB000491

Channell, J.E.T., Xuan, C., and Hodell, D.A., 2009. Stacking paleointensity and oxygen isotope data for the last 1.5 Myr (PISO-1500). *Earth Planet. Sci. Lett.,* 283(1–4):14–23. doi:10.1016/j.epsl.2009.03.012

Chapman, J.B., Pavlis, T.L., Gulick, S., Berger, A., Lowe, L., Spotila, J., Bruhn, R., Vorkink, M., Koons, P., Barker, A., Picornell, C., Ridgway, K., Hallet, B., Jaeger, J., and McCalpin, J., 2008. Neotectonics of the Yakutat collision: changes in deformation driven by mass redistribution. *In* Freymueller, J.T., Haeussler, P.J., Wesson, R.L., and Ekström, G. (Eds.), *Active Tectonics and Seismic Potential of Alaska.* Geophys. Monogr., 179:65–81. doi:10.1029/179GM04

Chase, Z., Strutton, P.G., and Hales, B., 2007. Iron links river runoff and shelf width to phytoplankton biomass along the U.S. West Coast. *Geophys. Res. Lett.,* 34:L04607. doi:10.1029/2006GL028069

Childers, A.R., Whitledge, T.E., and Stockwell, D.A., 2005. Seasonal and interannual variability in the distribution of nutrients and chlorophyll a across the Gulf of Alaska shelf: 1998–2000. *Deep-Sea Res., Part II,* 52(1–2):193–216. doi:10.1016/j.dsr2.2004.09.018

Christeson, G.L., Gulick, S.P.S., van Avendonk, H.J.A, Worthington, L.L., Reece, R.S., and Pavlis, T.L., 2010. The Yakutat terrane: dramatic change in crustal thickness across the Transition fault, Alaska. *Geology,* 38(10):895–898. doi:10.1130/G31170.1

Clapperton, C., 2000. Interhemispheric synchroneity of marine oxygen isotope Stage 2 glacier fluctuations along the American Cordilleras transect. *J. Quat. Sci.,* 15(4):435–468. doi:10.1002/1099-1417(200005)15:4<435::AID-JQS552>3.0.CO;2-R

Clark, P.U., and Bartlein, P.J., 1995. Correlation of late Pleistocene glaciation in the western United States with North Atlantic Heinrich events. *Geology,* 23(6):483–486. doi:10.1130/0091-7613(1995)023<0483:COLPGI>2.3.CO;2

Clark, P.U., Archer, D., Pollard, D., Blum, J.D., Rial, J.A., Brovkin, V., Mix, A.C., Pisias, N.G., and Roy, M., 2006. The middle Pleistocene transition: characteristics, mechanisms, and implications for long-term changes in atmospheric pCO_2. *Quat. Sci. Rev.,* 25(23–24):3150–3184. doi:10.1016/j.quascirev.2006.07.008

Clement, B.M., 2004. Dependence of the duration of geomagnetic polarity reversals on site latitude. *Nature (London, U. K.),* 428(6983):637–640. doi:10.1038/nature02459

Cowan, D.S., 1982. Geological evidence for post–40 m.y. B.P. large-scale northwestward displacement of part of southeastern Alaska. *Geology,* 10(6):309–313. doi:10.1130/0091-7613(1982)10<309:GEFPMB>2.0.CO;2

Cowan, E.A., Brachfeld, S.A., Powell, R.D., and Schoolfield, S.C., 2006. Terrane-specific rock magnetic characteristics preserved in glacimarine sediment from southern coastal Alaska. *Can. J. Earth Sci.,* 43(9):1269–1282. doi:10.1139/e06-042

Cowan, E.A., Cai, J., Powell, R.D., Clark, J.D., and Pitcher, J.N., 1997. Temperate glacimarine varves: an example from Disenchantment Bay, southern Alaska. *J. Sediment. Res.,* 67(3):536–549. doi:10.1306/D42685C7-2B26-11D7-8648000102C1865D

Cowan, E.A., Seramur, K.C., Cai, J., and Powell, R.D., 1999. Cyclic sedimentation produced by fluctuations in meltwater discharge, tides and marine productivity in an Alaskan fjord. *Sedimentology,* 46(6):1109–1126. doi:10.1046/j.1365-3091.1999.00267.x

Cox, A., and Doell, R.R., 1964. Long period variations of the geomagnetic field. *Bull. Seismol. Soc. Am.,* 54(6B):2243–2270.

Dahlgren, K.I.T., Vorren, T.O., Stoker, M.S., Nielsen, T., Nygård, A., and Sejrup, H.P., 2005. Late Cenozoic prograding wedges on the NW European continental margin: their formation and relationship to tectonics and climate. *Mar. Pet. Geol.,* 22(9–10):1089–1110. doi:10.1016/j.marpetgeo.2004.12.008

Davies, M.H., Mix, A.C., Stoner, J.S., Addison, J.A., Jaeger, J., Finney, B., and Wiest, J., 2011. The deglacial transition on the southeastern Alaskan margin: meltwater input, sea level rise, marine productivity, and sedimentary anoxia. *Paleoceanography,* 26(2):PA2223. doi:10.1029/2010PA002051

DeMets, C., and Dixon, T.H., 1999. New kinematic models for Pacific-North America motion from 3 Ma to present, I: evidence for steady motion and biases in the NUVEL-

1A model. *Geophys. Res. Lett.,* 26(13):1921–1924. **doi:10.1029/1999GL900405**

Donnelly, T.W., 1982. Worldwide continental denudation and climatic deterioration during the late Tertiary: evidence from deep-sea sediments. *Geology,* 10(9):451–454. **doi:10.1130/0091-7613(1982)10<451:WCDACD>2.0.CO;2**

Dumoulin, J.A., 1987. Sandstone composition of the Valdez and Orca groups, Prince William Sound, Alaska. *U.S. Geol. Surv. Bull.,* 1774. **http://www.dggs.dnr.state.ak.us/webpubs/usgs/b/text/b1774.PDF**

Dunbar, G.B., Naish, T.R., Barrett, P.J., Fielding, C.R., and Powell, R.D., 2008. Constraining the amplitude of late Oligocene bathymetric changes in western Ross Sea during orbitally-induced oscillations in the East Antarctic Ice Sheet, 1. Implications for glacimarine sequence stratigraphic models. *Palaeogeogr., Palaecoclimatol., Palaeoecol.,* 260(1–2):50–65. **doi:10.1016/j.palaeo.2007.08.018**

Eberhart-Philips, D., Christensen, D.H., Brocher, T.M., Hansen, R., Ruppert, N.A., Haeussler, P.J., and Abers, G.A., 2006. Imaging the transition from Aleutian subduction to Yakutat collision in central Alaska, with local earthquakes and active source data. *J. Geophys. Res.: Solid Earth,* 111(B11):B11303. **doi:10.1029/2005JB004240**

Eidvin, T., Jansen, E., and Riis, F., 1993. Chronology of Tertiary fan deposits off the western Barents Sea: implications for the uplift and erosion history of the Barents shelf. *Mar. Geol.,* 112(1–4):109–131. **doi:10.1016/0025-3227(93)90164-Q**

Elliott, J.L., Larsen, C.F., Freymueller, J.T., and Motyka, R.J., 2010. Tectonic block motion and glacial isostatic adjustment in southeast Alaska and adjacent Canada constrained by GPS measurements. *J. Geophys. Res.: Solid Earth,* 115(B9):B09407. **doi:10.1029/2009JB007139**

Elmore C.R., Gulick, S.P.S., Willems, B., and Powell, R., 2013. Seismic stratigraphic evidence for glacial expanse during glacial maxima in the Yakutat Bay region, Gulf of Alaska. *Geochem., Geophys., Geosyst.,* 14(4):1294–1311. **doi:10.1002/ggge.20097**

Elverhøi, A., Andersen, E.S., Dokken, T., Hebbeln, D., Spielhagen, R., Svendsen, J.I., Sørflaten, M., Rørnes, A., Hald, M., and Forsberg, C.F., 1995. The growth and decay of the Late Weichselian ice sheet in western Svalbard and adjacent areas based on provenance studies of marine sediments. *Quat. Res.,* 44(3):303–316. **doi:10.1006/qres.1995.1076**

Emile-Geay, J., Cane, M.A., Naik, N., Seager, R., Clement, A.C., and van Geen, A., 2003. Warren revisited: atmospheric freshwater fluxes and "why is no deep water formed in the North Pacific?" *J. Geophys. Res.: Oceans,* 108(C6):3178. **doi:10.1029/2001JC001058**

Engstrom, D.R., Hansen, B.C.S., and Wright, H.E., Jr., 1990. A possible Younger Dryas record in southeastern Alaska. *Science,* 250(4986):1383–1385. **doi:10.1126/science.250.4986.1383**

Enkelmann, E., Garver, J.I., and Pavlis, T.L., 2008. Rapid exhumation of ice-covered rocks of the Chugach–St. Elias orogen, southeast Alaska. *Geology,* 36(12):915–918. **doi:10.1130/G22252A.1**

Enkelmann, E., Zeitler, P.K., Garver, J.I., Pavlis, T.L., and Hooks, B.P., 2010. The thermochronological record of tectonic and surface process interaction at the Yakutat–North American collision zone in southeast Alaska. *Am. J. Sci.,* 310:231–260. **doi:10.2475/04.2010.01**

Enkelmann, E., Zeitler, P.K., Pavlis, T.L., Garver, J.I., and Ridgway, K.D., 2009. Intense localized rock uplift and erosion in the St. Elias orogen of Alaska. *Nat. Geosci.,* 2:360–363. **doi:10.1038/ngeo502**

Erickson, S.N., and Jarrard, R.D., 1998. Velocity-porosity relationships for water-saturated siliciclastic sediments. *J. Geophys. Res.: Solid Earth,* 103(B12):30385–30406. **doi:10.1029/98JB02128**

Escutia, C., Brinkhuis, H., Klaus, A., and the Expedition 318 Scientists, 2011. *Proc. IODP,* 318: Tokyo (Integrated Ocean Drilling Program Management International, Inc.). **doi:10.2204/iodp.proc.318.2011**

Eyles, C.H., Eyles, N., and Lagoe, M.B., 1991. The Yakataga Formation: a late Miocene to Pleistocene record of temperate glacial marine sedimentation in the Gulf of Alaska. *In* Anderson, J.B., and Ashley, G.M. (Eds.), *Glacial Marine Sedimentation: Paleoclimatic Significance.* Spec. Pap.—Geol. Soc. Am., 261:159–180. **doi:10.1130/SPE261-p159**

Feely, R.A., Baker, E.T., Schumacher, J.D., Massoth, G.J., and Landing, W.M., 1979. Processes affecting the distribution and transport of suspended matter in the northeast Gulf of Alaska. *Deep-Sea Res., Part A,* 26(4):445–464. **doi:10.1016/0198-0149(79)90057-8**

Ferris, A., Abers, G.A., Christensen, D.H., and Veenstra, E., 2003. High resolution image of the subducted Pacific (?) plate beneath central Alaska, 50–150 km depth. *Earth Planet. Sci. Lett.,* 214(3–4):575–588. **doi:10.1016/S0012-821X(03)00403-5**

Finzel, E.S., Trop, J.M., Ridgway, K.D., and Enkelmann, E., 2011. Upper plate proxies for flat-slab subduction processes in southern Alaska. *Earth Planet. Sci. Lett.,* 303(3–4):348–360. **doi:10.1016/j.epsl.2011.01.014**

Foster, H.L., Keith, T.E.C., and Menzie, W.D., 1994. Geology of the Yukon-Tanana area of east-central Alaska. *In* Plafker, G., and Berg, H.C. (Eds.), *The Geology of North America* (Vol. G): *The Geology of Alaska:* Boulder, CO (Geol. Soc. Am.), 205–240.

Galbraith, E.D., Jaccard, S.L., Pedersen, T.F., Sigman, D.M., Haug, G.H., Cook, M., Southon, J.R., and Francois, R., 2007. Carbon dioxide release from the North Pacific abyss during the last deglaciation. *Nature (London, U. K.),* 449(7164):890–893. **doi:10.1038/nature06227**

Gardner, J.V., Mayer, L.A., and Armstrong, A., 2006. Mapping supports potential submission to U.N. Law of the Sea. *Eos, Trans. Am. Geophys. Union,* 87(16):157. **doi:10.1029/2006EO160002**

Gebhardt, H., Sarnthein, M., Grootes, P.M., Kiefer, T., Kuehn, H., Schmieder, F., and Röhl, U., 2008. Paleonutrient and productivity records from the subarctic North Pacific for Pleistocene glacial terminations I to V. *Paleoceanography,* 23(4):PA4212. **doi:10.1029/2007PA001513**

Gehrels, G.E., and Berg, H.C., 1994. Geology of southeastern Alaska. *In* Plafker, G., and Berg, H.C. (Eds.), *The Geology of North America* (Vol. G): *The Geology of Alaska:* Boulder, CO (Geol. Soc. Am.), 451–468.

Gehrels, G.E., and Saleeby, J.B., 1987. Geologic framework, tectonic evolution, and displacement history of the Alexander terrane. *Tectonics,* 6(2):151–173. **doi:10.1029/TC006i002p00151**

Geiss, C.E., and Banerjee, S.K., 2003. A Holocene–late Pleistocene geomagnetic inclination record from Grandfather Lake, SW Alaska. *Geophys. J. Int.,* 153(2):497–507. **doi:10.1046/j.1365-246X.2003.01921.x**

Gilhousen, D.B., Quayle, R.G., Baldwin, R.G., Karl, T.R., and Brines, R.O., 1983. *Climatic Summaries for NOAA Data Buoys:* Asheville, NC (National Climatic Data Center).

Grigg, L.D., Whitlock, C., and Dean, W.E., 2001. Evidence for millennial-scale climate change during marine isotope Stages 2 and 3 at Little Lake, western Oregon, U.S.A. *Quat. Res.,* 56(1):10–22. **doi:10.1006/qres.2001.2246**

Gubbins, D., and Kelly, P., 1993. Persistent patterns in the geomagnetic field over the last 2.5 Myr. *Nature (London, U. K.),* 365:829–832. **doi:10.1038/365829a0**

Gubbins, D., Willis, A.P., and Sreenivasan, B., 2007. Correlation of Earth's magnetic field with lower mantle thermal and seismic structure. *Phys. Earth Planet. Inter.,* 162(3–4):256–260. **doi:10.1016/j.pepi.2007.04.014**

Gulick, S.P.S., Lowe, L.A., Pavlis, T.L., Gardner, J.V., and Mayer, L.A., 2007. Geophysical insights into the Transition fault debate: propagating strike slip in response to stalling Yakutat block subduction in the Gulf of Alaska. *Geology,* 35(8):763–766. **doi:10.1130/G23585A.1**

Gulick, S.P.S., Reece, R.S., Christeson, G.L., van Avendonk, H., Worthington, L.L., and Pavlis, T.L., 2013. Seismic images of the Transition fault and the unstable Yakutat–Pacific–North American triple junction. *Geology,* 41(5):571–574. **doi:10.1130/G33900.1**

Guyodo, Y., and Valet, J.-P., 1999. Global changes in intensity of the Earth's magnetic field during the past 800 kyr. *Nature (London, U. K.),* 399(6733):249–252. **doi:10.1038/20420**

Haeussler, P.J., Gehrels, G.E., and Karl, S.M., 2006. Constraints on the age and provenance of the Chugach accretionary complex from detrital zircons in the Sitka graywacke near Sitka, Alaska. *U.S. Geol. Surv. Prof. Pap.,* 1709-F. **http://pubs.usgs.gov/pp/pp1709f/**

Hallet, B., Hunter, L., and Bogen, J., 1996. Rates of erosion and sediment evacuation by glaciers: a review of field data and their implications. *Global Planet. Change,* 12(1–4):213–235. **doi:10.1016/0921-8181(95)00021-6**

Harrison, P.J., Boyd, P.W., Varela, D.E., Takeda, S., Shiomoto, A., and Odate, T., 1999. Comparison of factors controlling phytoplankton productivity in the NE and NW subarctic Pacific gyres. *Prog. Oceanogr.,* 43(2–4):205–234. **doi:10.1016/S0079-6611(99)00015-4**

Hay, W.W., Soeding, E., DeConto, R.M., and Wold, C.N., 2002. The late Cenozoic uplift—climate change paradox. *Int. J. Earth Sci.,* 91(5):746–774. **doi:10.1007/s00531-002-0263-1**

Hayes, D.E., Frakes, L.A., et al., 1975. *Init. Repts. DSDP,* 28: Washington, DC (U.S. Govt. Printing Office). **doi:10.2973/dsdp.proc.28.1975**

Hayes, S.P., 1979. Variability of current and bottom pressure across the continental shelf in the northeast Gulf of Alaska. *J. Phys. Oceanogr.,* 9(1):88–103. **doi:10.1175/1520-0485(1979)009<0088:VOCABP>2.0.CO;2**

Hayes, S.P., and Schumacher, J.D., 1976. Description of wind, current, and bottom pressure variations on continental shelf in northeast Gulf of Alaska from February to May 1975. *J. Geophys. Res.: Oceans,* 81(36):6411–6419. **doi:10.1029/JC081i036p06411**

Headley, R.M., Enkelmann, E., and Hallet, B., 2013. Examination of the interplay between glacial processes and exhumation in the Saint Elias Mountains, Alaska. *Geosphere,* 9(2):229–241. **doi:10.1130/GES00810.1**

Hendy, I.L., and Cosma, T., 2008. Vulnerability of the Cordilleran Ice Sheet to iceberg calving during late Quaternary rapid climate change events. *Paleoceanography,* 23(2):PA2101. **doi:10.1029/2008PA001606**

Hendy, I.L., and Kennett, J.P., 1999. Latest Quaternary North Pacific surface-water responses imply atmosphere-driven climate instability. *Geology,* 27(4):291–294. **doi:10.1130/0091-7613(1999)027<0291:LQNPSW>2.3.CO;2**

Hilgen, F.J., Lourens, L.J., and Van Dam, J.A., 2012. The Neogene period. *In* Gradstein, F.M., Ogg, J.G., Schmitz, M.D., and Ogg, G.M. (Eds.), *The Geologic Time Scale:* Oxford (Elsevier), 923–978. **doi:10.1016/B978-0-444-59425-9.00029-9**

Hill, H.W., Flower, B.P., Quinn, T.M., Hollander, D.J., and Guilderson, T.P., 2006. Laurentide Ice Sheet meltwater and abrupt climate change during the last glaciation. *Paleoceanography,* 21(1):PA1006. **doi:10.1029/2005PA001186**

Hogan, L.G., Scheidegger, K.F., Kulm, L.D., Dymond, J., and Mikkelsen, N., 1978. Biostratigraphic and tectonic implications of ^{40}Ar-^{39}Ar dates of ash layers from the northeast Gulf of Alaska. *Geol. Soc. Am. Bull.,* 89(8):1259–1264. **doi:10.1130/0016-7606(1978)89<1259:BATIOA>2.0.CO;2**

Hoth, S., Adam, J., Kukowski, N., and Oncken, O., 2006. Influence of erosion on the kinematics of bivergent orogens: results from scaled sandbox simulations. *Spec. Pap.—Geol. Soc. Am.,* 398:201–225. **doi:10.1130/2006.2398(12)**

Hu, F.S., Nelson, D.M., Clarke, G.H., Rühland, K.M., Huang, Y., Kaufman, D.S., and Smol, J.P., 2006. Abrupt climatic events during the last glacial–interglacial transition in Alaska. *Geophys. Res. Lett.,* 33:L18708. **doi:10.1029/2006GL027261**

Jaccard, S.L., Haug, G.H., Sigman, D.M., Pedersen, T.F., Thierstein, H.R., and Röhl, U., 2005. Glacial/interglacial changes in subarctic North Pacific stratification. *Science,* 308(5724):1003–1006. **doi:10.1126/science.1108696**

Jaeger, J.M., Gulick, S.P.S., LeVay, L.J., Asahi, H., Bahlburg, H., Belanger, C.L., Berbel, G.B.B., Childress, L.B., Cowan, E.A., Drab, L., Forwick, M., Fukumura, A., Ge, S., Gupta, S.M., Kioka, A., Konno, S., März, C.E., Matsuzaki, K.M., McClymont, E.L., Mix, A.C., Moy, C.M., Müller, J., Nakamura, A., Ojima, T., Ridgway, K.D., Rodrigues Ribeiro, F., Romero, O.E., Slagle, A.L., Stoner, J.S., St-Onge, G., Suto, I., Walczak, M.H., and Worthington, L.L., 2014. Site U1418. *In* Jaeger, J.M., Gulick, S.P.S., LeVay, L.J., and the Expedition 341 Scientists, *Proc. IODP,* 341: College Station, TX (Integrated Ocean Drilling Program). **doi:10.2204/iodp.proc.341.104.2014**

Jaeger, J.M., and Nittrouer, C.A., 1999. Sediment deposition in an Alaskan fjord: controls on the formation and preservation of sedimentary structures in Icy Bay. *J. Sediment. Res.,* 69(5):1011–1026. **doi:10.2110/jsr.69.1011**

Jaeger, J.M., Nittrouer, C.A., Scott, N.D., and Milliman, J.D., 1998. Sediment accumulation along a glacially impacted mountainous coastline: north-east Gulf of Alaska. *Basin Res.,* 10(1):155–173. **doi:10.1046/j.1365-2117.1998.00059.x**

Jaeger, J.M., Rosen, G.P., Kramer, B., Stoner, J., Cowan, E.A., and Channell, J., 2008. Cross-margin signal transfer in a glacial source-to-sink sedimentary system: Bering Glacier, southern Alaska [presented at the 2008 Ocean Sciences Meeting, Orlando, Florida, 2–7 March 2008]. **http://www.sgmeet.com/aslo/orlando2008/viewabstract2.asp?AbstractID=1794**

Jones, D.L., Silberling, N.J., and Hillhouse, J., 1977. Wrangellia—a displaced terrane in northwestern North America. *Can. J. Earth Sci.,* 14(11):2565–2577. **doi:10.1139/e77-222**

Keigwin, L.D., and Cook, M.S., 2007. A role for North Pacific salinity in stabilizing North Atlantic climate. *Paleoceanography,* 22(3):PA3102. **doi:10.1029/2007PA001420**

Keigwin, L.D., Rio, D., Acton, G.D., et al., 1998. *Proc. ODP, Init. Repts.,* 172: College Station, TX (Ocean Drilling Program). **doi:10.2973/odp.proc.ir.172.1998**

Keigwin, L.D., Rio, D., Acton, G.D., and Arnold, E. (Eds.), 2001. *Proc. ODP, Sci. Results,* 172. **doi:10.2973/odp.proc.sr.172.2001**

Koons, P.O., 1995. Modeling the topographic evolution of collisional belts. *Annu. Rev. Earth Planet. Sci.,* 23:375–408. **doi:10.1146/annurev.ea.23.050195.002111**

Koons, P.O., Hooks, B.P., Pavlis, T., Upton, P., and Barker, A.D., 2010. Three-dimensional mechanics of Yakutat convergence in the southern Alaskan plate corner. *Tectonics,* 29(4):TC4008. **doi:10.1029/2009TC002463**

Koons, P.O., Zeitler, P.K., and Hallet, B., 2013. Tectonic aneurysms and mountain building. *In* Shroder, J.F. (Ed.), *Treatise on Geomorphology* (Vol. 5): *Tectonic Geomorphology:* San Diego (Academic Press), 5:318–349. **doi:10.1016/B978-0-12-374739-6.00094-4**

Kreemer, C., Holt, W.E., and Haines, A.J., 2003. An integrated global model of present-day plate motions and plate boundary deformation. *Geophys. J. Int.,* 154(1):8–34. **doi:10.1046/j.1365-246X.2003.01917.x**

Krissek, L.A., 1995. Late Cenozoic ice-rafting records from Leg 145 sites in the North Pacific: late Miocene onset, late Pliocene intensification, and Pliocene–Pleistocene events. *In* Rea, D.K., Basov, I.A., Scholl, D.W., and Allan, J.F. (Eds.), *Proc. ODP, Sci. Results,* 145: College Station, TX (Ocean Drilling Program), 179–194. **doi:10.2973/odp.proc.sr.145.118.1995**

Kulm, L.D., von Huene, R., et al., 1973. *Init. Repts. DSDP,* 18: Washington, DC (U.S. Govt. Printing Office). **doi:10.2973/dsdp.proc.18.1973**

Kusky, T.M., Bradley, D.C., and Haeussler, P., 1997. Progressive deformation of the Chugach accretionary complex, Alaska, during a Paleogene ridge-trench encounter. *J. Struct. Geol.,* 19(2):139–157. **doi:10.1016/S0191-8141(96)00084-3**

Ladd, C., Mordy, C.W., Kachel, N.B., and Stabeno, P.J., 2007. Northern Gulf of Alaska eddies and associated anomalies. *Deep-Sea Res., Part I,* 54(4):487–509. **doi:10.1016/j.dsr.2007.01.006**

Lagoe, M.B., Eyles, C.H., Eyles, N., and Hale, C., 1993. Timing of late Cenozoic tidewater glaciation in the far North Pacific. *Geol. Soc. Am. Bull.,* 105(12):1542–1560. **doi:10.1130/0016-7606(1993)105<1542:TOLCTG>2.3.CO;2**

Lagoe, M.B., and Zellers, S.D., 1996. Depositional and microfaunal response to Pliocene climate change and tectonics in the eastern Gulf of Alaska. *Mar. Micropaleontol.,* 27(1–4):121–140. **doi:10.1016/0377-8398(95)00055-0**

Laj, C., Kissel, C., and Beer, J., 2004. High resolution global paleointensity stack since 75 kyr (GLOPIS-75) calibrated to absolute values. *In* Channell, J.E.T., Kent, D.V., Lowrie, W., and Meert, J.G. (Eds.), *Timescales of the Paleomagnetic Field.* Geophys. Monogr., 145:255–266. **doi:10.1029/145GM19**

Lam, P.J., and Bishop, J.K.B., 2008. The continental margin is a key source of iron to the HNLC North Pacific Ocean. *Geophys. Res. Lett.,* 35:L07608. **doi:10.1029/2008GL033294**

Landis, P.S., 2007. Stratigraphic framework and provenance of the Eocene–Oligocene Kulthieth formation, Alaska: implications for paleogeography and tectonics of the early Cenozoic continental margin of northwestern North America [M.S. thesis]. Purdue Univ., West Lafayette, Indiana.

Larsen, H.C., Saunders, A.D., Clift, P.D., et al., 1994. *Proc. ODP, Init. Repts.,* 152: College Station, TX (Ocean Drilling Program). **doi:10.2973/odp.proc.ir.152.1994**

Lisiecki, L.E., and Raymo, M.E., 2005. A Pliocene–Pleistocene stack of 57 globally distributed benthic $\delta^{18}O$ records. *Paleoceanography,* 20(1):PA1003. **doi:10.1029/2004PA001071**

Lund, S.P., 1996. A comparison of Holocene paleomagnetic secular variation records from North America. *J. Geophys. Res.: Solid Earth,* 101(B4):8007–8024. **doi:10.1029/95JB00039**

Lund, S.P., Acton, G.D., Clement, B., Okada, M., and Williams, T., 2001. Paleomagnetic records of Stage 3 excursions, Leg 172. *In* Keigwin, L.D., Rio, D., Acton, G.D., and Arnold, E. (Eds.), *Proc. ODP, Sci. Results,* 172: College Station, TX (Ocean Drilling Program), 1–20. **doi:10.2973/odp.proc.sr.172.217.2001**

Lund, S.P., Schwartz, M., Keigwin, L., and Johnson, T., 2005. Deep-sea sediment records of the Laschamp geomagnetic field excursion (~41,000 calendar years before present). *J. Geophys. Res.: Solid Earth,* 110(B4):B04101. **doi:10.1029/2003JB002943**

Mahowald, N.M., Baker, A.R., Bergametti, G., Brooks, N., Duce, R.A., Jickells, T.D., Kubilay, N., Prospero, J.M., and Tegen, I., 2005. Atmospheric global dust cycle and iron inputs to the ocean. *Global Biogeochem. Cycles,* 19(4):GB4024. **doi:10.1029/2004GB002402**

Malavieille, J., 2010. Impact of erosion, sedimentation, and structural heritage on the structure and kinematics of orogenic wedges: analog models and case studies. *GSA Today,* 20(1):4–10. **doi:10.1130/GSATG48A.1**

Manley, W., and Kaufman, D.S., 2002. *Alaska Paleoglacier Atlas:* Boulder, CO (Inst. Arct. Alp. Res., Univ. Colorado). **http://instaar.colorado.edu/QGISL/ak_paleoglacier_atlas/**

Mann, D.H., Crowell, A.L., Hamilton, T.D., and Finney, B.P., 1998. Holocene geologic and climatic history around the Gulf of Alaska. *Arct. Anthropol.,* 35(1):112–131. **http://www.jstor.org/pss/40316459**

Mann, D.H., and Peteet, D.M., 1994. Extent and timing of the Last Glacial Maximum in southwestern Alaska. *Quat. Res.,* 42(2):136–148. **doi:10.1006/qres.1994.1063**

Maus, S., Barckhausen, U., Berkenbosch, H., Bournas, N., Brozena, J., Childers, V., Dostaler, F., Fairhead, J.D., Finn, C., von Frese, R.R.B., Gaina, C., Golynsky, S., Kucks, R., Lühr, H., Milligan, P., Mogren, S., Müller, R.D., Olesen, O., Pilkington, M., Saltus, R., Schreckenberger, B., Thébault, E., and Caratori Tontini, F., 2009. EMAG2: a 2-arc min resolution Earth Magnetic Anomaly Grid compiled from satellite, airborne, and marine magnetic measurements. *Geochem., Geophys., Geosyst.,* 10(8):Q08005. **doi:10.1029/2009GC002471**

Mayer, L.A., Gardner, J.V., Armstrong, A., Calder, B.R., Malik, M., Angwenyi, C., Karlpata, S., Montoro-Dantes, H., Morishita, T., Mustapha, A., van Waes, M., Wood, D., and Withers, A., 2005. New views of the Gulf of Alaska margin mapped for UNCLOS applications. *Eos, Trans. Am. Geophys. Union,* 88(52)(Suppl.):T13D-0500. (Abstract) **http://www.agu.org/meetings/fm05/waisfm05.html**

Mazaud, A., Channell, J.E.T., Xuan, C., and Stoner, J.S., 2009. Upper and lower Jaramillo polarity transitions recorded in IODP Expedition 303 North Atlantic sediments: implications for transitional field geometry. *Phys. Earth Planet. Inter.,* 172(3–4):131–140. **doi:10.1016/j.pepi.2008.08.012**

Mazzotti, S., and Hyndman, R.D., 2002. Yakutat collision and strain transfer across the northern Canadian cordillera. *Geology,* 30(6):495–498. **doi:10.1130/0091-7613(2002)030<0495:YCASTA>2.0.CO;2**

McClymont, E.L., Sosdian, S.M., Rosell-Melé, A., and Rosenthal, Y., 2013. Pleistocene sea-surface temperature evolution: early cooling, delayed glacial intensification, and implications for the mid-Pleistocene climate transition. *Earth-Sci. Rev.,* 123:173–193. **doi:10.1016/j.earscirev.2013.04.006**

McDonald, D., Pedersen, T.F., and Crusius, J., 1999. Multiple late Quaternary episodes of exceptional diatom production in the Gulf of Alaska. *Deep-Sea Res., Part II,* 46(11–12):2993–3017. **doi:10.1016/S0967-0645(99)00091-0**

Meigs, A., Johnston, S., Garver, J., and Spotila, J., 2008. Crustal-scale structural architecture, shortening, and exhumation of an active, eroding orogenic wedge (Chugach/St. Elias Range, southern Alaska). *Tectonics,* 27(4):TC4003. **doi:10.1029/2007TC002168**

Menviel, L., Timmermann, A., Elison Timm, O., Mouchet, A., Abe-Ouchi, A., Chikamoto, M.O., Harada, N., Ohgaito, R., and Okazaki, Y., 2012. Removing the North Pacific halocline: effects on global climate, ocean circulation and the carbon cycle. *Deep-Sea Res., Part II,* 61–64:106–113. **doi:10.1016/j.dsr2.2011.03.005**

Mix, A.C., Bard, E., and Schneider, R., 2001. Environmental processes of the ice age: land, oceans, glaciers (EPILOG). *Quat. Sci. Rev.,* 20(4):627–657. **doi:10.1016/S0277-3791(00)00145-1**

Mix, A.C., Lund, D.C., Pisias, N.G., Bodén, P., Bornmalm, L., Lyle, M., and Pike, J., 1999. Rapid climate oscillations in the northeast Pacific during the last deglaciation reflect Northern and Southern Hemisphere sources. *In* Webb, R.S., Clark, P.U., and Keigwin, L. (Eds.), *Mechanisms of Millennial-scale Global Climate Change.* Geophys. Monogr., 112:127–148. **doi:10.1029/GM112p0127**

Molnar, P., 2004. Late Cenozoic increase in accumulation rates of terrestrial sediment: how might climate change have affected erosion rates? *Annu. Rev. Earth Planet. Sci.,* 32:67–89. **doi:10.1146/annurev.earth.32.091003.143456**

Molnar, P., and England, P., 1990. Late Cenozoic uplift of mountain ranges and global climate change: chicken or egg? *Nature (London, U. K.),* 346(6279):29–34. **doi:10.1038/346029a0**

Molnia, B.F., 1986. Late Wisconsin glacial history of the Alaskan continental margin. *In* Hamilton, T.D., Reed, K.M., and Thorson, R.M. (Eds.), *Glaciation in Alaska: The Geologic Record:* Anchorage, AK (Alaska Geol. Soc.), 219–236.

Molnia, B.F., and Sangrey, D.A., 1979. Glacially derived sediments in the northern Gulf of Alaska—geology and engineering characteristics. *Proc.—Annu. Offshore Technol. Conf.,* 1:647–655. **doi:10.4043/3433-MS**

Neal, E.G., Hood, E., and Smikrud, K., 2010. Contribution of glacier runoff to freshwater discharge into the Gulf of Alaska. *Geophys. Res. Lett.,* 37:L06404. **doi:10.1029/2010GL042385**

Ness, G.E., and Kulm, L.D., 1973. Origin and development of Surveyor Deep-sea Channel. *Geol. Soc. Am. Bull.,* 84(10):3339–3354. **doi:10.1130/0016-7606(1973)84<3339:OADOSD>2.0.CO;2**

Nokleberg, W.J., Parfenov, L.M., Monger, J.W.H., Norton, I.O., Khanchuk, A.I., Stone, D.B., Scotese, C.R., Scholl, D.W., and Fujita, K., 2000. Phanerozoic tectonic evolution of the circum-North Pacific. *U.S. Geol. Surv. Prof. Pap.,* 1626:1–133. **http://pubs.usgs.gov/pp/2000/1626/**

O'Brien, P.E., Cooper, A.K., Richter, C., et al., 2001. *Proc. ODP, Init. Repts.,* 188: College Station, TX (Ocean Drilling Program). **doi:10.2973/odp.proc.ir.188.2001**

ODP Leg 172 Scientific Party, Lund, S.P., Acton, G., Clement, B., Hastedt, M., Okada, M., and Williams, T., 1998.

Geomagnetic field excursions occurred often during the last million years. *Eos, Trans. Am. Geophys. Union,* 79(14):178–179. **doi:10.1029/98EO00134**

Okazaki, Y., Timmermann, A., Menviel, L., Harada, N., Abe-Ouchi, A., Chikamoto, M.O., Mouchet, A., and Asahi, H., 2010. Deepwater formation in the North Pacific during the Last Glacial Termination. *Science,* 329(5988):200–204. **doi:10.1126/science.1190612**

Pavlis, T.L., Chapman, J.B., Bruhn, R.L., Ridgway, K., Worthington, L.L., Gulick, S.P.S., and Spotila, J., 2012. Structure of the actively deforming fold-thrust belt of the St. Elias orogen with implications for glacial exhumation and three-dimensional tectonic processes. *Geosphere,* 8(5):991–1019. **doi:10.1130/GES00753.1**

Pavlis, T.L., Hamburger, M.W., and Pavlis, G.L., 1997. Erosional processes as a control on the structural evolution of an actively deforming fold and thrust belt: an example from the Pamir-Tien Shan region, central Asia. *Tectonics,* 16(5):810–822. **doi:10.1029/97TC01414**

Pavlis, T.L., Picornell, C., Serpa, L., Bruhn, R.L., and Plafker, G., 2004. Tectonic processes during oblique collision: insights from the St. Elias orogen, northern North American cordillera. *Tectonics,* 23(3):TC3001. **doi:10.1029/2003TC001557**

Perry, S.E., Garver, J.I., and Ridgway, K.D., 2009. Transport of the Yakutat terrane, Southern Alaska: evidence from sediment petrology and detrital zircon fission-track and U/Pb double dating. *J. Geol.,* 117(2):156–173. **doi:10.1086/596302**

Peteet, D.M., 2007. Muskeg archives of vegetation, migration, and climate history in the Gulf of Alaskan arc. *Abstr.—Geol. Soc. Am.* **http://gsa.confex.com/gsa/2007CD/finalprogram/abstract_120879.htm**

Peteet, D.M., and Mann, D.H., 1994. Late-glacial vegetational, tephra, and climatic history of southwestern Kodiak Island, Alaska. *Ecoscience,* 1(3):255–267. **http://www.ecoscience.ulaval.ca/en/paper/late-glacial-vegetational-tephra-and-climatic-history-of-southwestern-kodiak-island-alaska**

Pinter, N., and Brandon, M.T., 1997. How erosion builds mountains. *Sci. Am.,* 276(4):74–79. **doi:10.1038/scientificamerican0497-74**

Plafker, G., 1987. Regional geology and petroleum potential of the northern Gulf of Alaska continental margin. *In* Scholl, D.W., Grantz, A., and Vedder, J.G. (Eds.), *Geology and Resource Potential of the Continental Margin of Western North America and Adjacent Ocean Basins—Beaufort Sea to Baja California.* Earth Sci. Ser. (N. Y.), 6:229–268. **http://archives.datapages.com/data/circ_pac/0007/0229_f.htm**

Plafker, G., Moore, J.C., and Winkler, G.R., 1994. Geology of the southern Alaska margin. *In* Plafker, G., and Berg, H.C. (Eds.), *The Geology of North America* (Vol. G): *The Geology of Alaska:* Boulder, CO (Geol. Soc. Am.), 389–449.

Powell, R.D., and Cooper, J.M., 2002. A glacial sequence stratigraphic model for temperate, glaciated continental shelves. *In* Dowdeswell, J.A., and Ó'Cofaigh, C. (Eds.), *Glacier-Influenced Sedimentation on High-Latitude Continental Margins.* Geol. Soc. Spec. Publ., 203:215–244. **doi:10.1144/GSL.SP.2002.203.01.12**

Prueher, L.M., and Rea, D.K., 1998. Rapid onset of glacial conditions in the subarctic North Pacific region at 2.67 Ma: clues to causality. *Geology,* 26(11):1027–1030. **doi:10.1130/0091-7613(1998)026<1027:ROOGCI>2.3.CO;2**

Rasmussen, S.O., Andersen, K.K., Svensson, A.M., Steffensen, J.P., Vinther, B.M., Clausen, H.B., Siggaard-Andersen, M.-L., Johnsen, S.J., Larsen, L.B., Dahl-Jensen, D., Bigler, M., Röthlisberger, R., Fischer, H., Goto-Azuma, K., Hansson, M.E., and Ruth, U., 2006. A new Greenland ice core chronology for the Last Glacial Termination. *J. Geophys. Res.: Atmos.,* 111(D6):D06102. **doi:10.1029/2005JD006079**

Rea, D.K., Basov, I.A., Janecek, T.R., Palmer-Julson, A., et al., 1993. *Proc. ODP, Init. Repts.,* 145: College Station, TX (Ocean Drilling Program). **doi:10.2973/odp.proc.ir.145.1993**

Rea, D.K., and Snoeckx, H., 1995. Sediment fluxes in the Gulf of Alaska: paleoceanographic record from Site 887 on the Patton-Murray Seamount platform. *In* Rea, D.K., Basov, I.A., Scholl, D.W., and Allan, J.F. (Eds.), *Proc. ODP, Sci. Results,* 145: College Station, TX (Ocean Drilling Program), 247–256. **doi:10.2973/odp.proc.sr.145.122.1995**

Redfield, T.F., Scholl, D.W., Fitzgerald, P.G., and Beck, M.E., Jr., 2007. Escape tectonics and the extrusion of Alaska: past, present, and future. *Geology,* 35(11):1039–1042. **doi:10.1130/G23799A.1**

Reece, R.S., 2012. The impact of climate and tectonics on sedimentary and deformational processes, Gulf of Alaska [Ph.D. dissert.]. Univ. Texas, Austin.

Reece, R.S., Gulick, S.P.S., Christeson, G.L., Horton, B.K., van Avendonk, H., and Barth, G., 2013. The role of far-field tectonic stress in oceanic intraplate deformation, Gulf of Alaska. *J. Geophys. Res.: Solid Earth,* 118(5):1862–1872. **doi:10.1002/jgrb.50177**

Reece, R.S., Gulick, S.P.S., Horton, B.K., Christeson, G.L., and Worthington, L.L., 2011. Tectonic and climatic influence on the evolution of the Surveyor Fan and channel system, Gulf of Alaska. *Geosphere,* 7(4):830–844. **doi:10.1130/GES00654.1**

Richter, D.H., Preller, C.C., Labay, K.A., and Shrew, N.B., 2006. Geologic map of the Wrangell–Saint Elias National Park and Preserve, Alaska. *Sci. Invest. Rep. (U. S. Geol. Surv.),* SIM-2877. **http://pubs.usgs.gov/sim/2006/2877/**

Riis, F., 1992. Dating and measuring of erosion, uplift and subsidence in Norway and the Norwegian shelf in glacial periods. *Nor. Geol. Tiddskr. (1905–2000),* 72(3):325–331. **http://www.npd.no/Global/Norsk/3 - Publikasjoner/Forskningsartikler/Riis_1992.pdf**

Risley, D.E., Martin, G.C., Lynch, M.B., Flett, T.O., Larson, J.A., Horowitz, W.L., and Turner, R.F. (Ed.), 1992. Geologic report for the Gulf of Alaska planning area. *OCS Rep.,* MMS 92-0065.

Roe, G.H., Stolar, D.B., and Willett, S.D., 2006. Response of a steady-state critical wedge orogen to changes in climate and tectonic forcing. *Spec. Pap.—Geol. Soc. Am.,* 398:227–239. **doi:10.1130/2005.2398(13)**

Royer, T.C., 1981. Baroclinic transport in the Gulf of Alaska, Part II. Fresh water driven coastal current. *J. Mar. Res.,* 39:251–266.

Royer, T.C., 1982. Coastal fresh water discharge in the northeast Pacific. *J. Geophys. Res.: Oceans,* 87(C3):2017–2021. **doi:10.1029/JC087iC03p02017**

Royer, T.C., 2005. Hydrographic responses at a coastal site in the northern Gulf of Alaska to seasonal and interannual forcing. *Deep-sea Res., Part II,* 52(1–2):267–288. **doi:10.1016/j.dsr2.2004.09.022**

Ruth, U., Barnola, J.-M., Beer, J., Bigler, M., Blunier, T., Castellano, E., Fischer, H., Fundel, F., Huybrechts, P., Kaufmann, P., Kipfstuhl, S., Lambrecht, A., Morganti, A., Oerter, H., Parrenin, F., Rybak, O., Severi, M., Udisti, R., Wilhelms, F., and Wolff, E., 2007. “EDML1”: a chronology for the EPICA deep ice core from Dronning Maud Land, Antarctica, over the last 150,000 years. *Clim. Past,* 3:475–484. **doi:10.5194/cp-3-475-2007**

Schroth, A.W., Crusius, J., Sholkovitz, E.R., and Bostick, B.C., 2009. Iron solubility driven by speciation in dust sources to the ocean. *Nat. Geosci.,* 2:337–340. **doi:10.1038/ngeo501**

Schubert, C.J., and Calvert, S.E., 2001. Nitrogen and carbon isotopic composition of marine and terrestrial organic matter in Arctic Ocean sediments: implications for nutrient utilization and organic matter composition. *Deep-Sea Res., Part I,* 48(3):789–810. **doi:10.1016/S0967-0637(00)00069-8**

Severmann, S., McManus, J., Berelson, W.M., and Hammond, D.E., 2010. The continental shelf benthic iron flux and its isotope composition. *Geochim. Cosmochim. Acta,* 74(14):3984–4004. **doi:10.1016/j.gca.2010.04.022**

Shackleton, N.J., Hall, M.A., and Pate, D., 1995. Pliocene stable isotope stratigraphy of Site 846. *In* Pisias, N.G., Mayer, L.A., Janecek, T.R., Palmer-Julson, A., and van Andel, T.H. (Eds.), *Proc. ODP, Sci. Results,* 138: College Station, TX (Ocean Drilling Program), 337–355. **doi:10.2973/odp.proc.sr.138.117.1995**

Sheaf, M.A., Serpa, L., and Pavlis, T.L., 2003. Exhumation rates in the St. Elias Mountains, Alaska. *Tectonophysics,* 367(1–2):1–11. **doi:10.1016/S0040-1951(03)00124-0**

Siddall, M., Stocker, T.F., and Clark, P.U., 2009. Constraints on future sea level rise from past sea level change. *Nat. Geosci.,* 2:571–575. **doi:10.1038/ngeo587**

Sigman, D.M., Jaccard, S.L., and Haug, G.H., 2004. Polar ocean stratification in a cold climate. *Nature (London, U. K.),* 428(6978):59–63. **doi:10.1038/nature02357**

Simpson, G.D.H., 2010. Formation of accretionary prisms influenced by sediment subduction and supplied by sediments from adjacent continents. *Geology,* 38(2):131–134. **doi:10.1130/G30461.1**

Singer, B.S., Relle, M.K., Hoffman, K.A., Battle, A., Laj, C., Guillou, H., and Carracedo, J.C., 2002. Ar/Ar ages from transitionally magnetized lavas on La Palma, Canary Islands, and the geomagnetic instability timescale. *J. Geophys. Res.: Solid Earth,* 107(B11):2307. **doi:10.1029/2001JB001613**

Smith, W.H.F., and Sandwell, D.T., 1997. Global sea floor topography from satellite altimetry and ship depth soundings. *Science,* 277(5334):1956–1962. **doi:10.1126/science.277.5334.1956**

Spotila, J.A., and Berger, A.L., 2010. Exhumation at orogenic indentor corners under long-term glacial conditions: example of the St. Elias orogen, southern Alaska. *Tectonophysics,* 490(3–4): 241–256. **doi:10.1016/j.tecto.2010.05.015**

Spotila, J.A., Buscher, J.T., Meigs, A.J., and Reiners, P.W., 2004. Long-term glacial erosion of active mountain belts: example of the Chugach–St. Elias Range, Alaska. *Geology,* 32(6):501–504. **doi:10.1130/G20343.1**

Srivastava, S.P., Arthur, M., Clement, B., et al., 1987. *Proc. ODP, Init. Repts.,* 105: College Station, TX (Ocean Drilling Program). **doi:10.2973/odp.proc.ir.105.1987**

Stabeno, P.J., Bond, N.A., Hermann, A.J., Kachel, N.B., Mordy, C.W., and Overland, J.E., 2004. Meteorology and oceanography of the northern Gulf of Alaska. *Continent. Shelf Res.,* 24(7–8):859–897. **doi:10.1016/j.csr.2004.02.007**

Stabeno, P.J., Reed, R.K., and Schumacher, J.D., 1995. The Alaska Coastal Current: continuity of transport and forcing. *J. Geophys. Res.: Oceans,* 100(C2):2477–2485. **doi:10.1029/94JC02842**

Stevenson, A.J., and Embley, R., 1987. Deep-sea fan bodies, terrigenous turbidite sedimentation, and petroleum geology, Gulf of Alaska. *In* Scholl, D.W., Grantz, A., and Vedder, J.G. (Eds.), *Geology and Resource Potential of the Western North America and Adjacent Ocean Basins—Beaufort Sea to Baja California.* Circum-Pac. Counc. Energy Min. Resour., Earth Sci. Ser., 6:503–522.

Stolar, D.B., Willett, S.D., and Roe, G.H., 2006. Climatic and tectonic forcing of a critical orogen. *Spec. Pap.—Geol. Soc. Am.,* 398:241–50. **doi:10.1130/2006.2398(14)**

Stoner, J.S., 2009. Towards an understanding of paleomagnetic secular variation: observations from the North Atlantic, implications for the world? *Geol. Soc. Am. Abstr. Program,* 41(7):46. **http://gsa.confex.com/gsa/2009AM/finalprogram/abstract_166811.htm**

Stoner, J.S., Channell, J.E.T., Hillaire-Marcel, C., and Kissel, C., 2000. Geomagnetic paleointensity and environmental record from Labrador Sea Core MD95-2024: global marine sediment and ice core chronostratigraphy for the last 110 kyr. *Earth Planet. Sci. Lett.,* 183(1–2):161–177. **doi:10.1016/S0012-821X(00)00272-7**

Svensson, A., Andersen, K.K., Bigler, M., Clausen, H.B., Dahl-Jensen, D., Davies, S.M., Johnsen, S.J., Muscheler, R., Rasmussen, S.O., Röthlisberger, R., Steffensen, J.P., and Vinther, B.M., 2006. The Greenland ice core chronology 2005, 15–42 ka, Part 2. Comparison to other records. *Quat. Sci. Rev.,* 25(23–24):3258–3267. **doi:10.1016/j.quascirev.2006.08.003**

Tomkin, J.H., 2007. Coupling glacial erosion and tectonics at active orogens: a numerical modeling study. *J. Geophys. Res.: Earth Surface,* 112(F2):F02015. **doi:10.1029/2005JF000332**

Tomkin, J.H., and Roe, G.H., 2007. Climate and tectonic controls on glaciated critical-taper orogens. *Earth Planet.*

Sci. Lett., 262(3–4):385–397. **doi:10.1016/j.epsl.2007.07.040**

Trop, J.M., Ridgway, K.D., Manuszak, J.D., and Layer, P., 2002. Mesozoic sedimentary-basin development on the allochthonous Wrangellia composite terrane, Wrangell Mountains basin, Alaska: a long-term record of terrane migration and arc construction. *Geol. Soc. Am. Bull.,* 114(6):693–717. **doi:10.1130/0016-7606(2002)114<0693:MSBDOT>2.0.CO;2**

Tsuda, A., Kiyosawa, H., Kuwata, A., Mochizuki, M., Shiga, N., Saito, H., Chiba, S., Imai, K., Nishioka, J., and Ono, T., 2005. Responses of diatoms to iron-enrichment (SEEDS) in the western subarctic Pacific, temporal and special comparisons. *Prog. Oceanogr.,* 64(2–4):189–205. **doi:10.1016/j.pocean.2005.02.008**

Vagnes, E., Faleide, J.I., and Gudlaugsson, S.T., 1992. Glacial erosion and tectonic uplift in the Barents Sea. *Nor. Geol. Tidsskr. (1905–2000)*, 72(3):333–338.

Valet, J.-P., Meynadier, L., and Guyodo, Y., 2005. Geomagnetic dipole strength and reversal rate over the past two million years. *Nature (London, U. K.)*, 435(7043):802–805. **doi:10.1038/nature03674**

von Huene, R., and Kulm, L.D., 1973. Tectonic summary of Leg 18. *In* Kulm, L.D., von Huene, R., et al., *Init. Repts. DSDP,* 18: Washington (U.S. Govt. Printing Office), 961–976. **doi:10.2973/dsdp.proc.18.133.1973**

von Huene, R., Larson, E., and Crouch, J., 1973. Preliminary study of ice-rafted erratics as indicators of glacial advances in the Gulf of Alaska. *In* Kulm, L.D., von Huene, R., et al., *Init. Repts. DSDP,* 18: Washington (U.S. Govt. Printing Office), 835–842. **doi:10.2973/dsdp.proc.18.121.1973**

Walinsky, S.E., Prahl, F.G., Mix, A.C., Finney, B.P., Jaeger, J.M., and Rosen, G.P., 2009. Distribution and composition of organic matter in surface sediments of coastal southeast Alaska. *Cont. Shelf Res.,* 29(13):1565–1579. **doi:10.1016/j.csr.2009.04.006**

Walton, M.A.L., Gulick, S.P.S., Reece, R.S., and Barth, G.A., in press. Tectonic control on deposition and evolution of the Baranof Fan, Gulf of Alaska. *Geosphere.*

Weingartner, T.J., Danielson, S.L., and Royer, T.C., 2005. Freshwater variability and predictability in the Alaska Coastal Current. *Deep-Sea Res., Part II,* 52(1–2):161–191. **doi:10.1016/j.dsr2.2004.09.030**

Whipple, K.X., 2009. The influence of climate on the tectonic evolution of mountain belts. *Nat. Geosci.,* 2:97–104. **doi:10.1038/ngeo413**

Whipple, K.X., and Meade, B.J., 2004. Controls on the strength of coupling among climate, erosion, and deformation in two-sided, frictional orogenic wedges at steady state. *J. Geophys. Res.: Earth Surface,* 109(F1):F01011. **doi:10.1029/2003JF000019**

White, J.M., Ager, T.A., Adam, D.P., Leopold, E.B., Liu, G., Jetté, H., and Schweger, C.E., 1997. An 18 million year record of vegetation and climate change in northwestern Canada and Alaska: tectonic and global climatic correlates. *Palaeogeogr., Palaeoclimatol., Palaeoecol.,* 130(1–4):293–306. **doi:10.1016/S0031-0182(96)00146-0**

Willems, B.A., 2009. Quaternary glacial and climatic history of southern Alaska using high-resolution seismic reflection records [Ph.D. dissert.]. Northern Illinois Univ., DeKalb.

Willett, S.D., 1999. Orogeny and orography: the effects of erosion on the structure of mountain belts. *J. Geophys. Res.: Solid Earth,* 104(B12):28957–28981. **doi:10.1029/1999JB900248**

Willett, S.D., 2010. Late Neogene erosion of the Alps: a climate driver? *Annu. Rev. Earth Planet. Sci.,* 38:411–437. **doi:10.1146/annurev-earth-040809-152543**

Witmer, J.W., Ridgway, K.D., Enkelmann, E., Brennan, P., and Valencia, V.A., 2009. Deposition, provenance, and exhumation of Neogene strata at the syntaxis of the Chugach–St. Elias Range, southeast Alaska. *Geol. Soc. Am. Abstr. Program,* 41(7):306. **http://gsa.confex.com/gsa/2009AM/finalprogram/abstract_165389.htm**

Worthington, L.L, Gulick, S.P.S., and Pavlis, T.L., 2010. Coupled stratigraphic and structural evolution of a glaciated orogenic wedge, offshore St. Elias orogen, Alaska. *Tectonics,* 29:TC6013–TC6039. **doi:10.1029/2010TC002723**

Worthington, L., 2010. New geophysical parameters for understanding the evolution of the St. Elias orogen, southern Alaska [Ph.D. dissert]. Univ. Texas, Austin.

Worthington, L.L., Gulick, S.P.S., and Pavlis, T.L., 2008. Identifying active structures in the Kayak Island and Pamplona Zones: implications for offshore tectonics of the Yakutat microplate, Gulf of Alaska. *In* Freymueller, J.T., Haeussler, P.J., Wesson, R.L., and Ekström, G. (Eds.), *Active Tectonics and Seismic Potential of Alaska.* Geophys. Monogr., 179:257–268. **doi:10.1029/179GM14**

Worthington, L.L., Van Avendonk, H.J.A., Gulick, S.P.S., Christeson, G.L., and Pavlis, T.L., 2012. Crustal structure of the Yakutat terrane and the evolution of subduction and collision in southern Alaska. *J. Geophys. Res.: Solid Earth,* 117(B1):B01102. **doi:10.1029/2011JB008493**

Wu, J., Aguilar-Islas, A., Rember, R., Weingertner, T., Danielson, S., and Whitledge, T., 2009. Size-fractionated iron distribution on the northern Gulf of Alaska. *Geophys. Res. Lett.,* 36:L11606. **doi:10.1029/2009GL038304**

Yamazaki, T., and Oda, H., 2005. A geomagnetic paleointensity stack between 0.8 and 3.0 Ma from equatorial Pacific sediment cores. *Geochem., Geophys., Geosyst.,* 6(11):Q11H20. **doi:10.1029/2005GC001001**

You, Y., Suginohara, N., Fukasawa, M., Yasuda, I., Kaneko, I., Yoritaka, H., and Kawamiya, M., 2000. Roles of the Okhotsk Sea and Gulf of Alaska in forming the North Pacific Intermediate Water. *J. Geophys. Res.: Oceans,* 105(C2):3253–3280. **doi:10.1029/1999JC900304**

Zachos, J., Pagani, M., Sloan, L., Thomas, E., and Billups, K., 2001. Trends, rhythms, and aberrations in global climate 65 Ma to present. *Science,* 292(5517):686–693. **doi:10.1126/science.1059412**

Zahn, R., Pedersen, T.F., Bornhold, B.D., and Mix, A.C., 1991. Water mass conversion in the glacial subarctic Pacific (54°N, 148°W): physical constraints and the benthic-planktonic stable isotope record. *Paleoceanography,* 6(5):543–560. **doi:10.1029/91PA01327**

Zeitler, P.K., Meltzer, A.S., Koons, P.O., Craw, D., Hallet, B., Chamberlain, C.P., Kidd, W.S.F., Park, S.K., Seeber, L., Bishop, M., and Shroder, J., 2001. Erosion, Himalayan geodynamics, and the geomorphology of metamorphism. *GSA Today,* January 2001:4–9. **doi:10.1130/1052-5173(2001)011<0004:EHGATG>2.0.CO;2**

Zellers, S.D., 1995. Foraminiferal sequence biostratigraphy and seismic stratigraphy of a tectonically active margin: the Yakataga Formation, northeastern Gulf of Alaska. *Mar. Micropaleontol.,* 26(1–4):255–271. **doi:10.1016/0377-8398(95)00031-3**

Zhang, P., Molnar, P., and Downs, W.R., 2001. Increased sedimentation rates and grain sizes 2–4 Myr ago due to the influence of climate change on erosion rates. *Nature (London, U. K.),* 410(6831):891–897. **doi:10.1038/35073504**

Publication: 22 November 2014
MS 341-101

Figure F1. The Gulf of Alaska region: geography and location of previous DSDP and ODP drilling locations (see inset) and Expedition 341 drilling sites. There is significant regional coverage of seismic reflection data on the shelf. EW0408 lines were collected in 2004, STEEP-MGL0814 lines were collected in summer 2008, and UNCLOS-MGL1109 lines were collected in summer 2011.

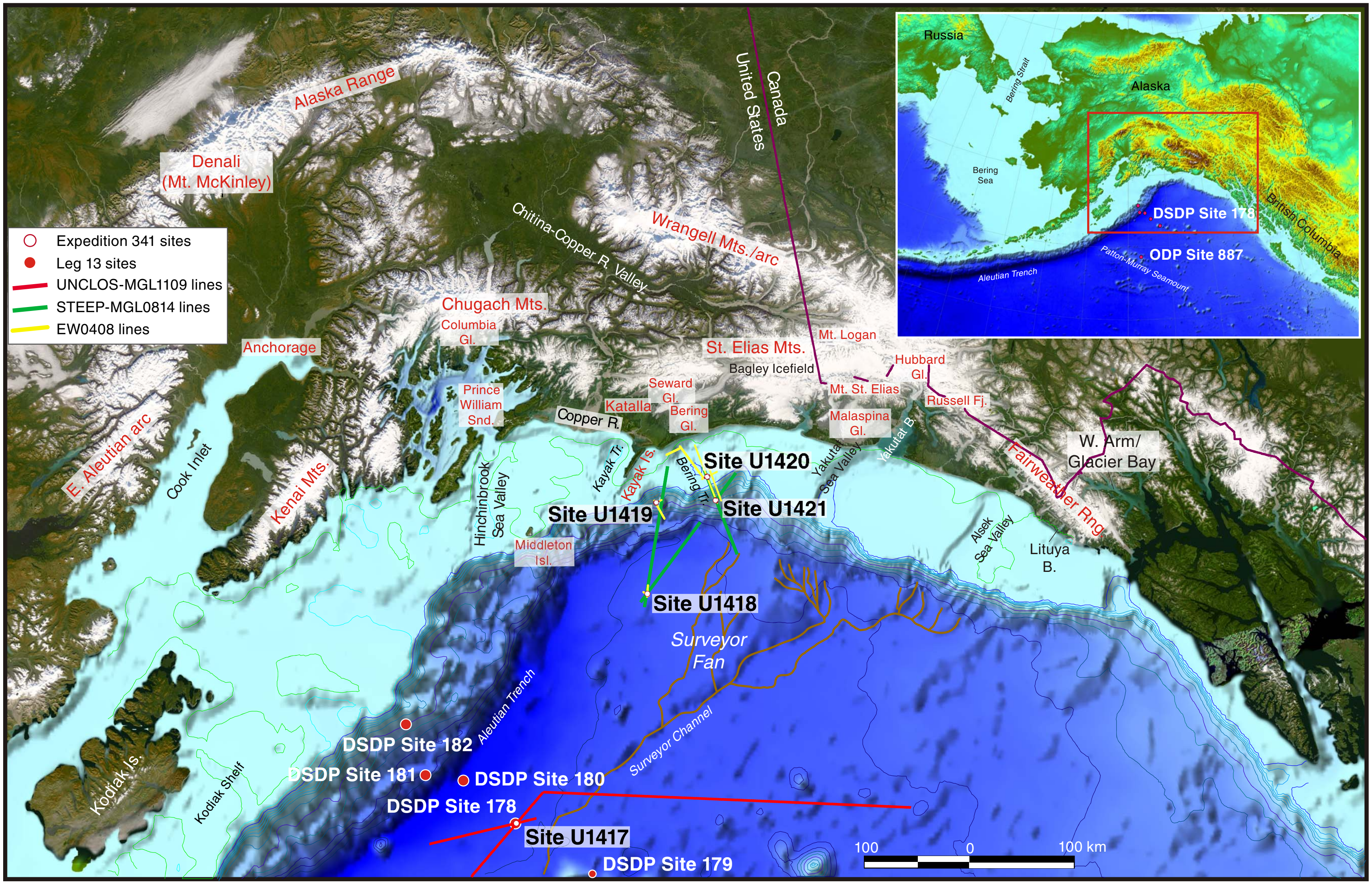

Figure F2. Stratigraphic, depositional, tectonic, and climatic history of the Gulf of Alaska (GoA) and adjacent regions as modified from Lagoe et al. (1993) and Berger et al. (2008a). Lithologic data are from Lagoe et al. (1993), Rea and Snoeckx (1995), and Lagoe and Zellers (1996). Bedrock temperature paths vs. time is from Berger et al. (2008a). Tectonic events are from Lagoe et al. (1993), Stevenson and Embley (1987), Berger et al. (2008a, 2008b), Enkelmann et al. (2010), and Finzel et al. (2011). Oxygen isotope data are from global stacks of Lisiecki and Raymo (2005) (black) and Zachos et al. (2001) (gray). IRD = ice-rafted debris. AHe = apatite (U-Th)/He, AFT = apatite fission track, ZHe = zircon (U-Th)/He.

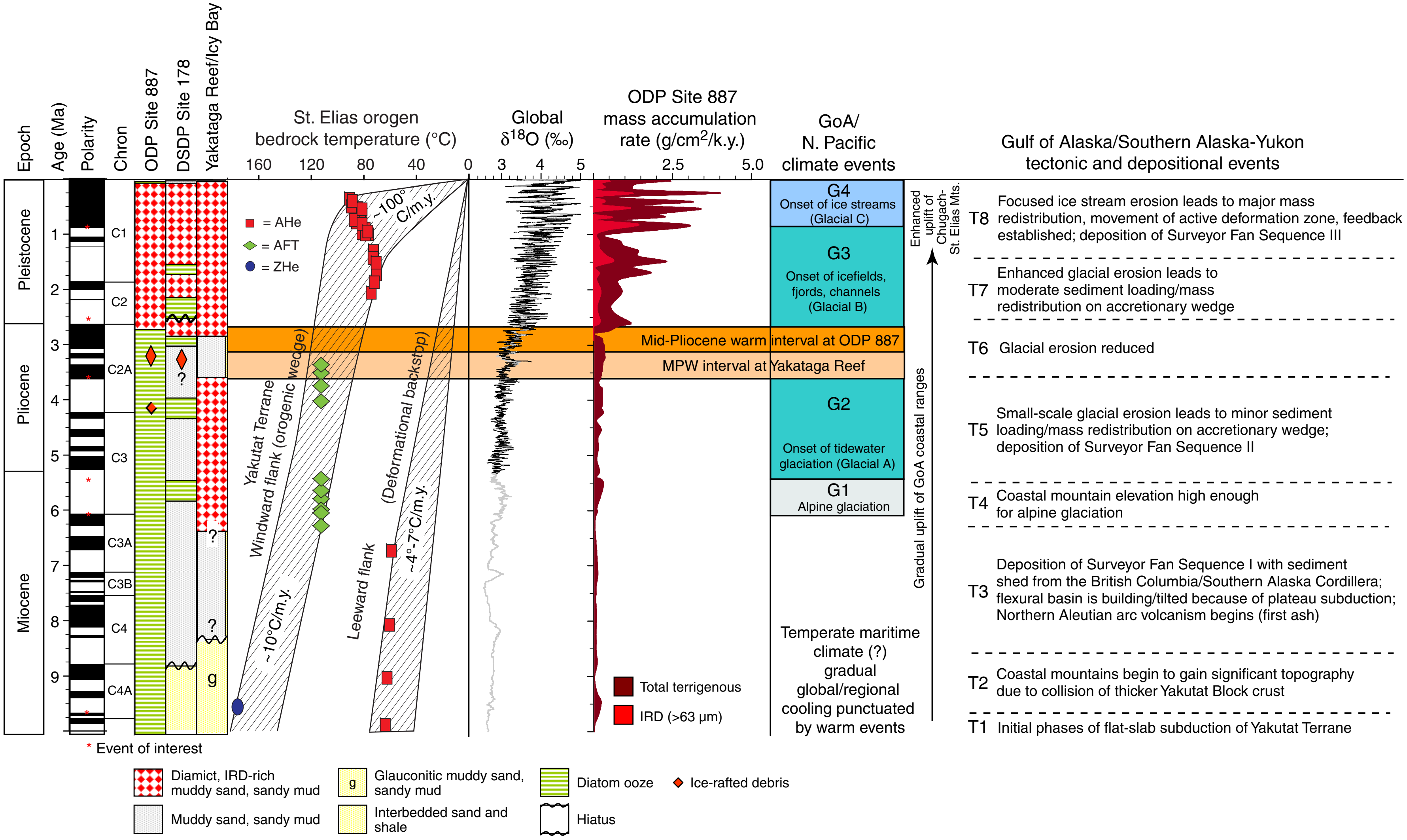

Figure F3. Regional tectonic map of southern Alaska showing major faults, topography, and geographic landmarks. Pacific plate velocity vector from Demets and Dixon (1999). Yakutat Terrane velocity with regard to North America (YAK-NA) in red arrows (average = 47 mm/y; from Elliot et al., 2010). Blue dashed line shows extent of subducted Yakutat slab from Eberhart-Phillips et al. (2006). Black dashed outline shows currently defined Yakutat Terrane. Benioff Zone depth contours at 50, 100, and 150 km. KIZ = Kayak Island zone, TACT = Trans-Alaska Crustal Transect (Brocher et al., 1994), PAC-NA = Pacific plate-North America plate convergence, BEARR = Broadband Experiment across the Alaska Range (Ferris et al., 2003). Proposed drilling sites (GOAL15-GOAL18) are shown. Figure modified from Worthington et al. (2012).

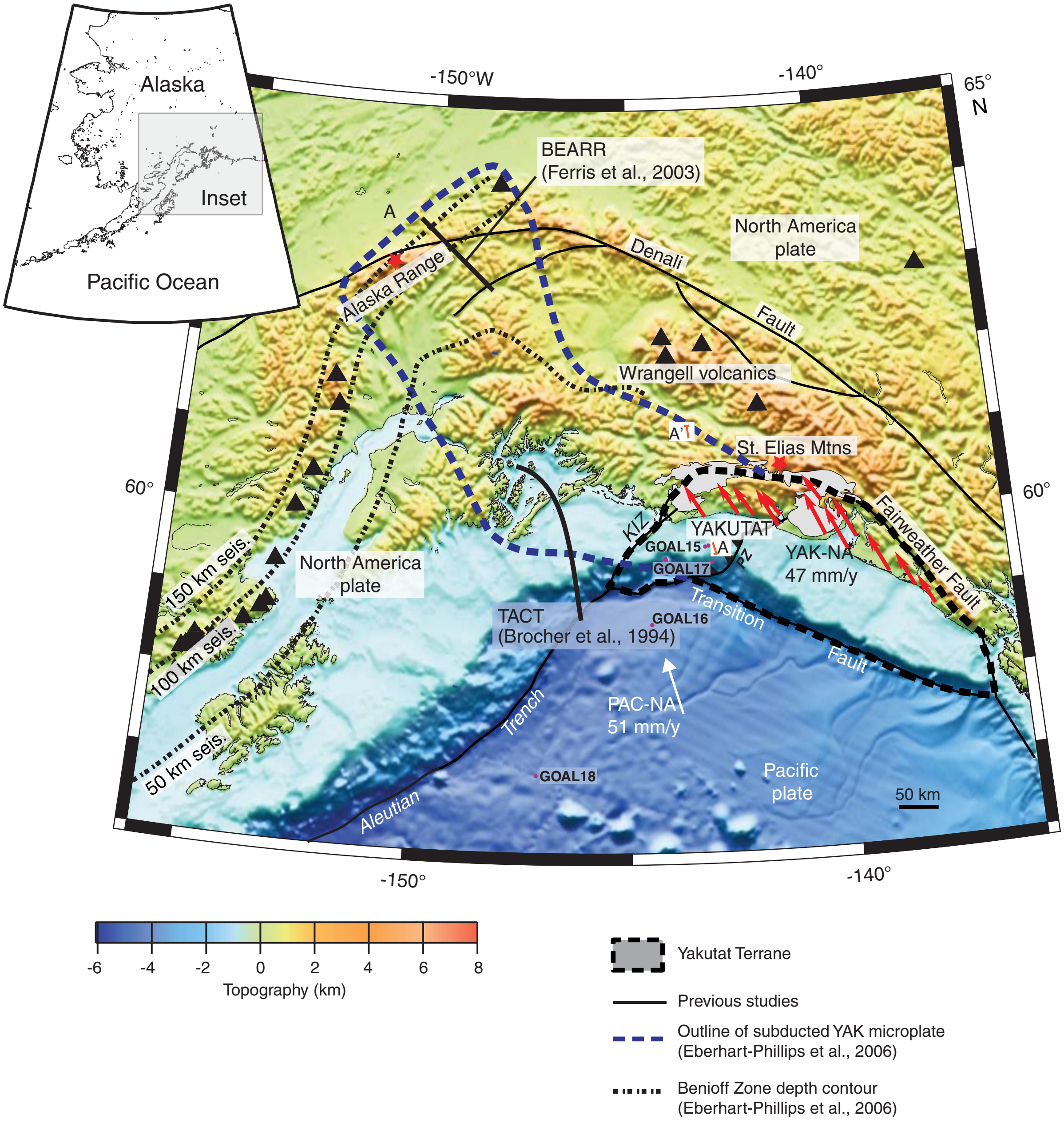

Figure F4. Map of Alaska showing major tectonostratigraphic terranes. Modified from Nokleburg et al. (2000).

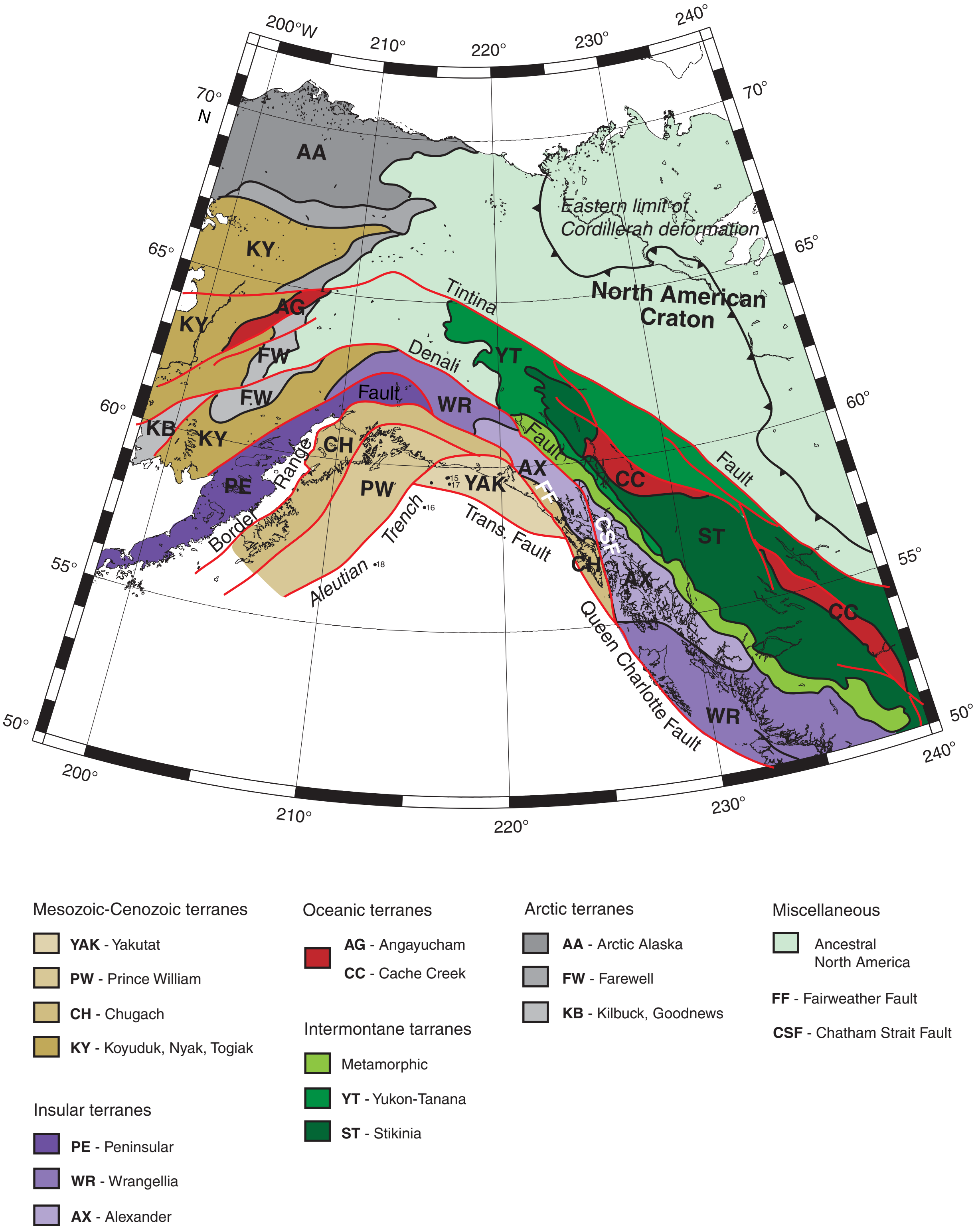

Figure F5. Proposed model of climate-related influences on orogen kinematics. Straight dashed lines depict structures with minor amounts of slip, and wavy dashed lines depict inactive structures. Strata along windward site: gray = Kultheith, green = Poul Creek, and brown = Yakataga Formations. **A.** Exhumational flux based on thermochronometry and architecture of the orogen prior to onset of Glacial Interval C at ~1 Ma, drawn along line A–A′ (Fig. F3) based on thermochronometry (Berger et al., 2008b; Spotila and Berger, 2010) and geologic data (Plafker et al., 1994; Bruhn et al., 2004). VE = vertical exaggeration. **B.** Exhumational flux based on thermochronometry and architecture of the orogen after the onset of Glacial Interval C. CSEF = Chugach-St. Elias Fault, KF = Kosakuts Fault, HCF = Hope Creek Fault, MCT = Miller Creek thrust fault, SF = Sullivan Fault, AHe = apatite (U-Th)/He. **C.** Interpretative model of the effect of glacial erosion and deposition on the St. Elias critical wedge. Before Glacial Interval C (left), the critical Coulomb wedge is wider and has greater relief. After the intensification of glaciation (right), increased glacial erosion and offshore deposition reduced relief, concentrated deformation, required enhanced back thrusting, and forced the termination of foreland structures, thereby narrowing the wedge. Modified from Berger et al. (2008a, 2008b).

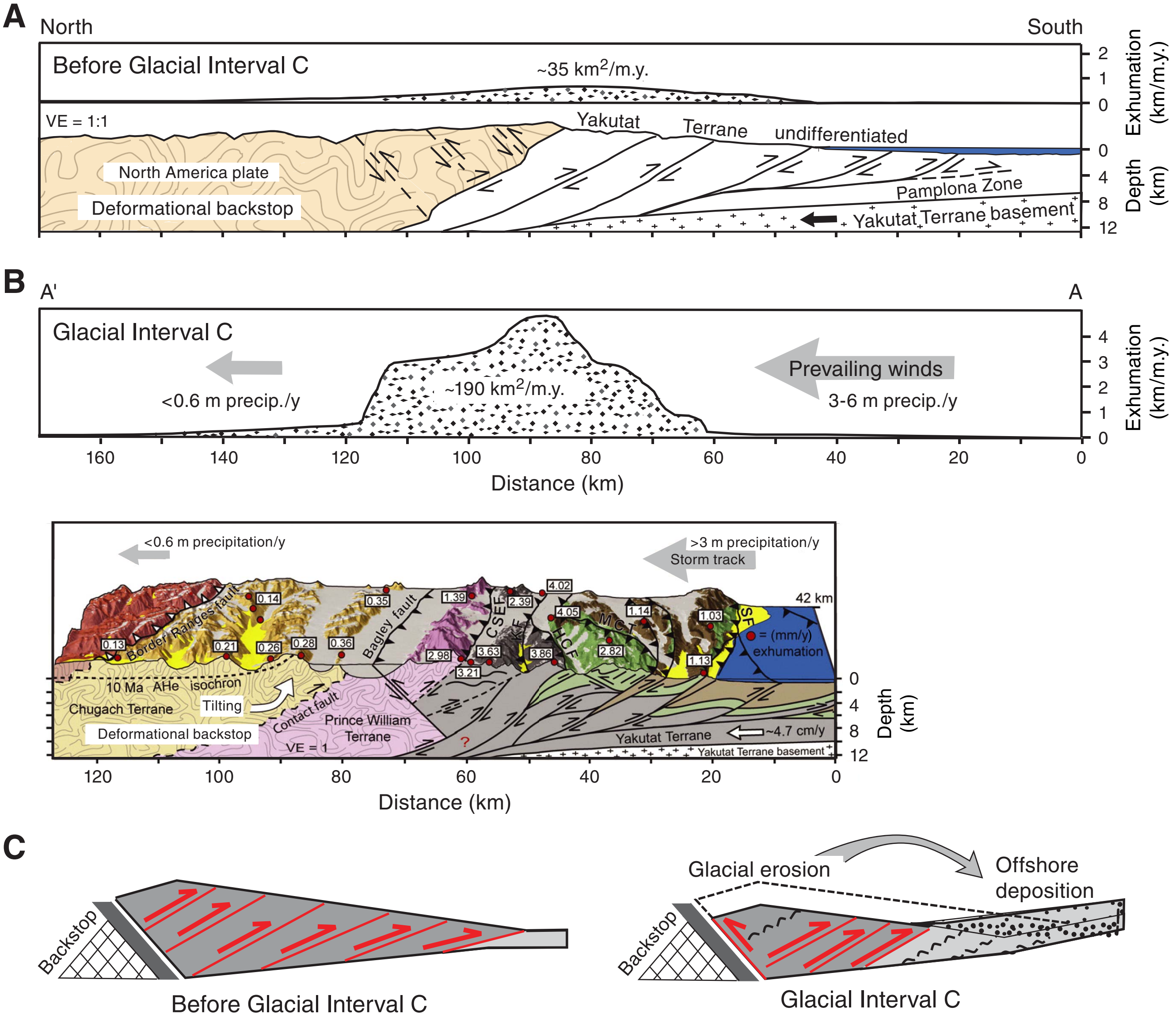

Figure F6. 3-D perspective view of the bathymetry/topography of the southern Alaska continental margin, showing tectonic boundaries and the Surveyor Fan in high-resolution bathymetry. HSV = Hinchinbrook Sea Valley, ASV = Alsek Sea Valley, BT = Bering Trough, GS = Giacomini Seamount, KT = Kayak Trough, PS = Pamplona Spur, YSV = Yakutat Sea Valley. Plate boundaries adapted from Gulick et al. (2007). High-resolution bathymetry from Gardner et al. (2006). Remaining bathymetry from Smith and Sandwell (1997). Yakutat Terrane motion relative to North America from Elliott et al. (2010). Pacific plate motion from Kreemer et al. (2003). Inset: Location of Alaska Coastal Current (ACC; purple), Alaska Current (AC; orange), and NOAA wave buoy 46001 (red star). Modified from Reece et al. (2013).

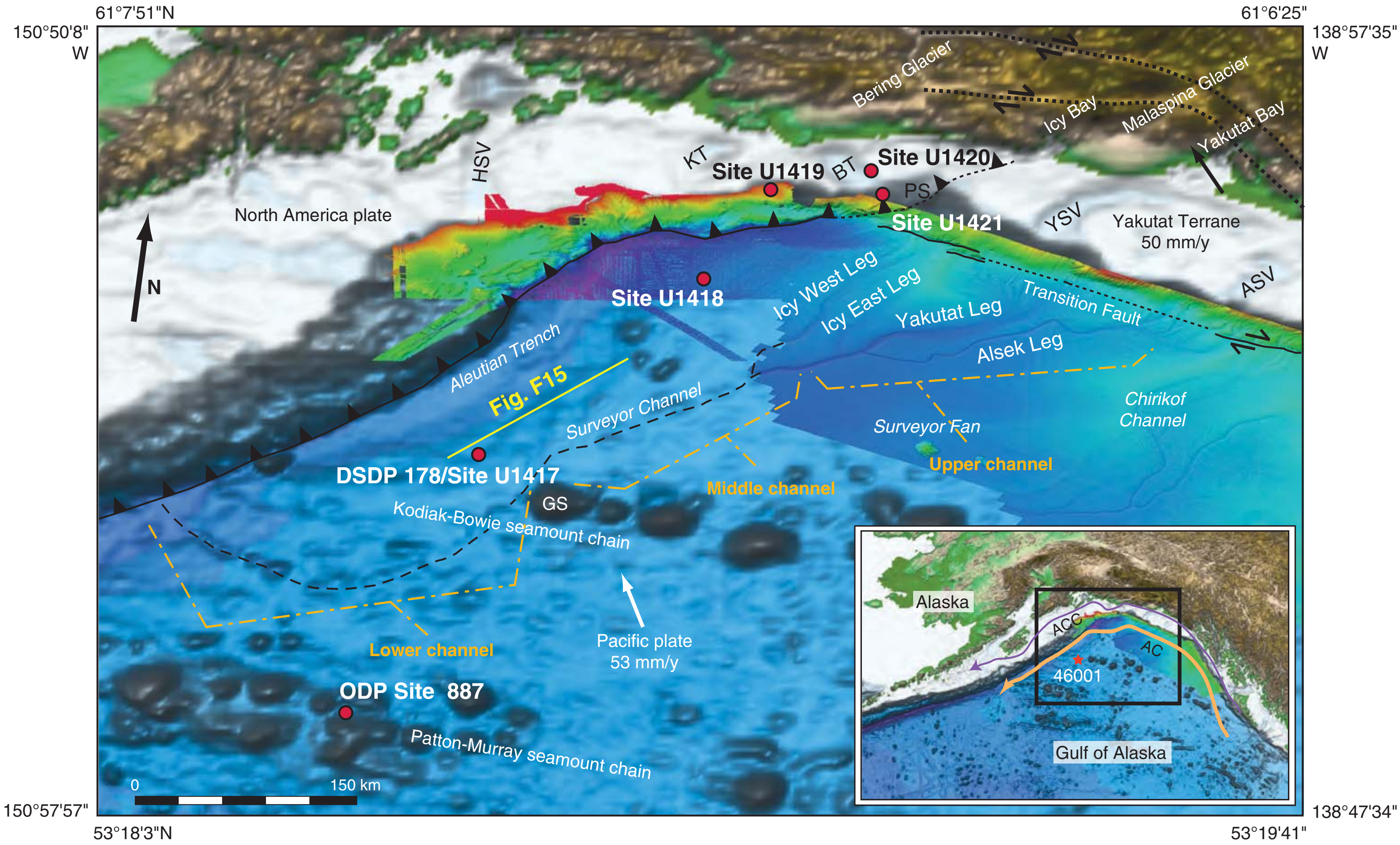

Figure F7. Summary of Pleistocene glaciations across Alaska. Extent of glaciers during the late Wisconsin (Last Glacial Maximum) glaciation and maximum extent reached during the last 3 m.y. by valley glaciers, ice caps, and the NCIS are shown. From Manley and Kaufmann (2002).

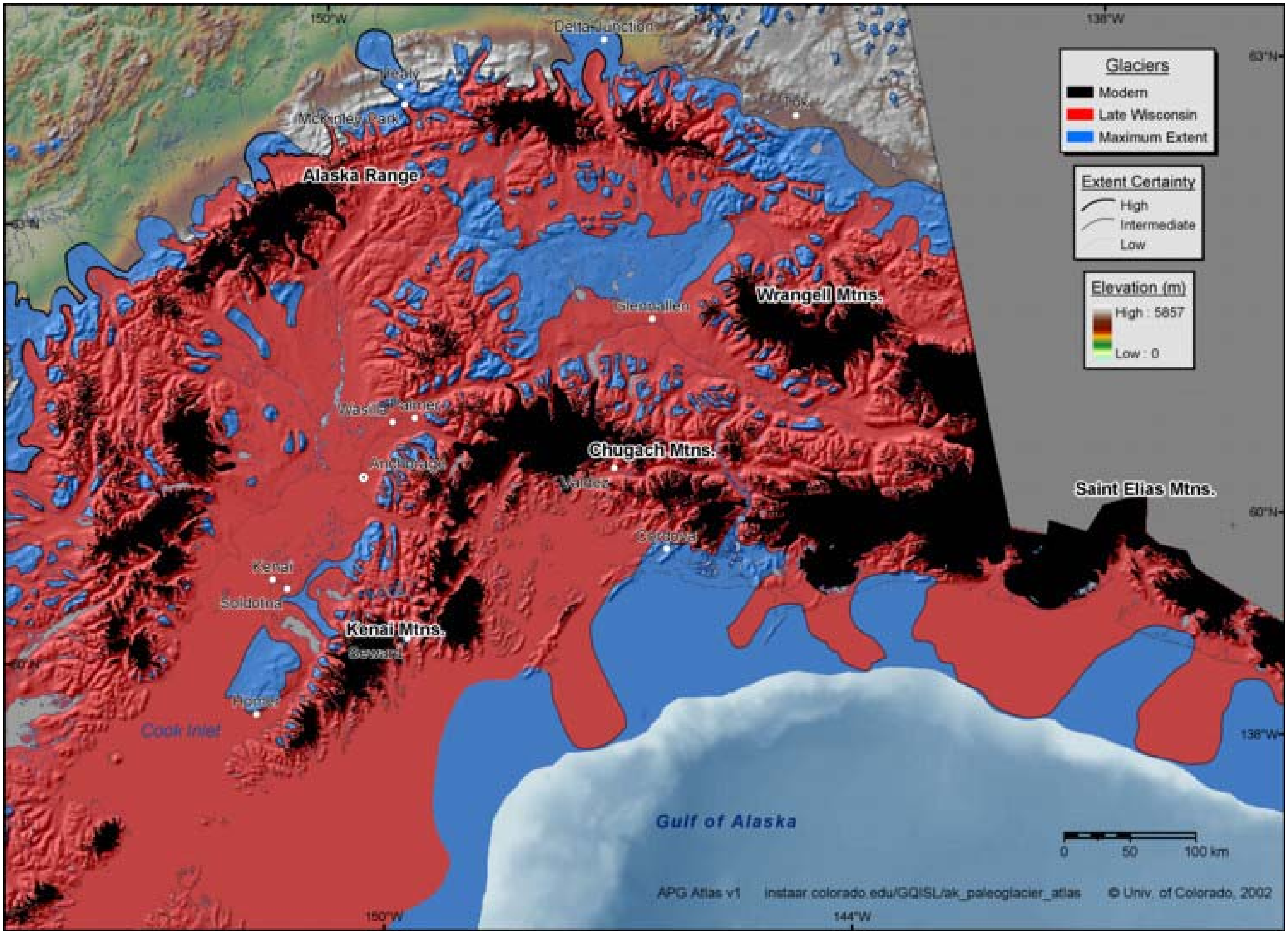

Figure F8. Seismic reflection data for the Gulf of Alaska (GoA) region relative to the drilling sites. Black lines = USGS or Industry acquired seismic profiles, red lines = 2008 R/V *Langseth* seismic profiles from the NSF ST. Elias Erosion and tectonics Project (STEEP), orange lines = 2011 Langseth Extended Continental Shelf seismic profiles, orange dots = Expedition 341 drill sites.

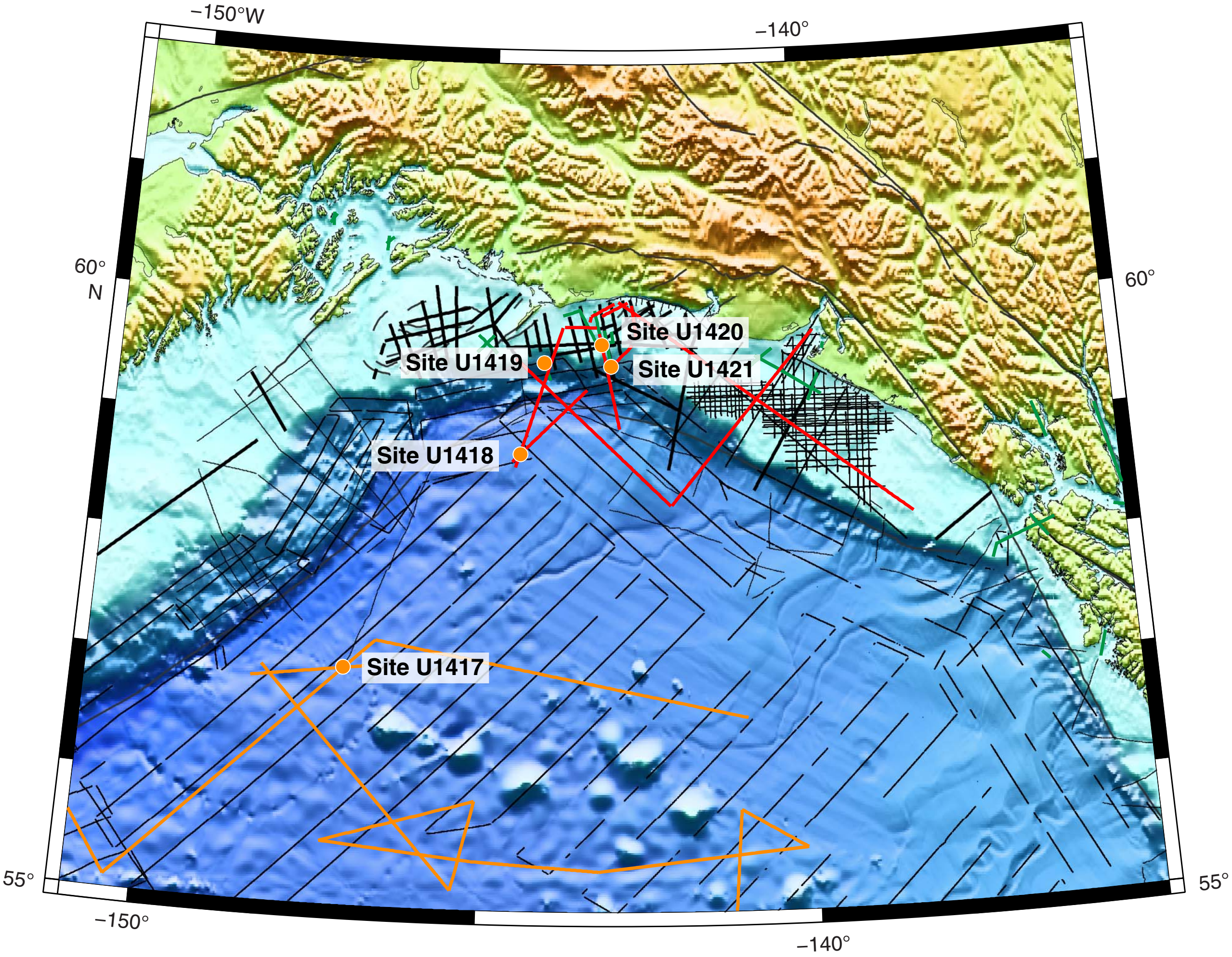

Figure F9. GOA-2505 seismic section, uninterpreted (top) and interpreted (bottom). Interpreted section shows structures BT4 and BT5, and key horizons (H1, H2, and H3). Colored horizons are regional horizons interpreted throughout the study area. Black horizons are interpreted locally to define glacial depositional sequences in the upper 2 s of the record. VE = vertical exaggeration. From Worthington et al. (2010).

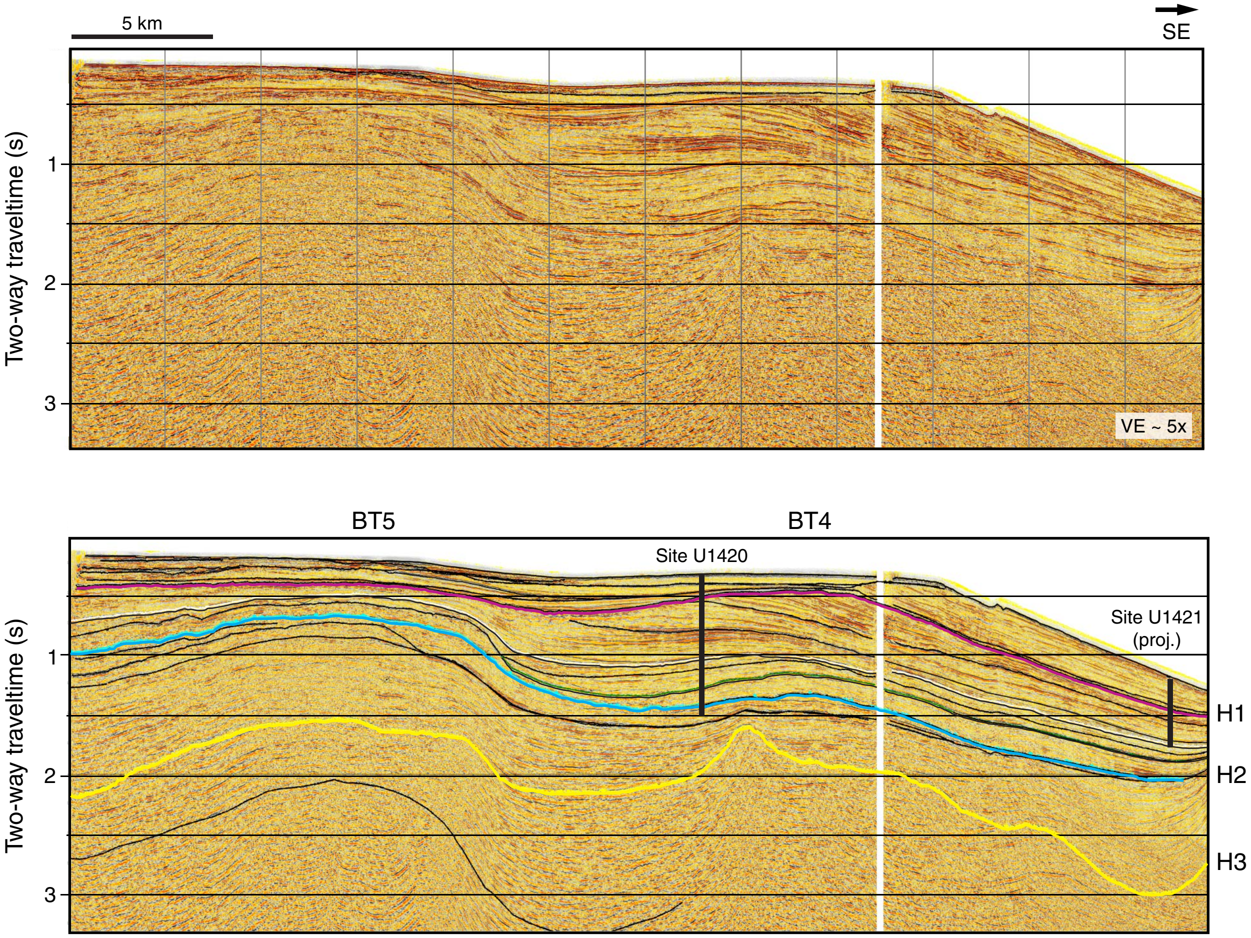

Figure F10. **A.** STEEP09 seismic line, uninterpreted (top) and interpreted (bottom), showing mappable horizons through the Bering Glacier shelf region. Targets for Site U1420 include Horizon H1, locally an angular unconformity at the base of glacial erosion surfaces, and Horizon H2, which marks the cessation of movement on the Pamplona Zone structures beneath the Bering Trough. Colored lines (H1–H5) are regional horizons interpreted throughout the study area. Black horizons (A–F) are interpreted locally to define glacial depositional sequences in the upper 2 s of the record. VE = vertical exaggeration assuming 1500 m/s sound velocity. BT1–BT4 = fault structures. **B.** Perspective view of the Bering Trough region, showing locations of the trough relative to active structures of the Pamplona Zone. YAK-NA = Yakutat-North America. Modified from Worthington et al. (2010).

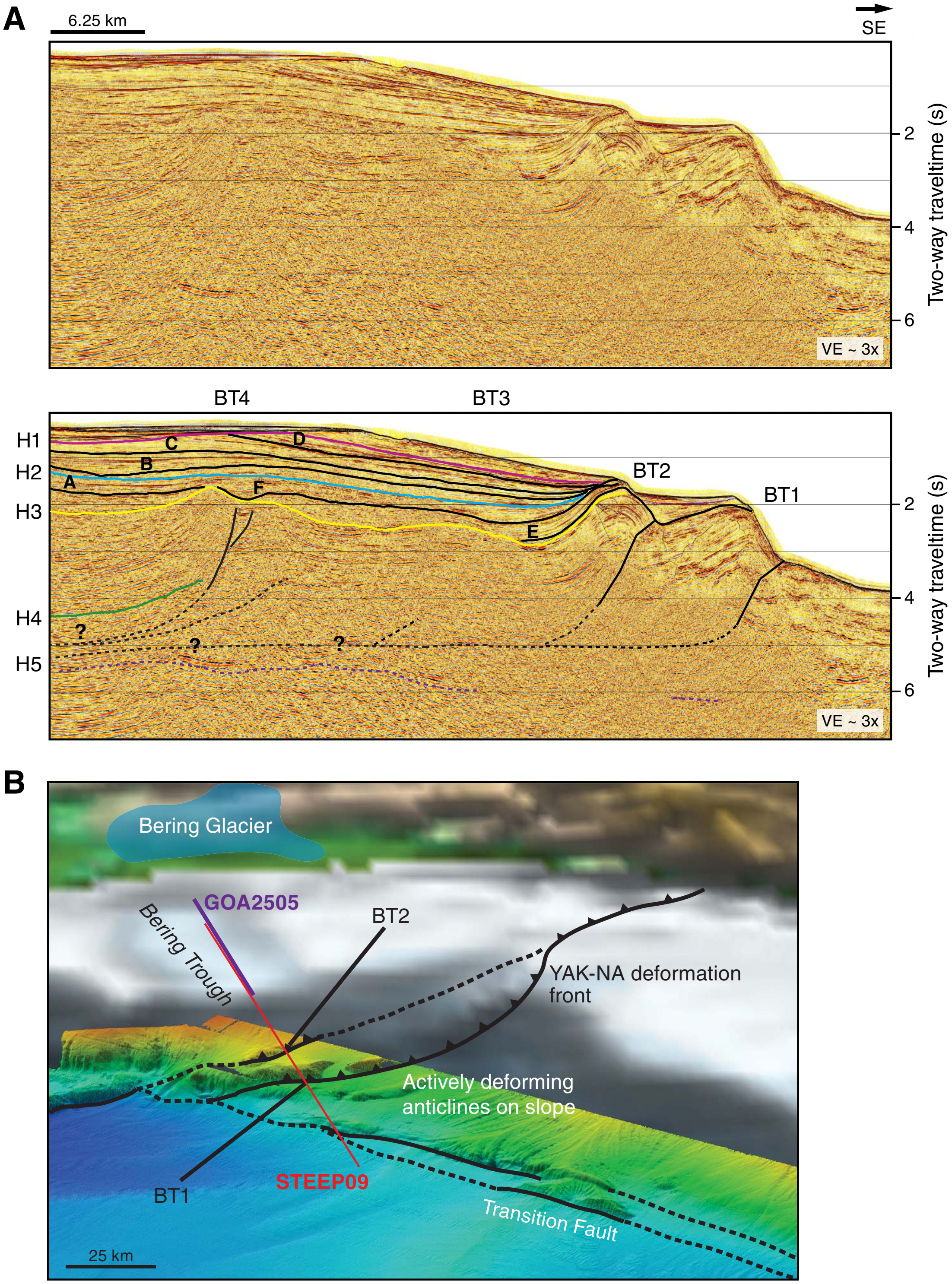

Figure F11. Glacial sequences and interpreted lithofacies of GOA-2505 seismic section based on glacial systems tracts at proposed drill sites. The Glacial Minimum Systems Tract (GMiST) includes sediment accumulated during interglacial periods. The Glacial Retreat Systems Tract (GRST) includes glacial sediment deposited at the glacial grounding-line, and the Glacial Maximum Systems Tract (GMaST) is composed of sediment deposited at the continental slope during glacial advance. Each proposed drill core should sample at least eight interglacial intervals with thicknesses up to 5 ms TWT. Sequence geometries indicate an overall reduction in shelf accommodation space over the past 2 m.y. Such a reduction in accommodation space could be eustatic in nature and influenced by fluctuations of the Cordilleran ice sheet. SB = seismic boundary. VE = vertical exaggeration. AK 1-1 to 1-9 = seismic stratigraphic Units 1–9. After Willems (2009).

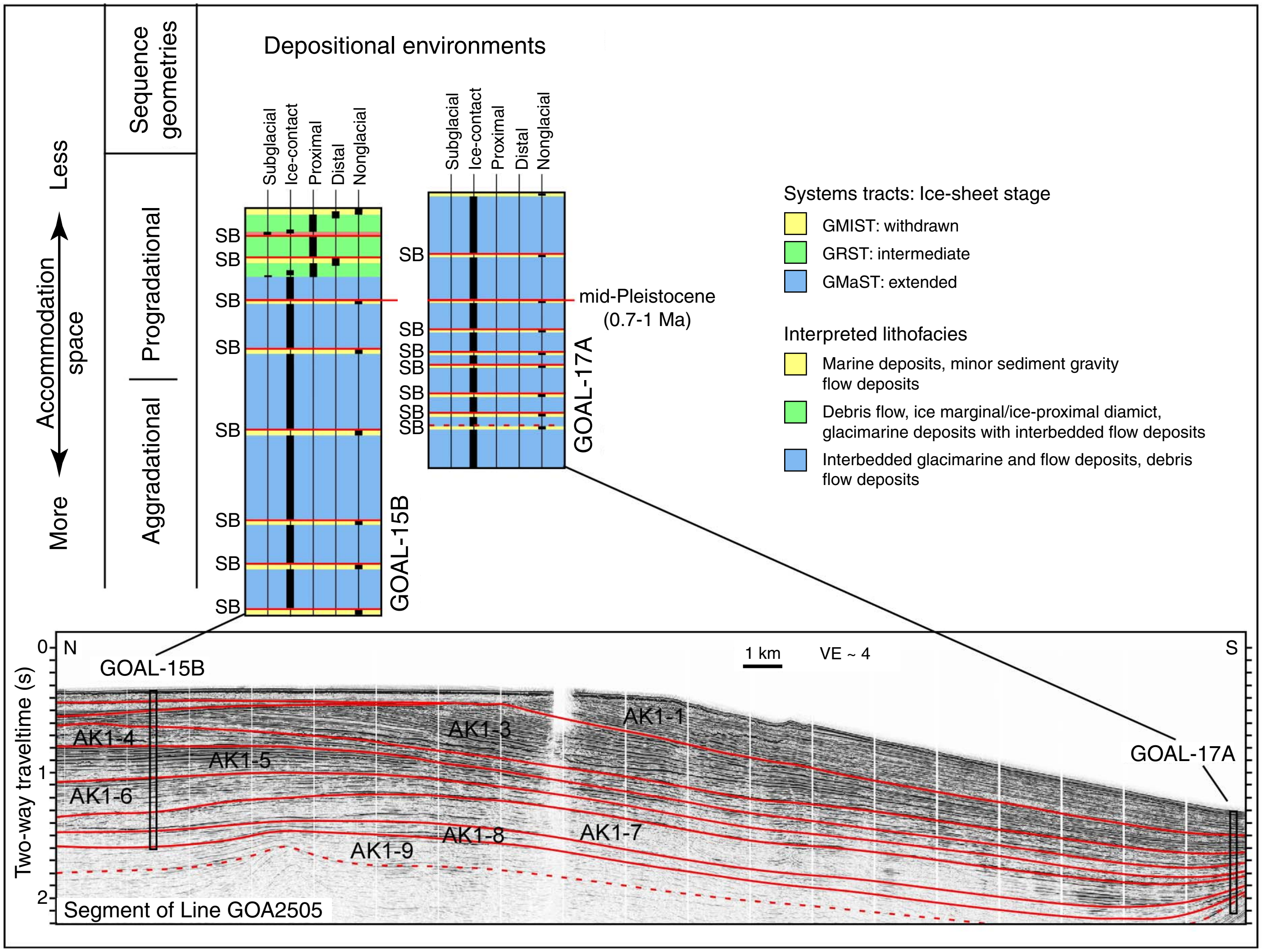

Figure F12. Seismic Profile GOA-2505. VE = vertical exaggeration. **A.** High-resolution seismic imaging of the Bering Trough showing a distinct change in margin architecture from tectonically to depositionally influenced at the labeled erosional unconformity. **B.** Interpretations for seismic Profile GOA-2505. Location of seismic profile shown in Figure F1. **C.** Schematic cross-section across frontal St. Elias wedge. Seds = Neogene sediments. Modified from Worthington et al. (2010).

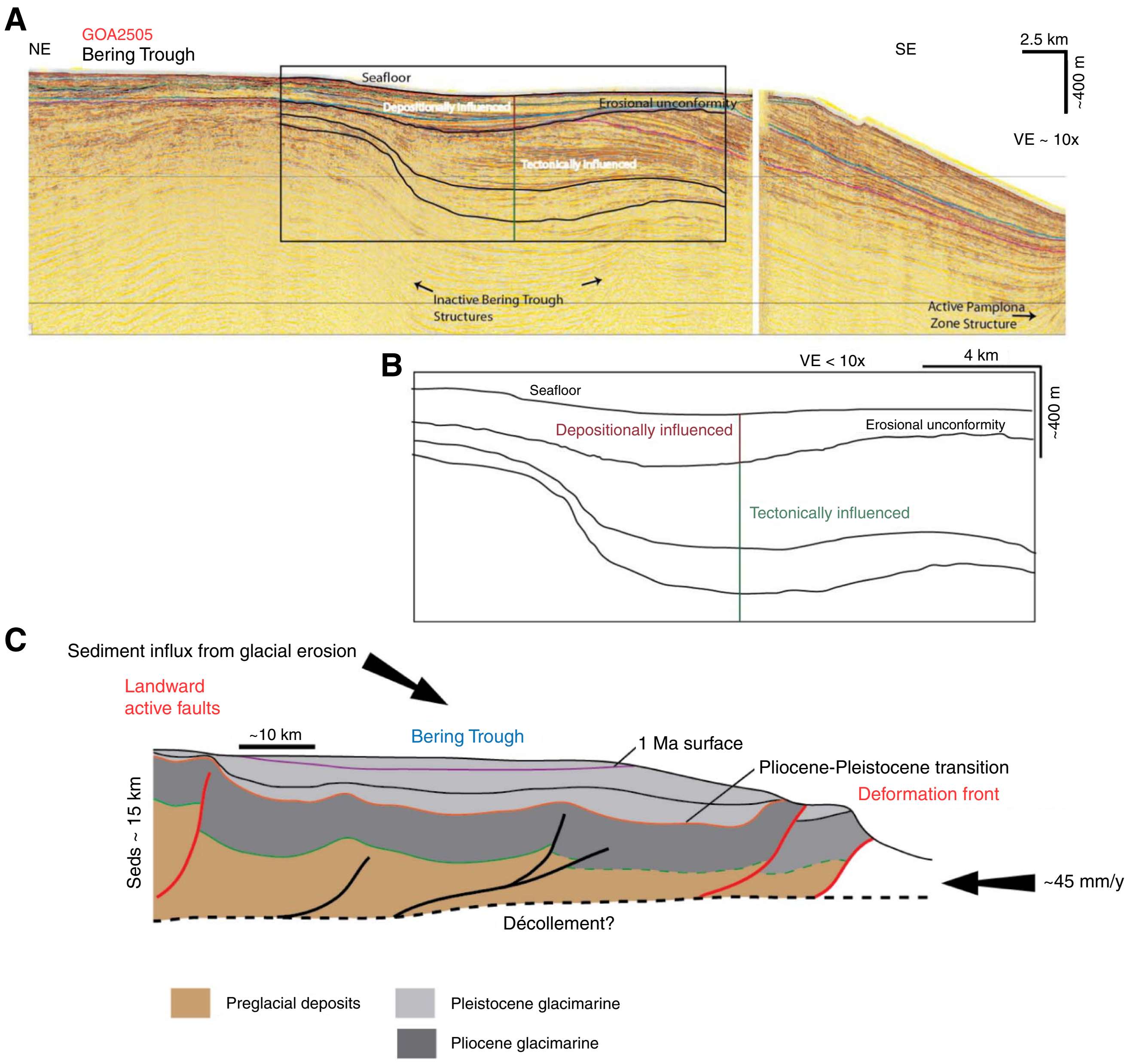

Figure F13. (**A**) High-resolution MCS Profiles GOA-3101 (top) and GOA-3102 (bottom) and (**B**) CHIRP images (collected coincident with MCS profiles) over Khitrov bank. Active deformation and faulting at seafloor soles into a transtensional flower structure, and Site U1419 is located upslope of these structures. Higher amplitude reflectors correspond with diamict in Core EW0408 85JC (located at the landward end of seismic Profile GOA3101) (Davies et al., 2011). LGM = Last Glacial Maximum. Proposed Expedition 341 sites KB-1A and KB-2A (Site U1419) shown with proposed drilling depths. Vertical depth scale in meters based on seismic velocity of 2000 m/s.

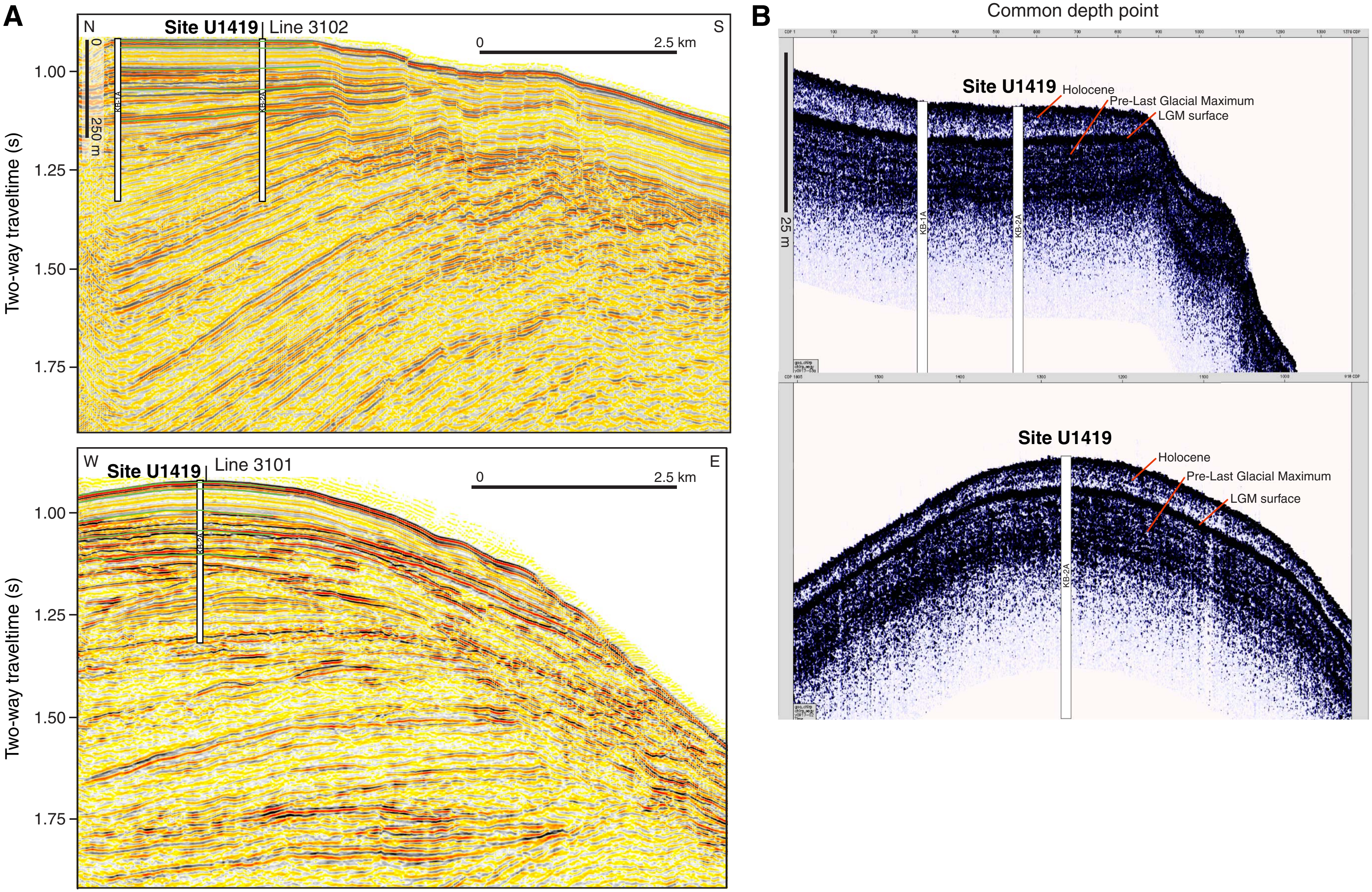

Figure F14. Lithology and age control, DSDP Site 178. Modified from Lagoe et al. (1993). Partial seismic section from Line 13 of 1989 USGS Survey F689 (Fig. F6). IRD = ice-rafted debris, Ja = Jaramillo, OI = Olduvai. GI A, GI B, GI C = Glacial Intervals A, B, and C. MPW = mid-Pliocene warm period. $^{40}Ar/^{39}Ar$ ages from Hogan et al. (1978). Magnetic polarity stratigraphy from von Huene et al. (1973). Modified from Reece et al. (2011).

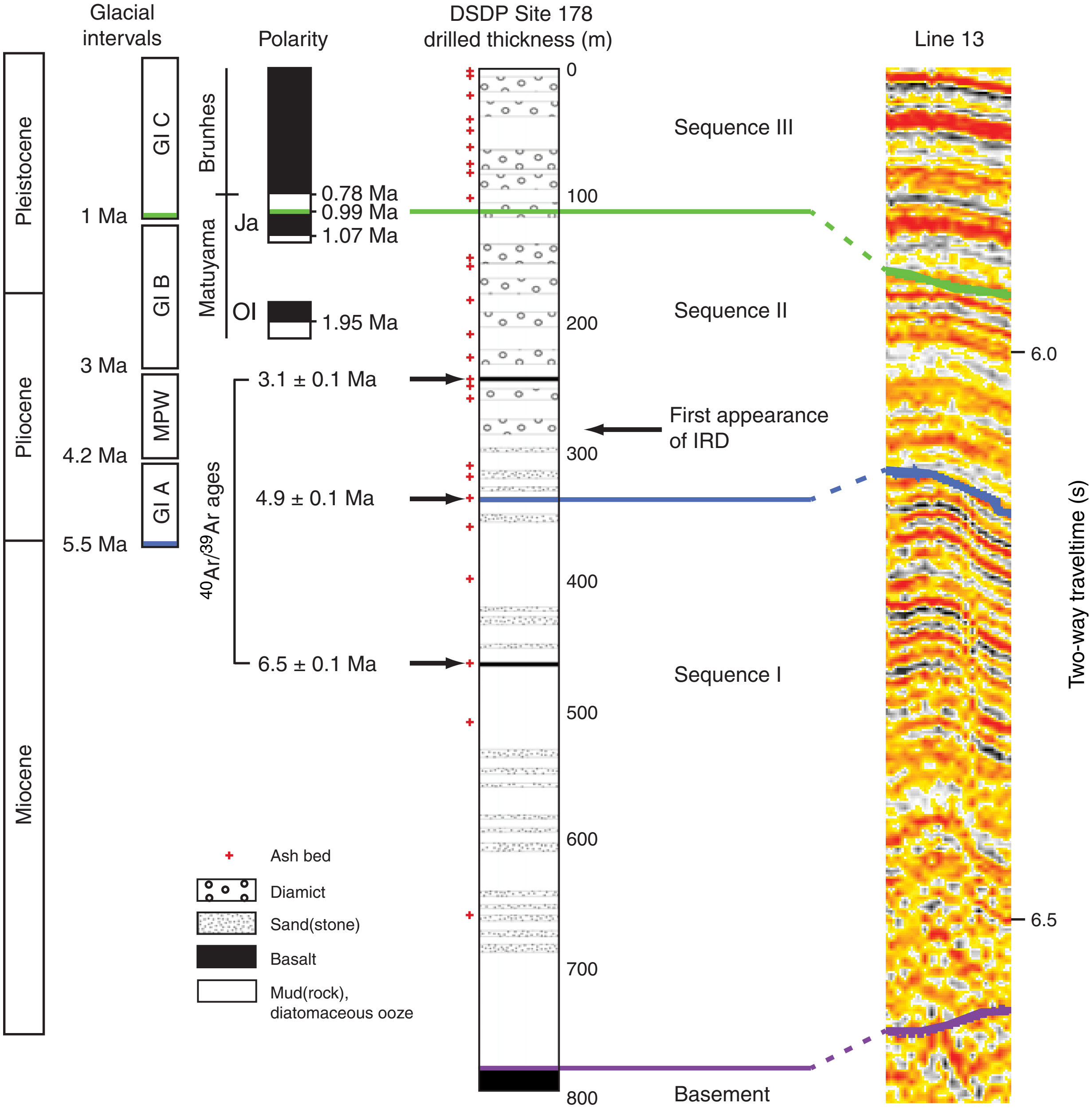

Figure F15. Seismic reflection Line 13 from 1989 USGS Survey F689 showing sequences newly defined by Reece et al. (2013), and approximate correlation to DSDP Site 178. See Figure **F6** for line location. Vertical exaggeration (VE) assumes 2000 m/s sediment acoustic velocity. Modified from Reece et al. (2011).

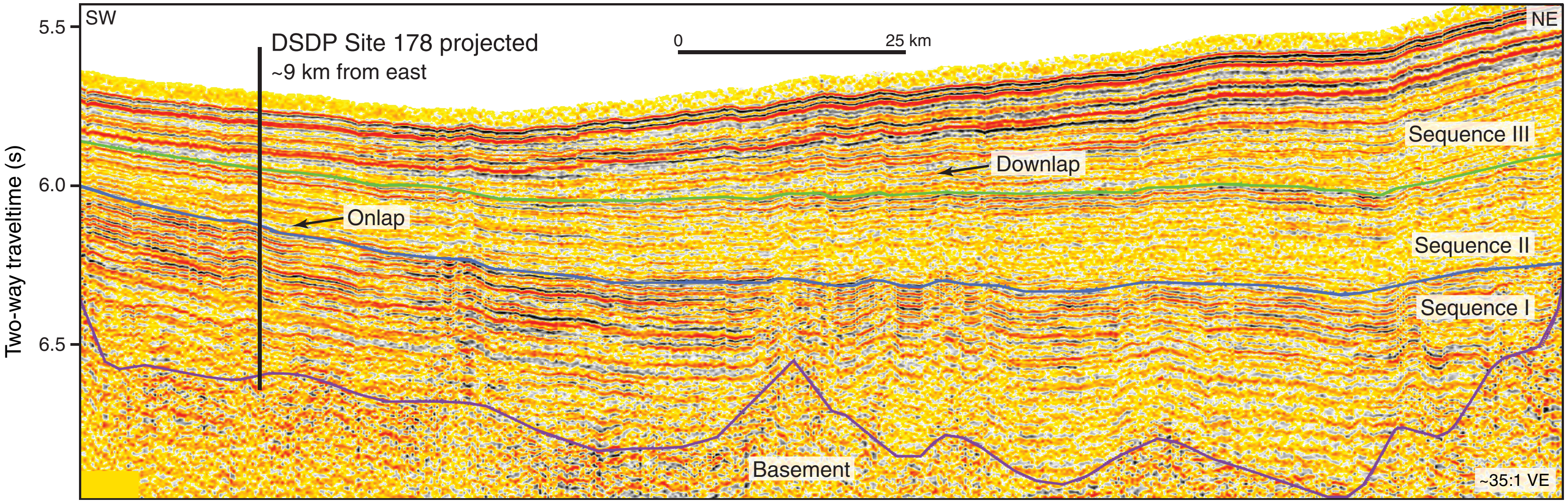

Figure F16. Two-way traveltime thickness maps. **A.** Sequence I, Pacific plate formation prior to ~5.5 Ma. **B.** Sequence II, ~5.5–1 Ma. **C.** Sequence III, ~1 Ma to present. **D.** Seismic reflection data track lines used in calculation. ASV = Alsek Sea Valley, BT = Bering Trough, KT = Kayak Trough, YSV = Yakutat Sea Valley. From Reece et al. (2011).

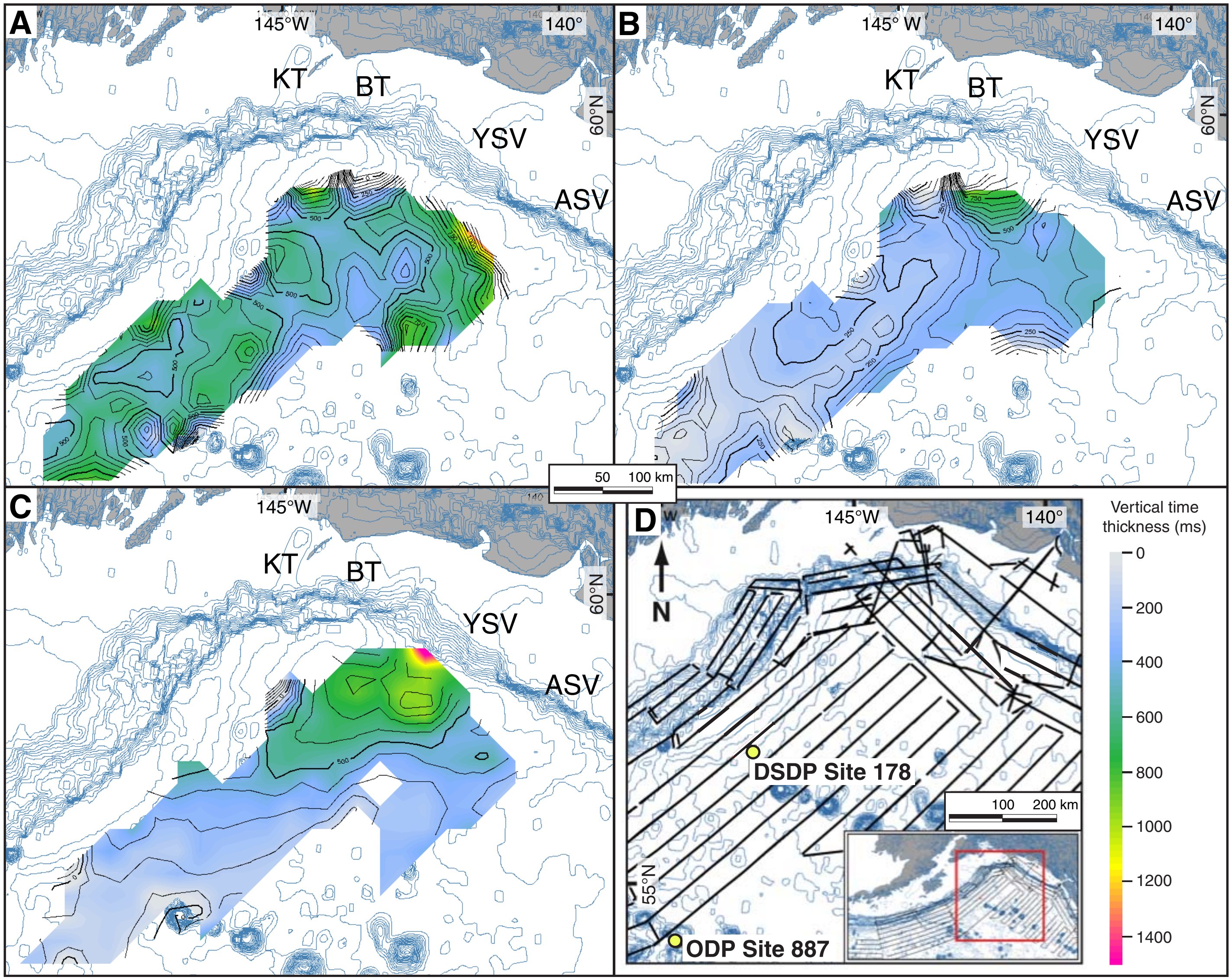

Figure F17. Schematic illustration of Surveyor Fan and southern Alaska margin sedimentary evolution over the last ~20 m.y. Gray area on seafloor represents the growth and evolution of the Surveyor Fan by channel-related processes. Red asterisk denotes the approximate location of Alsek Sea Valley through time. **A.** ~20–5.5 Ma. **B.** ~5.5 Ma. **C.** ~1 Ma. **D.** Last Glacial Maximum (LGM)–present. AT = Aleutian Trench, FWF = Fairweather Fault, IRD = ice-rafted debris, NA = North America, PSC = proto-Surveyor Channel, TF = transition fault, YAK = Yakutat Terrane. From Reece et al. (2011).

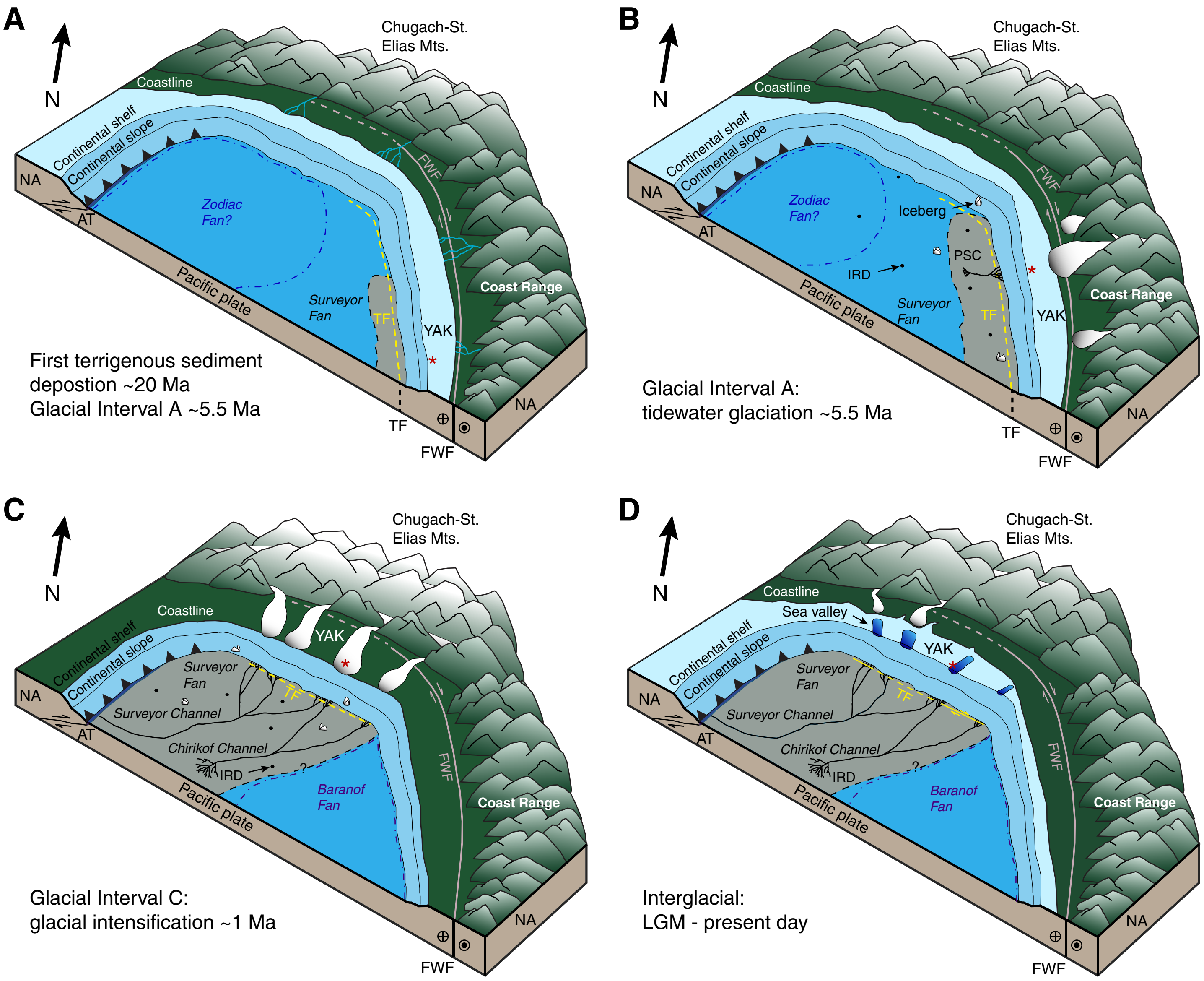

Figure F18. Lithofacies and paleoceanographic data from Core EW0408-85JC. **A.** Computed tomography (CT)-derived bulk density data. **B.** Opal (periods of lamination are delineated below the record by green bars). **C.** Planktonic $\delta^{18}O$ (dark blue = *Neogloboquadrina pachyderma*, light blue = *Globigerina bulloides*). **D.** Benthic $\delta^{18}O$ (solid squares = *Uvigerina peregrina*, open squares = *Cibicidoides wuellerstorfi* + 0.64, crossed squares = *Nonionella* sp. + 0.10). **E.** Planktonic-benthic $\delta^{18}O$ (light pink squares). **F.** Planktonic $\delta^{13}C$ (purple = *N. pachyderma* sinistral, pink-red = *G. bulloides*). **G.** Benthic $\delta^{13}C$ (orange = *U. peregrina* + 0.20, orange open canted triangles = *C. wuellerstorfi*). For global context these data are presented next to (**H**) the Greenland ice core $\delta^{18}O$ record (NGRIP; gray) (Andersen et al., 2006; Rasmussen et al., 2006; Svensson et al., 2006) and (**I**) the relative sea level (RSL) curve compiled in Sidall et al. (2009) (open blue squares). Timing of the North Atlantic Bølling-Allerød (B-A) and Younger Dryas (Y-D) climate anomalies is highlighted in yellow and blue, respectively, as well as meltwater pulse (MWP) 1A (yellow, coeval with the B-A), and 1B (green). From Davies et al. (2011).

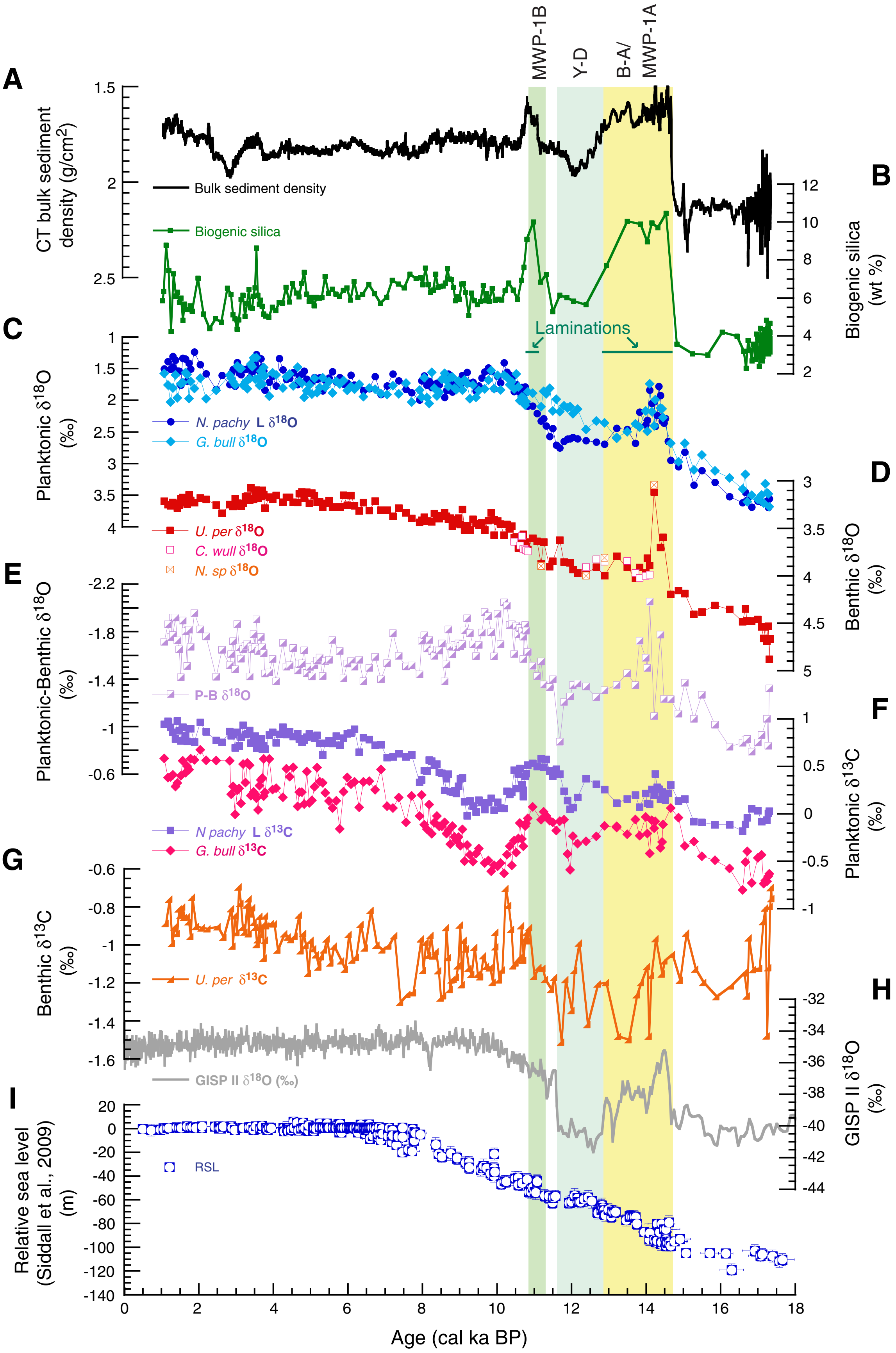

Figure F19. 5 m.y. time-averaged paleomagnetic field showing quasistationary nondipole features (Gubbins and Kelly, 1993).

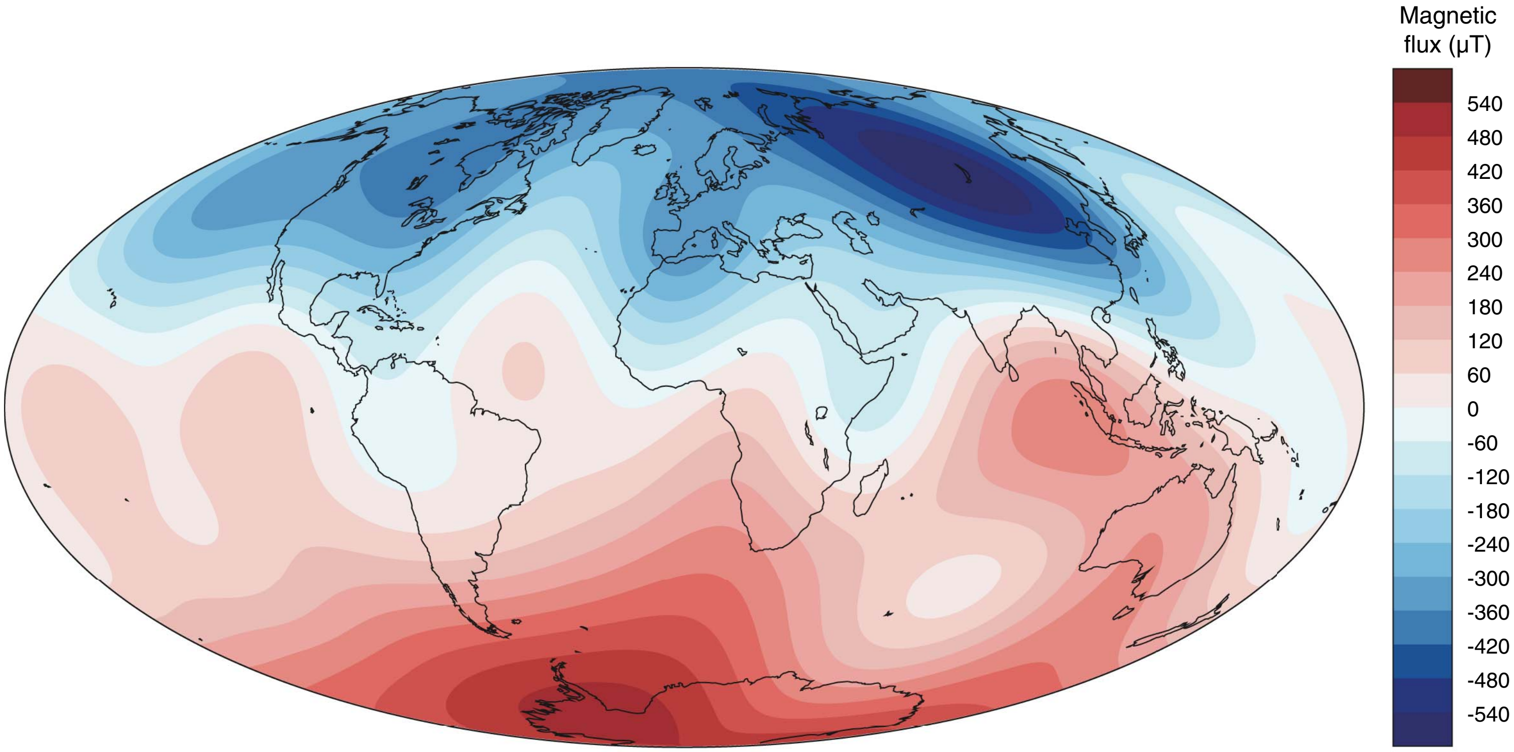

Figure F20. Expedition 341 lithology summary.

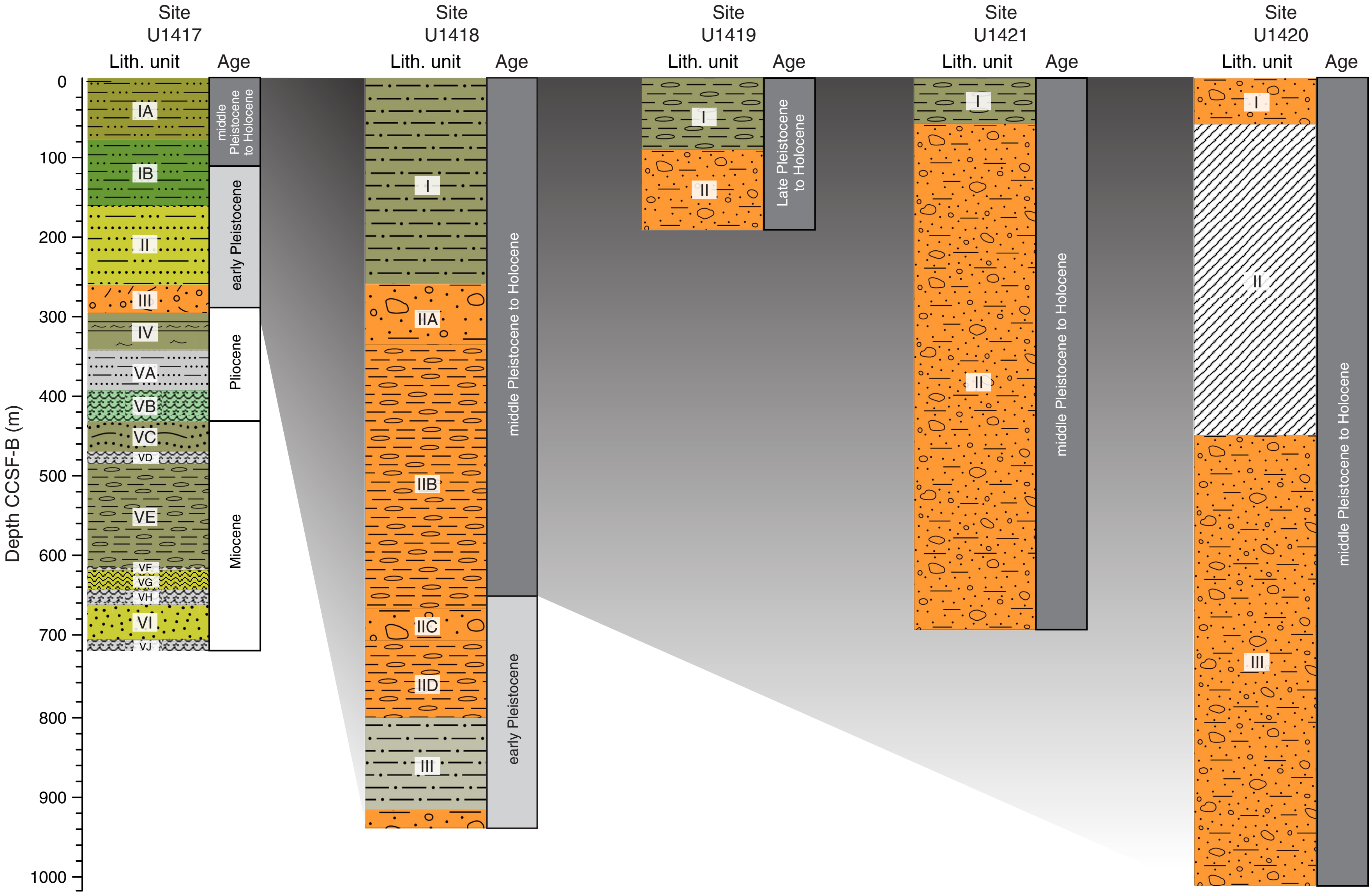

Figure F21. Representative topography through the IODP Expedition 341 drill sites, showing the principle lithologies at each site along with chronologies and accumulation rates in cm/k.y. Depths are in meters of core composite depth below the seafloor (CCSF-B) that approximates the drilled interval. B/M= Brunhes/Matuyama. G/M= Gauss/Matuyama. Vertical exaggeration ~18×.

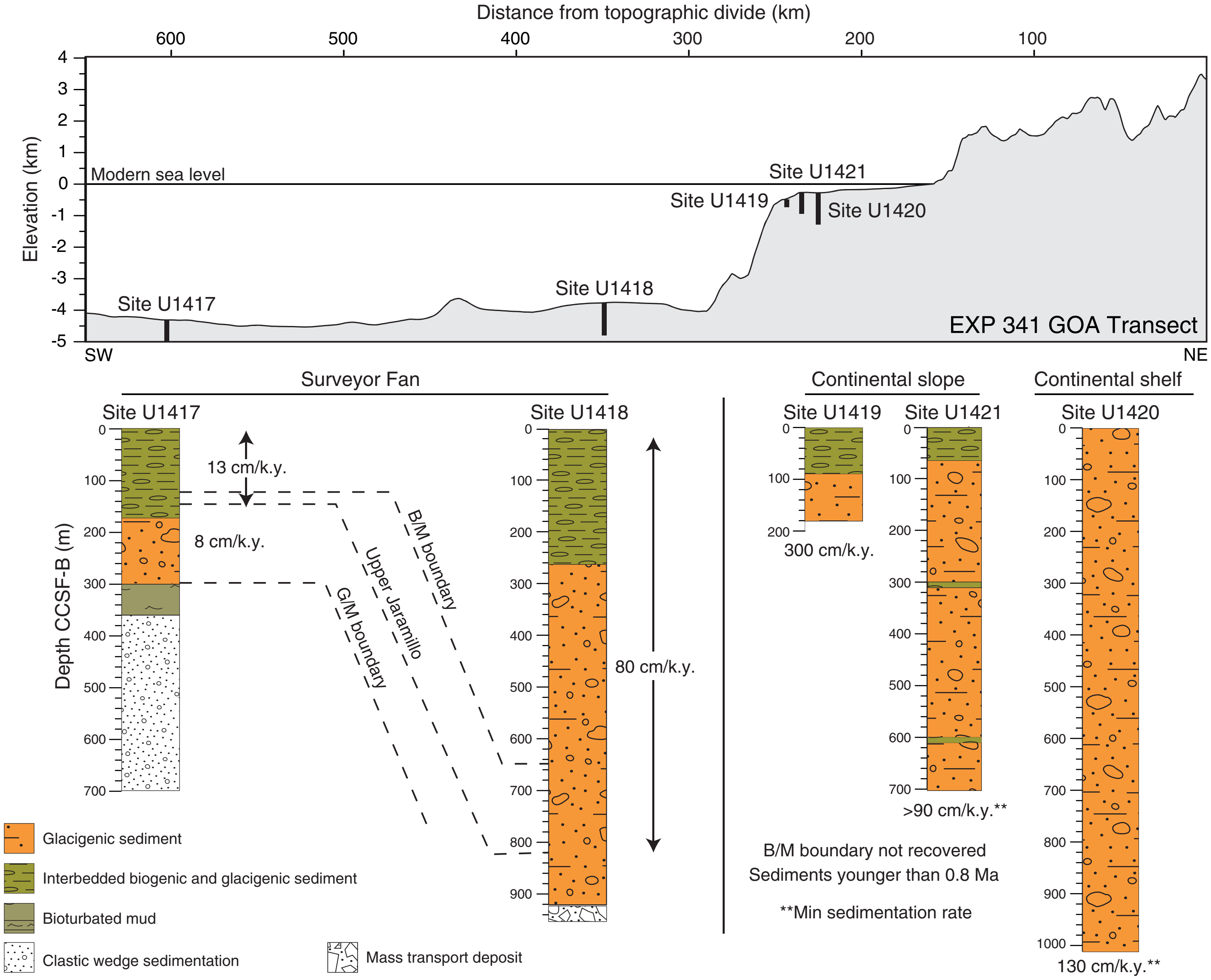

Figure F22. Ternary diagram showing the average abundances of the main lithology types of clasts larger than 2 mm in diameter at each Expedition 341 site.

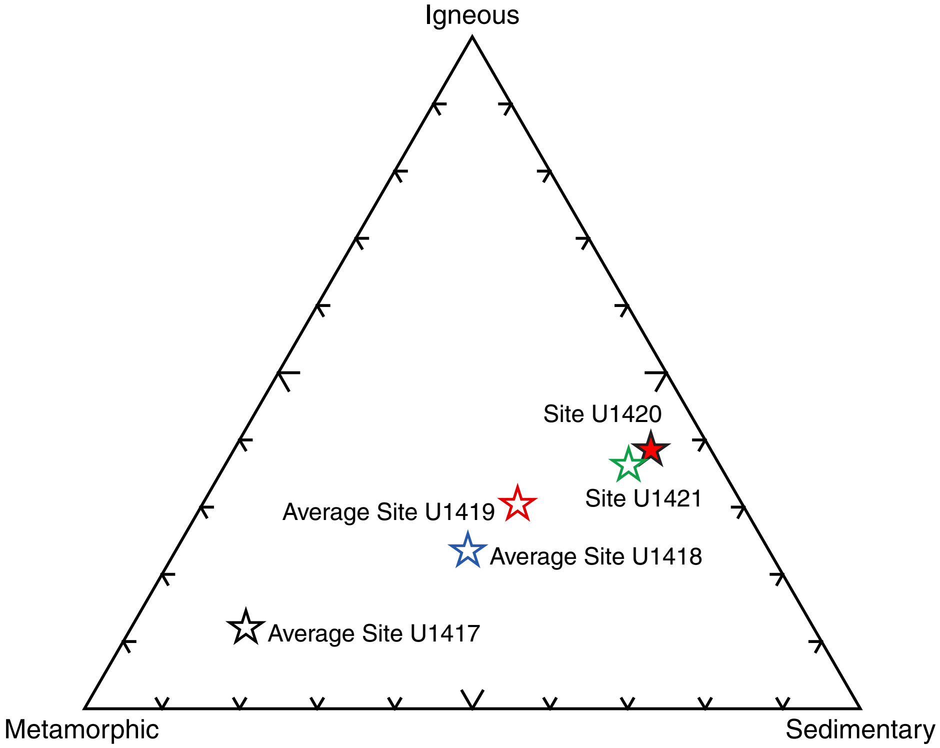

Figure F23. Expedition 341 velocity-porosity summary. PWC = *P*-wave caliper, PWL = *P*-wave logger. Blue and red lines after Erickson and Jarrard (1998) indicate global velocity-porosity relationships under normal-consolidation and high-consolidation conditions, respectively.

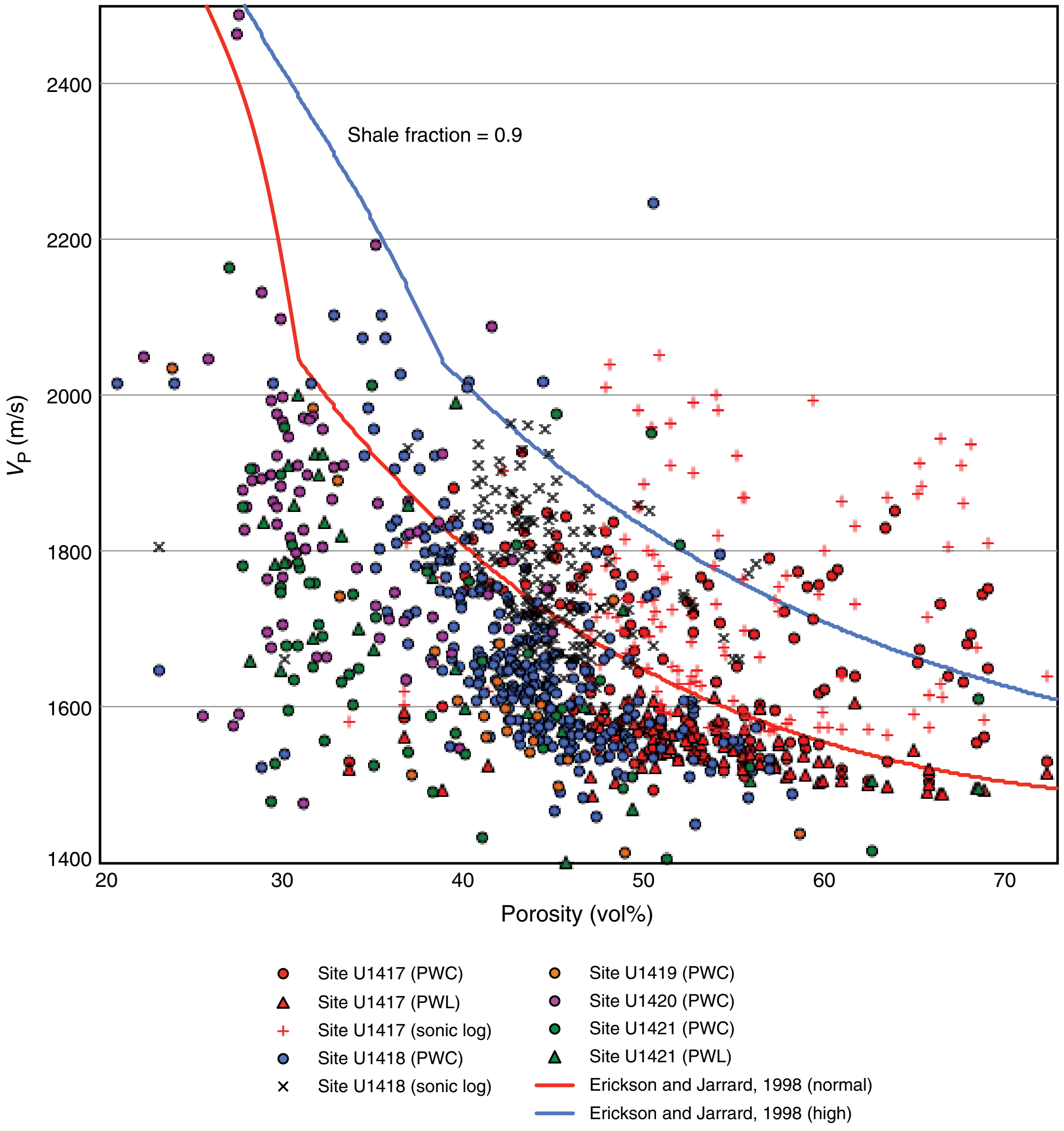

Figure F24. Uninterpreted and interpreted versions of MGL1109MCS14 showing location of Site U1417. Seismic sequences I–III are from Reece et al. (2011), and subsequences are broken out as seismic units for the purpose of core-log-seismic integration.

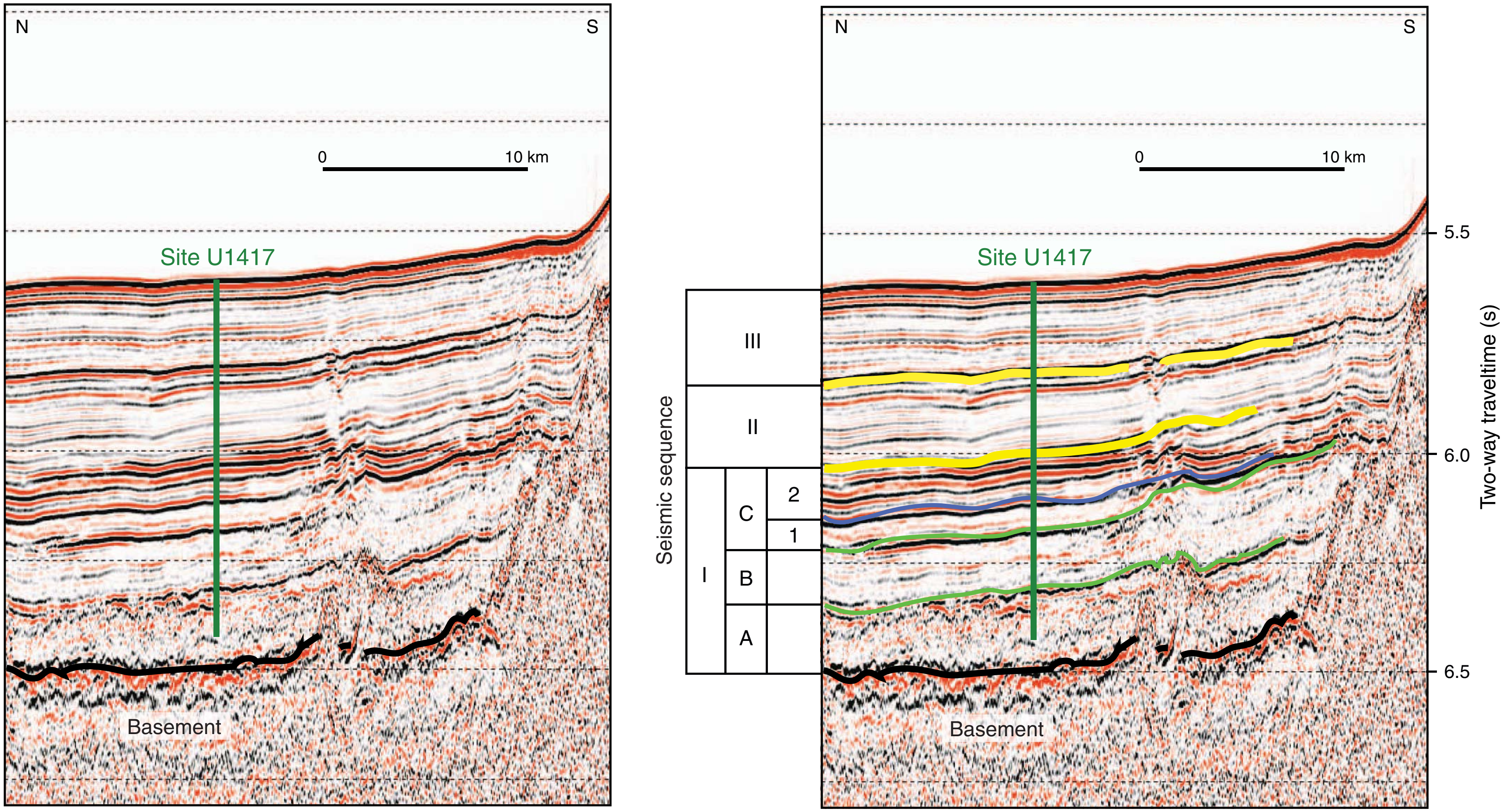

Figure F25. Interpreted STEEP07 seismic section showing seismic facies of Sequence III on the proximal Surveyor Fan and buried mass transport deposit (MTD; Reece et al., 2012). Proposed drill sites for the proximal fan penetrate all of Sequence III and terminate in a proposed MTD (Surveyor Slide). This line is oblique to Line F-6-89-Line26 and reveals a portion of the abandoned "Bering Channel" and erosion within the Aleutian Trench Channel. Modified from Reece (2012).

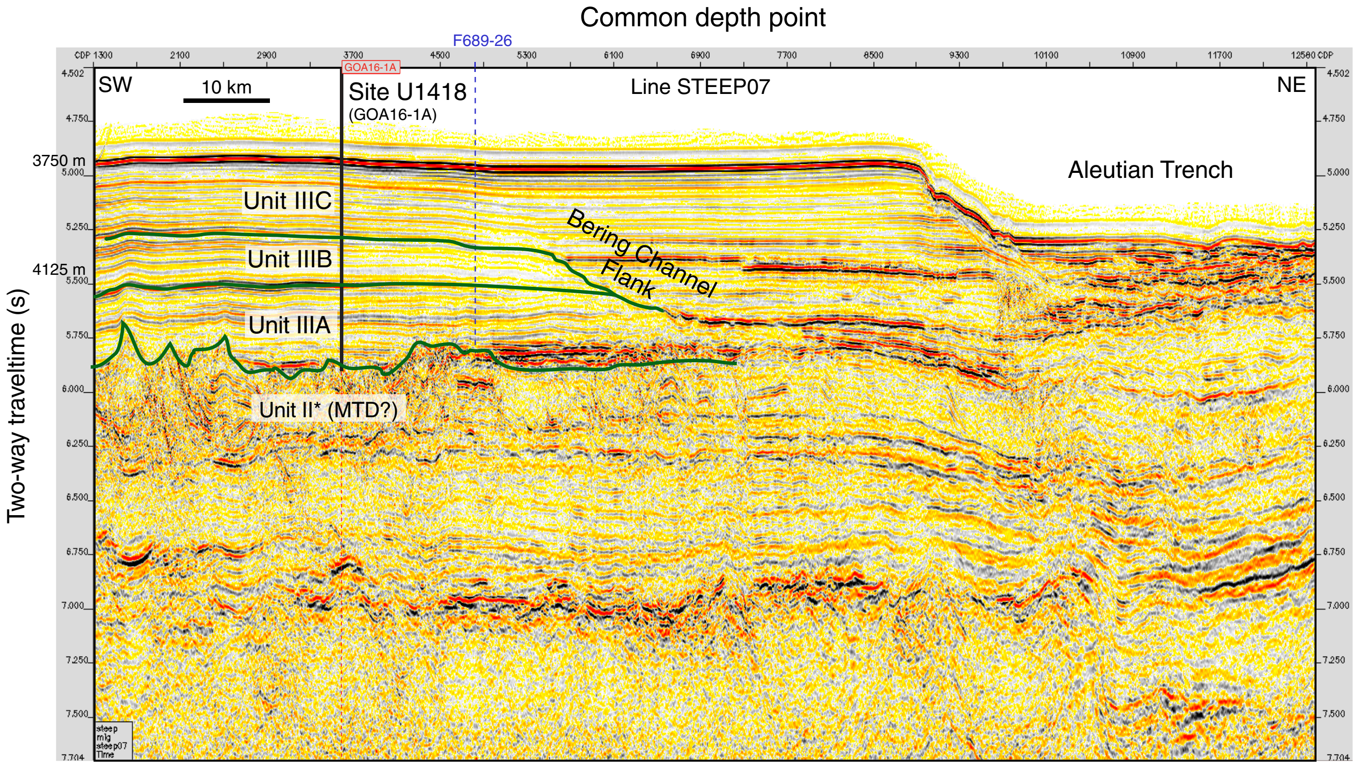

Figure F26. **A.** From left to right, a seismic transect from MGL1109 Line 1 toward the east, to MGL1109 Line 14 heading northeast, to MGL1109 Line 13 heading east. Seismic sequences can be mapped from Site U1417 to the Surveyor Channel. VE = vertical exaggeration. **B.** Multibeam bathymetry map showing location of Site U1417, DSDP Site 178, and seismic profiles relative to the Surveyor Channel, Kodiak-Bowie Seamounts, Aleutian Trench, and Kodiak Island, Alaska.

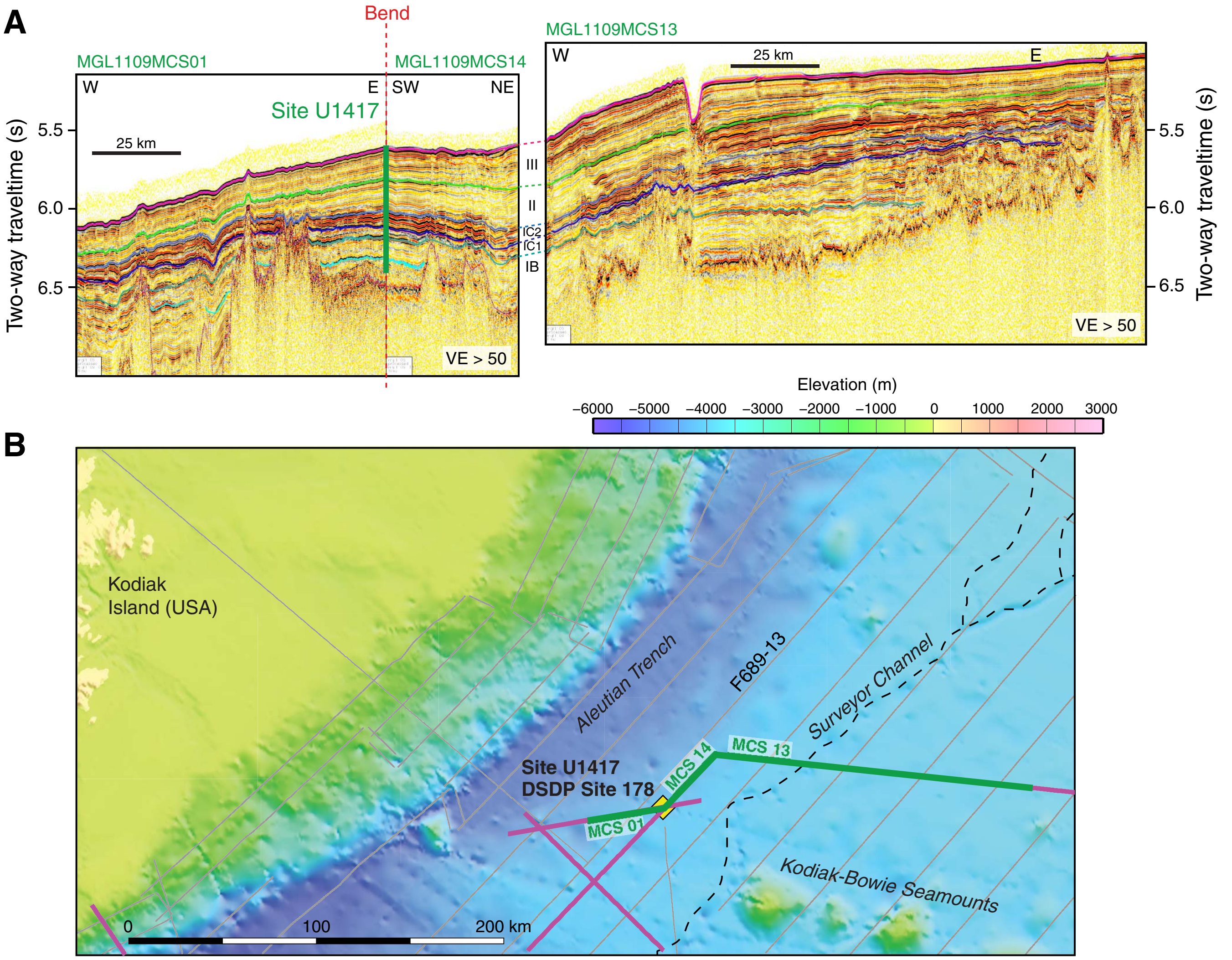

Figure F27. Core recovery, Site U1417.

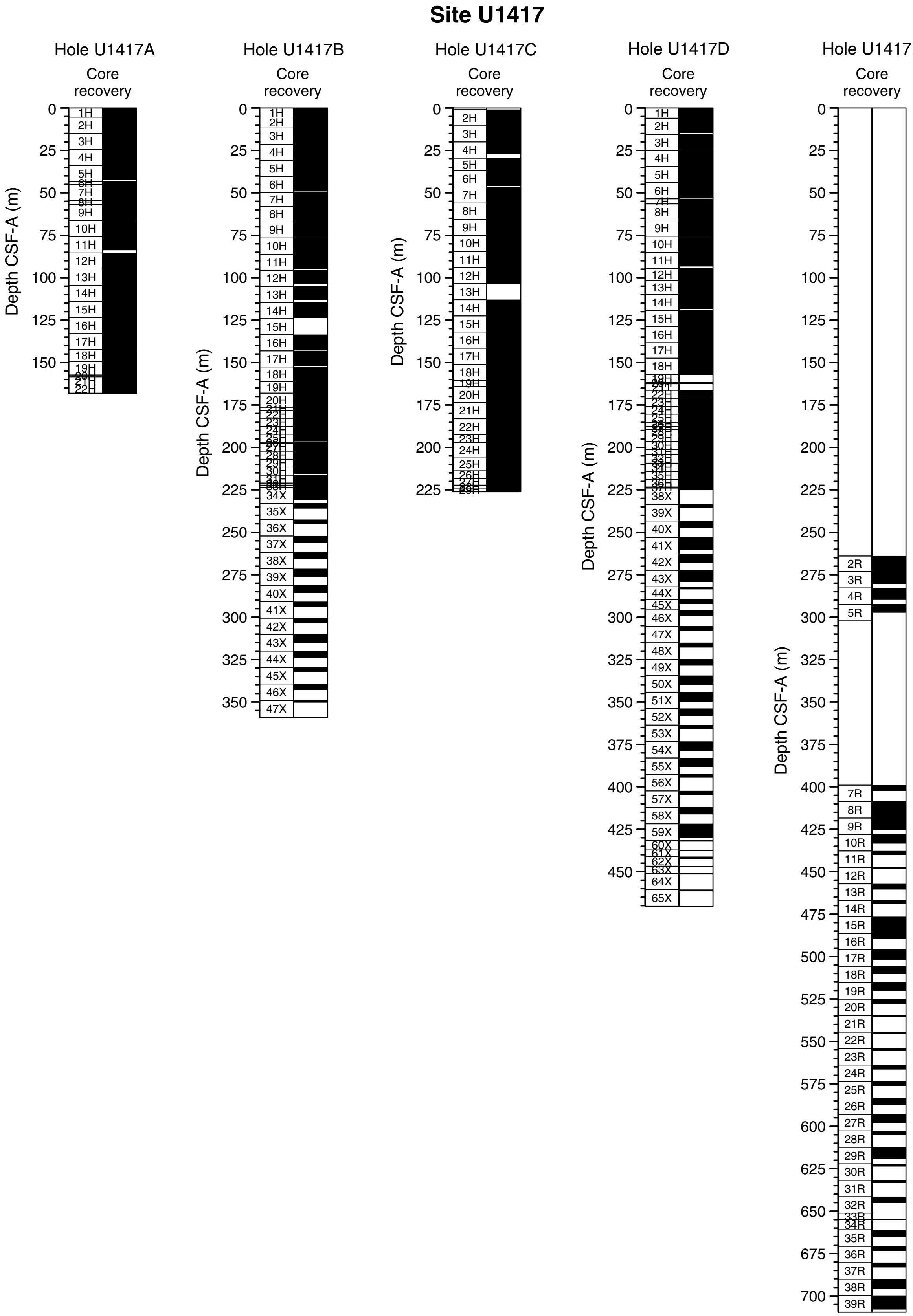

Figure F28. Site U1417 lithostratigraphic units and major lithologies used to define the lithostratigraphy, including ash and sediment containing volcaniclastic components, lonestones (>2 mm), diamict (ice-rafted interpretation), biosiliceous ooze, diamict (gravity flow interpretation), interbedded sand or silt with mud, and sand or silt beds. Data from all five holes were combined to produce a stratigraphic column showing the mid-depth location of each lithostratigraphic unit in the overall sedimentary sequence. Solid lines show where Neogene epoch boundaries coincide, or are within 10 m of a measured paleomagnetic reversal; dashed line separates the uncertain location of epoch boundaries estimated from the shipboard age model. Paleomagnetic age reversals in Ma are displayed to the right of the chronostratigraphic column.

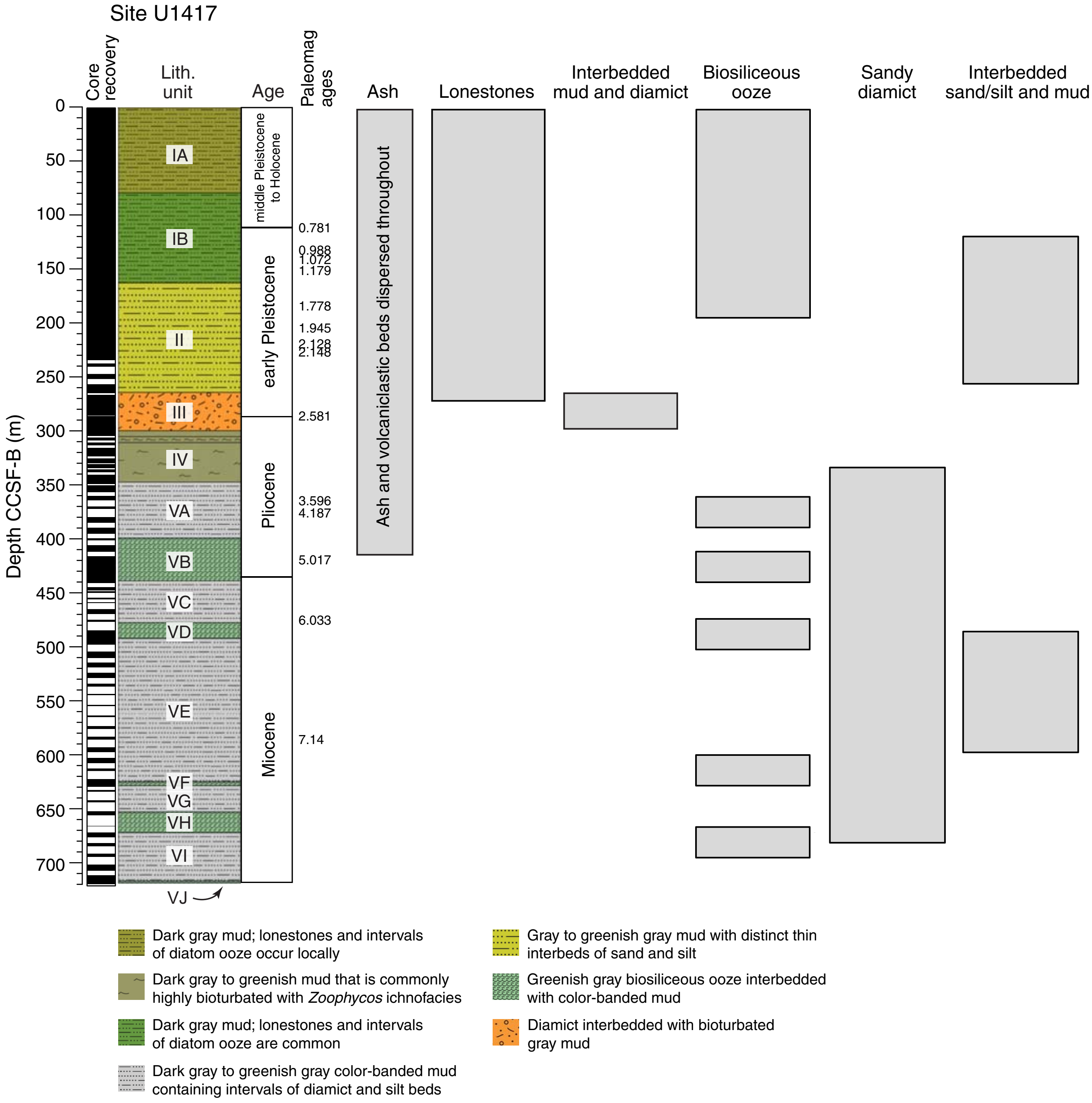

Figure F29. Diagram illustrating common relationships between lithology, clast count, and physical properties at the lithostratigraphic Subunit IB–Unit II transition (Sections 341-U1417C-17H-3A through 18H-1A). Decreases in magnetic susceptibility, gamma ray attenuation (GRA) bulk density, and natural gamma radiation, combined with increases in color reflectance index, highlight the location of diatom ooze. Mafic-rich sand corresponds to an increase in magnetic susceptibility, whereas volcanic ash dominated by glass shards shows no change in magnetic susceptibility. Photomicrographs of smear slides to right of the figure illustrate major lithologies present over specific intervals.

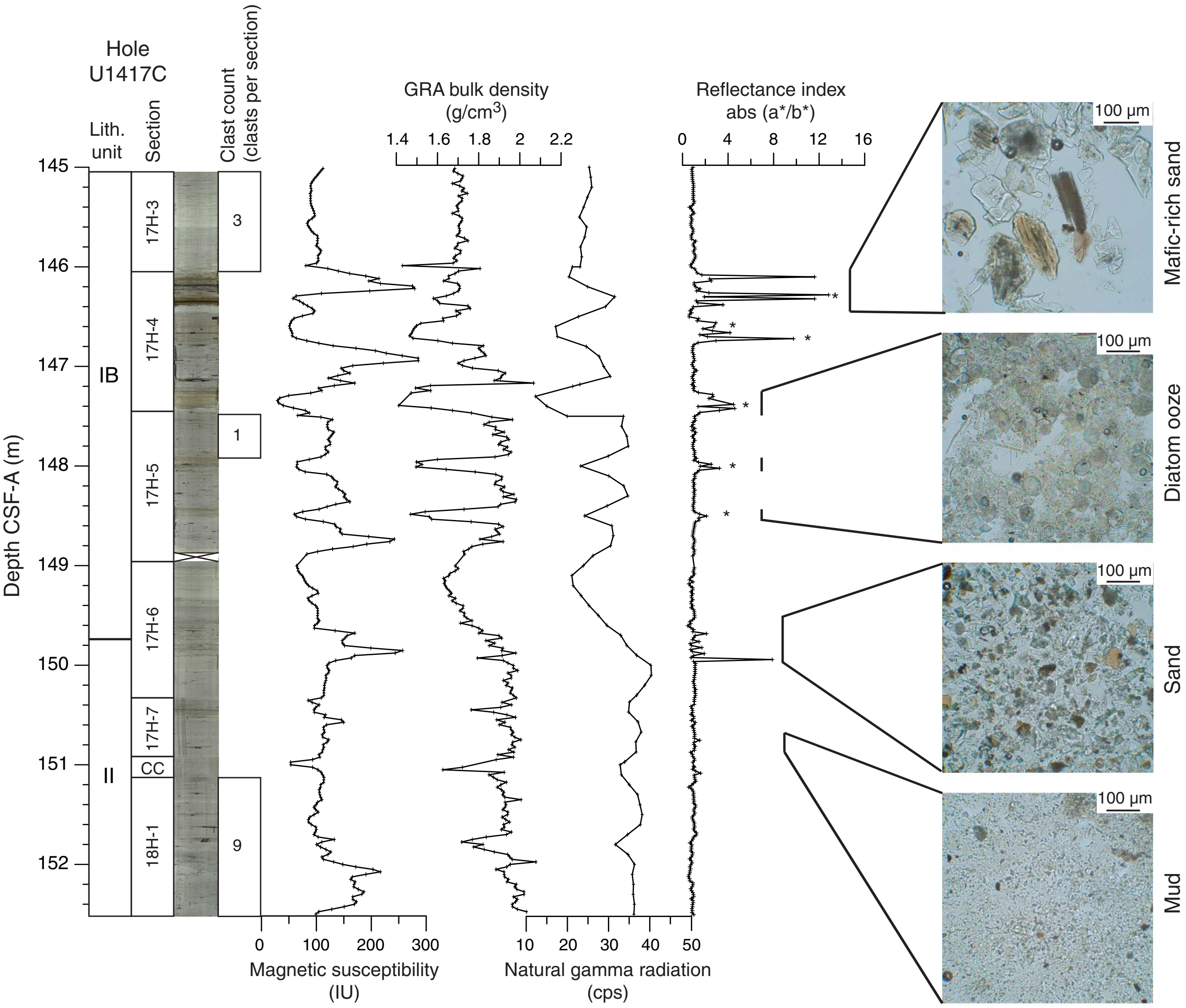

Figure F30. Micropaleontological and paleomagnetic age datums, micropaleontological group abundances, and rank abundances of important paleoenvironmental indicators, Site U1417. Data are a composite of Holes U1417A–U1417E. Abundance: D = dominant, A = abundant, C = common, F = few, R = rare, P or X = present, B = barren. **A.** Paleomagnetic data with chron boundary ages (JM = Jaramillo, OD = Olduvai). **B.** Biostratigraphic zones and boundary ages from diatoms, radiolarians, and planktonic foraminifers. **C–F.** Group abundances for (C) diatoms, (D) radiolarians, (E) planktonic foraminifers, and (F) benthic foraminifers. **G, H.** Rank abundances of (G) cold-water indicating diatom taxa and (H) litoral and neritic diatom taxa plotted using the highest abundance rank of individual species abundances within each species suite estimated from the number of valves per field of view. **I.** Rank abundances of cold-water radiolarian taxa estimated from the proportional abundances of cold-water species in the total radiolarian assemblage. **J.** Rank abundance of dextral coiling *Neogloboquadrina pachyderma*, a warm-water indicator, estimated from its proportional abundance in the total foraminiferal assemblage.

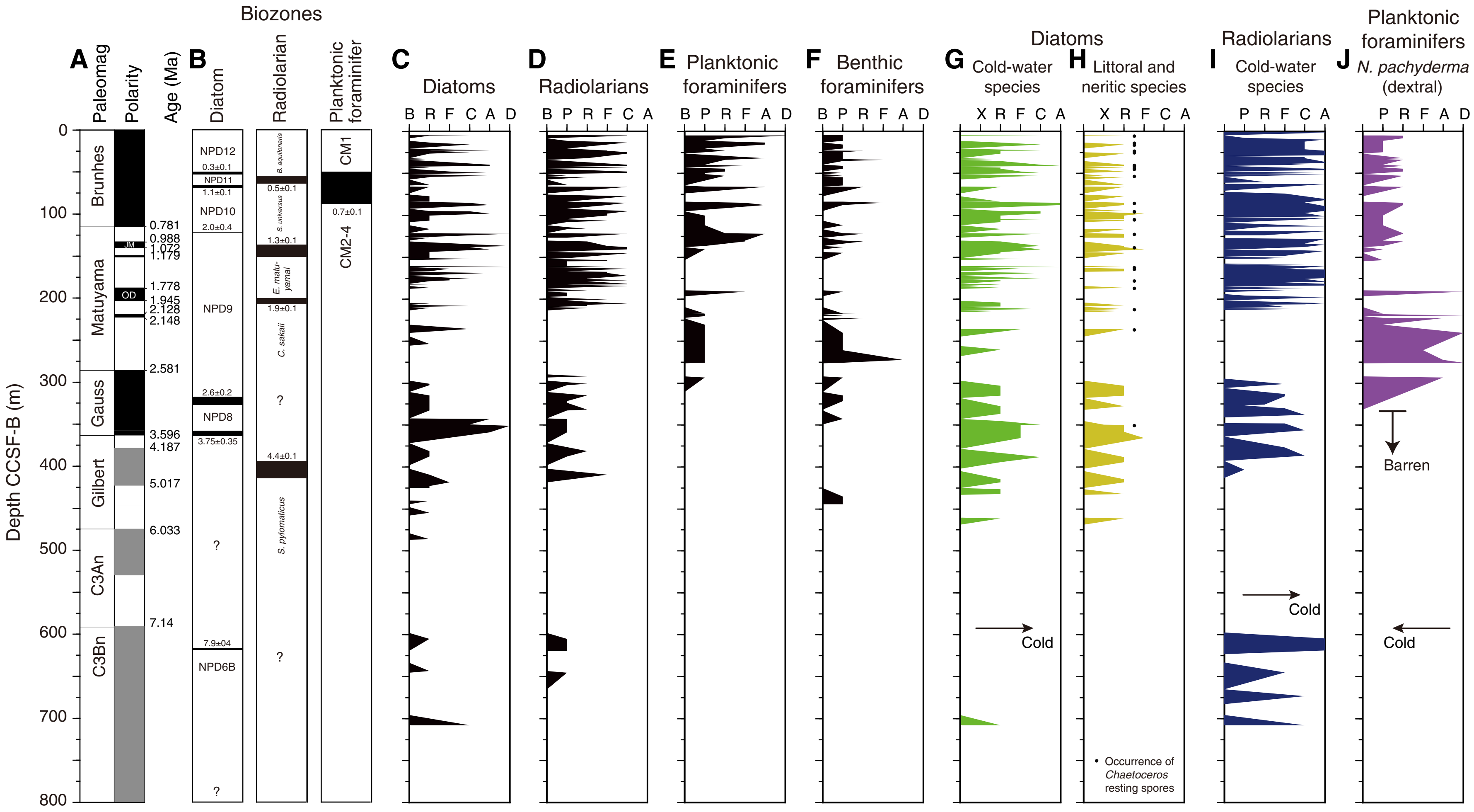

Figure F31. Inclination and polarity interpretations before and after peak AF demagnetization at 20 mT in recovered APC intervals, Site U1417. Polarity interpretation and correlation to the GPTS 2012 (Hilgen et al., 2012) is described in the text.

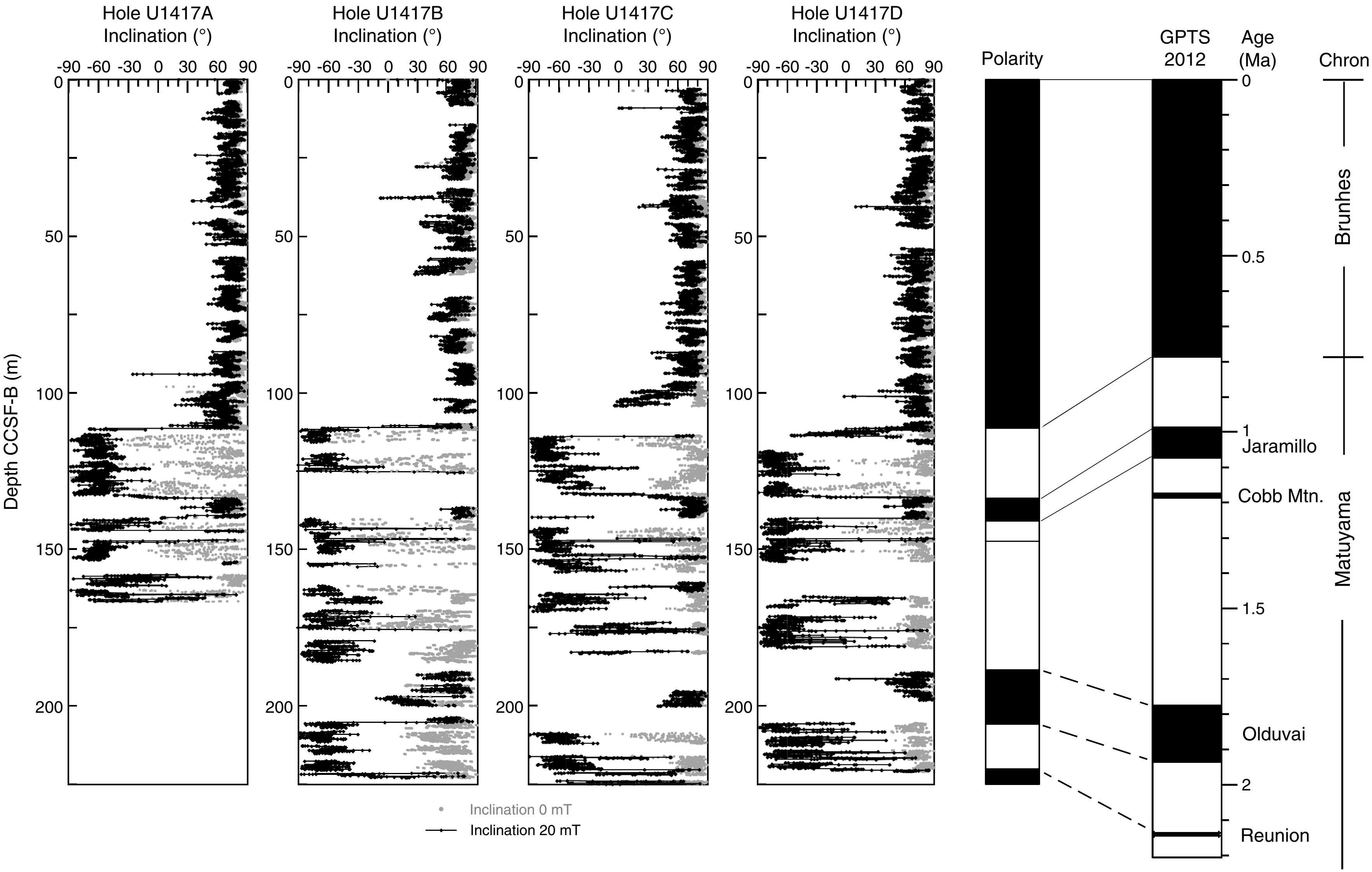

Figure F32. Shipboard age model, Site U1417. The two dashed curves represent the minimum and maximum initial age models described in the text. DSDP Site 178 basement age from Maus et al. (2009).

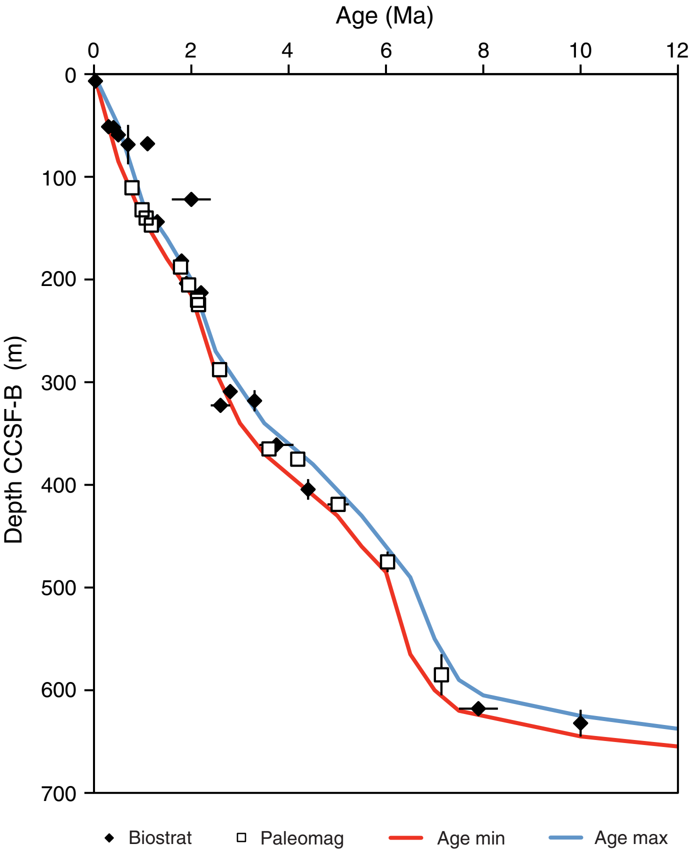

Figure F33. Whole-round Multisensor Logger (WRMSL) gamma ray attenuation (GRA) bulk density compared to WRMSL volume magnetic susceptibility (MS) data and natural gamma ray (NGR) data, Site U1417. Also shown are apparent GRA density–normalized WRMSL mass MS and NGR activity, corrected for variability in recovered sediment volume.

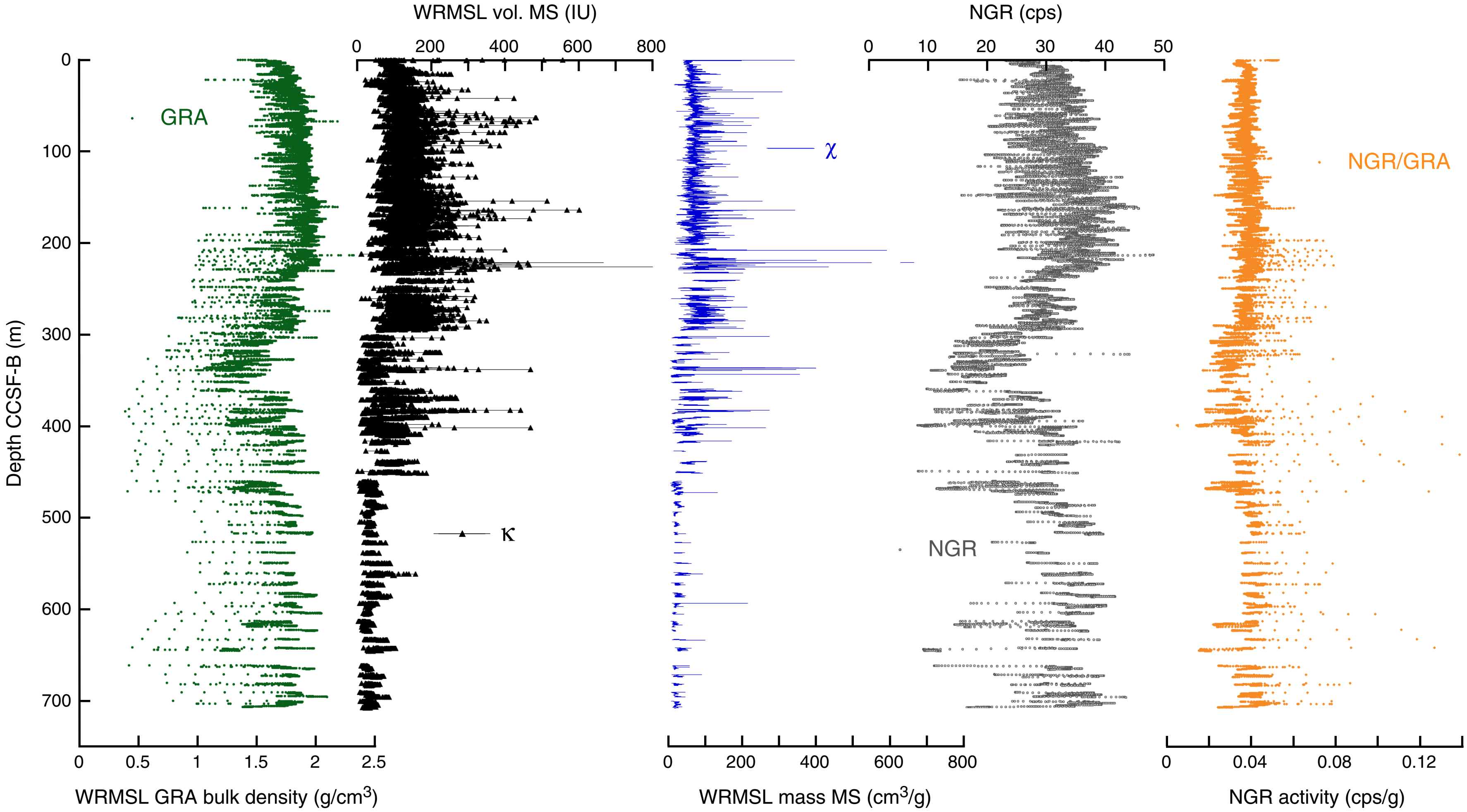

Figure F34. Comparison and tentative correlation of sonic and density logs with discrete physical properties measurements and seismic reflection profile LOS Line 1, Site U1417. Lithostratigraphic units (CCSF-B), logging units (WMSF), and seismic sequences (two-way traveltime [TWT]) are shown, but note the lack of a check shot calibration below 211 m WMSF and the ~10 m depth error when comparing CCSF-B and WMSF. VE = vertical exaggeration.

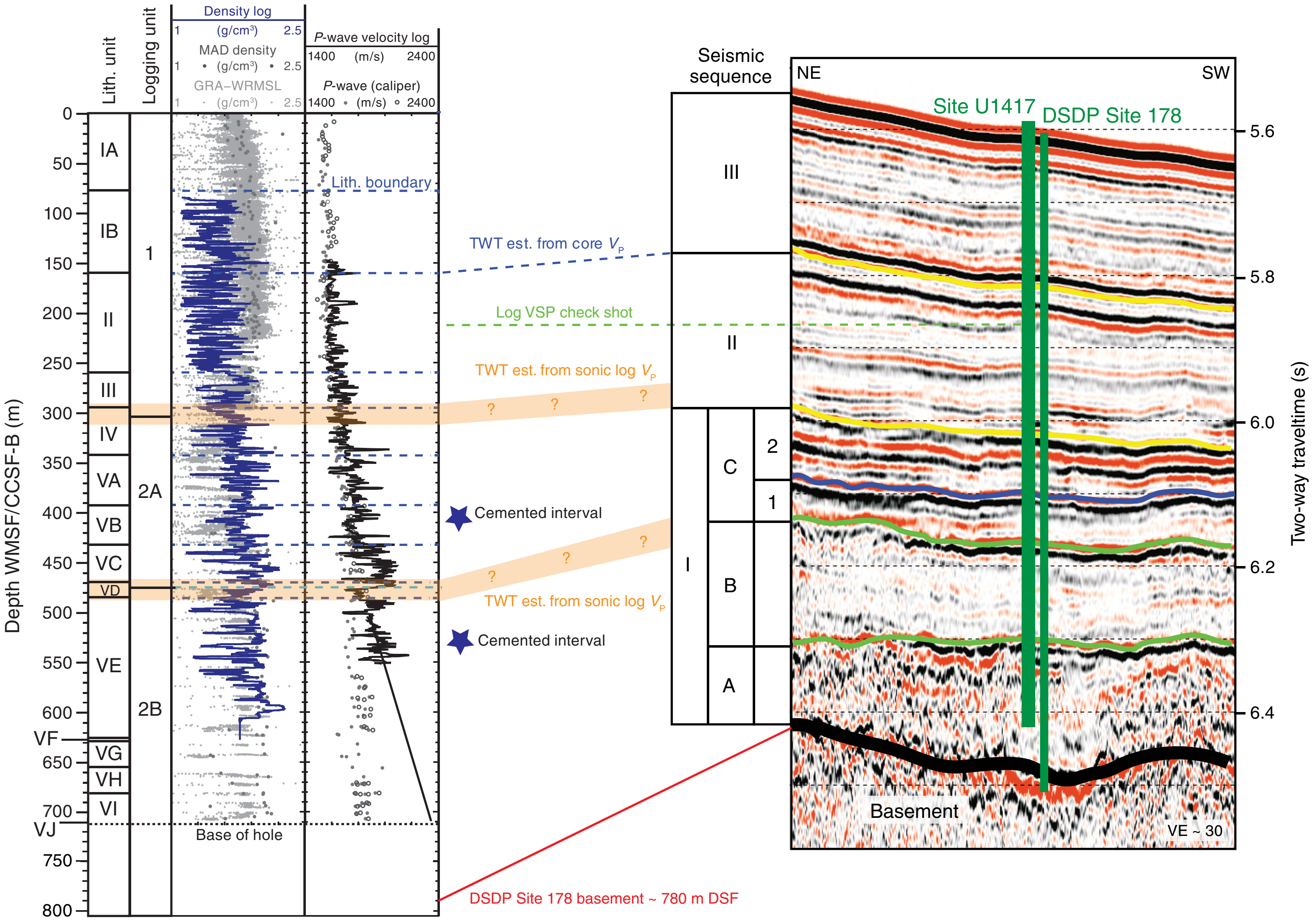

Figure F35. Chemical parameters determined in headspace and interstitial water samples, Site U1417. Downhole records are composites of samples from Holes U1417A, U1417C, U1417D, and U1417E. **A.** Alkalinity. **B.** pH. **C.** Sulfate. **D.** Ammonium. **E.** Bromide. **F.** Methane. **G.** Silica. **H.** Salinity. **I.** Chloride. **J.** Sodium.

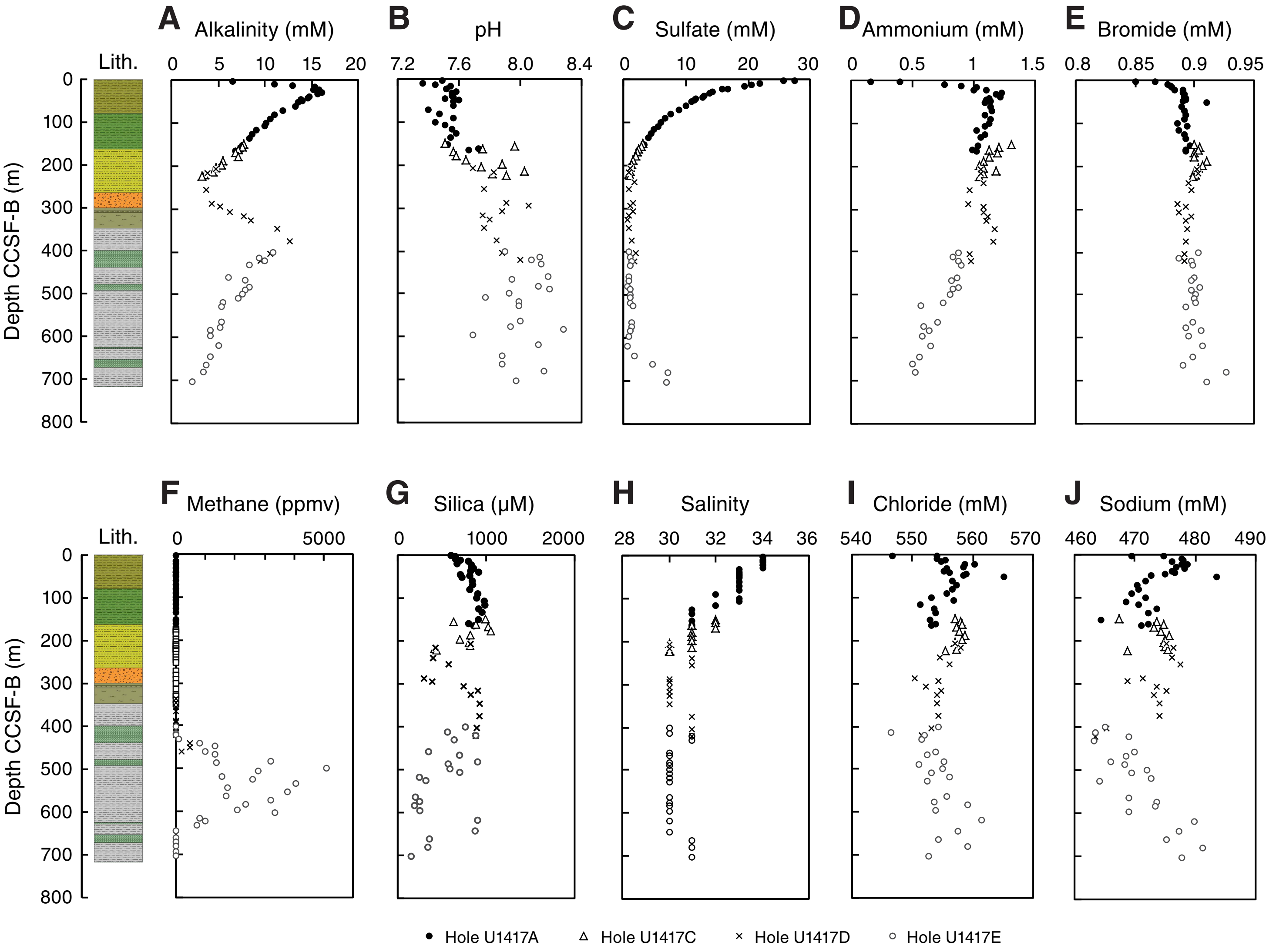

Figure F36. Comparison of an interval of Hole U1417E downhole wireline logging data (logging Unit 2) with Site U1417 core physical properties data. Data include borehole diameter, natural gamma ray log with volume-corrected core natural gamma radiation (NGR), density log with core bulk density from core logger data (GRA = gamma ray attenuation density) and discrete samples (MAD = moisture and density data), resistivity log, *P*-wave velocity log with discrete *P*-wave data from core (closed symbols = automatic velocity picks, open symbols = manual velocity picks), magnetic susceptibility (MS) log corrected with volume-corrected core susceptibility data, and logging and lithostratigraphic units. Depths are displayed as WMSF and CCSF-B for log and core data, respectively.

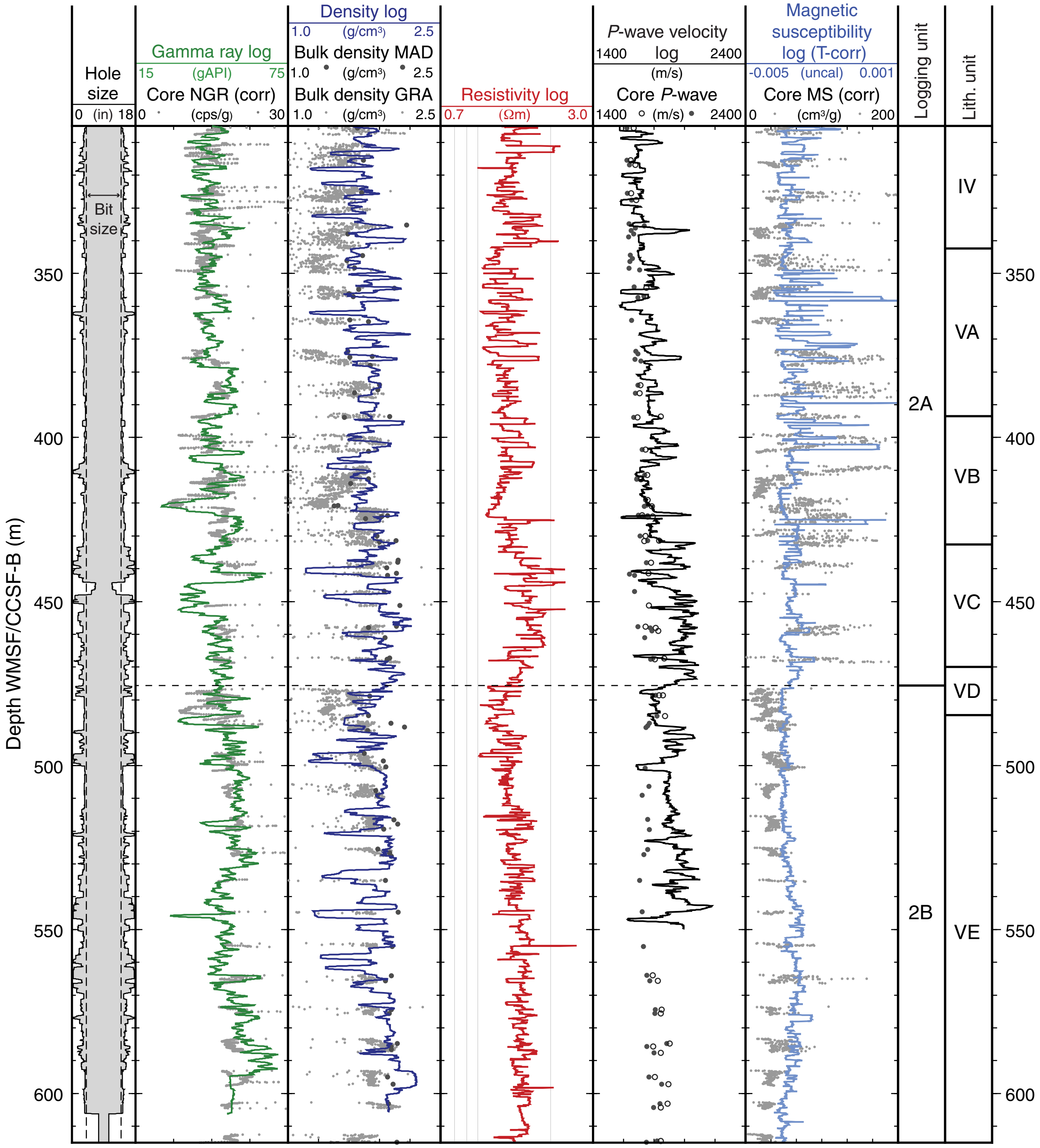

Figure F37. Lithostratigraphic units, borehole size, and core recovery, Site U1417. Magnetic susceptibility (MS) data were measured during downhole logging in Hole U1417E and on cores. Green box = interval of clast-rich and clast-poor diamict interbedded with mud where magnetic susceptibility is highest and most variable in the logging data. Horizontal dashed lines = transitions between lithostratigraphic units. The inset figure highlights the correlation between diamict intervals and high magnetic susceptibility values in the core data. The core image shows Section 341-U1417D-53X-1, 0–75 cm, the red star denotes its position. The inset figure provides evidence for the diamict intervals causing high magnetic susceptibility values in the logged data. A difference of as much as ~10 m may exist when comparing the CCSF-B and WMSF depth scales. WRMSL = Whole-Round Multisensor Logger.

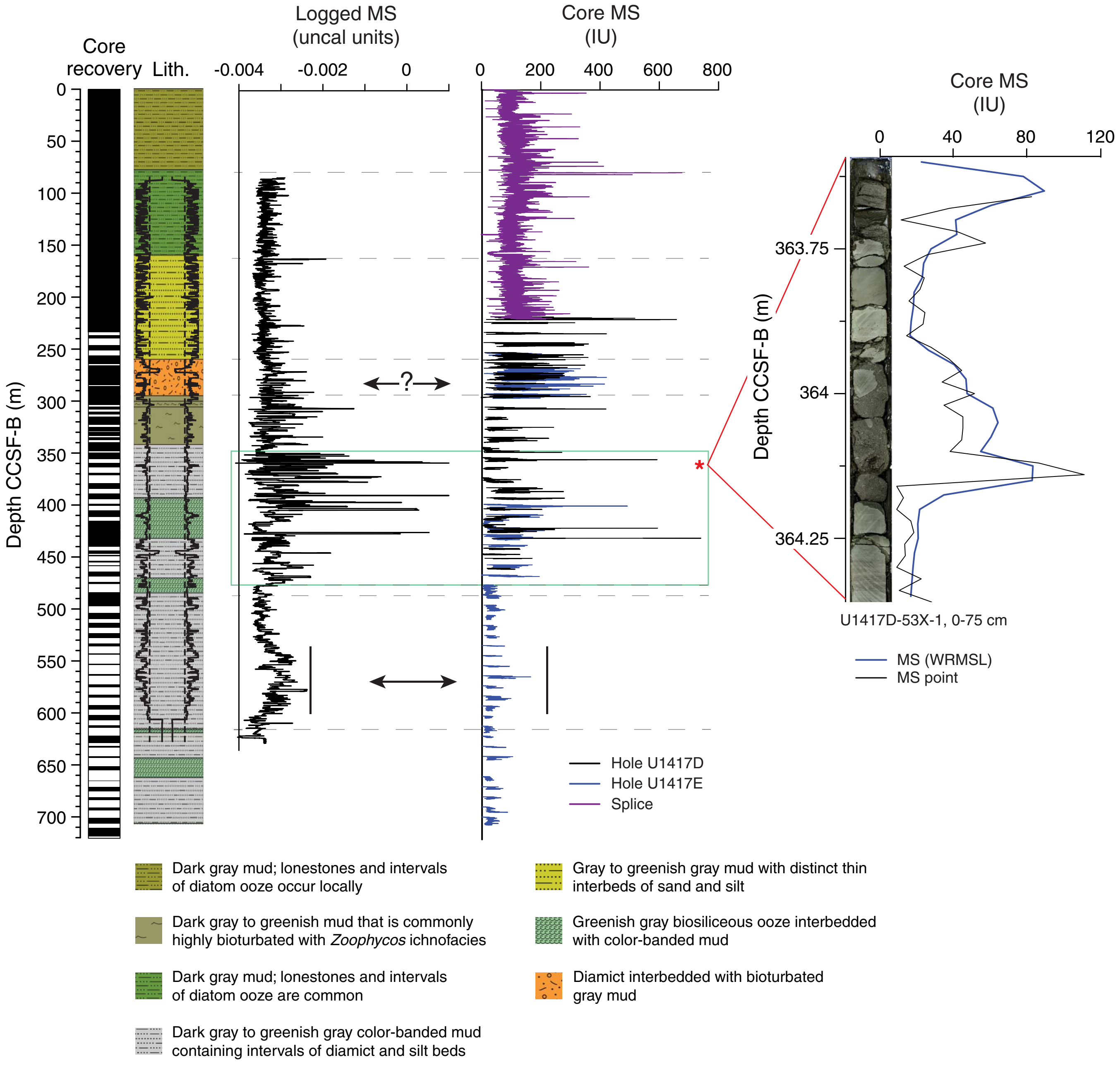

Figure F38. Perspective view of the northern Gulf of Alaska showing major tectonic elements with thrust faults in black and Sites U1418–U1421. Relief is shown at ~10× vertical exaggeration, with total vertical relief displayed ranging from <4000 m below sea level to >5000 m above sea level. Black = U.S. Geological Survey, green = Cruise EW0408, orange = seismic profiles from St. Elias Erosion/Tectonics Project (STEEP) draped over topography. Figure is modified from Gulick et al. (2013).

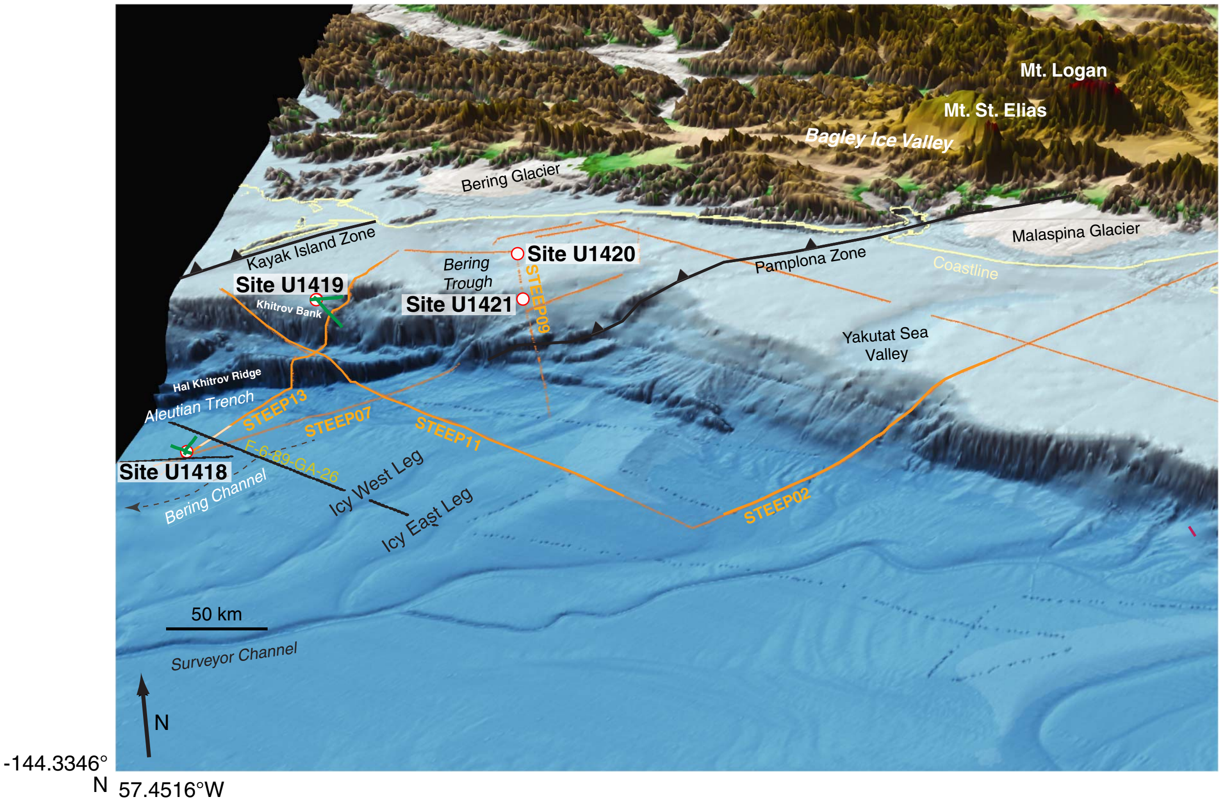

Figure F39. Comparison of sonic and density logs with discrete physical properties measurements and seismic reflection Profile GOA3202, Site U1418. Lithostratigraphic units (CCSF-B), logging units (WMSF), and seismic sequences (two-way traveltime [TWT]) are shown. MAD = moisture and density.

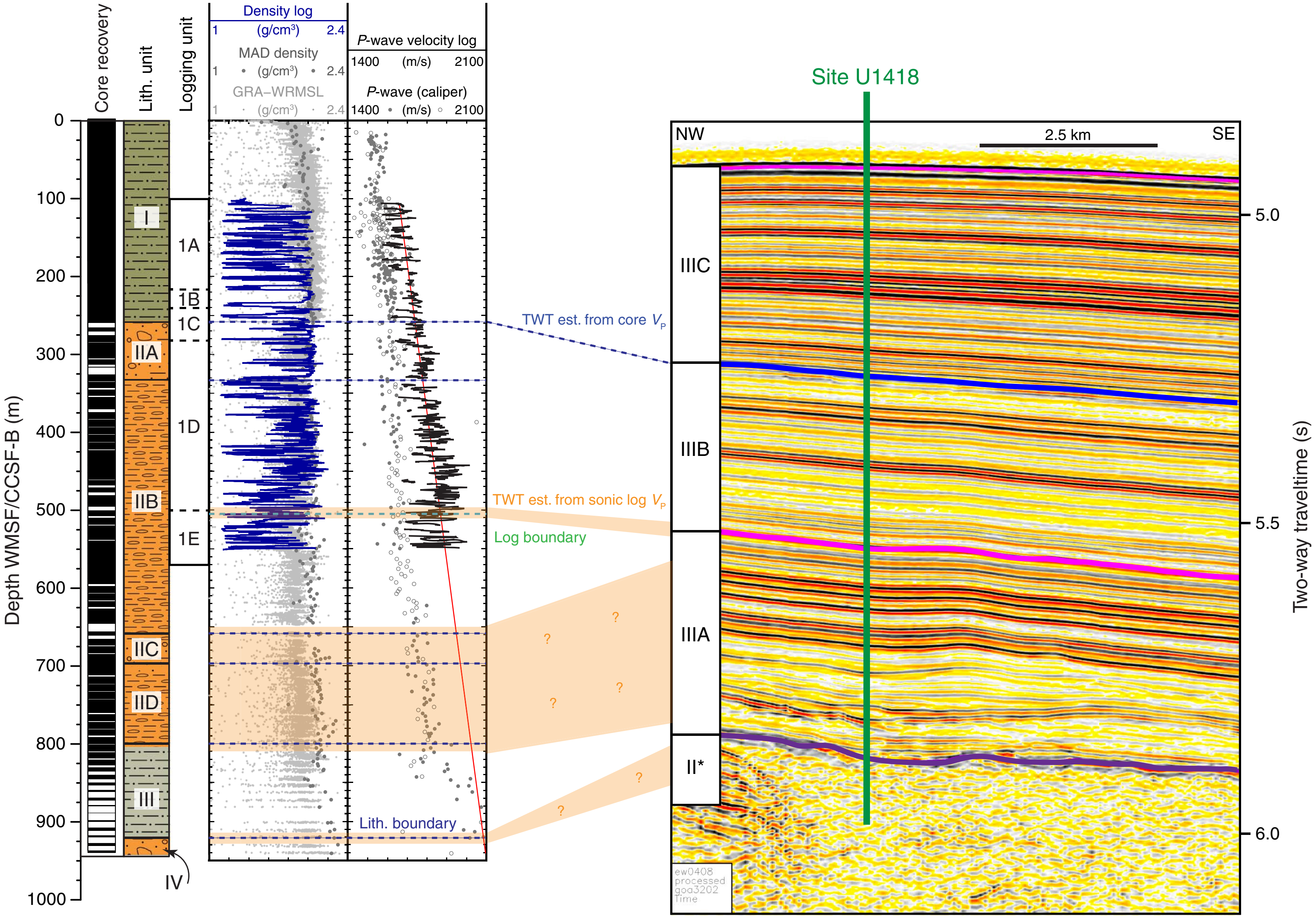

Figure F40. Core recovery, Site U1418.

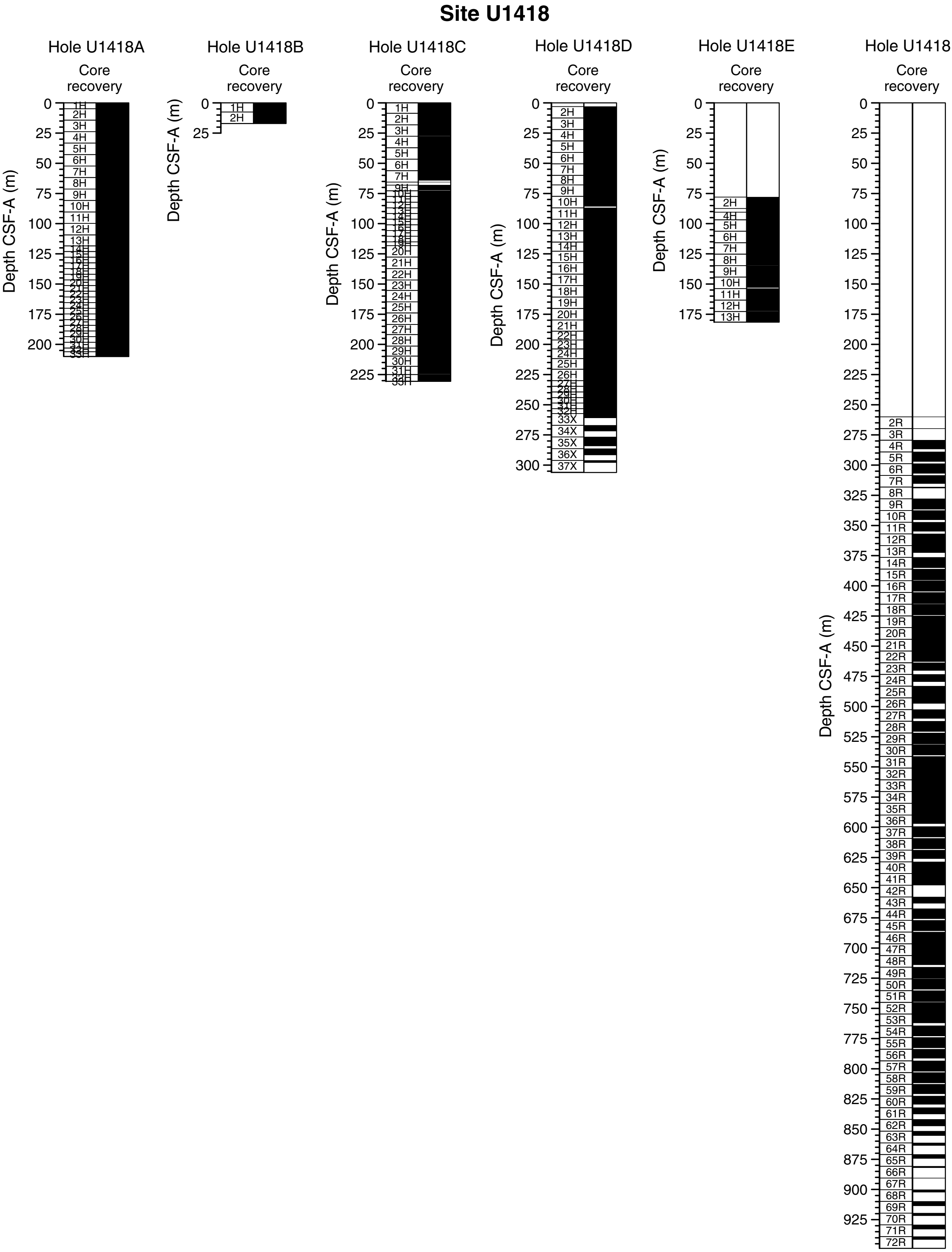

Figure F41. Schematic diagram of lithostratigraphic units and core recovery, Site U1418.

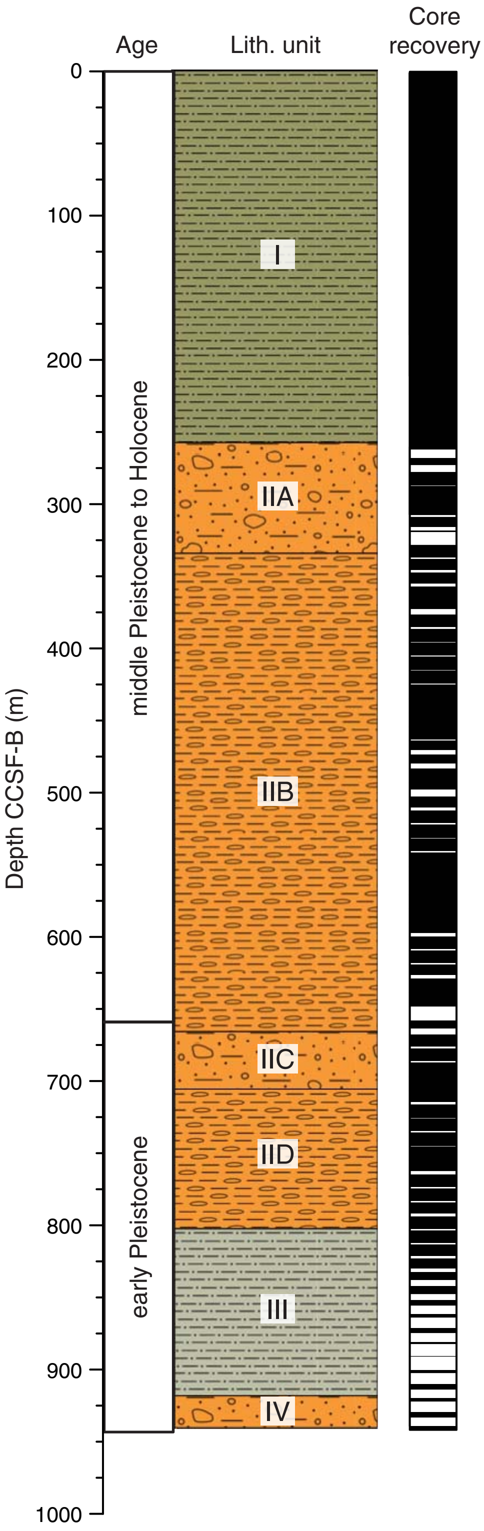

Figure F42. Paleomagnetic and micropaleontological age datums, and variations of rank abundances of paleoenvironmental indicators, Site U1418. Planktonic foraminifers include *Globigerina bulloides* and *Globigerina umbilicata* integrate. Abundance: D = dominant, A = abundant, C = common, F = few, R = rare, P or X = present, B = barren. Biozone black bars = depth uncertainty in biohorizon start/end periods. JM = Jarmillo.

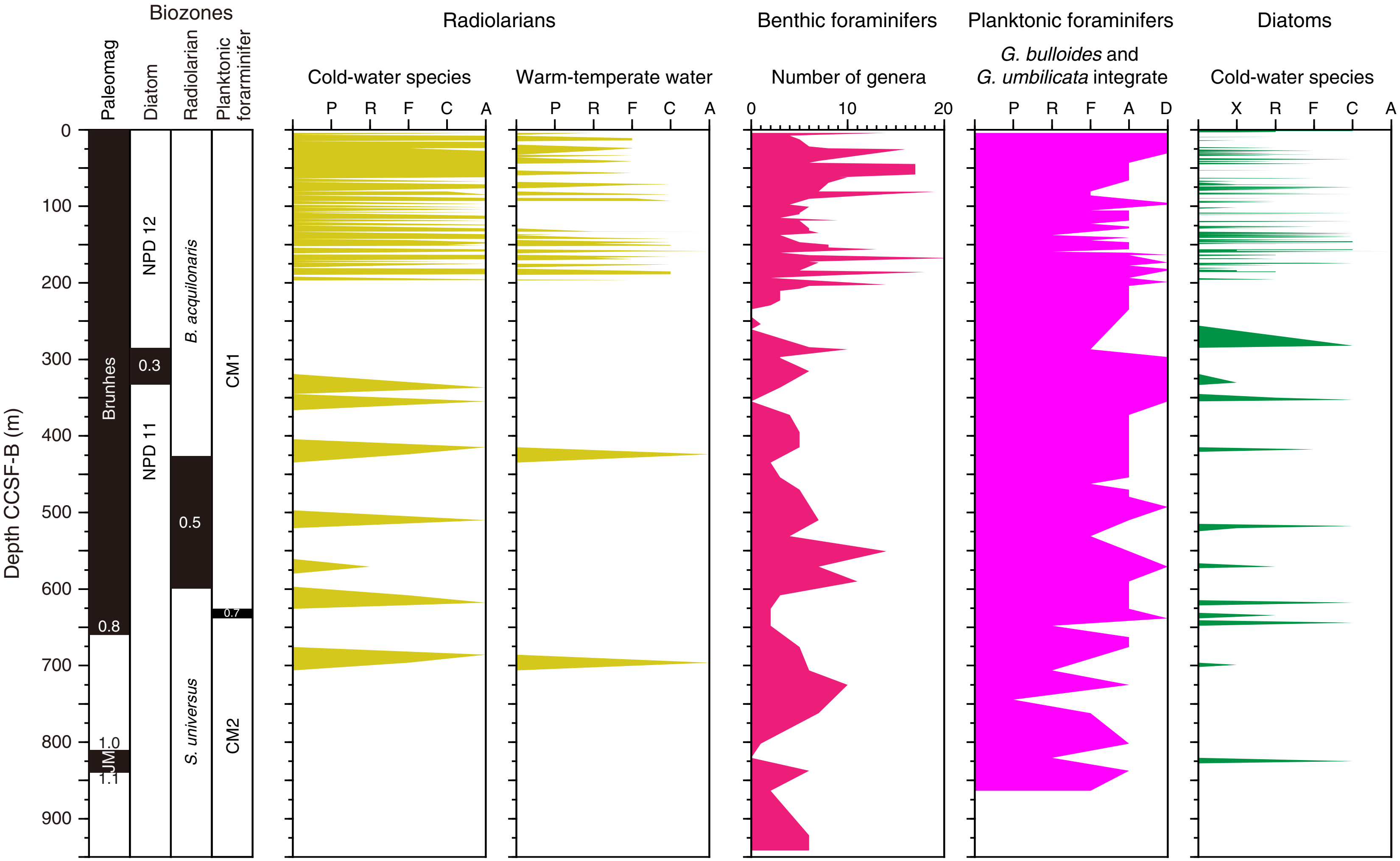

Figure F43. Shipboard age model, Site U1418. The two dashed curves represent the minimum and maximum initial age models described in the text.

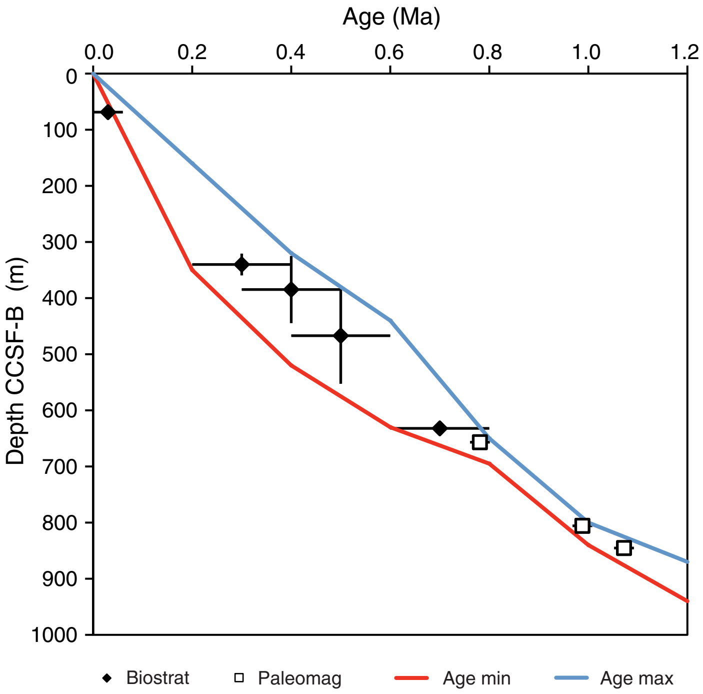

Figure F44. Intensity measured before and after 10 and 20 mT demagnetization, Hole U1418F. Declination and inclination measured after 20 mT peak AF demagnetization are also shown. GPTS 2012 from Hilgen et al. (2012). The bottom three Cores 341-U1418F-70R through 72R of mass transport deposit as chaotic unit are not included, though their intensities are similar.

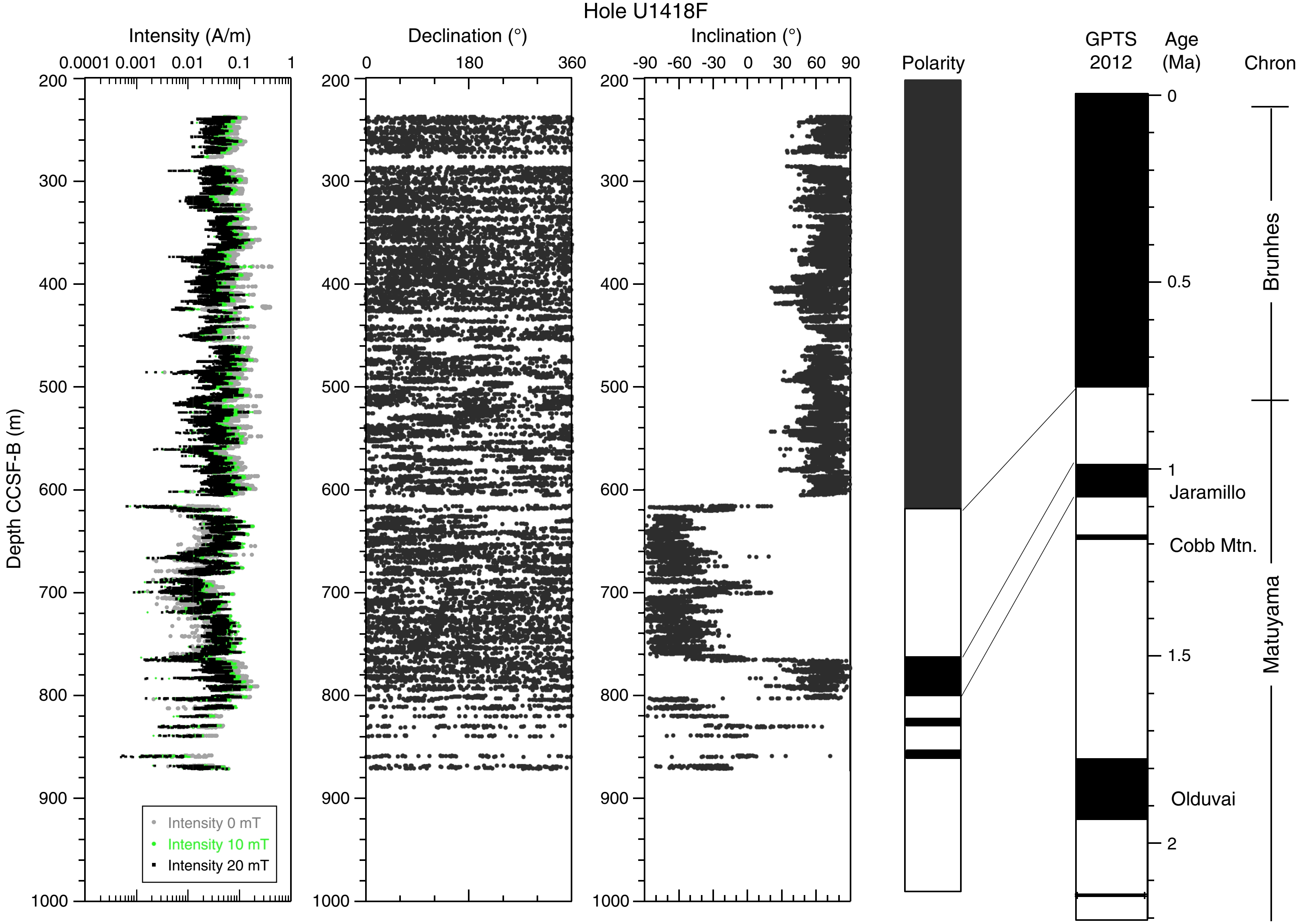

Figure F45. (**A**) Shipboard sedimentation rate versus drilled depth (**B**) sedimentation rate versus time for Site U1418, based on the CCSF-B depth model, the shipboard age models, and interval-averaged discrete dry density data. Values are calculated over 0.2 m.y. intervals from 0 to 1.2 Ma. Solid lines = averages within each interval, dashed lines = uncertainty bounds (minimum and maximum rates based on shipboard age models).

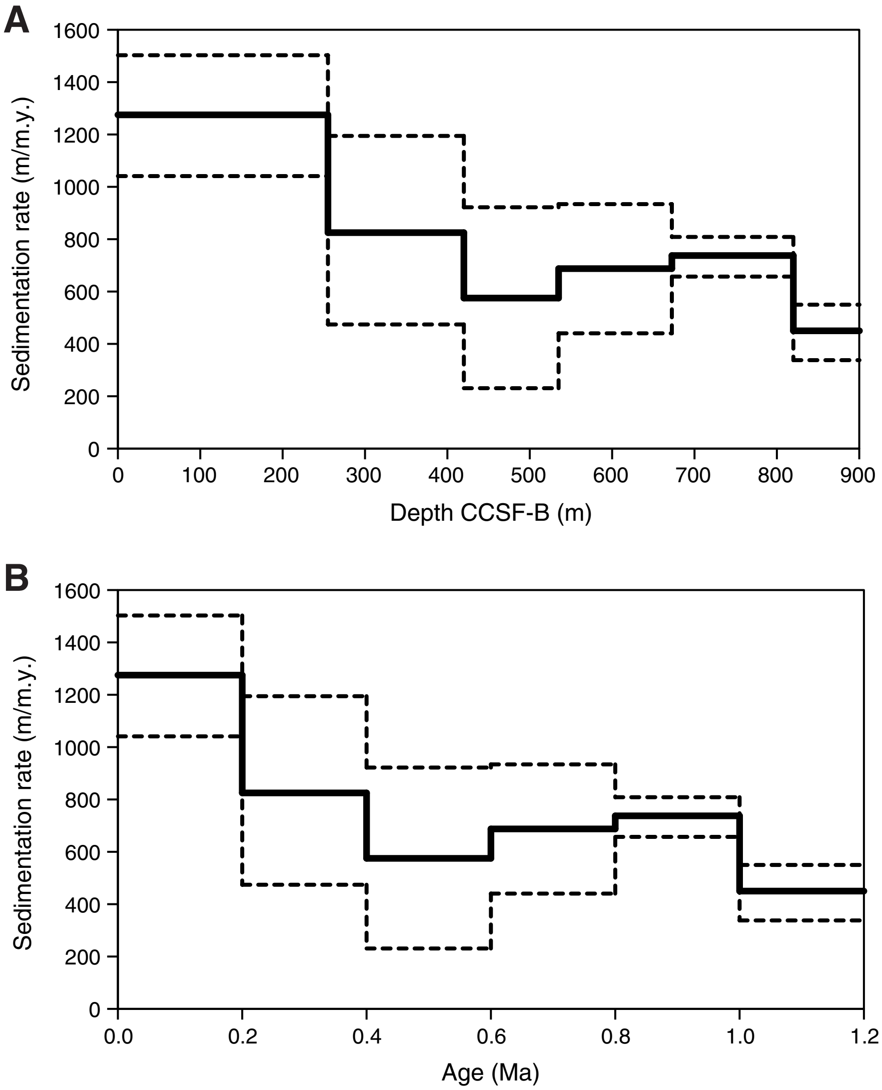

Figure F46. Comparison of Hole U1418F downhole wireline logging data with Site U1418 core physical properties data. Data include: borehole diameter, natural gamma ray log with volume-corrected core natural gamma ray (NGR), density log with core bulk density from core logger data (GRA = gamma ray attenuation density) and discrete samples (MAD = moisture and density data, *P*-wave velocity log with discrete *P*-wave data from core (closed symbols = automatic velocity picks, open symbols = manual velocity picks), temperature-corrected magnetic susceptibility (MS) log with volume-corrected core susceptibility data, and logging and lithostratigraphic units. Depths are displayed as m WMSF and CCSF-B for log and core data, respectively.

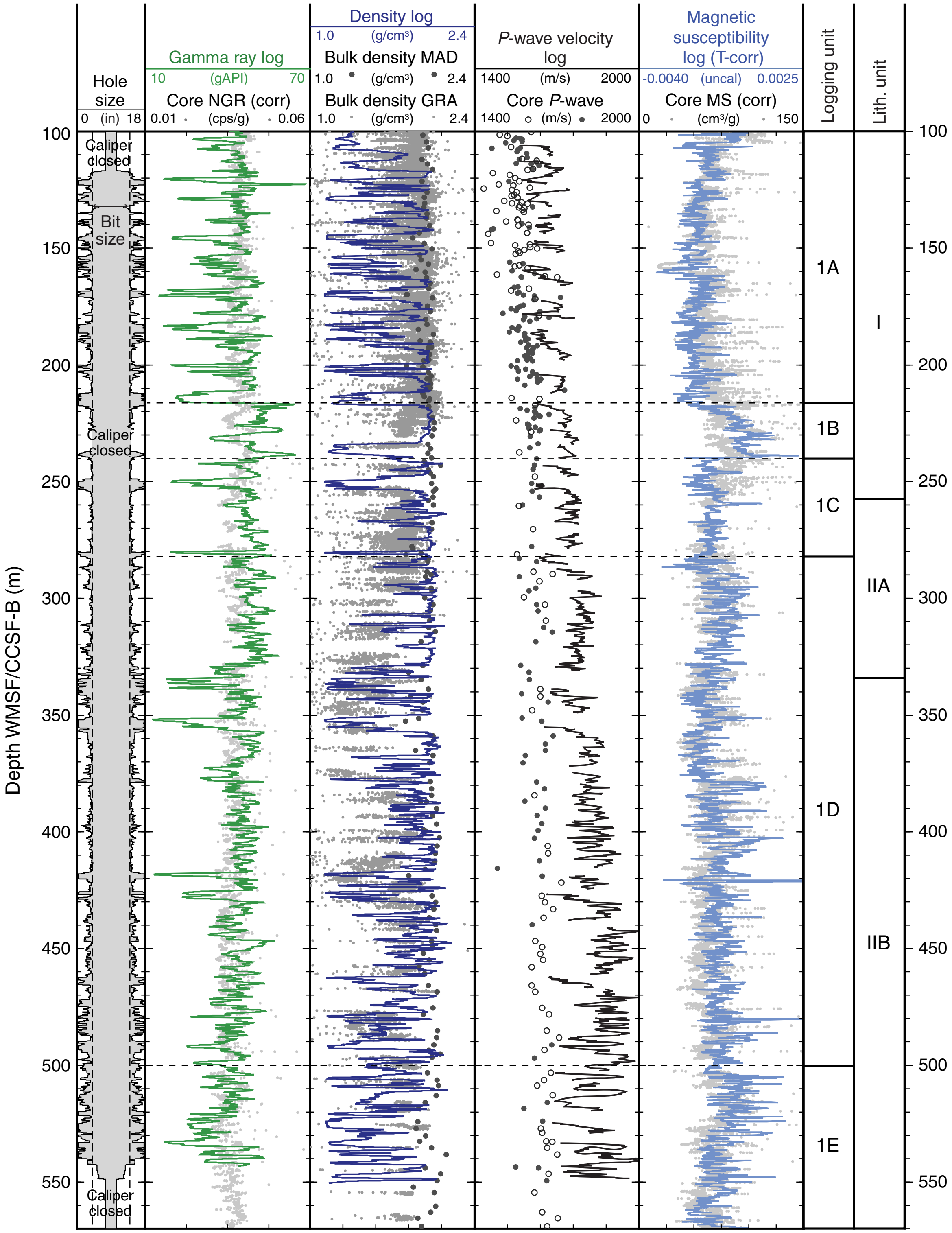

Figure F47. Lithostratigraphic units, borehole size, and core recovery, 0–600 m on the CCSF-B/WMSF scale, Site U1418. Diamict, diatom ooze, laminations, and bioturbation show the combined observations from Holes U1418A–U1418F (A = absent, P = present) and are compared to magnetic susceptibility (MS) data measured during downhole logging in Hole U1418F and on cores (integrated measurements made on splice). Downhole logging MS data are smoothed over a 40 cm sliding average and temperature corrected (T-corrected). Core MS has been smoothed over a 2.5 cm window and volumetric corrected. Inset figure shows the close correspondence between core (purple) and logged (blue) MS between 100 and 225 m CCSF-B/WMSF.

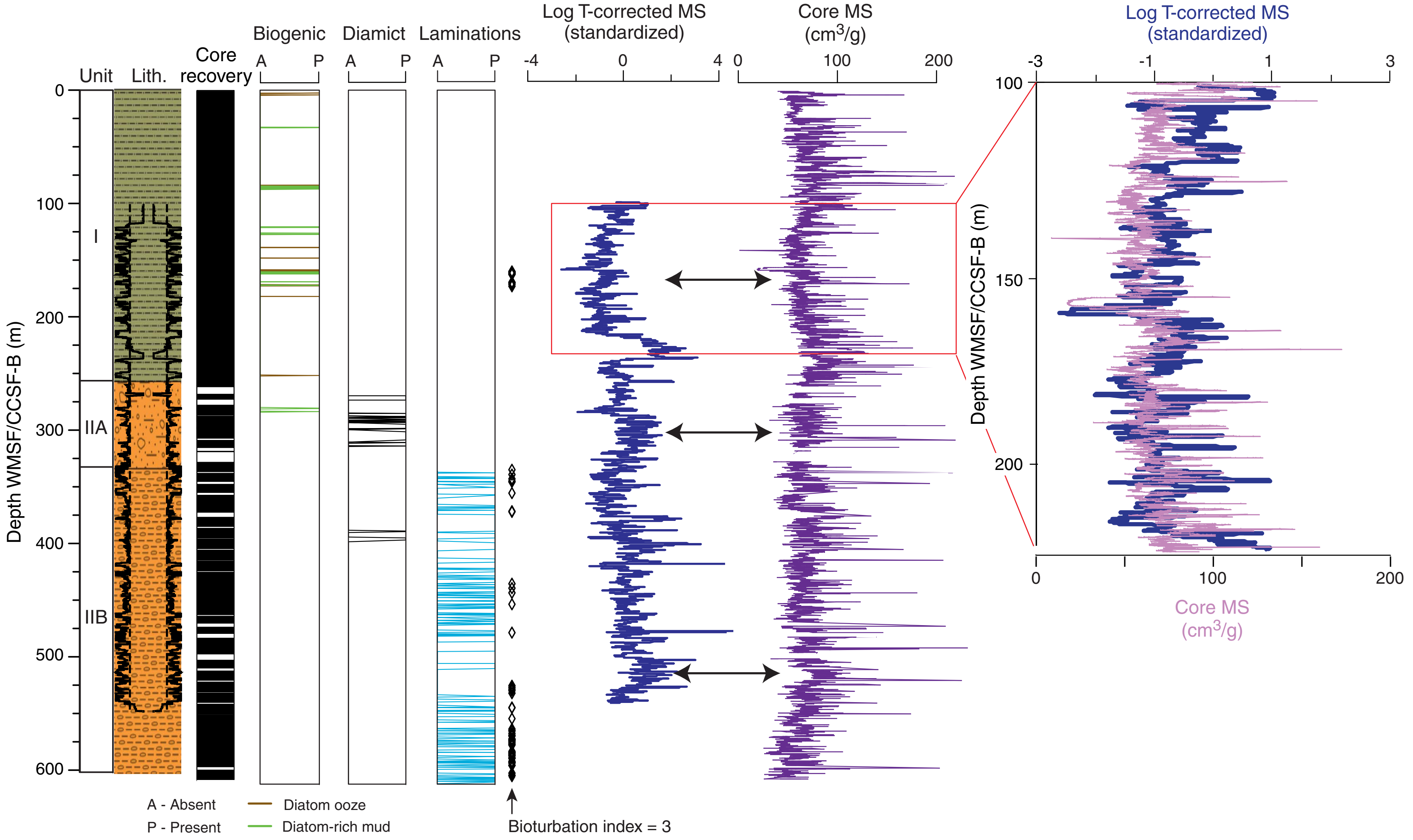

Figure F48. Chemical parameters determined in headspace and interstitial water samples, Site U1418. Downhole records are composites of samples from Holes U1418A–U1418D and U1418F. **A.** Alkalinity. **B.** pH. **C.** Sulfate. **D.** Ammonium. **E.** Bromide. **F.** Methane. **G.** Ethane. **H.** Silica. **I.** Salinity. **J.** Chloride. **K.** Sodium.

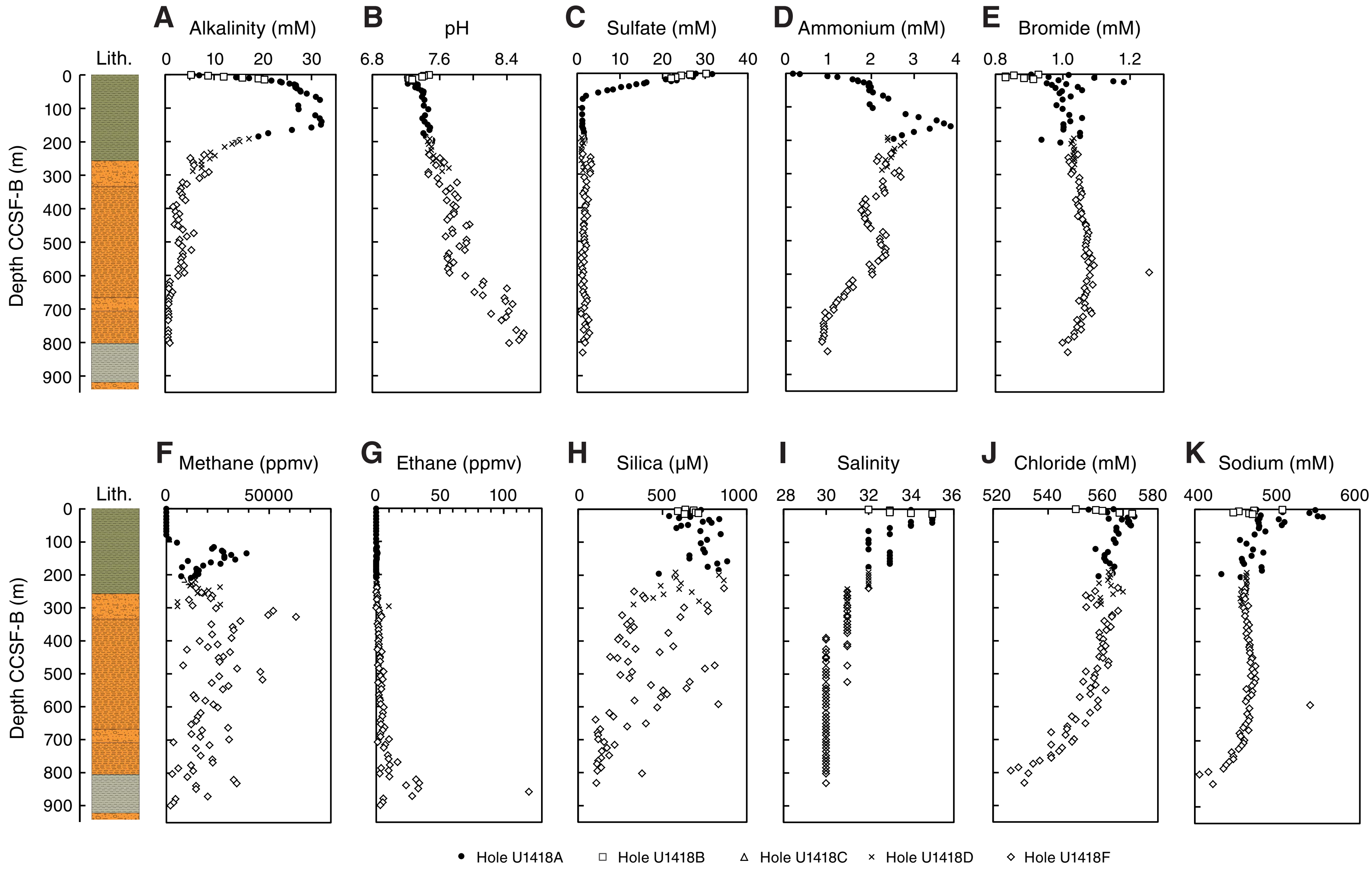

Figure F49. Close-up of high-resolution Profile GOA3101 with seismic Units A–K overlain. These units may represent strata formed under varying proximity to the ice margin and are the targets for drilling at Site U1419.

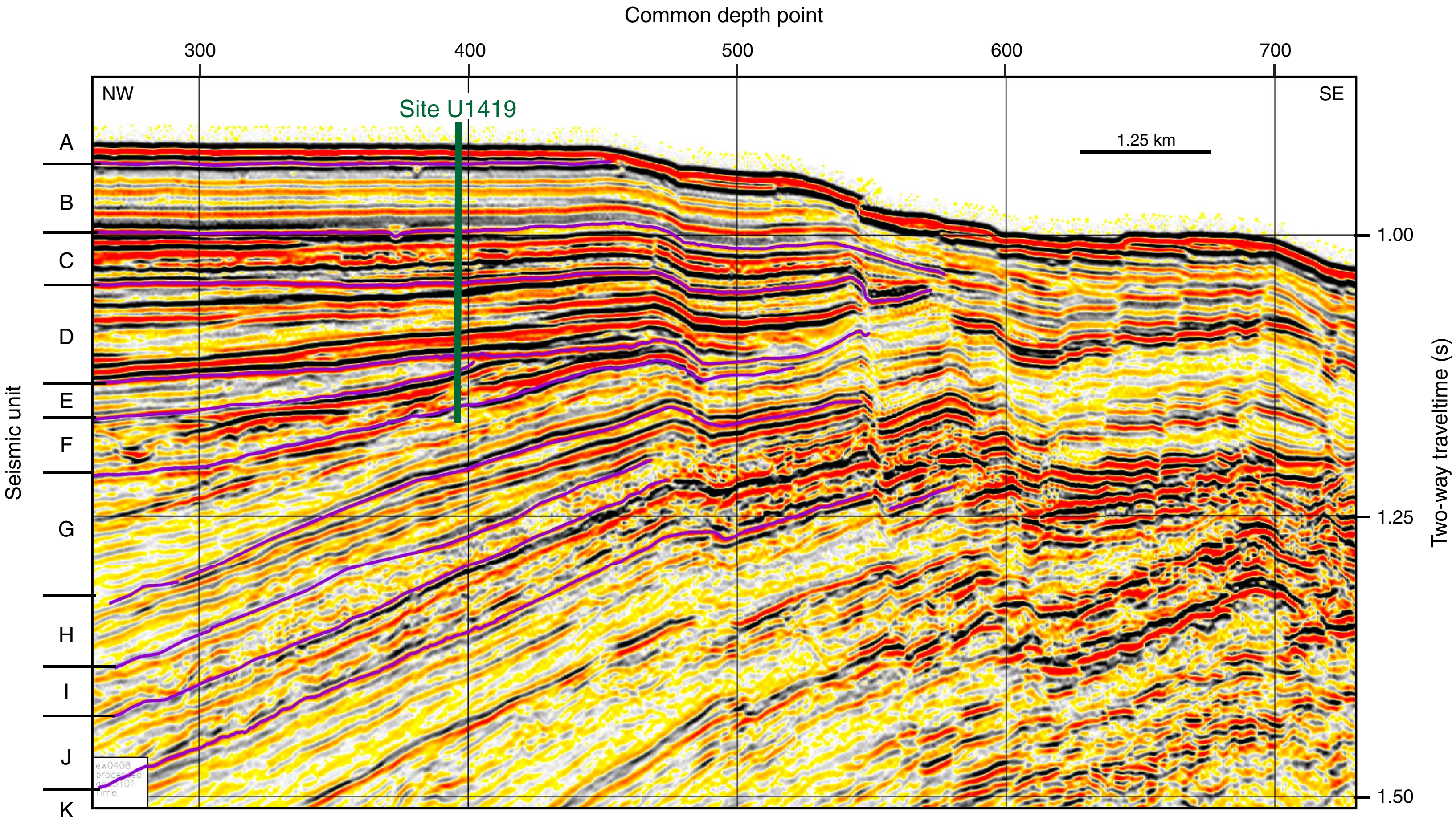

Figure F50. Core recovery, Site U1419.

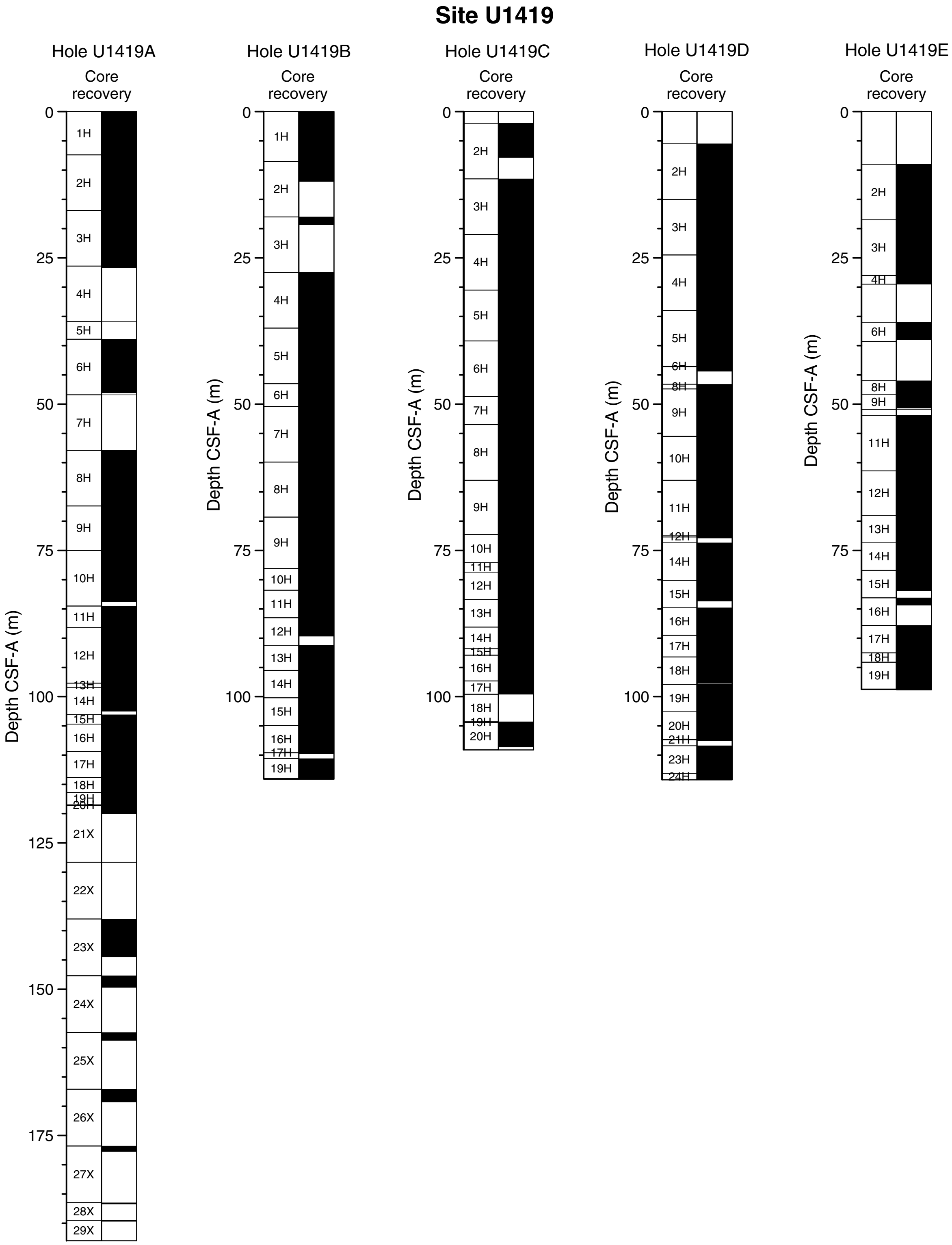

Figure F51. Lithostratigraphic observations, physical properties measurements, and integration with seismic data, Site U1419. MS = magnetic susceptibility, PWL = *P*-wave logger, PWC = *P*-wave caliper, GRA = gamma ray attenuation, MAD = moisture and density (discrete measurement).

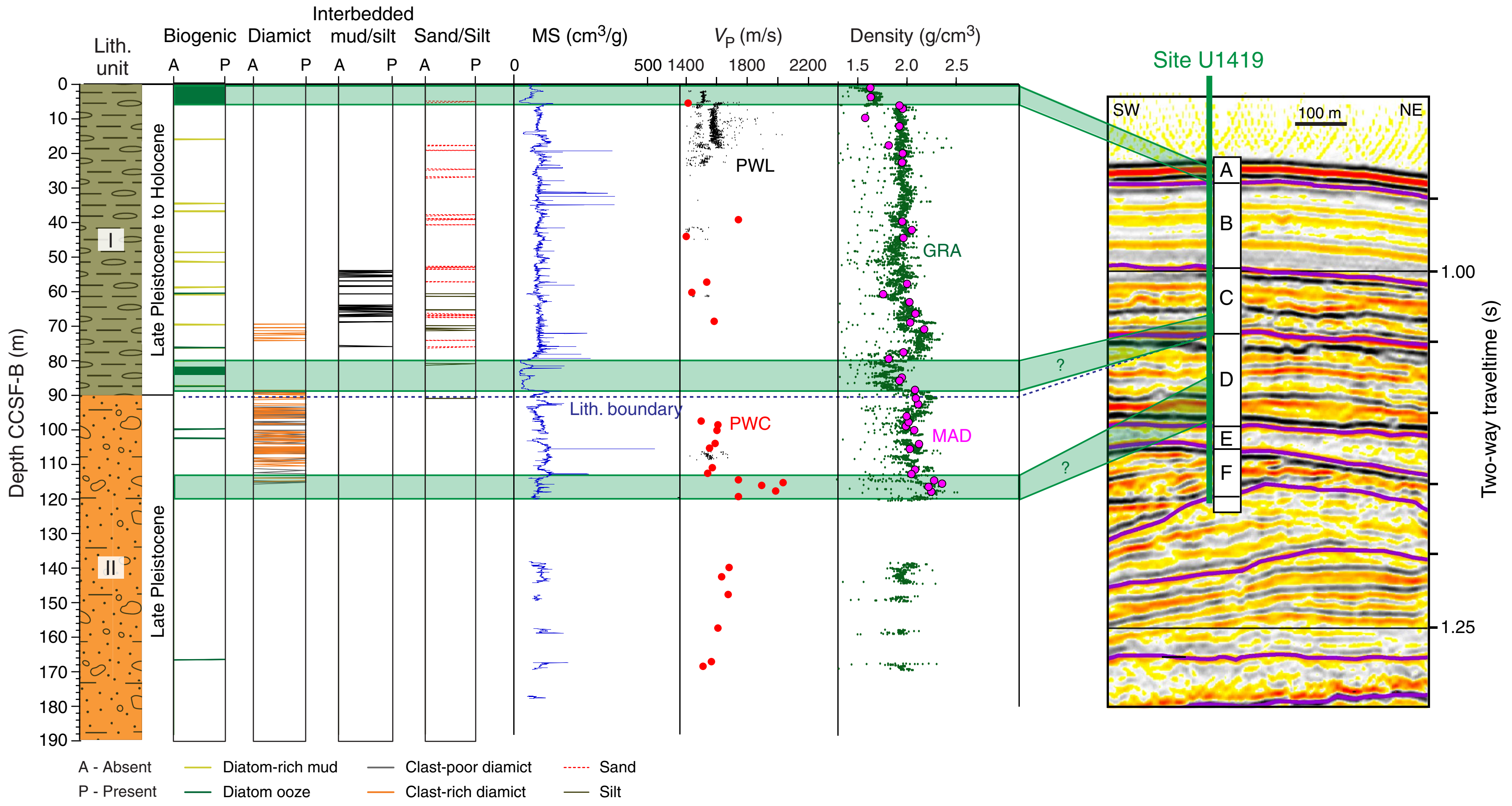

Figure F52. Abundance and preservation of diatoms, radiolarians, and planktonic and benthic foraminifers, Site U1419. Abundance: D = dominant, A = abundant, C = common, F = few, R = rare, P = present, B = barren. Preservation: VG = very good, G = good, M = moderate, P = poor.

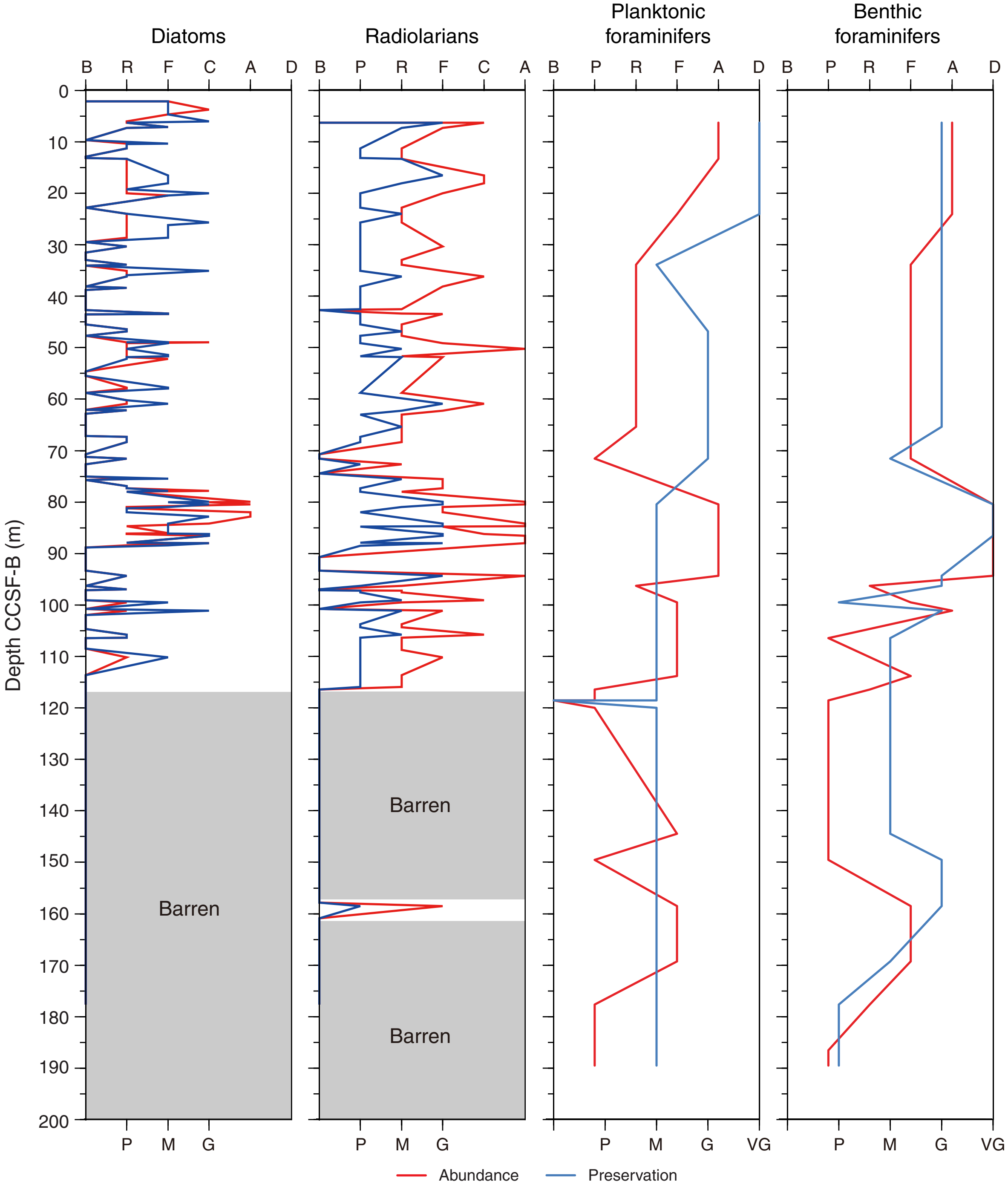

Figure F53. Diatom and radiolarian environmental indicators, Site U1419. Abundance: A = abundant, C = common, F = few, R = rare, P or X = present.

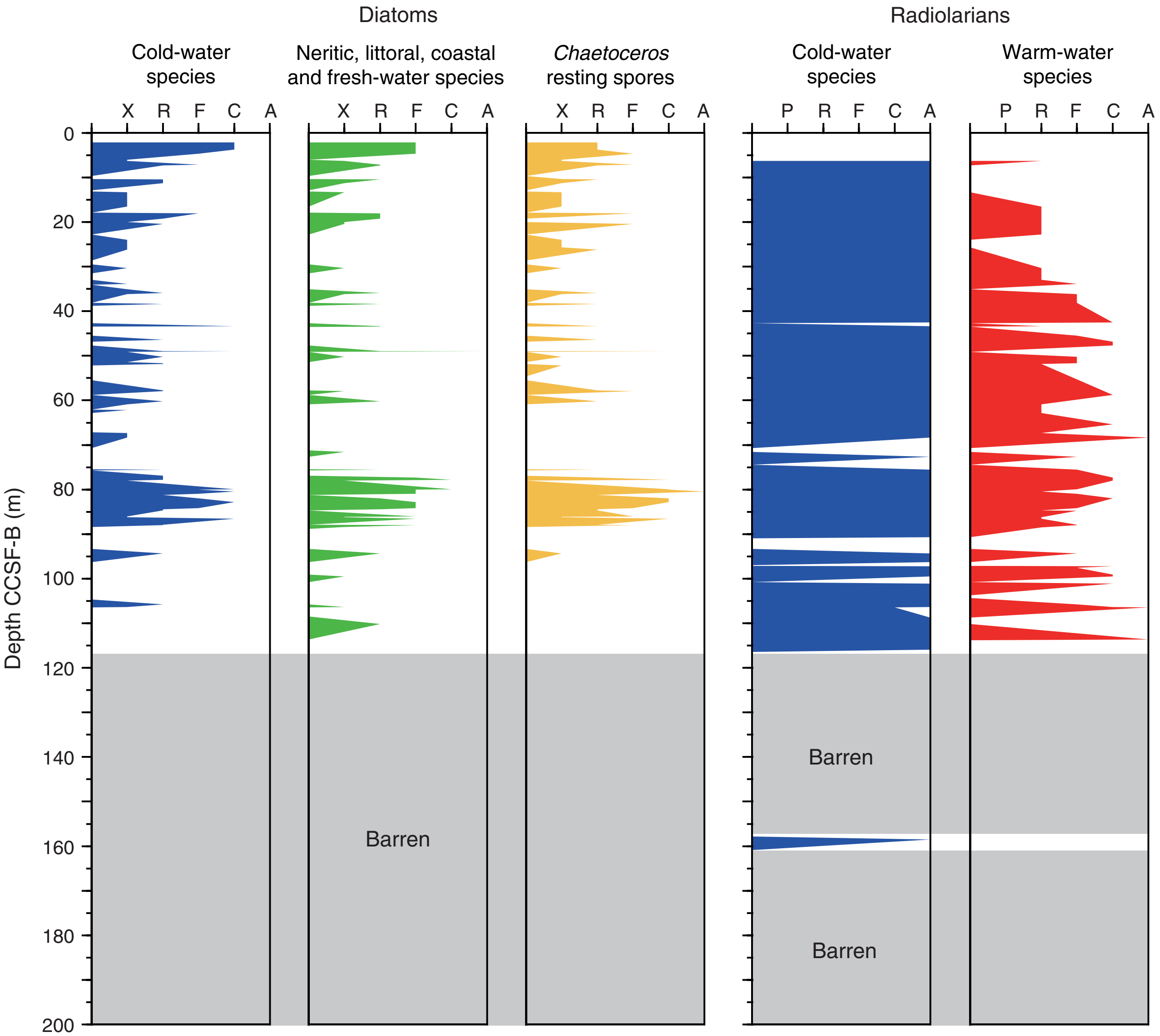

Figure F54. NRM intensities measured before and after 10 and 20 mT peak AF demagnetization, Holes U1419A–U1419E.

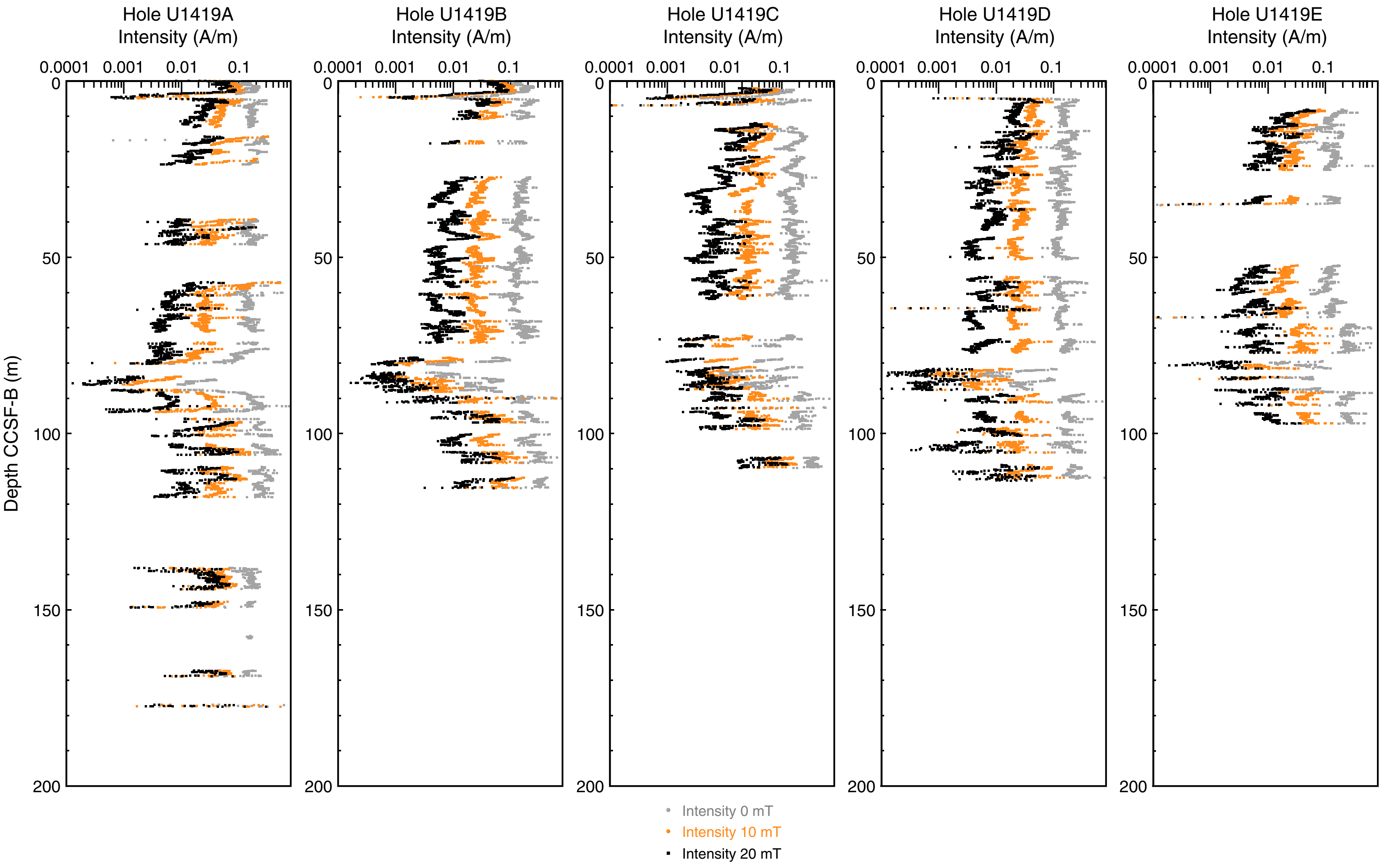

Figure F55. Whole-Round Multisensor Logger (WRMSL) gamma ray attenuation (GRA) bulk density compared to WRMSL magnetic susceptibility (MS) data, Site U1419. Both data sets are shown after Gaussian smoothing with a 10 cm window and interpolation to constant resolution at 2.5 cm. WRMSL MS is also shown corrected for variability in recovered sediment volume by normalizing to WRMSL GRA bulk density, generating specific MS. For the upper 90 m CCSF-B, data reflect the stratigraphic splice; at greater depths, data from Hole U1419A, U1419C, and U1419D cores are combined on their composite depth scales. In this lower interval, when depth horizons were recovered in multiple holes, we averaged all available interpolated data.

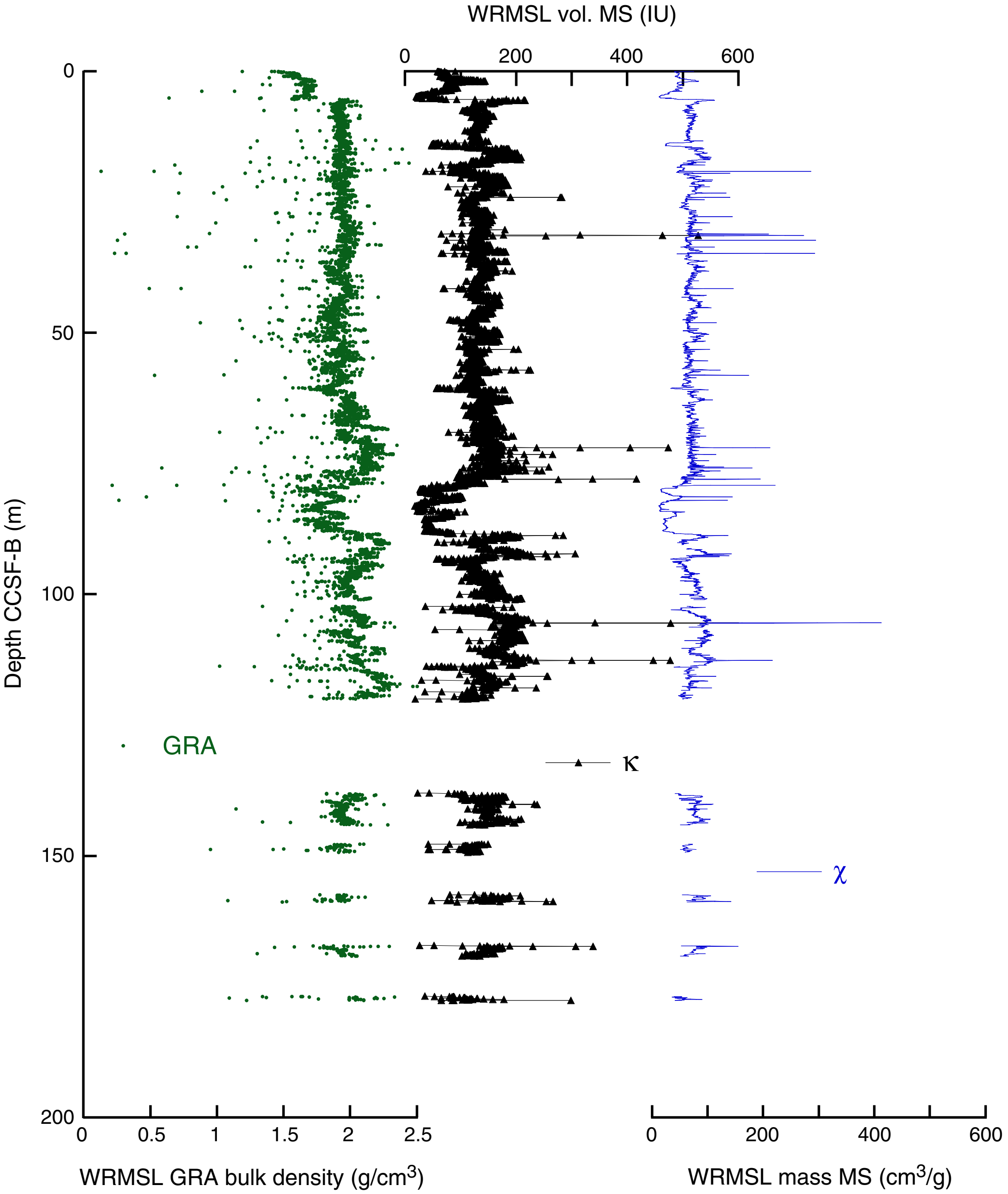

Figure F56. Whole-Round Multisensor Logger (WRMSL) gamma ray attenuation (GRA) bulk density compared to natural gamma radiation (NGR) data, Site U1419. Both data sets are shown after Gaussian smoothing with a 50 cm window and interpolation to constant resolution at 10 cm. NGR is also shown corrected for variability in recovered sediment volume by normalizing to WRMSL GRA bulk density. From 0 to 90 m CCSF-B, data follow the stratigraphic splice; at greater depths, data from Hole U1419A, U1419C, and U1419D cores are combined. In this lower interval, when depth horizons were recovered in multiple holes we use an average of all available interpolated data.

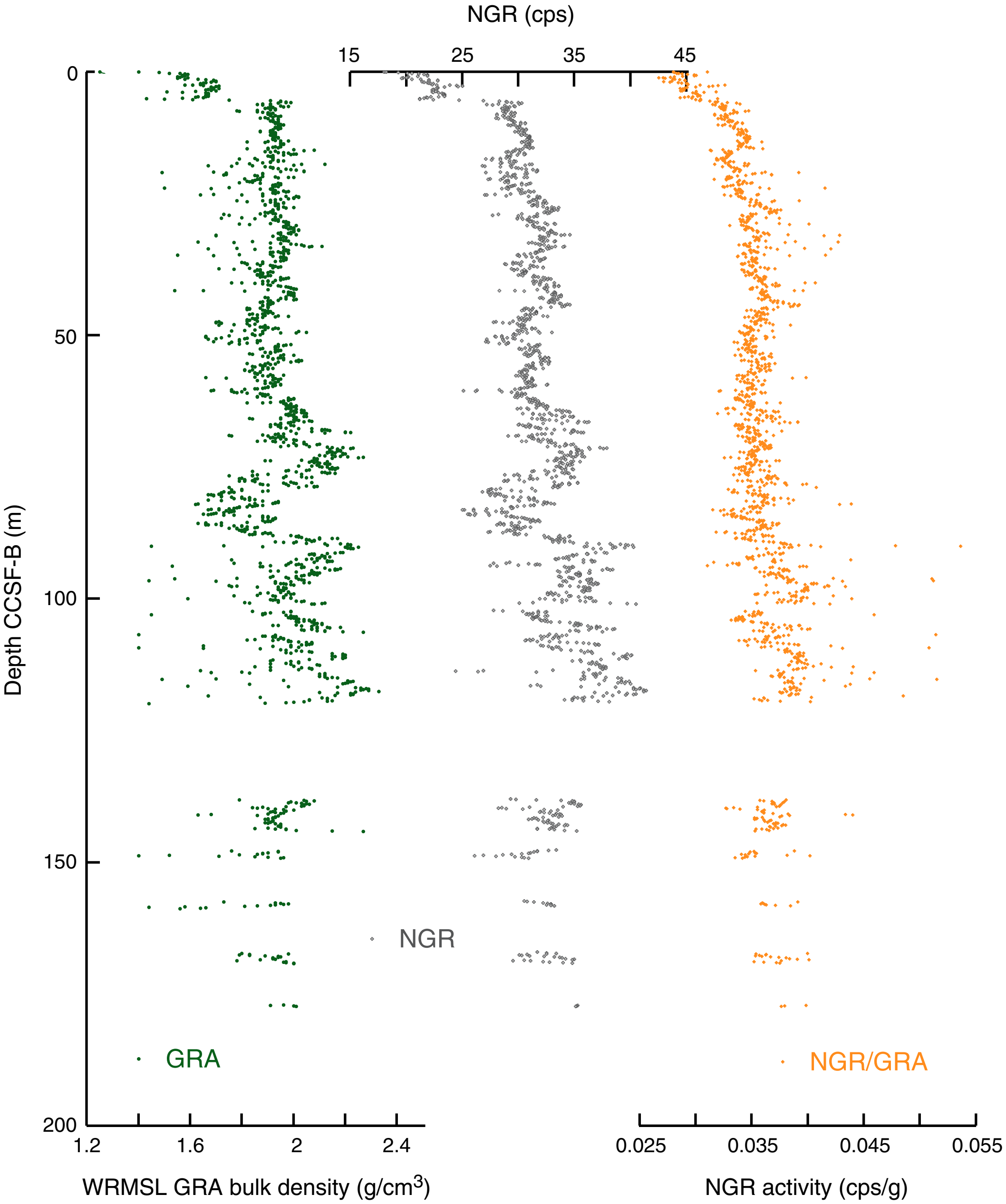

Figure F57. Sediment chemical parameters, Hole U1419A. **A.** Total organic carbon (TOC, wt%). **B.** Total nitrogen (TN, wt%). **C.** Total organic carbon to total nitrogen (C/N) ratio. **D.** Calcium carbonate ($CaCO_3$, wt%). **E.** TOC-TN scatter plot (the intersection of the linear regression line and the *y*-axis (TN) gives an indication of the potential contribution of inorganic N to the TN signal; e.g., Schubert and Calvert, 2001).

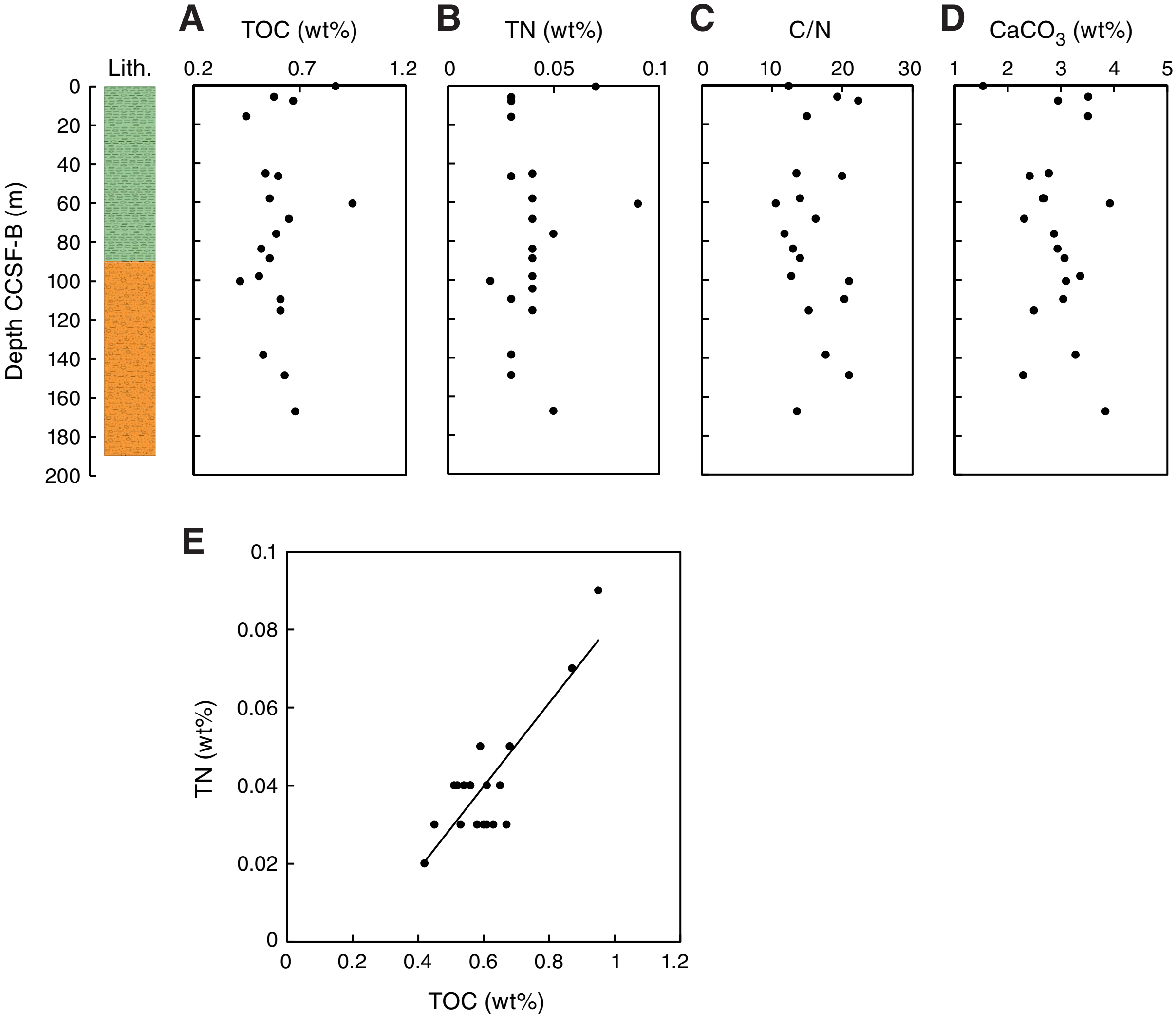

Figure F58. Core recovery, Site U1420. This site consists of a single deep borehole (U1420A).

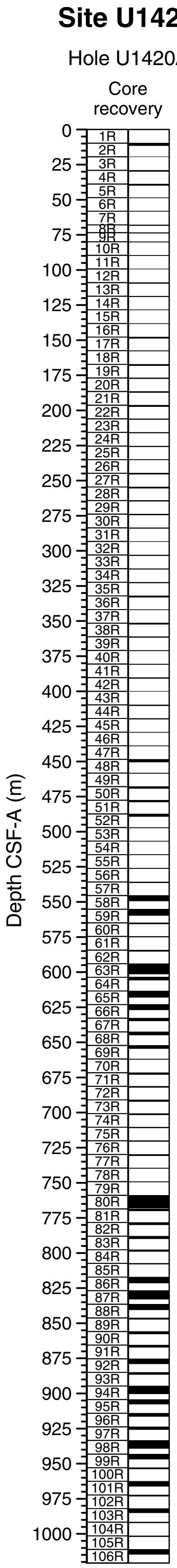

Figure F59. Core recovery, lithology, volcanic grain abundance, lithologic units, age, unit descriptions, and physical properties data, Hole U1420A. Volcanic grain abundance: 1 = trace, 2 = volcaniclastic bearing, 3 = volcaniclastic rich, 4 = ash. GRA = gamma ray attenuation.

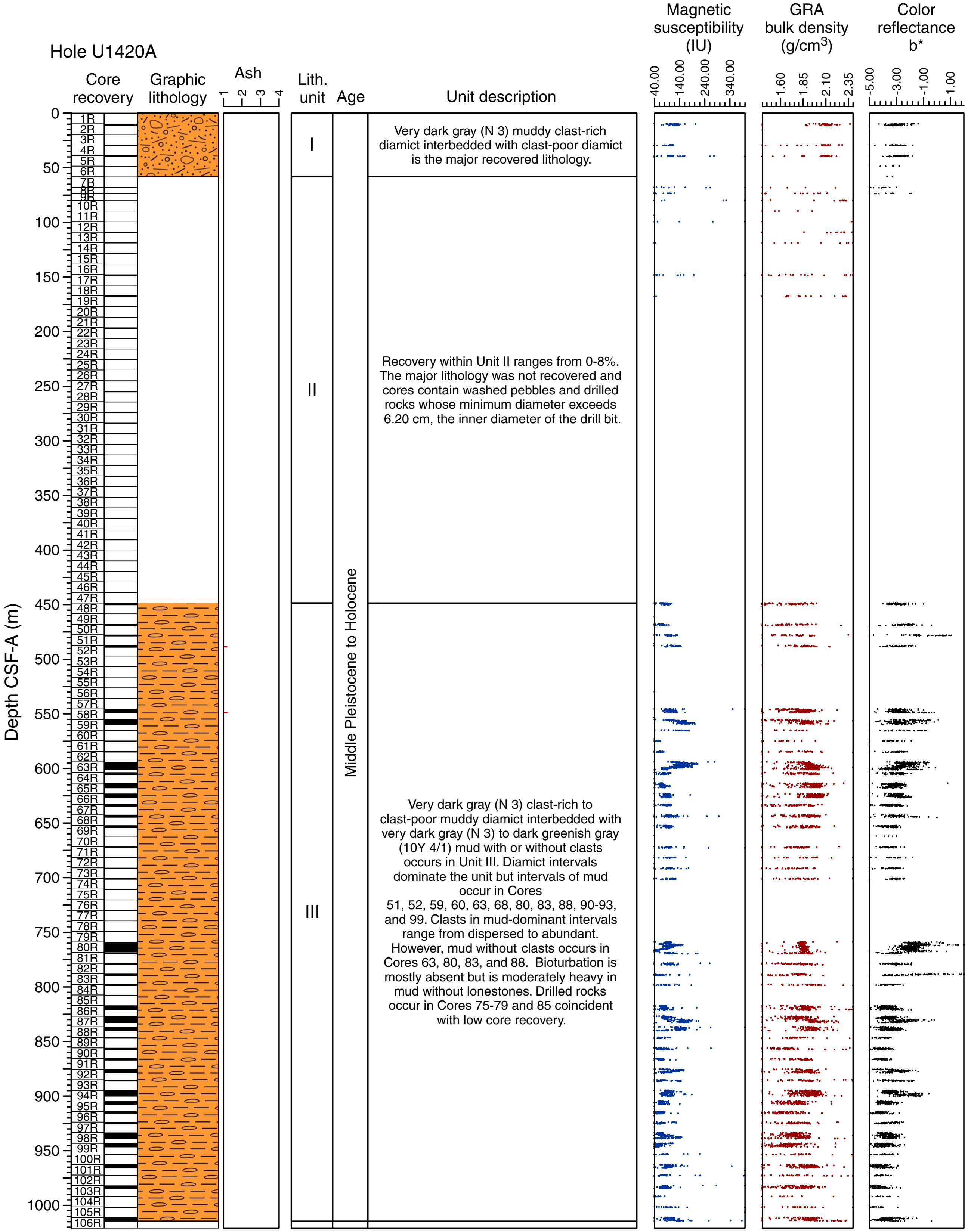

Very dark gray (N 3) muddy clast-rich diamict interbedded with clast-poor diamict is the major recovered lithology.

Recovery within Unit II ranges from 0-8%. The major lithology was not recovered and cores contain washed pebbles and drilled rocks whose minimum diameter exceeds 6.20 cm, the inner diameter of the drill bit.

Very dark gray (N 3) clast-rich to clast-poor muddy diamict interbedded with very dark gray (N 3) to dark greenish gray (10Y 4/1) mud with or without clasts occurs in Unit III. Diamict intervals dominate the unit but intervals of mud occur in Cores 51, 52, 59, 60, 63, 68, 80, 83, 88, 90-93, and 99. Clasts in mud-dominant intervals range from dispersed to abundant. However, mud without clasts occurs in Cores 63, 80, 83, and 88. Bioturbation is mostly absent but is moderately heavy in mud without lonestones. Drilled rocks occur in Cores 75-79 and 85 coincident with low core recovery.

Figure F60. Abundance and preservation of diatoms, radiolarians, and planktonic and benthic foraminifers, Site U1420. Abundance: D = dominant, A = abundant, C = common, F = few, R = rare, P or X = present, B = barren. Preservation: VG = very good, G = good, M = moderate, P = poor.

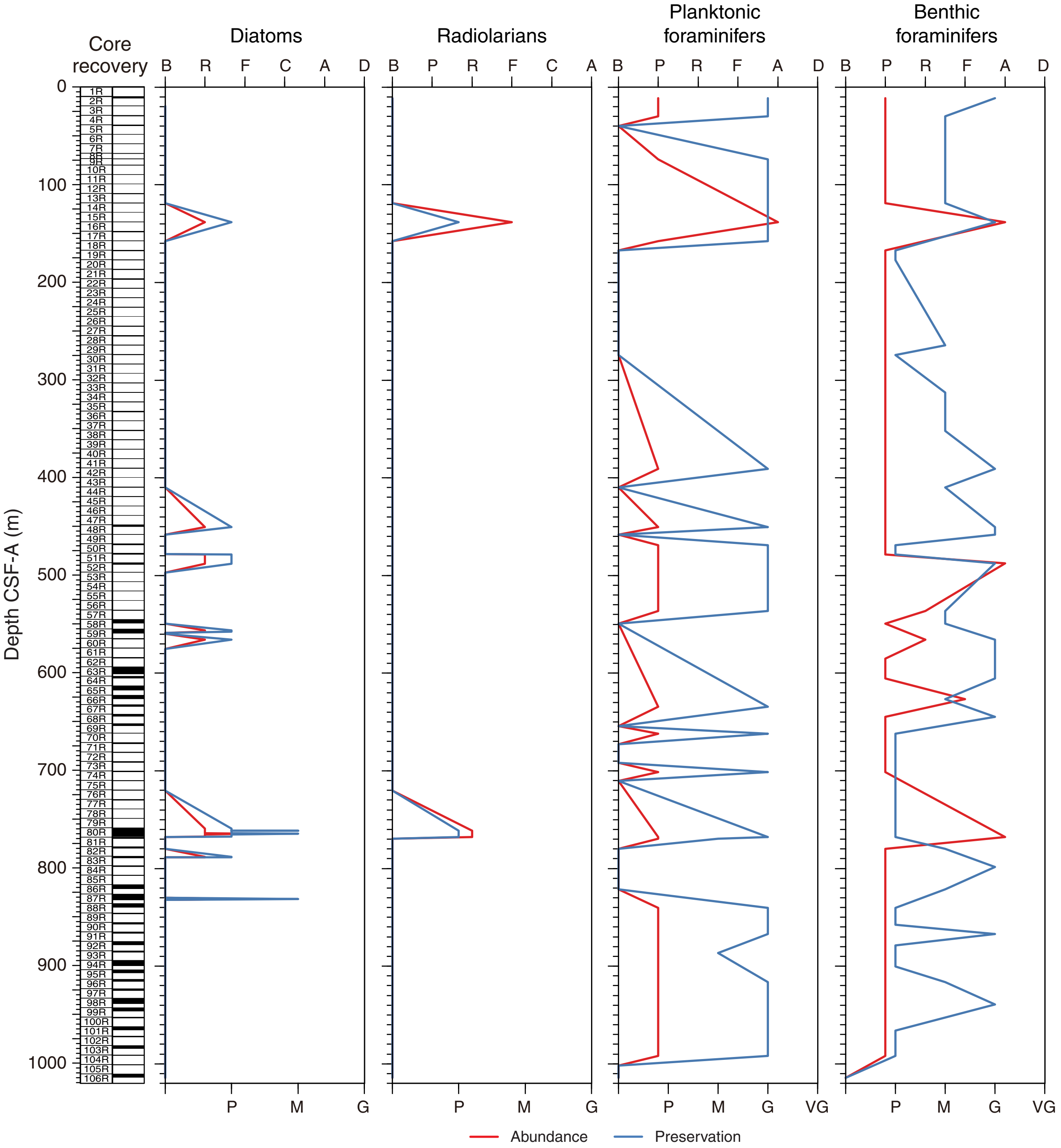

Figure F61. Integration of lithologic observations, and downhole logging and seismic data, Site U1420. Two-way traveltime is calculated from *P*-wave caliper measurements (PWC) and sonic log velocities. Velocities were interpolated using downhole sonic log values where no data were available.

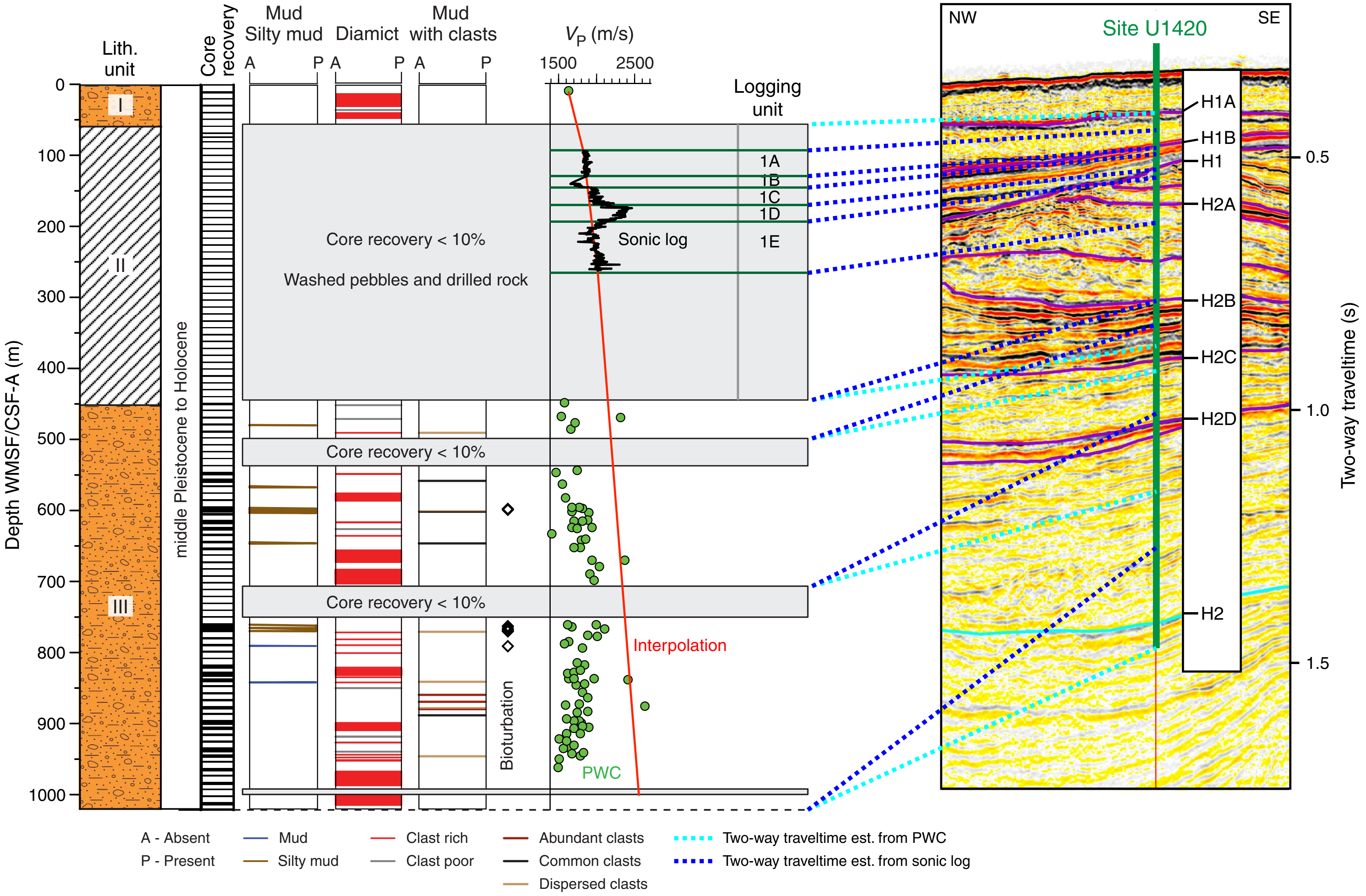

Figure F62. Bulk density, grain density, porosity, and void ratio measured using the moisture and density method, Hole U1420A.

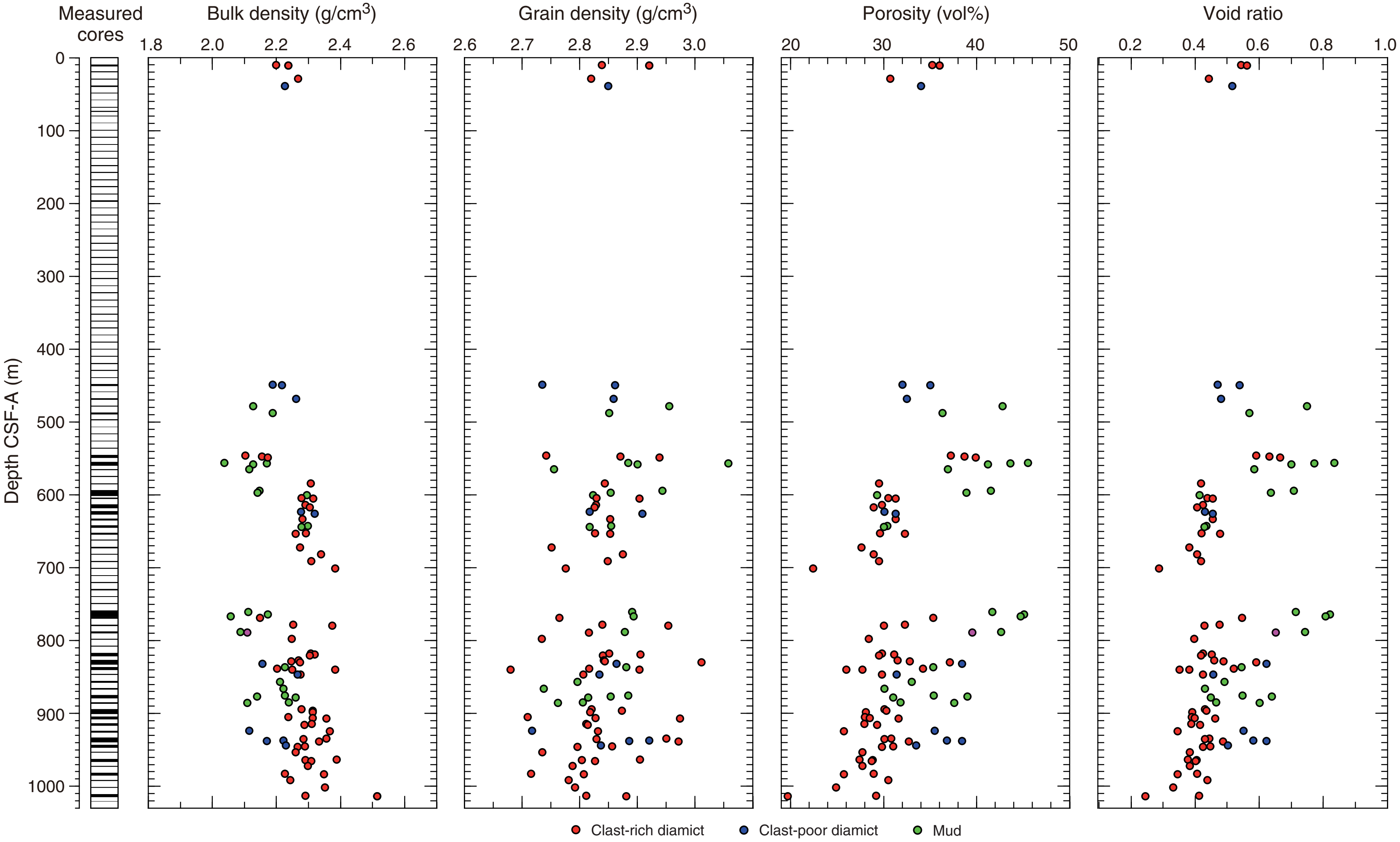

Figure F63. Chemical parameters determined in headspace and interstitial water samples, Hole U1420A. **A.** Alkalinity. **B.** pH. **C.** Sulfate. **D.** Ammonium. **E.** Bromide. **F.** Methane. **G.** Ethane. **H.** Silica. **I.** Salinity. **J.** Chloride. **K.** Sodium. Seawater values in I and J based on analyses of surface seawater sampled at Site U1420.

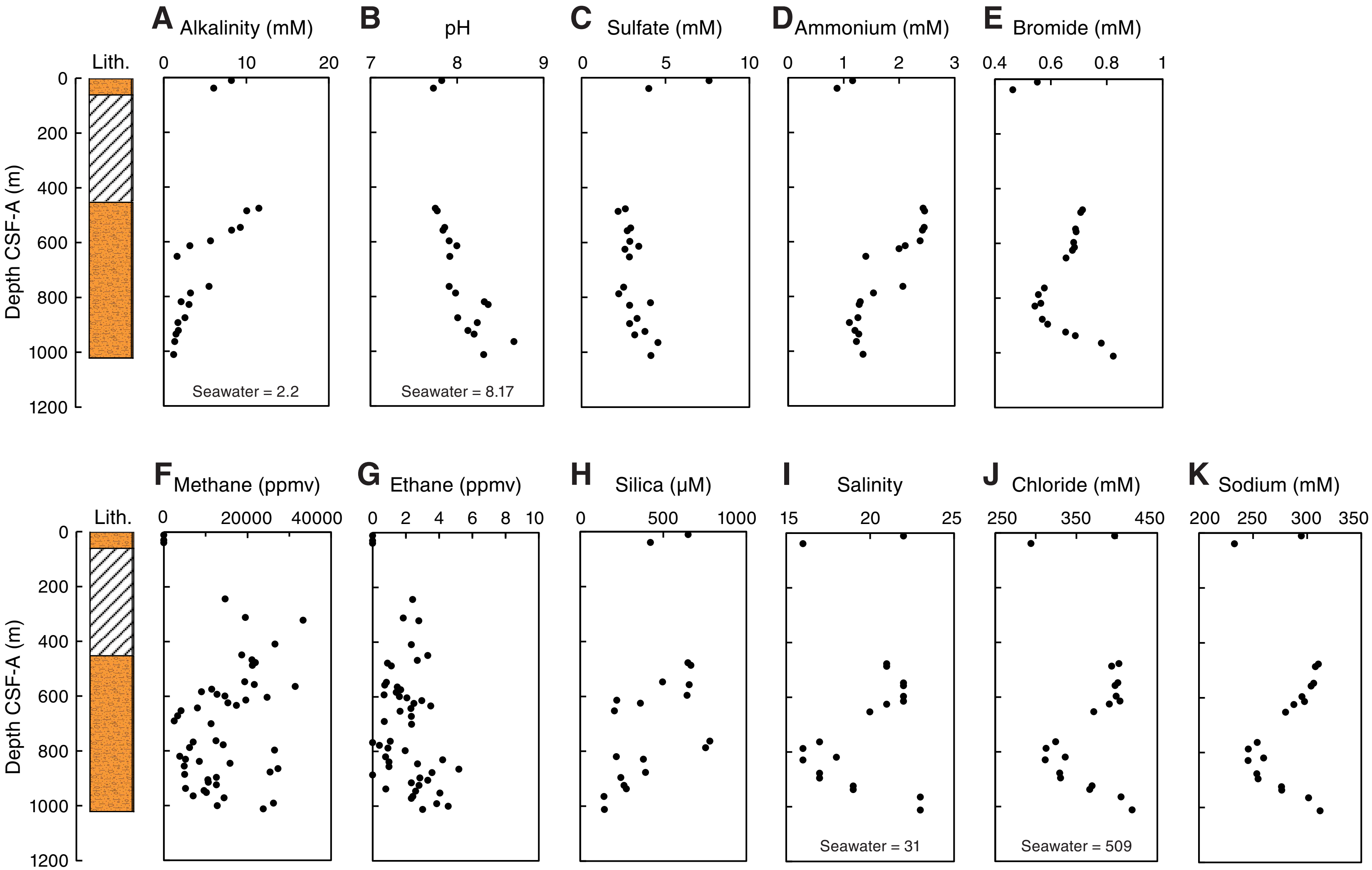

Figure F64. Summary of logs recorded by the sonic-induction tool string, Hole U1420A. Includes logs from the phasor dual induction–spherically focused resistivity tool: deep induction log (IDPH), medium induction log (IMPH), and shallow spherically focused resistivity log (SFLU). Also includes velocity logs and logging units.

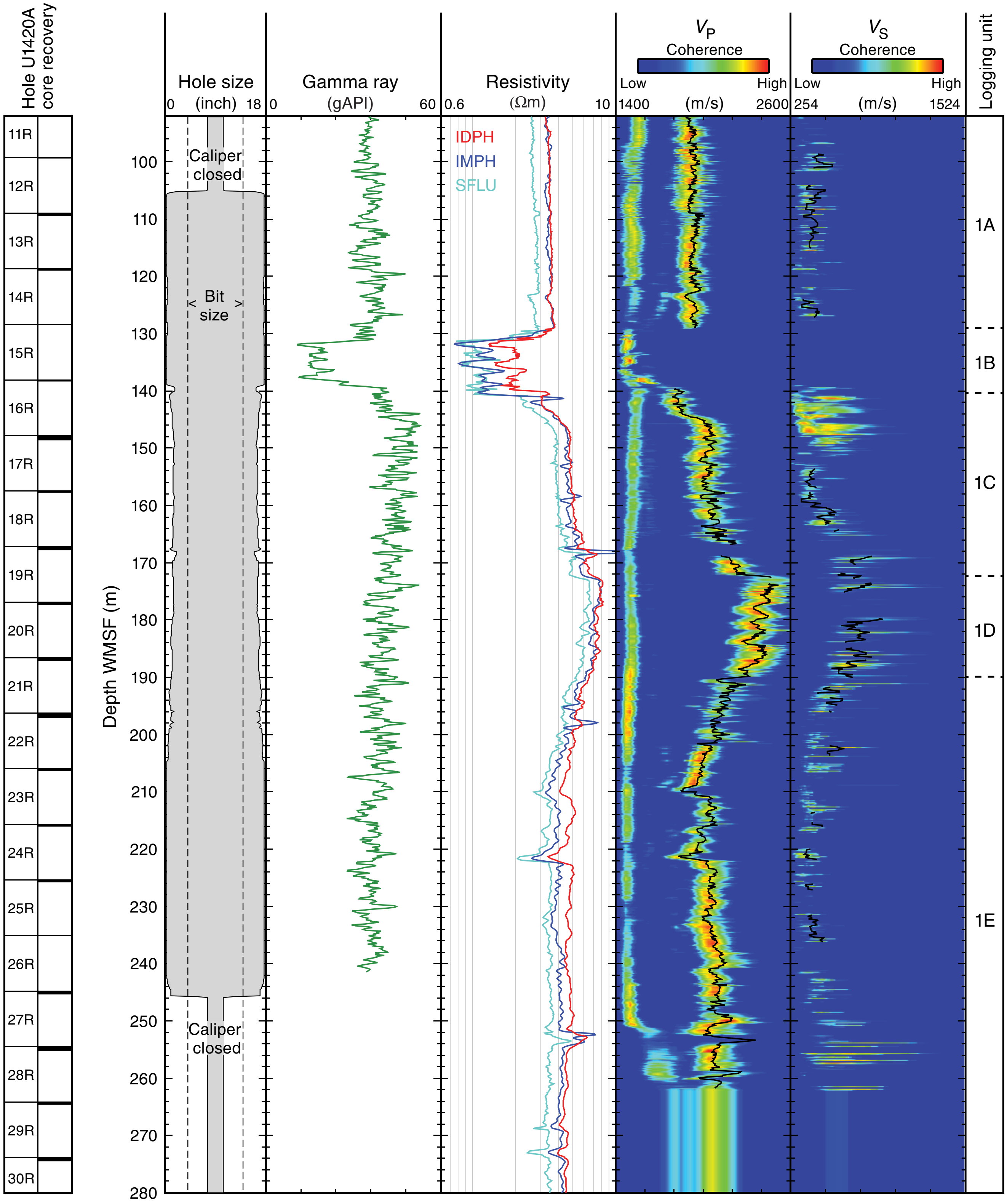

Figure F65. Hypothetical lithofacies motifs and facies succession for an upper slope location, such as Site U1421. Lithofacies are depicted by particle size variations with major facies types and sedimentary structures as described in the key. Associated columns are a descriptive summary for a facies, an inferred depositional environment, the major glacial systems tracts and bounding surfaces, and an inferred sediment accumulation rate. Modified from Powell and Cooper (2002). IRD = ice-rafted debris.

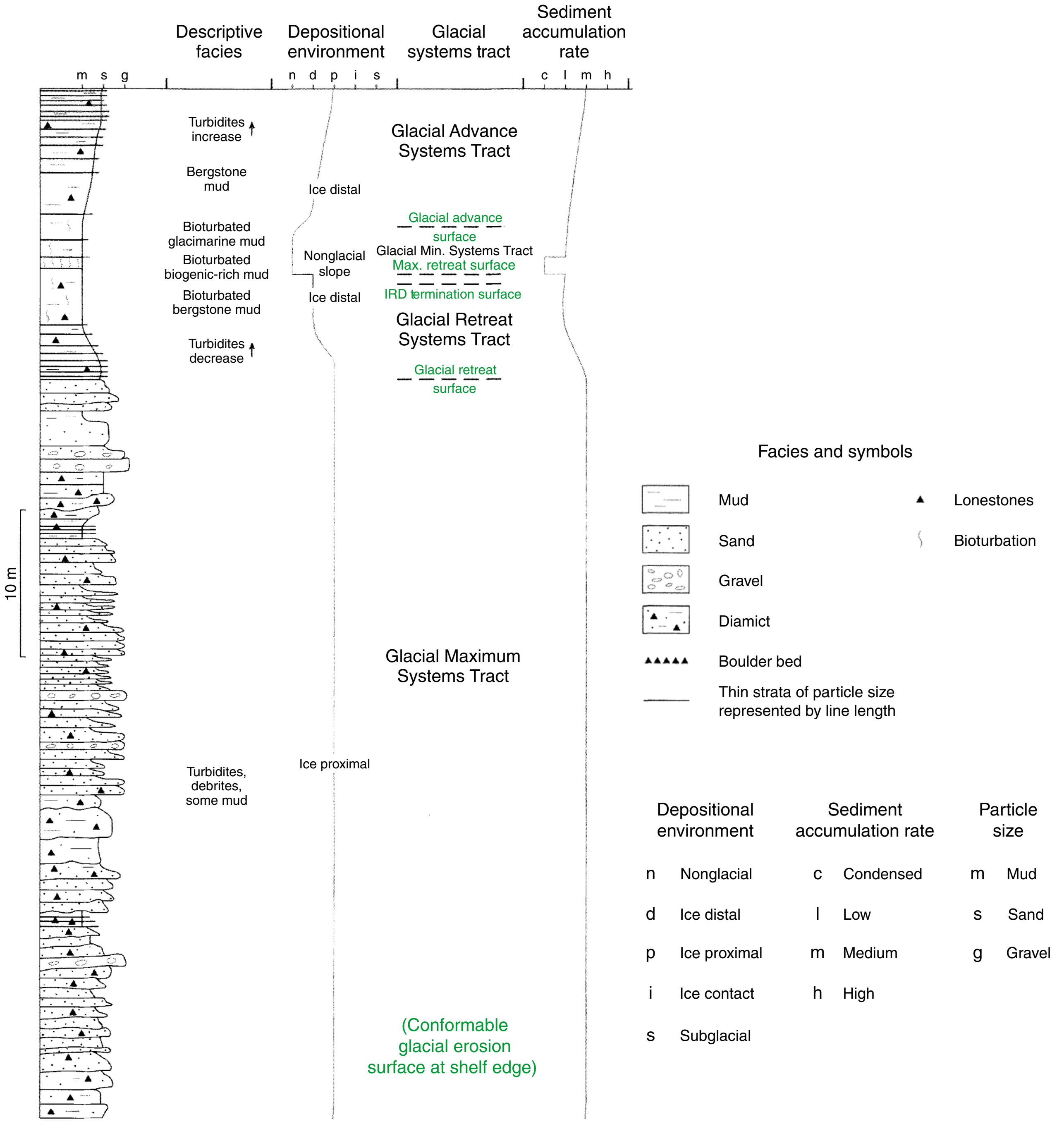

Figure F66. Core recovery, Site U1421.

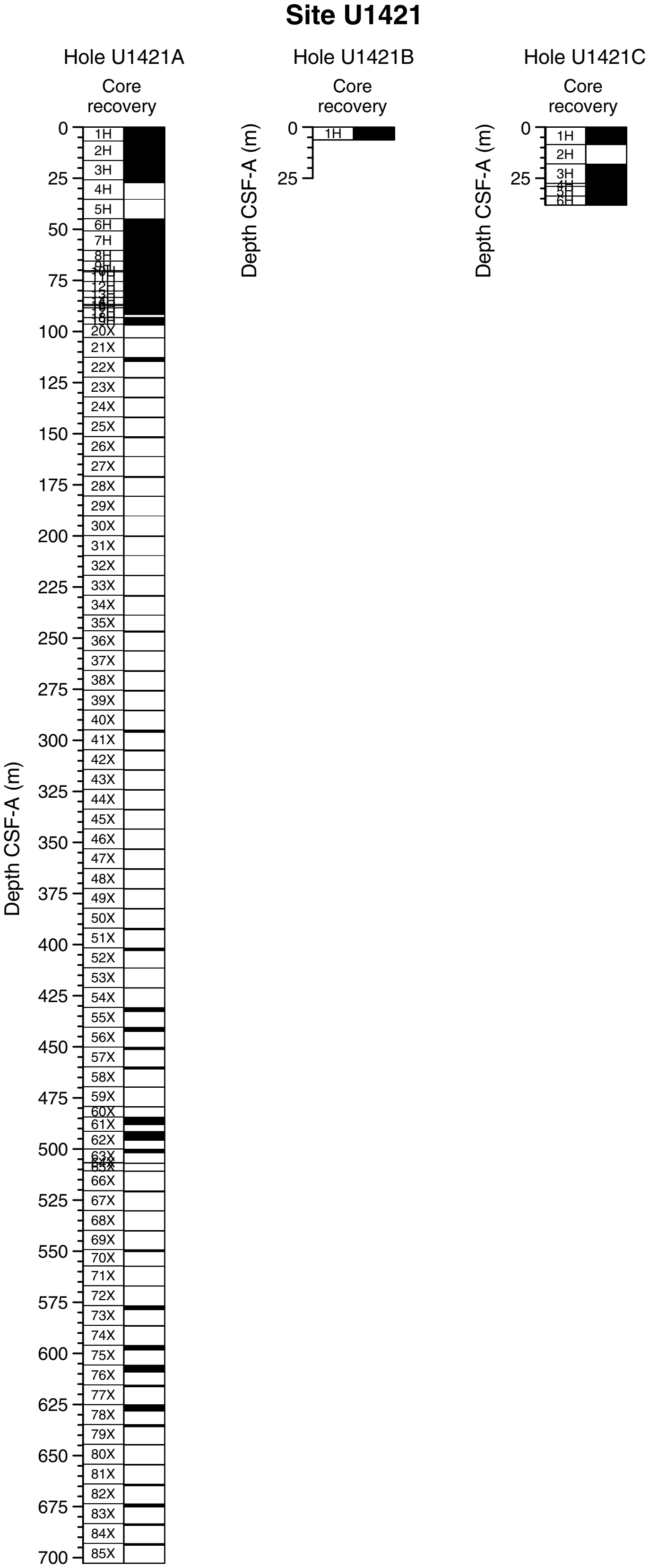

Figure F67. Variations of rank abundances of paleoenvironmental indicators, Site U1421. The right-hand scale applies only to planktonic foraminifers. Abundance: D = dominant, A = abundant, C = common, F = few, R = rare, P or X = present.

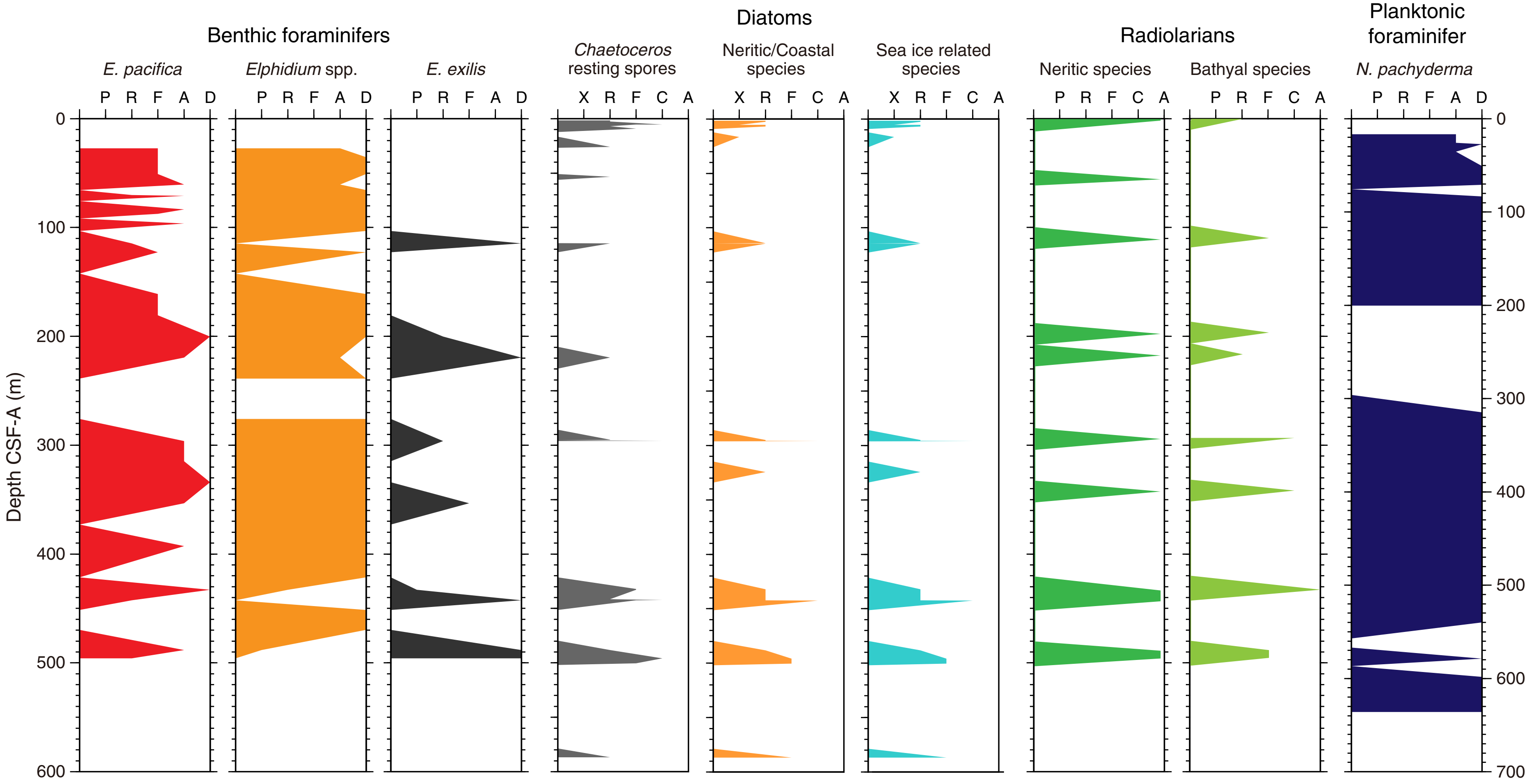

Figure F68. Natural remanent magnetization (NRM) intensities and inclination measured before and after 10 and 20 mT peak AF demagnetization, Hole U1421A.

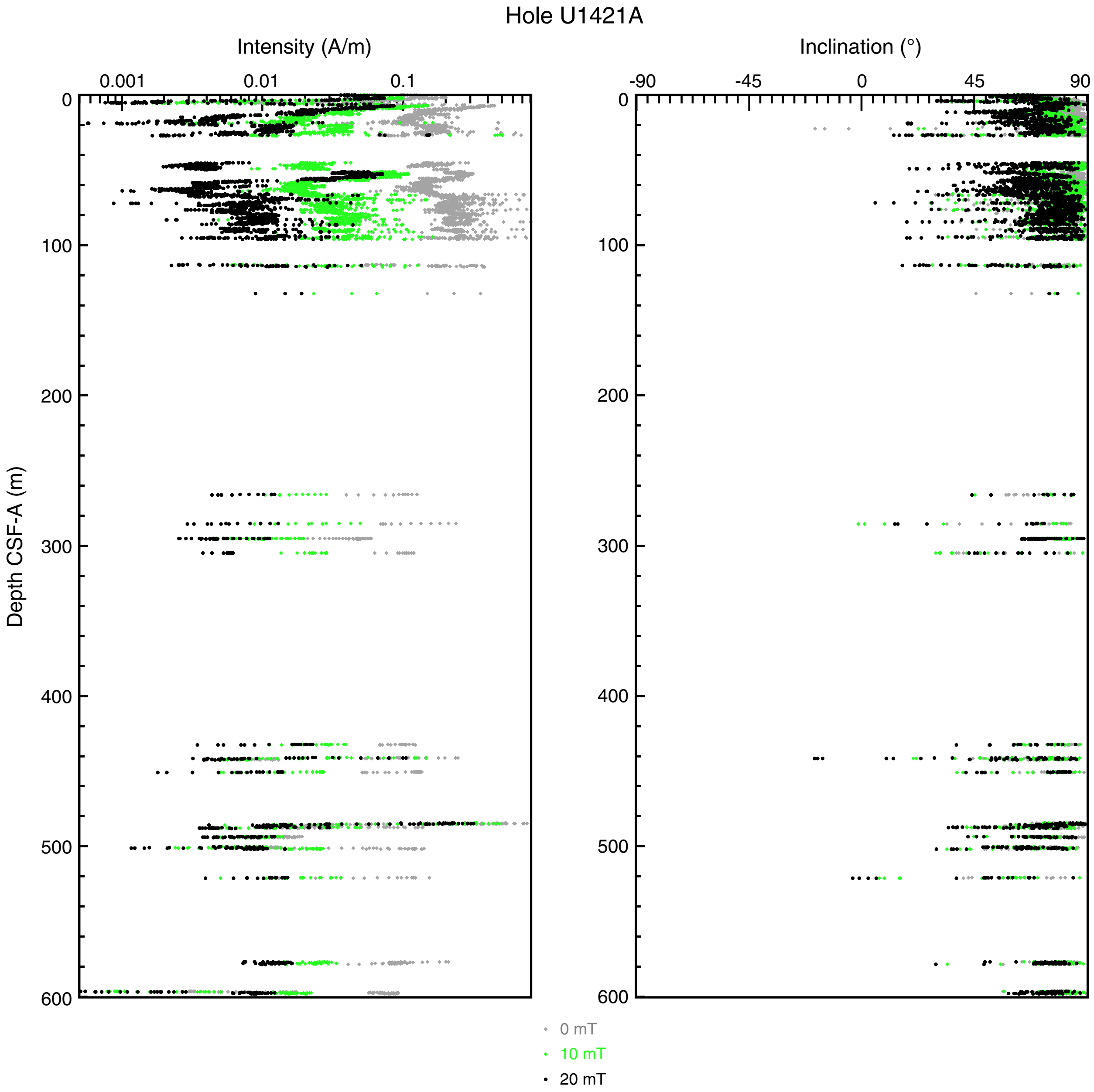

Figure F69. Chemical parameters determined in headspace and interstitial water samples, Hole U1421A. **A.** Alkalinity. **B.** pH. **C.** Sulfate. **D.** Ammonium. **E.** Bromide. **F.** Methane. **G.** Ethane. **H.** Silica. **I.** Salinity. **J.** Chloride. **K.** Sodium. Seawater values in I and J based on analyses of surface seawater sampled at Site U1421.

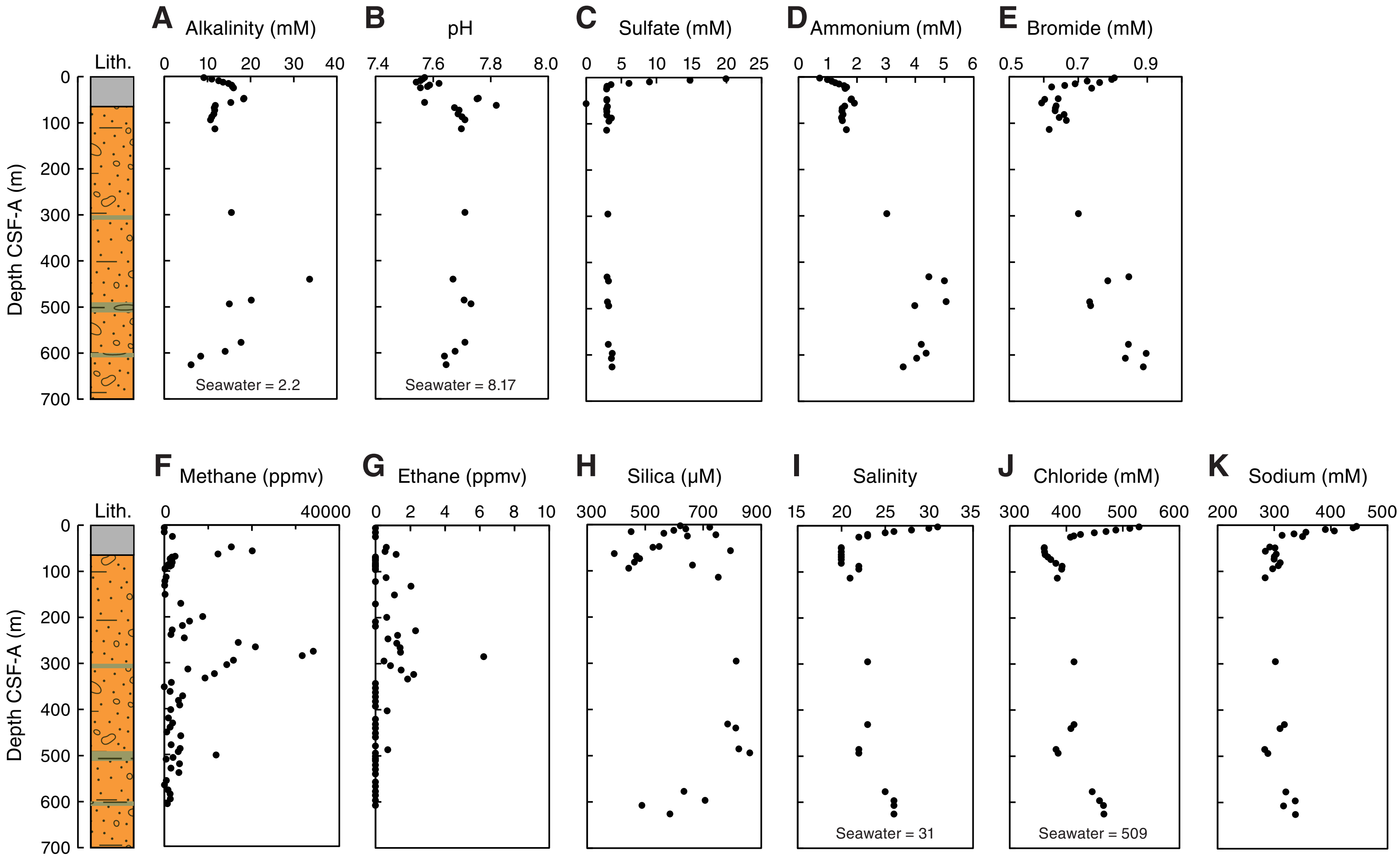

Figure F70. Summary of logs recorded by the sonic-induction tool string, Hole U1421A. Includes logs from the phasor dual induction–spherically focused resistivity tool: deep induction log (IDPH), medium induction log (IMPH), and shallow spherically focused resistivity log (SFLU). Logging units are also shown.

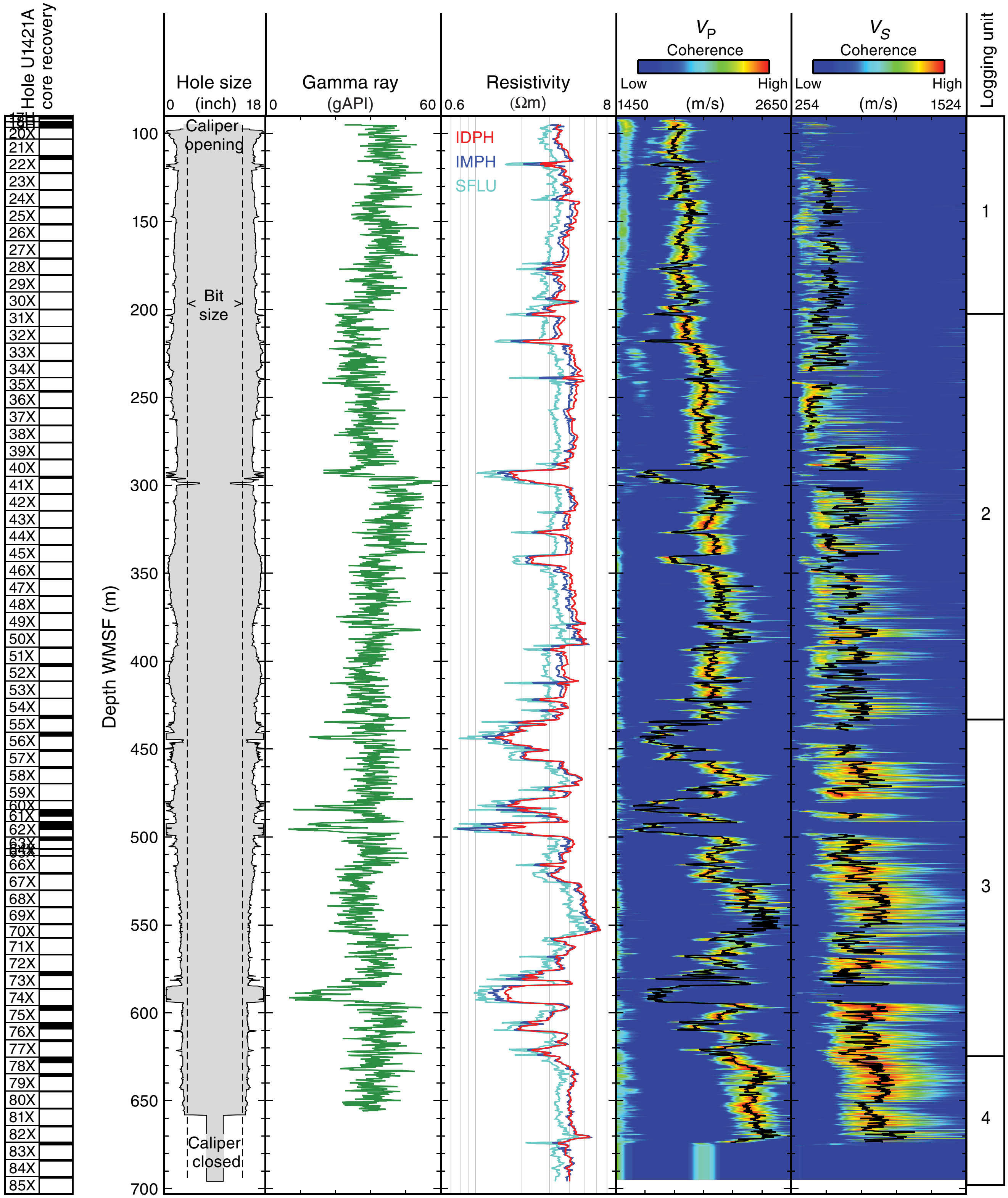

Table T1. Common lithofacies, Expedition 341. (Continued on next two pages.)

Main facies	Subfacies	Facies code	Description	Common marine microfossils	Sites of occurrence	Tentative depositional environment/diagenesis
Mud	Massive mud with lonestones	F1a	(Very) dark gray to (very) dark greenish gray; Varying amounts of lonestones from dispersed to abundant; Bioturbation mostly absent, but occasionally from slight to heavy; Occasional color banding and lamination; Occasional occurrence of silt/sand/granule pods; Occasional occurrence of black mottles and shell fragments; Rarely trace amounts of ash; May show signs of deformation and compaction at shelf-proximal sites	Diatoms, radiolarians, sponge spicules, foraminifers	U1417, U1418, U1419, U1420, U1421	Suspension fallout, ice rafting, or sediment gravity flows
	Massive mud without lonestones	F1b	(Dark) gray to (dark) greenish gray; Mostly massive, but occasional color banding and silt laminae; Bioturbation mostly absent; rarely slight to heavy; Occasional occurrence of black mottles, silt/sand pods, shell fragments, traces of ash, microorganisms and inclination; Often diatom bearing at Site U1421.	Rare diatoms and foraminifers	U1417, U1418, U1419, U1420, U1421	Suspension fallout or sediment gravity flows
	Laminated mud	F1c	(Dark) gray to (dark) greenish gray; Mostly none to slight bioturbation; Lamination resulting from slight color variations, presumably related to minor changes in grain size; Lamination mostly from sub-millimeter to 0.5 cm; occasional very thin bedding (<2.5 cm) possible Mostly gradational contacts; very rarely sharp; Rare lonestones;	Not documented	U1418	Suspension fallout, ice rafting, or sediment gravity flows
Silt	Silt	F2a	(Very) dark gray to greenish gray; Occasionally with lonestones and volcaniclastic bearing; Bioturbation mostly absent; Sharp to gradational upper and lower contacts; Plant debris and organic matter may occur; Massive or normally graded.	Occasional diatoms and foraminifers	U1417, U1418, U1419	Sediment gravity flows and possible ice rafting
	Interbedded/ Interlaminated silt and mud	F2b	(Very) dark gray to dark greenish gray; Mostly graded silt laminae (occasionally beds) with sharp lower and sharp to gradational upper contacts; Few to absent lonestones; Bioturbation mostly absent, but occasionally slight to moderate; Occasionally calcareous, diatom and volcaniclastic bearing.	Occasional diatoms	U1417, U1418, U1419	Mud: suspension fall-out from surface-water plumes and from sediment gravity flows Silt: sediment gravity flows
Sand	Very fine to coarse sand	F3a	(Very) dark gray to (very) dark greenish gray; Massive to normally graded; Mostly erosive lower contacts; Sharp and gradational upper contacts; Absent bioturbation Occasionally with diatoms and volcanic ash.	Occasionally diatoms and foraminifers	U1417, U1418, U1419	Sediment gravity flows
	Medium to coarse sand	F3b	Dark gray and to gray; With mud; Rip-up clasts common; Sharp bases and sharp to gradational upper contacts.	Barren	U1417	Sediment gravity flows
	Interbedded sand and mud	F3c	Dark gray; Interbedded (very) fine sand and mud occasionally with silt; Sand laminae and beds up to ~3.5 cm thick; Sandy beds typically graded and with erosive lower and sharp upper boundaries; Lonestones (<1 cm) occasionally present; Mostly no bioturbation; occasionally rare bioturbation.	Partly diatom bearing	U1417, U1419	Suspension fallout from surface-water plumes (mud), ice rafting (mud, sand, lonestones), and sediment gravity flows (sand, mud)

Table T1 (continued). (Continued on next page.)

Main facies	Subfacies	Facies code	Description	Common marine microfossils	Sites of occurrence	Tentative depositional environment/diagenesis
Diamict	Muddy diamict	F4a	(Very) dark gray to very dark greenish gray; Muddy matrix; Clast poor to clast rich; Mostly massive, but occasionally some centimeter-thick intervals with (<5 mm) thick laminae; Gradational lower contacts either sharp or defined by gradual increase in clast numbers; Sharp upper contacts due to marked drop in clast abundance; Bioturbation mostly absent; rarely moderate bioturbation; Rare color banding and volcanic ash.	Barren	U1417, U1418	Suspension settling and ice rafting (icebergs and/or sea ice)
	Muddy and sandy diamict with lithic and mud clasts and/or terrigenous organic components	F4b	Dark gray; Mud to sand matrix; Sharp upper and lower contacts; Lithic and mud clasts up to 12 cm; Occasional plant debris and terrestrial organic components (coal?).	Diatoms (partly freshwater)	U1417	Sediment gravity flows
	Breccia	F4c	Dark gray matrix of sandy mud; Sharp erosive lower contacts; Gradational upper contacts; Clasts of indurated diatom ooze.	Barren	U1417	Sediment gravity flows (e.g., slump)
	Interbedded mud and diamict	F4d	Dark gray to very dark gray; Diamict typically with sandy/gravelly mud matrix and up to 5 cm large clasts; Bioturbation mostly absent; occasionally slight or moderate bioturbation; Rare shell fragments and diatoms; Often gradational contacts between muddy and diamict intervals.	Rare diatoms	U1417, U1418, U1419, U1421	Suspension settling and ice rafting (icebergs and/or sea ice)
	Clast-poor diamict	F4e	(Very) dark gray; Often silty or sandy mud matrix; Occasional lamination/bedding due to (1) clayey laminae and (2) sand/granule laminae (<4 mm thick); Bioturbation absent; occasional shell fragments; Rare mud and clast pods of coarse sand; Very rare traces of volcanic ash; Subrounded to subangular granule and pebble clasts including argillite, basalt, shale, chert, conglomerate, diorite, feldspar, gneiss, granite, greenstone, greywacke, metasediment with quartz veins, mudstone, quartz, rhyolite, sandstone (massive and laminated), siltstone.	Not documented	U1419, U1420, U1421	Suspension settling and ice rafting (mainly by icebergs)
	Clast-rich diamict	F4f	(Very) dark gray; Mostly muddy or sandy mud matrix; Bioturbation absent; Very rarely trace amounts of volcanic ash and shell fragments; Interstratification with mud laminae/beds possible (mud laminae may contain diatoms); Subrounded to subangular granule and pebble clasts including argillite, basalt, shale, chert, conglomerate, diorite, feldspar, gneiss, quartzite, gabbro, vesicular basalt, granite, greenstone, greywacke, metasandstone, metasiltstone, metasediment with quartz veins, mudstone, quartz, rhyolite, sandstone, siltstone, quartz-mica schist, metasedimentary breccia.	Rare diatoms and foraminifers	U1419, U1420, U1421	Suspension settling and ice rafting (mainly by icebergs)
Diatom ooze		F5a	(Very) dark greenish gray, very dark grayish brown, and olive-gray; Sharp to gradational lower and upper contacts; Absent to heavy bioturbation; Occasional lamination or very thin bedding; Lonestones mostly absent, but occasionally present; Occasional black mottles and shell fragments; Occasionally trace amounts of volcanic ash.	Diatoms and occasional radiolarian and sponge spicules; occasional carbonate (foraminifers and coccolithophores	U1417, U1418, U1419, U1421	High-productivity environment and/or low terrigenous input and/or better preservation

Table T1 (continued).

Main facies	Subfacies	Facies code	Description	Common marine microfossils	Sites of occurrence	Tentative depositional environment/diagenesis
Biosiliceous ooze; biosiliceous-rich/bearing mud and/or sand; mud with diatoms/biosilica		F5b	(Very) dark gray to (very) dark greenish gray; Mostly in mud with absent to abundant clasts; Bioturbation mostly absent, but very rarely slight to heavy; Rare shell fragments, traces of volcanic ash, black mottles, and lamination.	Diatoms, sponge spicules, foraminifers, nannofossils	U1417, U1418, U1419, U1420, U1421	Temporarily increased productivity and/or reduced suspension settling and/or better preservation
Calcareous/Carbonate- bearing/rich mud, silt, sand, diamict, and/or diatom ooze		F5c	Gray, dark gray, very dark gray, dark greenish gray and very dark greenish gray, grayish green; Bioturbation from absent to heavy; Lonestones and black mottles occasionally present; Very rarely laminated or traces of volcanic ash.	Foraminifers, nannofossils; occasionally diatoms	U1417, U1418, U1419, U1420, U1421	Temporarily increased productivity and/or reduced suspension settling and/or better preservation
Ash	Volcanic ash	F6	Gray to brown; Sharp lower contacts; Sharp to gradational upper contacts; Primarily vitric shards (glass); Some intervals affected by moderate to heavy bioturbation so that distinct ash layers are occasionally no longer visible, but the material is included in burrow fill; Occasionally also without bioturbation.	Not documented	U1417, U1418, U1419	Suspension settling after subaerial eruptions
Volcaniclastic mud, sand, diamict, and/or ooze		F7	Gray, dark gray, very dark gray, dark greenish gray, and brown; Includes volcaniclastic rich/bearing or trace amounts of volcanic ash; Bioturbation mostly absent, but occasionally slight to heavy; Primarily vitric shards (glass); Gradational and sharp contacts; Often in association with mud with higher amounts of biosiliceous and calcareous components.	Biosiliceous and calcareous microfossils	U1417, U1418, U1419, U1420, U1421	Volcanic detritus either bioturbated or reworked/redeposited by sediment gravity flows
Rock		F8	Light to very dark gray siltstone and sandstone, most often with carbonate cement; Size: 1–6 cm thick, generally covering the entire core width; may include “flame structures” intruding into surrounding mud.	Not documented	U1417, U1418	In situ carbonate cementation
Intrastratal contorted mud and diamict		F9	Very dark greenish gray mud mixed with very dark greenish gray clast-rich muddy diamict; Intrastratal contortion and normal faults occur; Absent bioturbation.	Not documented	U1418	Sediment gravity flow

Table T2. Coring summary, Expedition 341.

Hole	Latitude	Longitude	Depth (mbrf)	Cores (*N*)	Cored (m)	Recovered (m)	Recovery (%)	Drilled (m)	Total penetration (m)	Total depth (mbrf)	Time on hole (h)	Time on site (days)
341-												
U1417A	56°57.5996′N	147°6.5985′W	4198.6	22	168.0	167.74	99.8	0.0	168.0	4366.6	46.50	
U1417B	56°57.5999′N	147°6.5781′W	4200.7	47	358.8	262.96	73.3	0.0	358.8	4559.5	79.30	
U1417C	56°57.5888′N	147°6.5769′W	4199.0	28	225.0	216.83	96.4	1.0	226.0	4425.0	38.75	
U1417D	56°57.5896′N	147°6.5973′W	4198.0	64	466.5	304.42	65.3	0.8	470.3	4668.3	127.00	
U1417E	56°57.5896′N	147°6.5993′W	4199.5	37	348.7	146.92	42.1	360.8	709.5	4909.0	155.25	
			Site U1417 totals:	198	1567.0	1098.87	70.1	362.6	1932.6			18.61
U1418A	58°46.6095′N	144°29.5777′W	3679.2	33	209.9	216.85	103.3	0.0	209.9	3889.1	45.00	
U1418B	58°46.6100′N	144°29.5559′W	3678.7	2	17.0	17.08	100.5	0.0	17.0	3695.7	3.50	
U1418C	58°46.5991′N	144°29.5570′W	3677.0	32	228.2	229.48	100.6	2.5	230.7	3907.7	39.75	
U1418D	58°46.5993′N	144°29.5579′W	3677.5	36	302.8	279.77	92.4	3.0	305.8	3983.3	49.75	
U1418E	58°46.5890′N	144°29.5771′W	3678.7	11	100.6	98.70	98.1	81.0	181.6	3860.3	34.00	
U1418F	58°46.5883′N	144°29.5986′W	3678.0	71	688.7	495.20	71.9	260.0	948.7	4626.7	213.50	
			Site U1418 totals:	185	1547.2	1337.08	86.4	346.5	1893.7			16.06
U1419A	59°31.9297′N	144°8.0282′W	698.6	29	193.0	111.24	57.6	0.0	193.0	891.6	30.50	
U1419B	59°31.9309′N	144°8.009′W	698.3	18	113.0	99.05	87.7	1.0	114.0	812.3	15.92	
U1419C	59°31.9204′N	144°8.0079′W	697.0	19	107.1	100.37	93.7	2.0	109.1	806.1	18.83	
U1419D	59°31.9200′N	144°8.0515′W	698.7	20	103.7	105.10	101.4	10.5	114.2	812.9	17.75	
U1419E	59°31.9310′N	144°8.0474′W	696.7	15	75.5	72.10	95.5	23.2	98.7	795.4	16.25	
			Site U1419 totals:	101	592.3	487.86	82.4	36.7	629.0			4.14
U1420A	59°41.3399′N	143°12.0599′W	259.4	106	1020.8	139.91	13.7	0.0	1020.8	1280.2	189.25	
			Site U1420 totals:	106	1020.8	139.91	13.7	0.0	1020.8			7.90
U1421A	59°30.4399′N	143°2.7395′W	729.7	85	702.7	140.72	20.0	0.0	702.7	1432.4	134.75	
U1421B	59°30.4284′N	143°2.7188′W	733.9	1	6.2	6.23	100.5	0.0	6.2	740.1	2.25	
U1421C	59°30.4298′N	143°2.7387′W	733.0	6	38.2	29.06	76.1	0.0	38.2	771.2	18.00	
			Site U1421 totals:	92	747.1	176.01	23.6	0.0	747.1			6.50
			Expedition 341 totals:	682	5474.4	3239.73	59.2	745.8	6223.2			53.21